University of Southampton

Faculty of Engineering and Physical Sciences
School of Engineering

Modelling and Analysis of High-Enthalpy Effects Coupled with Turbulence Using Direct Numerical Simulation

DOI: 10.5258/SOTON/PG/T108

by

Ali Musawi

MEng

ORCiD: 0000-0002-1975-4270

Final thesis for the degree of
Doctor of Philosophy

May 2026

University of Southampton

Abstract

Faculty of Engineering and Physical Sciences
School of Engineering

Doctor of Philosophy

Modelling and Analysis of High-Enthalpy Effects Coupled with Turbulence Using Direct Numerical Simulation

by Ali Musawi

Motivated by renewed interest in hypersonic flight, this work investigates the influence of thermo-chemical non-equilibrium on turbulent flows and evaluates key modelling approximations using scale-resolved simulations based on a multi-species compressible Navier–Stokes framework with finite-rate chemistry and multi-temperature formulations. Firstly, thermo-chemical non-equilibrium effects were examined through simulations of free shear mixing layers. Two-dimensional simulations showed reductions in turbulent kinetic energy of up to 8% under non-equilibrium conditions. In three-dimensional mixing layers, Reynolds stresses were largely unaffected; however, analysis of additional vibrational energy flux terms revealed that thermal non-equilibrium suppresses vibrational fluctuations due to weakened coupling between translational and vibrational modes. To support efficient high-enthalpy scale-resolved simulations, a streamlined viscosity and thermal conductivity model for air mixtures over 100–9000 K was developed. Compared with existing efficient formulations, the proposed model demonstrated improved accuracy under strongly non-equilibrium conditions, while achieving computational cost reductions of up to 45% in two-dimensional and 58.5% in three-dimensional simulations relative to the benchmark model. Finally, turbulent channel-flow simulations under thermo-chemical non-equilibrium were performed to assess high-enthalpy effects in a canonical wall-bounded configuration. Strong near-wall temperature gradients indicated thermally frozen behaviour. While thermal non-equilibrium had minimal impact on mean flow statistics, chemical non-equilibrium led to reduced local Mach number and temperature fluctuations due to steep nitrogen mass-fraction gradients. Overall, this study provides a systematic assessment of thermo-chemical non-equilibrium effects on turbulence across canonical flow configurations and establishes a robust foundation for high-fidelity modelling of high-enthalpy turbulent flows.

Contents

List of Figures

List of Tables

Declaration of Authorship

I declare that this thesis and the work presented in it is my own and has been generated by me as the result of my own original research.

I confirm that:

1. This work was done wholly or mainly while in candidature for a research degree at this University;
2. Where any part of this thesis has previously been submitted for a degree or any other qualification at this University or any other institution, this has been clearly stated;
3. Where I have consulted the published work of others, this is always clearly attributed;
4. Where I have quoted from the work of others, the source is always given. With the exception of such quotations, this thesis is entirely my own work;
5. I have acknowledged all main sources of help;
6. Where the thesis is based on work done by myself jointly with others, I have made clear exactly what was done by others and what I have contributed myself;
7. Parts of this work have been published as:
   A. Musawi and N. D. Sandham. Efficient Viscosity and Thermal Conductivity Formulation for Scale-Resolved Hypersonic Flow Simulations. *American Institute of Aeronautics and Astronautics*, 63(12), 2025. doi: https://doi.org/10.2514/1.J065564. URL `https://arc.aiaa.org/doi/full/10.2514/1.J065564`
   A. Musawi and N. D. Sandham. Effects of thermal non-equilibrium during transition to turbulence of a high enthalpy free shear layer. *Physics of Fluids*, 38(1):15157, 1 2026. ISSN 1070-6631. doi: 10.1063/5.0311454. URL `/aip/pof/article/38/1/015157/3378029/Effects-of-thermal-non-equilibrium-during`

Signed:..... Date:.....

Acknowledgements

I extend my deepest respect and appreciation to my supervisor, Prof. Neil D. Sandham, for his invaluable expertise and guidance throughout this lengthy research endeavour. His quiet patience, productive support, and forensic feedback has been transformative in both this project and my growth as a researcher. I also express my gratitude to Prof. Minkwan Kim for his insightful feedback regarding my work, and to Prof. Ralf Deiterding for providing me with an academic assistantship that firmly grounded me in the field of hypersonics.

I would like to thank my colleagues and friends, Teja Ala and Max Walker, for their intelligent problem-solving and wild discussions; they have been an essential support circle throughout this experience. You guys are some real smart-cookies! I am also grateful to Dr David Lusher and Dr Pushpender Sharma for their assistance in using OpenSBLI. In addition, I thank the university's HPC team for their timely support and technical guidance.

Most importantly, I thank my wife, whose unwavering belief in me was a constant source of comfort and strength throughout this journey. I am deeply grateful to my parents and siblings for nurturing my love of engineering and for their enduring patience during my studies.

Finally, I would like to thank Alex, who accompanied me in taking my first step towards pursuing engineering.

To those who are no longer here

Definitions and Abbreviations

Abbreviations

CF	Chemically Frozen
CFD	Computational Fluid Dynamics
CNE	Chemical Non-Equilibrium
DMS	Direct Molecular Simulation
DNS	Direct Numerical Simulation
EQ	Equilibrium
HT	High Temperature
LT	Low Temperature
MT	Multi-Temperature
PES	Potential Energy Surface
QCT	Quasi-Classical Trajectory
StS	State-to-State
TCNE	Thermo-Chemical Non-Equilibrium
TNE	Thermal Non-Equilibrium

Symbols

C_p	Constant pressure specific heat	$[\mathrm{J}/(\mathrm{kg}\cdot\mathrm{K})]$
D_s	Species diffusion coefficient	$[\mathrm{m}^2/\mathrm{s}]$
$\hat{D}_s$	Average vibrational energy (depletion term)	$[\mathrm{J}/\mathrm{kg}]$
E	Total energy per unit mass	$[\mathrm{J}/\mathrm{kg}]$
E_e	Translational energy of free electrons	$[\mathrm{J}]$
$E_{el,s}$	Species electronic energy	$[\mathrm{J}]$
e_r	Rotational energy per unit mass	$[\mathrm{J}/\mathrm{kg}]$
e_t	Translational energy per unit mass	$[\mathrm{J}/\mathrm{kg}]$
e_v	Total vibrational energy per unit mass	$[\mathrm{J}/\mathrm{kg}]$
$e_{v,s}$	Species vibrational energy per unit mass	$[\mathrm{J}/\mathrm{kg}]$
H	Enthalpy per unit mass	$[\mathrm{J}/\mathrm{kg}]$
h_s	Species enthalpy per unit mass	$[\mathrm{J}/\mathrm{kg}]$
$h_{f,s}$	Species enthalpy of formation	$[\mathrm{J}/\mathrm{kg}]$
K	Mixture thermal conductivity	$[\mathrm{W}/(\mathrm{m}\cdot\mathrm{K})]$
K_c	Equilibrium constant (concentration)	$[\mathrm{mol}/\mathrm{m}^3]^{\Delta \mathrm{n}}$

K_{int}	Internal thermal conductivity	$[\mathrm{W/(m \cdot K)}]$
K_p	Equilibrium constant (partial pressure)	$[\mathrm{Pa}]^{\Delta \mathrm{n}}$
K_{rot}	Rotational thermal conductivity	$[\mathrm{W/(m \cdot K)}]$
K_s	Species thermal conductivity	$[\mathrm{W/(m \cdot K)}]$
K_{tr}	Translational thermal conductivity	$[\mathrm{W/(m \cdot K)}]$
k	Boltzmann constant (1.380649×10^{-23})	[J/K]
M_s	Species molar mass	[kg/mol]
m	Mean molecular mass	[kg]
n_t	Total number density	$[\mathrm{m}^{-3}]$
P	Pressure	[Pa]
Q	Partition function	–
$R_{b,r}$	Backward reaction rate	$\left[\mathrm{mol/(m^3 \cdot s)}\right]^{\Delta \mathrm{n}}$
$R_{f,r}$	Forward reaction rate	$\left[\mathrm{mol/(m^3 \cdot s)}\right]^{\Delta \mathrm{n}}$
R_s	Species gas constant	$[\mathrm{J/(kg \cdot K)}]$
$\mathscr{R}$	Universal gas constant	$[\mathrm{J/(mol \cdot K)}]$
T_a	Multi-temperature model parameter	[K]
T_f	Activation temperature	[K]
T_r	Rotational temperature	[K]
T_t	Translational temperature	[K]
T_{tr}	Translational-rotational temperature	[K]
T_v	Vibrational temperature	[K]
X_s	Species mole fraction	–
Y_s	Species mass fraction	–

Greek symbols

$\alpha_{s,r}$	Reactant stoichiometric coefficient	–
$\beta_{s,r}$	Product stoichiometric coefficient	–
$\Theta_{v,s}$	Species vibrational characteristic temperature	[K]
μ	Mixture viscosity	$[\mathrm{N \cdot s/m^2}]$
μ_s	Species viscosity	$[\mathrm{N \cdot s/m^2}]$
μ_{sj}	Reduced mass of colliding pair	[kg/mol]
ν	Stoichiometric coefficient	–
ρ	Mixture density	$[\mathrm{kg/m^3}]$
ρ_s	Species density	$[\mathrm{kg/m^3}]$
σ_v	Excitation cross section	$[\mathrm{m^2}]$
τ_s	Species vibrational relaxation time	[s]
$\dot{\omega}_s$	Production rate of species s	$[\mathrm{kg/(m^3 \cdot s)}]$

Chapter 1

Introduction

Since the turn of the 21st century, the privatisation of the space industry has ushered in a new era of space missions. An increasing number of private companies—most notably SpaceX, Blue Origin, and Virgin Galactic—have entered the sector with the objective of reducing launch costs through technological innovations such as reusable launch vehicles, thereby improving access to space. High-profile milestones, including SpaceX's reusable Falcon 9 landings and crewed Dragon missions, as well as suborbital tourist flights conducted by Blue Origin and Virgin Galactic, have revitalised public interest and inspired a new generation of engineers. This commercial momentum has been accompanied by a substantial increase in launch activity. In the early 2000s, global orbital launch attempts numbered approximately 60–70 per year; by contrast, 2025 marked a record year with around 329 launch attempts, of which 321 successfully reached orbit or marginal orbits (Klotz, 2026). This sustained growth underscores the increasing importance of accurately modelling the extreme flow environments associated with atmospheric ascent and re-entry. In this context, the ability to simulate high-enthalpy flows with high fidelity has become increasingly critical.

Beyond civilian and commercial applications, the accurate characterisation of hypersonic flow conditions has also gained strategic importance in the military domain. This is driven by the development of hypersonic vehicles, particularly boost-glide systems. A boost-glide vehicle—also referred to as a hypersonic glider or waverider—shares certain similarities with intercontinental ballistic missiles (ICBMs), but operates along lower-altitude trajectories and exhibits significant manoeuvrability, rendering detection and interception more challenging (Lin et al., 2025). Research into such systems dates back to the mid-20th century and remains an active area of investigation. The United States has conducted several flight tests under programmes such as the Hypersonic Technology Vehicle 2 (HTV-2), while China and Russia are also believed to have made notable advances in hypersonic weapon capabilities (Lin et al., 2025; McFarland, 2023; Kessler, 2022; Sevastopulo and Hille, 2021). In light of recent geopolitical developments, a comprehensive understanding of the thermo-chemical and aerodynamic environments

encountered by these vehicles is essential, both for their design and for the development of effective interception and defence strategies.

The importance of accurately accounting for high-enthalpy effects in aerodynamic flows has been evident throughout the history of space exploration. A frequently cited example is the estimation of the shock-layer temperature during the atmospheric entry of the Apollo 11 command module. When high-enthalpy effects are neglected—such as by assuming perfect-gas behaviour—the predicted shock temperature can be grossly overestimated. A simplified analysis yields a temperature of approximately 58,128 K, whereas more accurate modelling places the true value closer to 11,600 K (Anderson, 2019). Such discrepancies have profound implications for thermal protection system design and vehicle guidance. In one documented instance, an error in modelling contributed to the Apollo command module landing approximately 200 km from its intended target (Park, 2013).

Although the study of hypersonic flight and its associated flow phenomena is no longer in its infancy, recent advances in computational power, together with the application of statistical thermodynamics, have enabled substantial progress. In particular, significant improvements have been made in the modelling and understanding of thermo-chemical non-equilibrium flows, which are fundamental to accurately representing the extreme environments encountered during high-speed atmospheric entry and hypersonic flight.

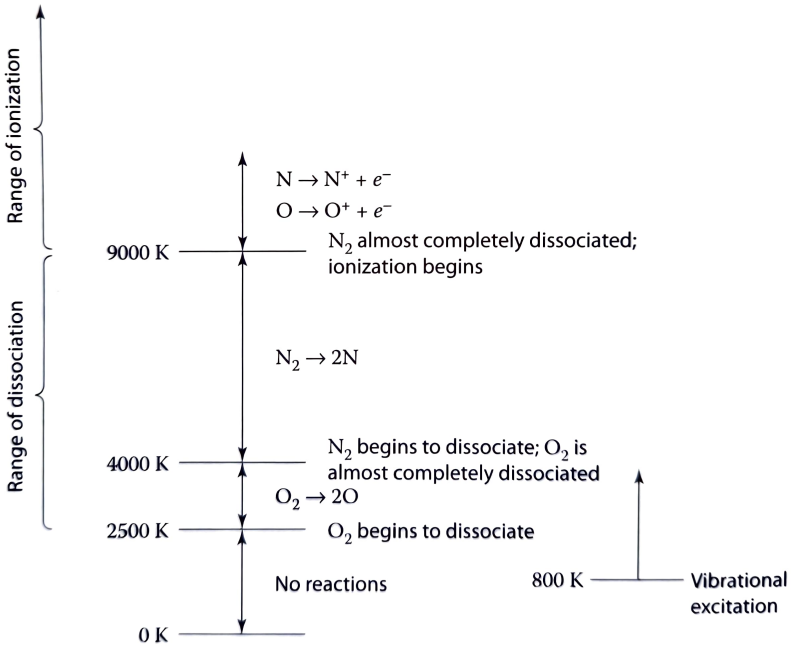

FIGURE 1.1: Ranges for vibrational excitation, dissociation and ionisation at one atmospheric pressure (Anderson, 2019).

Vibrational and chemical processes in gases are governed by molecular collisions, which inherently require a finite time to occur. Under equilibrium conditions, it is assumed that sufficient time has elapsed for all relevant collisional processes to take place, allowing the system to attain a stable thermodynamic state. Owing to the extensive availability of spectroscopic data, the equilibrium thermodynamic properties of air are known with high accuracy. The molecular and atomic energy levels required for such calculations are well documented and are accessible through a wide range of established thermodynamic databases (Mcbride et al., 2002).

Under non-equilibrium conditions, however, these molecular processes may not have had sufficient time to reach completion. As a result, time-dependent effects must be explicitly accounted for in the analysis. In such regimes, conventional equilibrium-based thermodynamic descriptions become inadequate. Accurately modelling non-equilibrium flows therefore necessitates specialised approaches capable of capturing the temporal evolution of internal energy modes, which fundamentally alters the mathematical formulation of the governing equations. A rigorous treatment of non-equilibrium phenomena must thus be founded on a clear understanding of these modelling techniques, together with a careful assessment of the assumptions and limitations inherent to them.

A critical aspect of high-enthalpy flows is the role of chemical reactions in air. As illustrated in Figure 1.1, vibrational excitation begins to significantly influence chemical reaction rates at temperatures above approximately 800 K, while remaining largely independent of pressure. At temperatures around 2500 K, dissociation of molecular oxygen (O_2) becomes important, followed by dissociation of molecular nitrogen (N_2) at approximately 4000 K. Ionisation processes become significant at temperatures approaching 9000 K. Each of these reactions alters the composition of the gas mixture and, consequently, its thermodynamic and transport properties. In thermal non-equilibrium conditions, the flow can no longer be characterised by a single temperature. Energy exchange through molecular collisions involves not only translational motion but also internal degrees of freedom, including rotational, vibrational, and electronic energy modes. To accurately capture the underlying physics of such flows, these internal modes must be treated separately and assigned their own characteristic temperatures.

In addition to high-enthalpy effects, any vehicle exposed to extreme thermodynamic conditions during atmospheric flight will inevitably encounter regions of turbulent flow. Although the Navier–Stokes equations provide, in principle, a complete mathematical description of turbulence, obtaining analytical solutions for flow variables that depend on both space and time is not feasible. Consequently, turbulence must be investigated using numerical methods (Moin and Mahesh, 1998). Direct Numerical Simulation (DNS) offers the most accurate numerical approach by resolving all dynamically relevant turbulent scales without the introduction of modelling assumptions. However, the application of DNS to practical engineering configurations—such as external turbulent flow over a re-entry vehicle—is computationally prohibitive due to the exceedingly fine spatial

and temporal resolution required. As a result, engineering practice typically relies on approximate approaches based on statistical representations of turbulence, including Reynolds-Averaged Navier–Stokes (RANS) and Large Eddy Simulation (LES).

DNS is therefore primarily employed as a research tool for the investigation of turbulence under carefully prescribed and controlled conditions. Its value lies both in advancing fundamental understanding of turbulent flow physics and in providing high-quality statistical data for the development, validation, and calibration of reduced-fidelity turbulence models. In this regard, DNS complements experimental investigations by offering detailed spatio-temporal information that is often difficult or impossible to obtain experimentally. The objective of DNS is not to replicate full-scale engineering flows, but rather to conduct idealised studies that yield deeper insight into the underlying mechanisms governing turbulent behaviour (Moin and Mahesh, 1998).

As will be discussed in subsequent chapters, while the modelling of high-enthalpy effects was largely established by the end of the 20th century, and turbulence has been studied extensively using DNS for several decades, a substantial gap remains in the literature concerning the interaction between turbulence and high-enthalpy phenomena. One of the principal obstacles has been the prohibitive computational cost associated with resolving both turbulence and detailed thermo-chemical non-equilibrium effects simultaneously. However, ongoing advances in computational resources, together with the development of efficient flow solvers optimised for modern hardware architectures—such as GPU-accelerated frameworks (Lusher et al., 2025; Candler et al., 2015; Di Renzo et al., 2020)—have made it increasingly feasible to address this challenge. Consequently, a more comprehensive understanding of one of the central problems in hypersonic flow physics is now within reach. This research therefore focuses on the investigation of turbulence in thermo-chemical non-equilibrium flows using high-fidelity computational fluid dynamics (CFD).

1.1 Literature Overview

When assessing the state of the art in this field, the existing literature can be broadly categorised into three principal areas. The first concerns the development and application of high-fidelity approaches for the modelling of turbulent flows. The second focuses on the modelling of high-enthalpy effects, including the required extensions to the governing equations to account for thermo-chemical non-equilibrium and related physical processes. The third encompasses studies that combine high-fidelity turbulence modelling with high-enthalpy flow physics, representing an emerging and increasingly important area of research.

1.1.1 Direct Numerical Simulation Turbulent Flows

The foundations of Direct Numerical Simulation were laid at the *National Center for Atmospheric Research* (NCAR), with pioneering publications emerging as early as 1972 (Moin and Mahesh, 1998). Although early simulations were limited to very low Reynolds numbers (as low as 35) and used relatively coarse computational domains, these studies laid the groundwork for the development of DNS as a powerful research tool. In the domain of homogeneous turbulence, Rogallo's work set the standard for DNS algorithms and frameworks (Rogallo, 1981). This was followed by studies on coarse-grid free shear layers, and eventually, more complex simulations including wall-bounded flows and investigations into near-wall turbulence physics (Riley and Metcalfe, 1980; Rogallo and Moin, 1984). Of particular relevance to this thesis are the early DNS studies on plane channel flows, beginning with the landmark work of Kim et al. (1987). In the compressible regime, a key contribution was made by Coleman et al. (1995), who conducted DNS of compressible turbulent channel flow. Additionally, notable contributions to the study of compressible mixing layers include the works of Sandham and Reynolds (1989) and Rogers and Moser (1994). These studies mark some of the earliest and most influential efforts in the DNS of turbulent flows and continue to serve as a foundation for modern DNS research. Given the focus of this thesis, the scope is narrowed to two canonical flow configurations: turbulent channel flows and compressible mixing layers, both of which have played critical roles in the development and validation of turbulence models.

Mixing layers are considered an archetype for the development of compressible turbulence in high-speed free shear flows, with significant implications for understanding such flow conditions. They have been widely used for developing and validating turbulence models, analysing the structure and dynamics of coherent turbulent motions, and evaluating the accuracy of experimental measurement techniques (Lele, 1989). One of the earliest DNS studies of compressible shear layers was conducted by Sandham and Reynolds (1989), examining the influence of compressibility on turbulence growth rates. This was followed by Sandham and Reynolds (1990), where linear stability theory was employed to demonstrate that linear amplification could predict experimental trends in mixing layer growth. Subsequently, Rogers and Moser (1994) performed a detailed DNS of a self-similar incompressible mixing layer, supported by comparisons with experimental data. In parallel, Lele (1994) explored the relationship between the maximum linear amplification rate and the spreading rate of compressible mixing layers. Further work by Vreman et al. (1996) employed statistical methods to investigate the reduction in growth rates across a wide range of convective Mach numbers, highlighting the compressibility-induced suppression of turbulence. Pantano and Sarkar (2002) advanced the state of the art by conducting DNS of mixing layers at high convective Mach number ($M_c = 2.5$), with particular emphasis on the role of pressure–strain correlation and dilatational dissipation mechanisms.

Channel flows, in particular, have proven to be an invaluable framework for investigating wall-bounded turbulence due to their relative simplicity and practical relevance. A fully developed turbulent channel flow is statistically stationary and one-dimensional, with velocity statistics varying only in the wall-normal (channel height) direction, and statistical symmetry about the channel centreline (Pope, 2000). Building on the seminal DNS by Kim et al. (1987), Moser et al. (1999) extended the friction Reynolds number (Re_τ) range up to 590, providing a detailed account of how turbulence statistics evolve with friction Reynolds number. Their data set remains a standard benchmark for DNS validation. Later, Hoyas and Jiménez (2006, 2008) pushed the friction Reynolds number up to 2003 using spectral methods and parallel computing, offering detailed insights into turbulence budgets, energy spectra, and near-wall scaling behaviour. More recently, Lee and Moser (2015) set a new benchmark by performing DNS of channel flows up to 5200, producing a comprehensive dataset for turbulence structure and scaling validation at high Reynolds numbers.

1.1.2 High Enthalpy Effects and Their Simulation

When addressing developments in high-enthalpy flow modelling, two principal aspects must be considered. The first is the chemical non-equilibrium state of the flow, which arises from ongoing chemical reactions. The second is the thermal non-equilibrium state, which results from delayed relaxation between different internal energy modes (e.g. translational, rotational, vibrational, and electronic).

For chemical non-equilibrium, physics-based modelling of hypersonic flows relies heavily on accurate representations of reaction rates and collision cross sections. These are typically derived from potential energy surfaces (PES), which are computed using ab initio quantum mechanical methods. Given a PES, collisional cross sections can be obtained, and with the Quasi-Classical Trajectory (QCT) method, individual molecular collisions are simulated by integrating Hamilton's equations of motion. Reaction rate coefficients are then calculated by averaging the cross sections over a distribution of collision energies (Jaffe et al., 2017). While highly accurate, this approach is computationally intensive and often applied only to specific reaction pairs rather than full air chemistry models. For example, Jo et al. (2021) focused on ro-vibrational-specific collisions between nitrogen molecules and oxygen atoms.

Another approach is Direct Molecular Simulation (DMS), where particle trajectories are computed dynamically on a given PES during the flow simulation. This method has been explored in studies such as Valentini et al. (2015); Torres and Schwartzentruber (2020, 2021), though a complete, publicly available model covering all air species has not yet been published.

Alternatively, a finite-rate chemistry model can be adopted. The foundational form for chemical reaction rates in terms of absolute temperature was first introduced by Arrhenius (1889). Although widely accepted, this model assumes a single temperature and is insufficient for multi-temperature environments. To address this, Park (1985, 1986) extended the classical Arrhenius formulation by incorporating temperature dependencies based on the internal energy mode most affected by the reaction (e.g. vibrational temperature for dissociation), allowing better representation of non-equilibrium conditions.

The most common approaches for modelling energy exchange in thermally non-equilibrium flows are the State-to-State (StS) and Multi-Temperature (MT) methods. In the StS approach, thermal non-equilibrium is modelled by individually tracking the population of internal energy states—typically translational, rotational, and vibrational levels—through a set of master equations (Jaffe et al., 2017). Similar to the Quasi-Classical Trajectory (QCT) method, StS modelling is computationally expensive due to the large number of energy levels involved. To reduce computational cost, strategies such as coarse-graining are employed, where ro-vibrational levels are grouped into larger energy bins. This approach was demonstrated by Torres et al. (2018) in their modelling of the N_2–N system. Hybrid approaches have also emerged, such as the work by MacDonald et al. (2019), which proposed a reduced-order hybrid StS model for N_2–N energy exchange.

In contrast, the multi-temperature model assumes that internal energy modes, typically translational, rotational, and vibrational, can be characterised by separate temperatures. The foundation of this approach was introduced by Landau and Teller (1936), and was later developed into quantitative form through the first-order perturbation theory known as the SSH model by Schwartz et al. (1952). These foundational studies laid the groundwork for widely used empirical correlations such as those of Millikan and White (1963), which remain standard in computational analyses of vibrational relaxation. The Millikan–White model, along with its corrected or modified forms, such as those proposed by Park (1984, 1987, 1993), has become one of the most widely used and computationally efficient sources for estimating vibrational relaxation times in hypersonic flow simulations over the past several decades.

1.1.3 Direct Numerical Simulation of High-Enthalpy Turbulent Flows

While a substantial body of research has addressed high-temperature effects in hypersonic flows, only a limited number of studies have employed Direct Numerical Simulation, and focused investigations of thermo-chemical non-equilibrium have emerged only relatively recently. For example, Kerkar and Ghosh (2019) examined high-enthalpy effects on turbulent flows through DNS of decaying isotropic turbulence. Similarly, Khurshid and Donzis (2019) investigated the influence of thermal non-equilibrium on decaying

turbulence, demonstrating its strong dependence on both the degree of non-equilibrium and the ratio of vibrational relaxation timescales to hydrodynamic timescales.

More recent DNS studies of thermal non-equilibrium in shear-layer configurations include the works of Fiévet et al. (2019) and Neville et al. (2015). Both investigations, however, assume chemical equilibrium. Notably, Fiévet et al. (2019) adopted a state-to-state formulation, whereas Neville et al. (2015) employed a multi-temperature model to describe internal energy exchange. In the multi-temperature framework, vibrational energy states are assumed to follow a Boltzmann distribution, implying identical relaxation timescales across all vibrational levels. In contrast, Fiévet et al. (2019) demonstrated that increasing vibrational quantum number leads to decreasing energy gaps between adjacent states, resulting in faster relaxation of higher vibrational levels. This behaviour has important implications for local transport properties, particularly gas viscosity and energy transfer mechanisms.

In comparison, relatively little work has been conducted on high-enthalpy channel flows. Notable exceptions include Chen et al. (2024), who performed DNS of a temporally evolving high-enthalpy channel flow incorporating finite-rate chemistry, and Cao et al. (2022), who investigated supersonic turbulent channel flow of carbon dioxide using a three-temperature model.

The effects of chemical non-equilibrium within boundary layers have also received increasing attention in recent years. Passiatore (2021) and Di Renzo and Urzay (2021) conducted DNS studies of boundary-layer flows incorporating finite-rate chemistry, although both assumed thermal equilibrium. In particular, Di Renzo and Urzay (2021) examined the spatial development of a transitional boundary layer over a cold isothermal wall, analysing the transition from laminar to turbulent flow under thermochemical non-equilibrium conditions. In contrast, Passiatore et al. (2022) investigated a turbulent boundary layer subject to wall cooling using DNS with a five-species air model and a two-temperature formulation to represent thermo-chemical non-equilibrium. More recent contributions within the boundary-layer framework include studies by Williams et al. (2025) and Passiatore et al. (2024), which examined turbulence–chemistry interactions, as well as the works of Passiatore et al. (2023, 2022), which focused on turbulence–thermal interactions under high-enthalpy conditions.

1.2 Research Gap and Motivation

Recent advances in statistical thermodynamics have enabled the development of modelling approaches that compute chemical and thermal states from first principles, offering highly accurate representations of thermo-chemical non-equilibrium. Although a number of reduced-order and simplified models have been proposed to approximate the accuracy of such detailed formulations at a lower computational cost, a complete and rigorously validated set of reaction mechanisms for air remains unavailable for these approaches. Furthermore, much of the existing literature focuses on extreme high-temperature regimes in which rotational–vibrational coupling becomes dominant due to the breakdown of the rotational equilibrium assumption, particularly as rotational relaxation times decrease to values comparable to those of vibrational modes.

While state-to-state models have demonstrated considerable potential in capturing non-equilibrium effects, their application to turbulent flows remains limited. For instance, Fiévet et al. (2019) investigated non-Boltzmann vibrational distributions under turbulent, non-equilibrium conditions; however, the analysis was restricted to a simplified flow configuration, limiting broader conclusions regarding the influence of non-equilibrium processes on turbulence dynamics. In the context of air chemistry, Torres et al. (2023) employed Direct Molecular Simulation and Quasi-Classical Trajectory methods to study five-species air reactions, representing some of the most accurate modelling techniques currently available. Nevertheless, their investigation focused on extremely high temperatures in the range of 8000–30,000 K, where ionisation and radiative effects dominate, and is therefore not necessarily representative of more moderate high-enthalpy flow regimes.

At present, multi-temperature models provide the most computationally tractable framework for simulating thermo-chemical non-equilibrium in complex flow configurations. These models are widely adopted across broad temperature ranges, yet their accuracy in regimes below approximately 9000 K—where ionisation and radiation are negligible, but vibrational and chemical non-equilibrium effects remain significant—has not been systematically assessed. This raises important questions regarding the validity and limitations of MT assumptions in such intermediate high-enthalpy conditions.

Recent studies by Williams et al. (2025); Passiatore et al. (2024, 2023, 2022); Di Renzo and Urzay (2021) have investigated boundary-layer flows under thermo-chemical non-equilibrium using MT formulations. While these works have provided valuable insights, their focus on spatially developing boundary layers introduces additional complexities that can obscure the fundamental coupling between turbulence, chemical kinetics, and thermal relaxation. Simplified, canonical flow configurations that enable these interactions to be isolated and systematically analysed remain relatively unexplored.

As a result, a comprehensive understanding of thermo-chemical non-equilibrium effects in turbulent flows is still lacking. Several critical questions remain unresolved: to what extent do the assumptions inherent in widely used MT models influence predicted flow behaviour? What are the sources and magnitudes of uncertainty introduced by these modelling choices? How do key flow parameters affect model fidelity? And which regions or quantities within the flow field are most sensitive to non-equilibrium effects?

Motivated by these gaps, the primary objective of this thesis is to assess the influence of thermo-chemical non-equilibrium on turbulence characteristics within a scale-resolved simulation framework, and to evaluate how such effects can be reliably modelled using the multi-temperature approach within a high-fidelity computational setting. This is achieved through a systematic investigation of established non-equilibrium flow models applied to canonical turbulent configurations that enable controlled and interpretable analysis.

1.3 Objectives and Research Scope

This research is structured around four principal research questions:

1. **What is the most suitable form of a thermo-chemical non-equilibrium multi-temperature kinetic framework in the context of turbulence simulation?**
   This objective aims to evaluate the uncertainties associated with commonly used thermo-chemical non-equilibrium assumptions and approximations embedded in the multi-temperature modelling approach. It seeks to assess the degree of model completeness within the flow regimes of interest and to determine the relevance and practical applicability of these models for time-dependent non-equilibrium flows. In addition, this question examines whether improvements in model fidelity justify the associated increase in computational cost, particularly in the context of turbulence-resolving simulations.

2. **What is the influence of non-equilibrium effects on time-dependent characteristics of turbulent structures, specifically related to a temporally developing mixing layer?**
   The objective of this question is to investigate the impact of high-enthalpy effects on canonical turbulent shear flows using high-fidelity computational fluid dynamics. This includes examining the coupling between thermal, chemical, and turbulent phenomena under different flow conditions. The aim is to characterise the resulting flow regimes and qualitatively describe the interactions between time-dependent turbulent structures and thermo-chemical non-equilibrium effects. Where relevant, the study further assesses whether qualitative behaviours observed

in two-dimensional non-equilibrium analyses persist in fully three-dimensional configurations.

3. **What are the quantitative influences of thermo-chemical non-equilibrium on turbulence characteristics?**
   This question focuses on the quantitative assessment of the coupling between thermo-chemical non-equilibrium and turbulence through statistical analysis of two flow configurations: a free shear layer (temporally evolving mixing layer) and a wall-bounded flow field (turbulent channel flow). It aims to determine whether non-equilibrium effects lead to measurable changes in turbulence characteristics and, if so, whether these changes are sufficiently significant to challenge the validity of lower-fidelity modelling approaches. In addition to analysing time-dependent behaviour, this objective seeks to evaluate the characteristics of non-equilibrium turbulent flows from a statistically averaged perspective.

4. **What are the driving mechanisms of non-equilibrium states in relation to turbulent flows and their characteristics?**
   While the presence of thermo-chemical non-equilibrium behind a strong discontinuity such as shock waves have been extensively evaluated, the objective here is to identify and understand the mechanisms responsible for the emergence and persistence of thermo-chemical non-equilibrium regions within turbulent flow fields. This includes examining the relationship between non-equilibrium effects and key flow characteristics, as well as how this relationship varies across different flow configurations and operating conditions.

Thesis Outline

In accordance with the objectives outlined in the preceding section, this thesis is organised into seven chapters. Chapter 1 presents the introduction, outlining the motivation for the research, a review of the current state of the literature, and the specific objectives of the thesis. Chapter 2 introduces the governing equations, detailing the formulation and modelling considerations associated with high-enthalpy flows and thermo-chemical non-equilibrium effects. Chapter 3 focuses on the validation of the models employed in this work, evaluating the assumptions and individual components of the proposed framework. Chapter 4 investigates high-enthalpy effects in a canonical shear-layer configuration, with particular emphasis on thermo-chemical non-equilibrium effects in time-dependent flows. Chapter 5 addresses the modelling of transport properties, proposing an efficient formulation for viscosity and thermal conductivity in reacting air flows. Chapter 6 extends the analysis to turbulent channel flow under full thermo-chemical non-equilibrium conditions, assessing turbulence characteristics from a statistically averaged perspective. Finally, Chapter 7 summarises the main findings of the thesis and outlines potential directions for future research related to high-enthalpy flow simulations.

Publications and Conferences

The publications and conference presentations arising from the PhD research and directly related to the work presented in this thesis are listed below.

Conferences

- **HyFAR-ARA:** 2nd European Symposium on Laminar–Turbulent Transition in the Hypersonic Regime, Bordeaux, October 2023. Title: *Thermal Non-Equilibrium of a High-Enthalpy Free Shear Layer During Breakdown to Turbulence*
- **UK-Fluids:** The UK Fluids Network (UKFN), Glasgow, October 2023. Title: *Thermal Non-Equilibrium Breakdown to Turbulence of High Enthalpy Mixing Layer*
- **AIAA SciTech:** AIAA Science and Technology Forum and Exposition, January, 2025. Title: *Efficient Transport Property Formulation for Scale-resolved Hypersonic Flow Simulations*

Publications and Contributions

- Musawi, A., ; Sandham, N. D.; (2025). Efficient Viscosity and Thermal Conductivity Formulation for Scale-Resolved Hypersonic Flow Simulations. American Institute of Aeronautics and Astronautics Journal, 63(12). https://doi.org/https://doi.org/10.2514/1.J065564
- Musawi, A., ; Sandham, N. D.; (2026). Effects of thermal non-equilibrium during transition to turbulence of a high enthalpy free shear layer. Physics of Fluids, 38(1), 15157. https://doi.org/10.1063/5.0311454
- Musawi, A., ; Sandham, N. D.; (2026). Effects of Thermo-Chemical Non-Equilibrium on Turbulent Channel Flow Using Direct Numerical Simulation. (In Preparation)
- Ala, T., ; Musawi, A.; Lusher, D. J.; Sandham, N. D.; (2026). OpenSBLI v4.0: Domain-Specific Automation for Thermo-Chemical DNS on Structured Grids. (In Preparation)

Chapter 2

Governing Equations & Numerical Methods

When evaluating the numerical simulation of high-enthalpy flows, one needs to consider the numerical strategy, the physical modelling of high-enthalpy effects, and their correct implementation within the solver framework. To address these aspects comprehensively, the computational framework can be divided into three main parts. First, the governing equations that define a scale-resolved simulation. Second, the gas-dynamic modelling of high-enthalpy effects, including how they are incorporated into the flow physics. Third, the numerical methods and tools used to implement and solve these models effectively. In addition, the post-processing approach, particularly the statistical techniques used to interpret the results, such as energy budgets and Reynolds averaging, is also an essential part of the workflow.

Accordingly, the outline of this chapter is as follows. An introduction to the governing equations is first presented in Section 2.1. The modelling of high-enthalpy effects is then addressed, comprising the chemical kinetic model described in Section 2.2, the thermal kinetic model detailed in Section 2.3, and the evaluation of transport properties presented in Section 2.4. Finally, Section 2.5 describes the computational framework, including the numerical methods and implementation details employed in this study.

2.1 Governing Equations

The governing equations for thermo-chemical non-equilibrium simulations comprise of the conservation laws for mass, momentum, vibrational energy, and total energy (Gnoffo et al., 1989). These equations incorporate the effects of chemical reactions as well as energy exchange between the translational–rotational (ro-translational) and vibrational energy modes. In this study, a simplified two-temperature model is employed, in which

the electronic energy mode is not modelled, and only the five neutral species of air are considered. This assumption is appropriate for flow conditions where ionisation effects are negligible. While the general formulation originates from the foundational work of Lee (1984, 1985), the specific form of the governing equations adopted here follows that presented by Gnoffo et al. (1989).

The governing equations employed in this study are derived under three primary assumptions (Lee, 1984). First, the flow is assumed to behave as a continuum, thereby permitting the use of the Navier–Stokes equations. Second, the vibrational energy is assumed to follow a Boltzmann distribution characterised by a single vibrational temperature. This assumption is based on the Harmonic Oscillator (HO) model, which is strictly valid only for low vibrational energy levels. However, since the contribution from higher vibrational states is typically negligible under the conditions considered here, the HO approximation is deemed adequate. Third, the internal energy modes are represented using a two-temperature formulation: the translational and rotational modes are assumed to be in equilibrium and are jointly described by the translational temperature T, while the vibrational mode is characterised by the vibrational temperature T_v. The electronic energy mode, along with its associated temperature T_e, is neglected, as ionisation effects are assumed to be insignificant for the flow conditions examined in this work.

$$\underbrace{\frac{\partial}{\partial t}(\rho_s)}_{(1)} + \underbrace{\frac{\partial}{\partial x_j}(\rho_s u_j)}_{(2)} = \underbrace{\frac{\partial}{\partial x_j}\left(\rho D_s \frac{\partial X_s}{\partial x_j}\right)}_{(3)} + \underbrace{\dot{w}_s}_{(4)} + \underbrace{\rho_s \sum_{s=1}^{N} D_s \frac{\partial X_s}{\partial x_j}}_{(5)} \tag{2.1}$$

$$\underbrace{\frac{\partial}{\partial t}(\rho u_i)}_{(1)} + \underbrace{\frac{\partial}{\partial x_j}(\rho u_i u_j)}_{(2)} = \underbrace{-\frac{\partial p}{\partial x_i}}_{(3)} + \underbrace{\frac{\partial}{\partial x_j}\left[\mu\left(\frac{\partial u_i}{\partial x_j} + \frac{\partial u_j}{\partial x_i}\right) - \left(\frac{2}{3}\mu - \mu_b\right)\frac{\partial u_k}{\partial x_k}\delta_{ij}\right]}_{(4)} \tag{2.2}$$

$$\underbrace{\frac{\partial}{\partial t}(\rho e_v)}_{(1)} + \underbrace{\frac{\partial}{\partial x_j}(\rho e_v u_j)}_{(2)} = \underbrace{\frac{\partial}{\partial x_j}\left(K_v \frac{\partial T_v}{\partial x_j}\right)}_{(3)} + \underbrace{\frac{\partial}{\partial x_j}\left(\rho \sum_{s=1}^{N} e_{v,s} D_s \frac{\partial X_s}{\partial x_j}\right)}_{(4)} + \underbrace{\sum_{s\in\text{mol}} \rho_s \frac{(e^*_{v,s} - e_{v,s})}{\tau_s}}_{(5)} + \underbrace{\sum_{s\in\text{mol}} \dot{\omega}_s \hat{D}_s}_{(6)} \tag{2.3}$$

$$\underbrace{\frac{\partial}{\partial t}\left(\rho E\right)}_{(1)} + \underbrace{\frac{\partial}{\partial x_j}\left(\rho H u_j\right)}_{(2)} = \underbrace{\frac{\partial}{\partial x_j}\left(K_{tr}\frac{\partial T}{\partial x_j} + K_v\frac{\partial T_v}{\partial x_j}\right)}_{(3)} + \underbrace{\frac{\partial}{\partial x_j}\left(\rho\sum_{s=1}^{N} h_s D_s \frac{\partial X_s}{\partial x_j}\right)}_{(4)} + \underbrace{\frac{\partial u_i}{\partial x_j}\left[\mu\left(\frac{\partial u_i}{\partial x_j} + \frac{\partial u_j}{\partial x_i}\right) - \left(\frac{2}{3}\mu + \mu_b\right)\frac{\partial u_k}{\partial x_k}\delta_{ij}\right]}_{(5)} \quad (2.4)$$

For the species mass conservation equation defined in Equation 2.1, term (1) represents the rate of change of mass for species s, where ρ_s denotes the mass density of species s. Term (2) corresponds to the convective transport of species s by the mixture velocity u_j in the j-th coordinate direction. Term (3) represents the diffusive flux of species s, which is defined in Section 2.4.3; here, ρ is the total mixture density, D_s is the diffusion coefficient of species s, and X_s is its mole fraction. Term (4) denotes the net mass production rate of species s due to chemical reactions, represented by $\dot{\omega}_s$. Finally, term (5) represents the diffusion correction term, which is introduced to enforce overall mass conservation when the species diffusion coefficients do not strictly satisfy the constraint of zero net diffusive mass flux.

For the mixture momentum conservation equation given in Equation 2.2, term (1) represents the rate of change of momentum in the i-th direction. Term (2) denotes the convective transport of momentum in the i-th direction by the mixture velocity u_j along the j-th coordinate direction. Term (3) corresponds to the pressure force acting in the i-th direction. Term (4) represents the viscous stress contribution in the i-th direction, where μ is the dynamic viscosity of the mixture, u_k denotes the velocity component in the k-th direction, δ_{ij} is the Kronecker delta, and μ_b is the bulk viscosity.

For the molecular-mixture vibrational energy conservation equation defined in Equation 2.3, term (1) represents the rate of change of the total vibrational energy of the mixture, where e_v denotes the mixture vibrational energy. Term (2) corresponds to the convective transport of vibrational energy by the mixture velocity u_j in the j-th coordinate direction. Term (3) describes the conductive transport of vibrational energy driven by gradients in the vibrational temperature T_v, where K_v denotes the vibrational contribution to the thermal conductivity. Term (4) accounts for the diffusive transport of vibrational energy arising from molecular species concentration gradients, with $e_{v,s}$ representing the vibrational energy of species s. Term (5) represents the energy exchange between the ro-translational and vibrational modes, modelled using the Landau–Teller formulation; here, $e_{v,s}$ is the instantaneous vibrational energy of species s, $e^*_{v,s}$ denotes its equilibrium vibrational energy, and τ_s is the corresponding vibrational relaxation time. Finally, term (6) accounts for the gain or loss of vibrational energy associated with molecular production or depletion, where $\hat{D}_s$ is defined in Section 2.3.3.

For the total energy conservation equation defined in Equation 2.4, term (1) represents the rate of change of the total energy. Term (2) denotes the convective transport of

total energy by the mixture velocity u_j in the j-th coordinate direction, where H is the specific total enthalpy of the mixture. Term (3) corresponds to conductive heat transfer arising from gradients in both the ro-translational temperature T and the vibrational temperature T_v, where K_{tr} denotes the ro-translational contribution to the thermal conductivity. Term (4) accounts for the diffusive transport of enthalpy due to species concentration gradients, with h_s representing the specific enthalpy of species s. Finally, term (5) represents the work done by viscous (shear) stresses.

To complete the set of governing equations, the gas mixture is assumed to exhibit negligible intermolecular forces and is therefore modelled as a perfect gas. The ideal gas equation of state is employed, and, together with Dalton's law of partial pressures, it is incorporated into the governing equations. Consequently, the total pressure of the mixture is expressed as

$$p = \rho R T = \sum_{s=1}^{N} p_s = \sum_{s=1}^{N} \rho_s \frac{\mathscr{R}}{M_s} T \quad . \tag{2.5}$$

Experimentally, it has been shown that at pressures around or below one atmosphere and temperatures above 273 K, Equation 2.5 predicts the thermodynamic behaviour of pure gases with an accuracy of approximately 1 percent. At higher pressures, however, gas molecules become more closely packed, and intermolecular interactions can no longer be neglected, requiring the gas to be treated as a real gas. This consideration is particularly relevant for polyatomic molecules. Under such conditions, the ideal gas equation must be replaced by a more accurate equation of state, such as the Van der Waals formulation

$$\left(p + \frac{a}{v^2}\right)(v - b) = RT \quad , \tag{2.6}$$

where the constants a and b are specific to the gas under consideration.

Throughout the main body of this thesis, the ideal gas equation given by Equation 2.5 is employed. However, for the treatment of CO_2, the applicability of this equation requires separate assessment, as discussed in Appendix C.

Additional relations utilised in the governing equations include the total enthalpy per unit mass, defined as

$$H = E + \frac{p}{\rho} \quad , \tag{2.7}$$

the total specific vibrational energy of the mixture expressed in terms of the species vibrational energies

$$e_v = \sum_{s \in \text{mol}} \frac{\rho_s e_{v,s}}{\rho} \quad , \tag{2.8}$$

and the species mole fraction defined in terms of the species mass densities

$$X_s = \frac{\rho_s M_s}{\sum_{m=1}^{N} \rho_m M_m} \quad , \tag{2.9}$$

2.1.1 Species Vibrational Energy

Equation 2.3 is formulated following the approach presented by Gnoffo et al. (1989), in which a single conservation equation is used to represent the combined vibrational energy of all molecular species. While this formulation provides a compact and computationally efficient representation, a more detailed description can be achieved by modelling the transport of vibrational energy separately for each molecular species. Under this formulation, the vibrational energy transport equation for an individual species can be written as

$$\frac{\partial}{\partial t}\left(\rho_s e_{v,s}\right) + \frac{\partial}{\partial x_j}\left(\rho_s e_{v,s}\, u_j\right) = \frac{\partial}{\partial x_j}\left(K_{v,s}\frac{\partial T_v}{\partial x_j}\right) + \frac{\partial}{\partial x_j}\left(\rho_s e_{v,s}\, D_s \frac{\partial X_s}{\partial x_j}\right) + \frac{\rho_s(e^*_{v,s} - e_{v,s})}{\tau_s} + \dot{\omega}_s \hat{D}_s \tag{2.10}$$

Equation 2.10 represents the species-specific formulation from which Equation 2.3 is derived. This formulation was originally presented by Lee (1984) and later referenced by Gnoffo et al. (1989). Although the single-equation formulation for vibrational energy is often regarded as an approximation, a key distinction between these two formulations lies in the definition of the transport density. Specifically, Lee (1984) define the transport density as the sum of the molecular species densities, whereas Gnoffo et al. (1989) define it as the total mixture density. In principle, this difference should not affect the final solution, provided that the chosen definition is applied consistently in the evaluation of all related transport and source terms throughout the simulation. For completeness, the conservation equation presented by Lee (1984) is written in the form

$$\frac{\partial}{\partial t}\left(\rho_m e_v\right) + \frac{\partial}{\partial x_j}\left(\rho_m e_v\, u_j\right) = \frac{\partial}{\partial x_j}\left(K_v^{'}\frac{\partial T_v}{\partial x_j}\right) + \frac{\partial}{\partial x^j}\left(\rho \sum_{s\in\text{mol}} e_{v,s}\, D_s \frac{\partial X_s}{\partial x^j}\right) + \sum_{s\in\text{mol}} \rho_s \frac{(e^*_{v,s} - e_{v,s})}{\tau_s} + \sum_{s\in\text{mol}} \dot{\omega}_s \hat{D}_s \quad , \tag{2.11}$$

where ρ_m denotes the total density of molecular species.

Despite being formulated separately for each species, the vibrational energy conservation equation defined in this manner implicitly assumes that there is no vibrational–vibrational

energy exchange between different species; that is, the vibrational modes are entirely decoupled. This assumption contrasts with the conventional practice in hypersonic CFD simulations, where full coupling between vibrational modes is typically assumed. While the fully coupled formulation is largely motivated by computational efficiency, it raises important questions regarding the physical validity of the assumption and the extent to which it accurately represents real flow behaviour. These issues are examined in greater detail in the subsequent chapters.

Vibrational-Vibrational Relaxation

At this stage, it is necessary to expand upon and clarify the role of vibrational–vibrational (V–V) relaxation and to justify the modelling choice adopted in Equation 2.10, in which no explicit V–V energy exchange is included.

At low temperatures ($T < 300\,\mathrm{K}$), molecular vibrational modes are only weakly excited, and energy exchange involving vibrational degrees of freedom is negligible. As the temperature increases into the intermediate range ($1000 < T < 3000\,\mathrm{K}$), vibrational excitation becomes increasingly significant. In this regime, vibrational–translational (V–T) energy exchange begins to contribute to vibrational relaxation, while V–V interactions also start to occur. At higher temperatures ($5000 < T < 10000\,\mathrm{K}$), which are characteristic of shock-heated air and many high-enthalpy flows, V–V relaxation processes are generally faster than V–T processes and therefore occur earlier in the relaxation sequence, with V–T relaxation lagging behind. This behaviour underpins the common assumption in the literature that vibrational modes of different molecular species rapidly equilibrate, leading to the adoption of fully coupled V–V formulations. For example, simulations incorporating V–V relaxation for N_2 have shown a reduction in the overall vibrational relaxation time by up to a factor of three compared to cases in which only V–T relaxation is considered (Andrienko and Boyd, 2018). In contrast, the inclusion of V–V relaxation has been shown to reduce the relaxation rate of O_2.

As the temperature increases further into the range $10000 < T < 20000\,\mathrm{K}$, V–T relaxation rates increase substantially and become comparable to those associated with V–V processes. In this regime, neglecting V–V relaxation or assuming instantaneous full coupling can introduce significant modelling errors, as the relative timescales of the competing mechanisms become similar.

The above trends are generally valid at moderate to high pressures, on the order of atmospheric pressure. At very low pressures, however, the relative importance of V–V relaxation changes markedly. Under such conditions, V–V relaxation can become significant at lower temperatures due to its timescale becoming comparable to that of V–T relaxation. Experimental studies conducted at pressures in the range 10–500 Torr

($\sim$ 1300–66,000 Pa) have shown that V–V relaxation between O_2 and N_2 can be an order of magnitude slower than V–T relaxation (Streicher et al., 2020b, 2021, 2020c,a).

It is therefore important to emphasise that, while the assumption of fully coupled vibrational modes may be reasonable under certain conditions, this coupling can break down at high temperatures and low pressures. Furthermore, the absence of well-validated V–V relaxation models for air over wide temperature ranges raises legitimate concerns regarding the universal applicability of the full-coupling assumption across the conditions typically studied in high-enthalpy flows.

Consequently, in light of the modelling uncertainties under investigation in this work (Chinnappan and Kim, 2025), two limiting cases are considered. The first assumes full coupling between molecular vibrational modes, while the second assumes no V–V coupling whatsoever. Both limiting cases correspond to the omission of explicit V–V source terms in the vibrational energy conservation equations presented here, allowing the sensitivity of the results to these extreme assumptions to be systematically assessed.

2.1.2 Microscopic Evaluation of Energy

When a flow field is defined under equilibrium conditions, any two independent thermodynamic state variables uniquely determine the complete thermodynamic state of the gas. These properties may be obtained either through experimental measurement or theoretical prediction. With the development of statistical mechanics and the advent of quantum mechanics in the early twentieth century, a rigorous theoretical framework—statistical thermodynamics—was established, enabling accurate prediction of the thermodynamic properties of high-temperature gases (Anderson, 2021). While a full derivation of these properties using statistical thermodynamics is extensive and well beyond the scope of this thesis, including the detailed formulation of the energy equations, a brief overview of the underlying concepts is provided. This overview is intended to highlight specific assumptions and modelling choices that influence the formulation of the governing equations and may impact the accuracy of high-enthalpy flow simulations.

At the microscopic level, a gas is composed of atoms or molecules that interact through intermolecular forces. Each molecule possesses several distinct modes of energy storage (Anderson, 2021), which are summarised as follows:

- *Translational energy* ($\varepsilon'_{\text{trans}}$): The translational motion of a molecule through space contributes kinetic energy associated with the motion of its centre of mass. Since motion occurs along three orthogonal spatial directions, this mode has three degrees of freedom.
- *Rotational energy* ($\varepsilon'_{\text{rot}}$): Rotational energy arises from the rotation of a molecule about its principal axes and is associated with angular velocity and the moment

of inertia. For a diatomic molecule modelled as a rigid dumbbell, rotation about the molecular axis (typically the z-axis) is negligible, resulting in two rotational degrees of freedom. Linear polyatomic molecules, such as CO_2, exhibit the same behaviour, whereas nonlinear polyatomic molecules, such as H_2O, possess three rotational degrees of freedom.

- *Vibrational energy* ($\varepsilon'_{\text{vib}}$): Vibrational energy is associated with oscillatory motion of atoms about their equilibrium positions within a molecule. This mode is commonly modelled using the harmonic oscillator approximation. For a diatomic molecule, vibrational motion consists of a kinetic component associated with atomic motion and a potential component associated with the intermolecular restoring force. Although this mode has a single geometric degree of freedom, it contributes two thermal degrees of freedom. In polyatomic molecules, the vibrational energy structure is more complex and may involve multiple vibrational modes.

- *Electronic energy* (ε'_{el}): Electronic energy arises from the motion of electrons around atomic nuclei and includes both kinetic energy and electrostatic potential energy contributions. This mode is highly complex and cannot be readily characterised by a fixed number of degrees of freedom.

Therefore, the total internal energy of a molecule can be expressed as the sum of its individual energy modes

$$\varepsilon^{'} = \varepsilon^{'}_{\text{trans}} + \varepsilon^{'}_{\text{rot}} + \varepsilon^{'}_{\text{vib}} + \varepsilon^{'}_{\text{el}} \quad \text{(molecule)} \,, \tag{2.12}$$

$$\varepsilon^{'} = \varepsilon^{'}_{\text{trans}} + \varepsilon^{'}_{\text{el}} \quad \text{(atom)} \,. \tag{2.13}$$

According to quantum mechanics, each energy mode is quantised and can only assume discrete energy values. A detailed treatment of this behaviour is provided by Anderson (2021); however, for the purposes of this work, it is sufficient to note that each energy mode may be visualised as a ladder diagram, in which each rung corresponds to a quantised energy level. The spacing between successive levels depends on the specific energy mode under consideration, while the lowest level, referred to as the ground state, represents the energy at absolute zero temperature. In subsequent evaluations, energies are expressed relative to this ground state and are denoted using a prime symbol ($'$). The zero-point energy itself is accounted for through the chemical contribution to the internal energy, as discussed later.

Each quantised energy level may contain multiple degenerate states, denoted by g_j, which are determined either theoretically or through spectroscopic measurements. For a system containing N molecules distributed among the available energy levels, the exact molecular arrangement varies continuously in time. The macrostate of the system is defined by the number of molecules occupying each energy level, whereas microstates correspond to the

specific arrangements of individual molecules within those levels. Multiple microstates may correspond to the same macrostate. From a statistical mechanics perspective, the most probable macrostate is the one associated with the largest number of microstates, and this distribution can be determined using quantum statistical methods.

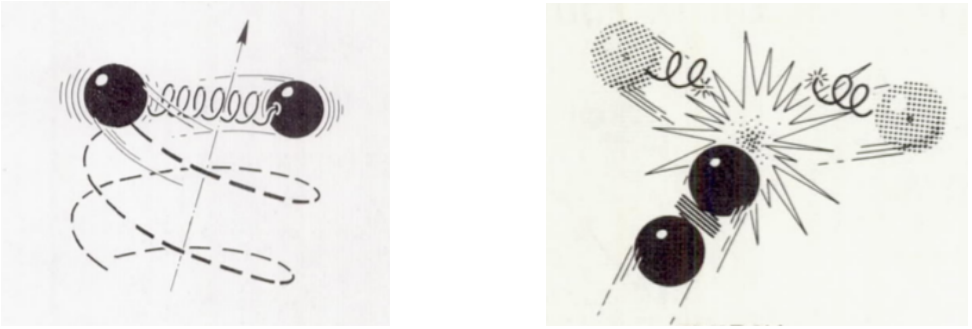

(a) Diatomic Molecule. (b) Atom.

FIGURE 2.1: Schematic representation of the energy modes considered for a diatomic molecule and a monatomic species (Hansen and Heims, 1958). The diagram illustrates the partitioning of internal energy into translational, rotational, vibrational, and electronic contributions, highlighting the absence of rotational and vibrational modes for monatomic species.

The distribution of molecules across quantised energy levels under thermodynamic equilibrium is described by

$$N_j^* = N \frac{g_j \exp\left(-\varepsilon_j / kt\right)}{Q} \ . \tag{2.14}$$

where N is the total number of molecules in the system, g_j is the degeneracy of energy level j, ε_j is the energy of level j, k is the Boltzmann constant, T is the temperature of the system, and Q is the partition function, which depends on the temperature and volume of the system.

This expression follows from the Boltzmann distribution, which assumes that at sufficiently high temperatures molecules are distributed among a large number of energy levels, such that the occupancy of individual levels remains sparse ($N_j \ll g_j$). While this assumption is generally valid for many practical conditions, the resulting distribution is not strictly accurate across all energy levels, particularly at higher energies, and does not account for the differing relaxation times associated with individual energy levels under non-equilibrium conditions. Nevertheless, it provides a reliable approximation for the lower vibrational energy levels within the range of conditions considered in this thesis.

Using the definition of the partition function, thermodynamic properties may be evaluated directly. The total internal energy per unit mass above the zero-point energy is given by

$$e^{'} = RT^2 \left(\frac{\partial \ln Q^{'}}{\partial T} \right)_V \ , \tag{2.15}$$

where the total partition function is expressed as

$$Q^{'} = Q_{\text{trans}} Q_{\text{rot}} Q_{\text{vib}} Q_{\text{el}} \, . \tag{2.16}$$

Accordingly, the total sensible energy above the zero-point energy can be written as

$$e^{'} = e^{'}_{\text{trans}} + e^{'}_{\text{rot}} + e^{'}_{\text{vib}} + e^{'}_{\text{el}} = \frac{3}{2}RT + RT + \frac{hv/k}{e^{hv/kT_v} - 1}R + e^{'}_{el} \, , \tag{2.17}$$

where $e^{'}$ denotes the sensible energy per unit mass, R is the specific gas constant, T is the ro-translational temperature, and T_v is the vibrational temperature. Here, h is Planck's constant, ν is the vibrational frequency obtained from spectroscopic measurements, and k is the Boltzmann constant. The quantity $h\nu/k$ may be expressed as the characteristic vibrational temperature Θ_v. In this formulation, the vibrational energy mode is represented using the vibrational temperature T_v, which is essential for accurately modelling thermal non-equilibrium conditions.

2.1.3 Multi-Species Formulation of the Energy Equation

When considering a moving, multi-species system, the total energy of the mixture is obtained by summing the energy contributions of all constituent species (Candler and Nompelis, 2009)

$$\rho E = \sum_{s=1}^{N} \rho_s e_{\text{trans},s} + \sum_{s=1}^{N} \rho_s e_{\text{rot},s} + \sum_{s=1}^{N} \rho_s e_{vib,s} + E_e + \sum_{s=1}^{N} E_{el,s} + \frac{1}{2}\rho u_i u_i + \sum_{s=1}^{N} \rho_s \Delta h_{f,s} \, , \tag{2.18}$$

where E denotes the specific total energy of the mixture, ρ_s is the species density and N refers to the number of species considered. The terms $e_{\text{trans},s}$, $e_{\text{rot},s}$, and $e_{\text{vib},s}$ represent the translational, rotational, and vibrational energies of species s per unit mass, respectively. The term E_e denotes the translational energy of free electrons, while $E_{\text{el},s}$ represents the electronic energy of species s. The kinetic energy of the mixture is given by $\frac{1}{2}\rho u_i u_i$, where u_i is the velocity component in the i-th direction. The final contribution, $\rho_s \Delta h_{f,s}$, accounts for the chemical energy, including the effective zero-point energy associated with species formation. For the temperature range considered in this study, ionisation effects are neglected; consequently, both the electron translational energy and the electronic energy contributions are omitted from the formulation.

Following the evaluation of partition functions for the sensible energy associated with the various molecular energy modes, as expressed for a single molecule in Equation 2.17, and assuming that the translational and rotational modes are in equilibrium and therefore characterised by a common temperature, the translational–rotational energy of a gas

mixture can be written as

$$\rho e_{tr} = \sum_{s=1}^{N} \frac{3}{2}\rho_s R_s T_t + \rho_s R_s T_r = \mathscr{R} T \left[\sum_{s\in\text{atom}} \frac{3}{2}\frac{\rho_s}{M_s} + \sum_{s\in\text{mol}} \frac{5}{2}\frac{\rho_s}{M_s} \right] \quad , \tag{2.19}$$

where ρ_s is the density of species s, R_s is the species-specific gas constant, T_t and T_r denote the translational and rotational temperatures, respectively, $\mathscr{R}$ is the universal gas constant, and M_s is the molecular mass of species s. In this context, "mol" refers to molecular species (N_2, O_2, NO), while "atom" denotes atomic species (N, O). When translational and rotational equilibrium is assumed, these modes are described by a single ro-translational temperature, denoted by T.

Similarly, the vibrational energy (e_v hereafter) of each molecular species is modelled using the simple harmonic oscillator approximation evaluated at the vibrational temperature

$$\rho e_v = \sum_{s\in\text{mol}} \rho_s e_{v,s} = \sum_{s\in\text{mol}} \rho_s \frac{\mathscr{R}}{M_s} \frac{\Theta_{v,s}}{e^{\Theta_{v,s}/T_{v,s}} - 1} \quad , \tag{2.20}$$

where $\Theta_{v,s}$ denotes the characteristic vibrational temperature of species s, and $T_{v,s}$ is the corresponding species-specific vibrational temperature. Equation 2.20 adopts the Rigid Rotor–Harmonic Oscillator (RRHO) approximation, which assumes fixed bond lengths between atoms in diatomic molecules (rigid rotor assumption) and represents vibrational motion as a simple harmonic oscillator. The different molecular energy modes considered under this approximation are illustrated in Figure 2.1 for both diatomic molecules and monatomic species.

The formulation of vibrational energy in terms of fundamental constants and vibrational temperatures enables the determination of the species-specific vibrational temperature through

$$T_{v,s} = \frac{\Theta_{v,s}}{\ln\left(1 + \frac{\Theta_{v,s} R_s}{e_{v,s}}\right)} \quad . \tag{2.21}$$

Evaluation of the vibrational temperature is required when assessing the conservation of energy in the governing equations, as it directly affects the computation of thermal diffusion rates. Furthermore, in the definition of the chemical kinetic model described in Section 2.2, a single vibrational temperature is required to represent the total vibrational energy when evaluating chemical reaction rates using Park's multi-temperature formulation.

Since species-specific constants are embedded within the vibrational energy formulation given in Equation 2.20, a direct analytical inversion for a single vibrational temperature is not possible. As a result, two alternative approaches may be considered. The first introduces an approximation to improve computational efficiency by employing weighted averages of the species-specific constants. Under this approach, the total vibrational

TABLE 2.1: Thermodynamic properties of the species considered (Mcbride et al., 2002).

	O	O_2	N	N_2	NO
M (kg/mol)	0.016	0.032	0.014	0.028	0.030
$\Theta_{v,s}$ (K)	–	2270	–	3393	2739
$\Delta h_{f,s}$ (kJ/kg)	15575	0	33764.3	0	3259.6

temperature is defined as

$$T_v = \frac{\overline{\Theta_v}}{\ln\left(1 + \frac{\overline{\Theta_v}\,\overline{R}}{e_v}\right)} \quad , \tag{2.22}$$

where $\overline{\Theta_v}$ and $\bar{R}$ denote weighted averages of the characteristic vibrational temperature and the species gas constant, respectively.

Alternatively, for improved accuracy in time-dependent simulations, a single vibrational temperature at each time step may be obtained numerically from the species vibrational energies using an iterative procedure. In particular, a Newton–Raphson method may be employed to compute the overall vibrational temperature T_v, which is expressed as

$$T_v^{n+1} = T_v^n + \frac{\left(\rho e_v - \sum_{s=1}^{N} \rho_s e_{v,s}\right)}{\sum_{s=1}^{N} \rho_s \frac{\partial e_{v,s}}{\partial T_v}} \quad , \tag{2.23}$$

with

$$\frac{\partial e_{v,s}}{\partial T_v} = \frac{\Theta_{v,s}^2 \mathscr{R}}{T_v^2 \overline{M}_s} \frac{\exp\left(\Theta_{v,s}/T_v\right)}{\left(\exp\left(\Theta_{v,s}/T_v\right) - 1\right)^2} \quad .$$

To evaluate the heat of formation at absolute zero (0 K), representative of the effective zero-point energy of the mixture, experimentally determined values are used. These values are reported in Table 2.1. When adopting the parameters provided by Gnoffo et al. (1989), a conversion factor of 4.1868×10^6 must be applied to convert from units of cal/cm^3 to J/m^3. Table 2.1 summarises the thermodynamic properties of the species considered in this thesis, including molecular mass, characteristic vibrational temperature, and heat of formation.

2.1.4 Enthalpy and Heat Capacity

To perform flow-field calculations, thermodynamic properties such as the specific heat at constant pressure, C_p, and the enthalpy, h, are required. For a chemically reacting gas

mixture, the enthalpy per unit mass of the mixture can be expressed as (Anderson, 2019)

$$h = \sum_{s=1}^{N} Y_s \, h_s \quad , \tag{2.24}$$

where h denotes the total enthalpy of the mixture, Y_s is the mass fraction of species s, and h_s is the enthalpy per unit mass of species s, which is defined as

$$h_s = (h - e_\circ)_s + (\Delta h_f)_s \quad , \tag{2.25}$$

where $e_\circ$ represents the zero-point energy, which generally cannot be calculated directly or measured experimentally, and $(\Delta h_f)_s$ denotes the heat of formation of species s at absolute zero temperature. Substituting this expression into the mixture formulation yields

$$h = \sum_{s=1}^{N} Y_s (h - e_\circ)_s + \sum_{s=1}^{N} Y_s (\Delta h_f)_s \quad . \tag{2.26}$$

In this formulation, $(h_s - e_\circ)$ represents the species-specific sensible enthalpy above the zero-point energy, while $(\Delta h_f)_s$ corresponds to the enthalpy of formation, often referred to as the chemical enthalpy. This term represents the effective zero-point energy of the mixture relative to the chosen reference state.

Expanding upon the discussion above, while the sensible energy of a gas can be evaluated using statistical thermodynamics, the zero-point energy cannot be determined directly. However, within the context of the governing equations, it is generally unnecessary to define the absolute value of the total enthalpy h. Instead, the quantity of interest is the change in enthalpy. As a result, the zero-point energy may be represented through an effective zero-point energy, which is treated as a constant parameter specific to a given mixture and characterises the enthalpy change associated with chemical reactions (Anderson, 2021).

The complete expression for the sensible enthalpy per unit mass of a species can be written as

$$(h - e_\circ)_s = \underbrace{\frac{3}{2}\frac{\mathscr{R}T}{M_s}}_{\text{Translation}} + \underbrace{\frac{\mathscr{R}T}{M_s}}_{\text{Rotation}} + \underbrace{\frac{\Theta_s/T_v}{\exp\left(\Theta_s/T_v\right) - 1}\frac{\mathscr{R}T}{M_s}}_{\text{Vibration}} + \frac{\mathscr{R}T}{M_s} + \text{electronic energy} \quad , \tag{2.27}$$

where $\mathscr{R}$ is the universal gas constant, T is the translational temperature, T_v is the vibrational temperature, and M_s is the molecular mass of species s.

Similarly, the specific heat at constant pressure for a gas mixture may be expressed as

$$C_p = \frac{\partial}{\partial T}\left(\sum_{s=1}^{N} Y_s\, h_s\right) \quad .$$

from which it follows that

$$C_p = \underbrace{\sum_{s=1}^{N} Y_s C_{p,s}}_{\text{Frozen Specific Heat}} + \underbrace{\sum_{s=1}^{N} h_s \left(\frac{\partial Y_s}{\partial T}\right)}_{\text{Due to Chemical Reaction}} \quad , \tag{2.28}$$

where C_p denotes the mixture-specific heat at constant pressure and $C_{p,s}$ represents the species-specific heat at constant pressure. This formulation corresponds to the frozen specific heat, in which species mass fractions are assumed constant and no contribution from chemical production or depletion is included.

Based on statistical thermodynamics and under the rigid rotor–harmonic oscillator approximation, the species-specific heat at constant pressure, $C_{p,s}$, can be expressed as

$$C_{p,s} = \frac{3}{2}\frac{\mathscr{R}}{M_s} + \frac{\mathscr{R}}{M_s} + \frac{(\Theta_{v,s}/T_v)^2\ \exp\left(\Theta_{v,s}/T_v\right)}{\left(\exp\left(\Theta_{v,s}/T_v\right)-1\right)^2}\ \frac{\mathscr{R}}{M_s} + \frac{\mathscr{R}}{M_s} + \frac{\partial e_{el}}{\partial T} \quad . \tag{2.29}$$

similarly, the species-specific heat at constant volume, $C_{v,s}$, is expressed as

$$C_{v,s} = \frac{3}{2}\frac{\mathscr{R}}{M_s} + \frac{\mathscr{R}}{M_s} + \frac{(\Theta_{v,s}/T_v)^2\ \exp\left(\Theta_{v,s}/T_v\right)}{\left(\exp\left(\Theta_{v,s}/T_v\right)-1\right)^2}\ \frac{\mathscr{R}}{M_s} + \frac{\partial e_{el}}{\partial T} \quad . \tag{2.30}$$

where the specific heat ratio, γ, is then defined as

$$\gamma = \frac{C_p}{C_v} = \frac{\sum_{s=1}^{N} Y_s\ C_{p,s}}{\sum_{s=1}^{N} Y_s\ C_{v,s}} \quad . \tag{2.31}$$

Alternatively, species enthalpies and specific heats may be obtained from tabulated thermodynamic data represented in polynomial form. Two such polynomial formulations are discussed in the following sections.

NASA-9 Polynomial

The NASA-7 and NASA-9 thermodynamic polynomial databases, originally developed by Sanford and Mcbride (1976) and later extended by Mcbride et al. (2002), are widely used for evaluating thermodynamic properties in high-temperature gas flows. These datasets have been incorporated into the *Chemical Equilibrium with Applications* (CEA) program, which is commonly employed to compute equilibrium compositions and thermodynamic properties of reacting gas mixtures (Gordon and McBride, 1994).

Within the NASA-9 formulation, the dimensionless specific heat at constant pressure, $C_p^\circ(T)/R$, is represented by an empirical polynomial consisting of seven coefficients, with two additional coefficients used in the evaluation of entropy and enthalpy. A known limitation of the NASA-9 database, as discussed by Scoggins et al. (2017), is the presence of inconsistencies in species enthalpies of formation arising from the use of a combination of experimental measurements and computational chemistry data. To address this issue, Ruscic et al. (2004) introduced the thermochemical network (TN) approach, which enforces consistency among species enthalpies of formation through a systematically constrained network of thermo-chemical data derived from the literature. Owing to the specific scope and modelling requirements of the present study, the TN methodology is not pursued further.

The dimensionless form of the specific heat at constant pressure as given by the NASA-9 polynomial database is expressed as

$$C_p^\circ(T)/R = a_1T^{-2} + a_2T^{-1} + a_3 + a_4T + a_5T^2 + A_6T^3 + a_7T^4 \quad , \tag{2.32}$$

The corresponding expressions for enthalpy and entropy are obtained by integrating $C_p^\circ(T)$ and $C_p^\circ(T)/T$, respectively

$$\begin{aligned} H^\circ(T)/RT = -a_1T^{-2} + a_2\ln(T)/T + a_3 + a_4T/2 + a_5T^2/3 + A_6T^3/4 \\ +a_7T^4/5 + b_1/T \end{aligned} \tag{2.33}$$

$$\begin{aligned} S^\circ(T)/R = -a_1T^{-2}/2 - a_2/T + a_3\ln(T) + a_4T + a_5T^2/2 + A_6T^3/3 \\ +a_7T^4/4 + b_2 \end{aligned} \tag{2.34}$$

where a_i denote the first seven polynomial coefficients and b_i are the integration constants associated with the enthalpy and entropy formulations (Mcbride et al., 2002).

To convert the resulting quantities into units of J/kg · K for the specific heat and J/kg for the enthalpy, the following unit conversions are applied

$$C_{p,s} = \frac{C_p^\circ(T)}{R} \times \frac{\mathscr{R}}{M_s} \quad , \tag{2.35}$$

$$h_s = \frac{H^\circ(T)}{RT} \times \frac{\mathscr{R}}{M_s}T \quad , \tag{2.36}$$

where $\mathscr{R}$ is the universal gas constant, equal to 8.314 J/K · mol, and M_s is the molecular mass of species s expressed in kg/mol.

Gupta Polynomials

Following a similar approach to that adopted by Mcbride et al. (2002), Gupta et al. (1990) expresses the species-specific heat at constant pressure, $C_{p,s}$, using a polynomial

representation

$$C_{p,s} = \left(A_1 + A_2 T + A_3 T^2 + A_4 T^3 + A_5 T^4\right) \times \frac{\mathscr{R}}{M_s} \times 4186.8, \tag{2.37}$$

where $\mathscr{R} = 1.978$ cal/(g · mol · K), M_s is the molecular mass of species s expressed in g/mol, and the factor 4186.8 is used to convert from cal/(g · K) to J/(kg · K).

In addition, Gupta et al. (1991) provides a polynomial expression for the specific heat of an 11-species air mixture under a range of pressures, which is written as

$$C_{p_{air}} = \exp\left(A_{C_p} Z^4 + B_{C_p} Z^3 + C_{C_p} Z^2 + D_{C_p} Z + E_{C_p}\right) \times 4186.8 \quad , \tag{2.38}$$

$$Z = \ln(T/10000) \quad , \tag{2.39}$$

where the coefficients A_{C_p}, B_{C_p}, C_{C_p}, D_{C_p}, and E_{C_p} are given in Gupta et al. (1991). The same conversion factor of 4186.8 is applied to express the specific heat in SI units.

A comparison between the NASA-9 database, the Gupta polynomial formulation, and the rigid rotor–harmonic oscillator model employed in this study reveals that the specific heats of nitrogen and oxygen begin to diverge at temperatures of approximately 4000 K when using the RRHO approach. This discrepancy arises from the neglect of electronic energy contributions in the RRHO formulation, which are explicitly accounted for in both the NASA-9 and Gupta models. As illustrated in Figure 2.2, the electronic contribution to the specific heat of the nitrogen molecule becomes significant at temperatures of approximately 6000 K, while for atomic nitrogen this contribution becomes non-negligible at around 4000 K.

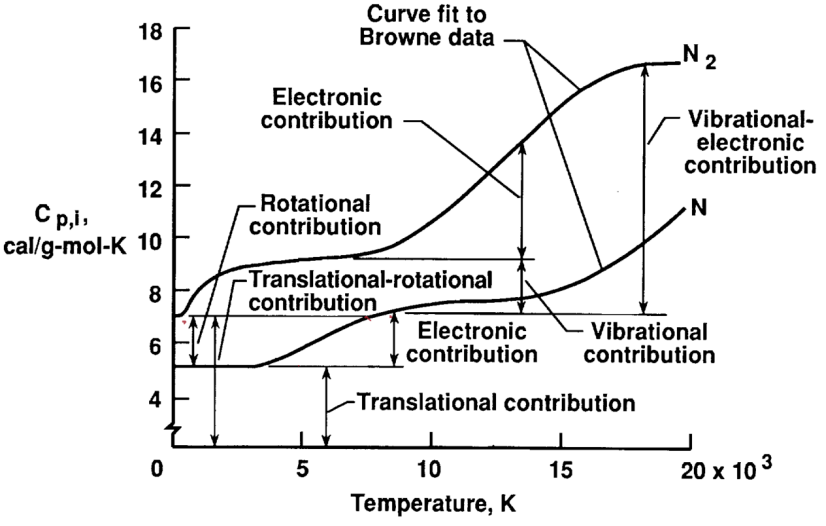

FIGURE 2.2: Specific heat capacity of atomic nitrogen and molecular nitrogen as a function of temperature (Gupta et al., 1990).

2.2 Chemical Kinetic Model

Physics-based modelling of hypersonic flows relies critically on accurate descriptions of chemical reaction rates and collisional cross-sections. In many cases, these quantities are derived from Potential Energy Surfaces (PES) computed using *ab initio* quantum-chemical methods. Once a PES is available, collisional cross-sections can be evaluated, and reaction rate coefficients may be obtained by simulating individual molecular collisions using Quasi-Classical Trajectory (QCT) methods, in which particle dynamics are governed by Hamilton's equations of motion. The resulting cross-sections are then integrated over a range of collision energies to yield temperature-dependent reaction rates (Jaffe et al., 2017). While this approach is physically rigorous, it remains computationally expensive and has thus far been limited to a small number of reaction systems rather than a complete air chemistry model. For example, Jo et al. (2021) investigated ro-vibrationally specific collisions between nitrogen molecules and oxygen atoms.

An alternative strategy is Direct Molecular Simulation (DMS), in which particle trajectories are solved in real time on a given PES during the flow simulation itself. Notable studies employing this approach include Valentini et al. (2015); Torres and Schwartzentruber (2020, 2021), which focused on a limited set of reactions, primarily involving nitrogen and oxygen species. Although substantial progress has been achieved, a fully comprehensive DMS-based air chemistry model is not yet available. To date, the most extensive effort is that of Jo et al. (2022), who developed a master-equation framework incorporating six collisional processes for an air mixture at a fixed temperature of 10,000 K.

In practical CFD applications, chemical kinetics are most commonly modelled using Arrhenius-type expressions for reaction rate coefficients, originally introduced by Arrhenius (1889). While this formulation is widely adopted, it does not adequately represent environments characterised by thermal non-equilibrium. To address this limitation, Park (1985) proposed reaction-rate models that incorporate different temperatures associated with the colliding particles while retaining the Arrhenius functional form. Subsequently, Park (1986) compared three formulations—the one-temperature model, the vibrational-temperature model, and the average-temperature model widely known as the two-temperature model—and concluded that the average-temperature model provides the most accurate representation of reaction rates in high-enthalpy flows.

Multiple variants of Park's average-temperature model have since been developed, differing primarily in two aspects. The first concerns the evaluation of the equilibrium composition of air, which directly affects the equilibrium constant. The second involves updates to reaction rate coefficients based on new experimental or empirical data. Representative examples include Park (1985, 1987, 1989, 1993); Park et al. (1994, 2001), along with refinements to specific reaction mechanisms such as those discussed in Park (1988).

It is important to note that several rate coefficients employed in Park's original models are based on experimental data obtained more than three decades ago. As a result, recent studies have sought to update these coefficients using improved experimental techniques and datasets. For instance, Johnston and Brandis (2014) revised key parameters using measurements from *NASA Ames' Electric Arc Shock Tube Facility*, while Jaffe et al. (2017) presented updated rate coefficients relevant to hypersonic Mars entry conditions. Among Park's body of work, the most frequently cited formulations in contemporary hypersonic flow simulations include Park (1989), Park (1993), and Park et al. (2001), as also referenced by Gnoffo et al. (1989).

The chemical kinetic model implemented in this thesis considers a five-species air mixture consisting of O, O_2, N, N_2, and NO, and includes five chemical reactions

$$\begin{aligned} N_2 + M &\longleftrightarrow 2N + M \\ O_2 + M &\longleftrightarrow 2O + M \\ NO + M &\longleftrightarrow N + O + M \\ N_2 + O &\longleftrightarrow NO + N \\ NO + O &\longleftrightarrow O_2 + N \end{aligned} \tag{2.40}$$

2.2.1 Equilibrium Chemical Composition

The chemical composition of a reacting mixture is defined at a specified pressure and temperature. For a compressible system with constant mass and only quasi-equilibrium work modes, the first and second laws of thermodynamics may be combined under conditions of constant temperature and pressure, yielding

$$\begin{aligned} \delta Q - PdV &= dU \\ dS &\geq \delta Q/T \\ dU + PdV - TdS &\leq 0 \end{aligned} \tag{2.41}$$

Furthermore,

$$dG = dU + PdV - TdS \leq 0$$

Under these thermodynamic constraints, the differential form of the Gibbs free energy indicates that a chemical reaction proceeds until the Gibbs function of the system reaches a minimum. Consequently, the condition for chemical equilibrium is obtained as

$$dG = 0 \quad , \tag{2.42}$$

For a general chemical reaction of the form

$$\nu_a A + \nu_b B \rightleftharpoons \nu_c C + \nu_d D \quad , \tag{2.43}$$

the equilibrium condition may be expressed as

$$\nu_c \bar{g}_C + \nu_d \bar{g}_D - \nu_a \bar{g}_A - \nu_b \bar{g}_B = 0 \quad , \tag{2.44}$$

where $\bar{g}$ denotes the chemical potential, or molar Gibbs free energy, of each species.

For an isothermal process, the relationship between the entropy change and the Gibbs function allows the Gibbs free energy of an individual species to be written as

$$\bar{g} = \mathscr{R}\ T\ \ln \frac{P_2}{P_1} \quad . \tag{2.45}$$

Equation 2.46 therefore represents the Gibbs function of component i at its partial pressure P_i and mixture temperature T

$$\bar{g}_i(T, P_i) = \bar{g}_i^*(T) + \mathscr{R} T \ln(P_i) \tag{2.46}$$

where the superscript $*$ denotes the standard state at one atmospheric pressure.

Substituting Equation 2.46 into the equilibrium criterion given in Equation 2.44, and introducing the standard-state Gibbs function change, yields

$$\Delta G^*(T) = \nu_c \bar{g}_C^*(T) + \nu_d \bar{g}_D^*(T) - \nu_a \bar{g}_A^*(T) - \nu_b \bar{g}_B^*(T) \quad , \tag{2.47}$$

$$\begin{aligned} \Delta G^*(T) &= -\mathscr{R} T(\nu_c \ln(P_C) + \nu_d \ln(P_D) - \nu_a \ln(P_A) - \nu_b \ln(P_B)) \quad , \\ &= -\mathscr{R} T \ln \left[\frac{P_C^{\nu_c} P_D^{\nu_d}}{P_A^{\nu_a} P_B^{\nu_b}} \right] \quad . \end{aligned} \tag{2.48}$$

In this expression, the logarithmic term defines the equilibrium constant K_p in terms of partial pressures

$$K_p = \frac{P_C^{\nu_c} P_D^{\nu_d}}{P_A^{\nu_a} P_B^{\nu_b}} \tag{2.49}$$

Thus, the equilibrium composition of a reacting gas mixture may be determined through evaluation of the equilibrium constant.

In addition to the pressure-based formulation given in Equation 2.49, the equilibrium constant for a reaction of the form Equation 2.43 may also be expressed in terms of molar concentrations (Cengel et al., 2019)

$$K_c = \frac{[C]^{\nu_c} [D]^{\nu_d}}{[A]^{\nu_a} [B]^{\nu_b}}. \tag{2.50}$$

By invoking the ideal gas equation of state, the relationship between the pressure-based and concentration-based equilibrium constants is obtained as

$$K_p = K_c(RT)^{\Delta n} \quad , \tag{2.51}$$

where $\Delta n = (\nu_c + \nu_d) - (\nu_a + \nu_b)$ and $\mathscr{R}$ is the universal gas constant. The units of the equilibrium constant depend on the specific reaction and is given by $(\text{kg-mole/m}^3)^{\Delta n}$ in its concentration form.

Equilibrium Constant

Within the multi-temperature (MT) chemical kinetic models presented in studies such as Park et al. (2001); Park (1984); Gnoffo et al. (1989), the equilibrium constant governing chemical equilibrium is expressed as a function of temperature through polynomial representations with empirically determined coefficients. These coefficients depend on the selected temperature ranges, the specific polynomial form employed, and the underlying thermodynamic data used in their construction. As a result, different formulations can yield variations in the predicted equilibrium composition of air mixtures.

Several approaches are commonly employed to evaluate the equilibrium composition at a prescribed temperature. Two representative methods are outlined below.

NASA-9 Polynomials

The equilibrium constant may be evaluated using the NASA-9 polynomial database by computing the Gibbs free energy for each species participating in a given reaction. The Gibbs function is obtained from the species enthalpy and entropy, both of which are evaluated using polynomial fits as described previously. For an individual species, the standard-state Gibbs function is written as

$$\Delta G_s^o(T) = H^\circ(T) - S^\circ(T) \times T \quad , \tag{2.52}$$

$$\Delta G_R^o(T) = \nu_c G_C^o(T) + \nu_d G_D^o(T) - \nu_a G_A^o(T) - \nu_b G_B^o(T) \quad , \tag{2.53}$$

where the subscript R denotes the reaction and s refers to the species.

As an illustrative example, consider the dissociation reaction of molecular oxygen

$$R = \mathrm{O_2} + \mathrm{M} \longleftrightarrow 2\mathrm{O} + \mathrm{M}$$
$$\Delta G_R^o(T) = 2 \times G_O^o(T) - G_{O2}^o(T) \quad .$$

For this reaction, the equilibrium constant is then evaluated in dimensionless form as

$$K = \exp\left(\frac{\Delta G_R^o(T)}{RT}\right) \quad . \tag{2.54}$$

Park's Polynomial

Park et al. (2001) evaluated the equilibrium constant, K_c, at a set of discrete temperatures (3000, 6000, 9000, 12,000, and 15,000 K) using stoichiometric data and derived a fourth-order polynomial expression that is valid over the temperature range 2000–10,000 K, as given in Equation 2.55. Similarly, Gnoffo et al. (1989) employed stoichiometric data from Park (1985), using a different set of temperature points (1000, 2000, 4000, 8000, and 16,000 K) and a distinct polynomial formulation, which is provided in Equation 2.56.

$$K_{c_{P01}} = \exp\left[A_1/Z + A_2 + A_3\, ln(Z) + A_4 Z + A_5 Z^2\right] \tag{2.55}$$

$$K_{c_{P85}} = \exp\left[A_1 + A_2\, \ln(Z) + A_3 Z + A_4 Z^2 + A_5 Z^3\right] \tag{2.56}$$

In these expressions, $Z = 10{,}000/T$ and A_i are fitted polynomial coefficients. The subscript c in the equilibrium constant denotes that the value is derived from stoichiometric expressions. The coefficients corresponding to these polynomial formulations are listed in Appendix A.1.

2.2.2 Non-Equilibrium Chemical Composition

In a chemically non-equilibrium state, the source term for each species is expressed as the net balance between its production and consumption through chemical reactions. Accordingly, the rate of production of species s per unit volume can be written as

$$\dot{\omega}_s = M_s \sum (\beta_{s,r} - \alpha_{s,r})(R_{f,r} - R_{b,r}) \quad , \tag{2.57}$$

where $\beta_{s,r}$ and $\alpha_{s,r}$ are the stoichiometric coefficients of the products and reactants, respectively, and $R_{f,r}$ and $R_{b,r}$ denote the forward and backward reaction rates for reaction r.

The forward and backward reaction rates are defined as

$$R_{f,r} = 1000 \left[k_{f,r} \prod_{s=1}^{5} (0.001\rho_s/M_s)^{\alpha_{s,r}}\right] \quad , \tag{2.58}$$

$$R_{b,r} = 1000 \left[k_{b,r} \prod_{s=1}^{5} (0.001\rho_s/M_s)^{\beta_{s,r}}\right] \quad , \tag{2.59}$$

where $k_{f,r}$ and $k_{b,r}$ are the forward and backward reaction rate coefficients, respectively. These coefficients are typically reported in *CGS* units. As a result, conversion factors of 1000 and 0.001 are applied to ensure consistency with *MKS* units.

In Park's chemical kinetic models, the forward reaction rate coefficient is expressed in Arrhenius form as

$$k_{r_f} = C T_a^n \exp(-T_f/T_a) \tag{2.60}$$

where T_a is the effective temperature governing the reaction rate, C is the pre-exponential factor with units of $\mathrm{cm}^3/\mathrm{mol}$, n is the temperature exponent, and T_f is the activation temperature.

Experimental evidence suggests that the time required for a system to reach chemical equilibrium is often longer than that predicted by conventional single-temperature models. To address this discrepancy, the multi-temperature formulation introduced by Park (1986) incorporates a separate vibrational temperature to account for thermal non-equilibrium effects. By coupling the translational–rotational and vibrational temperatures, the model captures the influence of vibrational relaxation on chemical reaction rates. The effective reaction temperature is defined as

$$T_a = T^{\,L}\, T_v^{\,1-L} \quad , \tag{2.61}$$

where L is a weighting parameter, typically chosen in the range 0.5–0.7 (Park, 1993). In the present study, a value of $L = 0.5$ is adopted.

The backward reaction rate coefficient is related to the forward coefficient through the equilibrium constant according to

$$k_{r_b} = \frac{k_{r_f}(T)}{K_c} \quad . \tag{2.62}$$

where the forward reaction rate used to evaluate $k_{b,r}$ is based solely on the translational temperature, rather than the two-temperature formulation. Further details on temperature modelling approaches, including extensions to ionised flows, are provided in Park (1985) and Casseau (2017).

2.3 Thermal Kinetic Model

The two most widely adopted approaches for modelling energy exchange in thermo-chemical non-equilibrium flows are the State-to-State (StS) and Multi-Temperature (MT) methods. In the StS framework, thermal non-equilibrium is resolved by explicitly modelling individual energy states—translational, rotational, and vibrational—through a master equation formulation (Jaffe et al., 2017). Similar to Quasi-Classical Trajectory (QCT) methods, this approach is computationally demanding and often necessitates the use of simplification strategies. One such strategy is coarse-graining, in which rovibrational levels are grouped into larger energy bins. This approach was employed by Torres et al. (2018) for an N_2–N system. To further reduce computational cost while retaining accuracy, MacDonald et al. (2019) proposed a hybrid reduced-order model for N_2–N interactions, which demonstrated excellent agreement with StS simulations, although its current applicability is limited to a restricted set of reactions.

Alternative modelling efforts include the work of Fiévet et al. (2019), who investigated the coupling between vibrational non-equilibrium and turbulent mixing using a state-specific relaxation model. In this approach, relaxation times were derived from QCT simulations, allowing non-Boltzmann distributions of vibrational states to be captured explicitly. Unlike MT formulations, this method resolves state-level population dynamics. In their study, inelastic collision rates were computed across nine discrete temperatures, and a reduced summation technique was employed to represent vibrational populations in the non-linear energy exchange terms.

The foundation of the multi-temperature approach can be traced back to the work of Landau and Teller (1936), and was subsequently formalised by Schwartz et al. (1952), who developed a quantitative description of vibrational relaxation using first-order perturbation theory. This formulation, commonly referred to as the SSH model, provided the basis for widely used empirical correlations, most notably the Millikan–White model introduced by Millikan and White (1963). Despite its simplicity, the Millikan–White correlation, including its corrected forms, has remained one of the most computationally efficient and frequently employed models for estimating vibrational relaxation times over several decades. The model is based on two key observations: first, that vibrational relaxation time exhibits an approximately linear dependence on temperature; and second, that experimental data tend to collapse onto a common linear trend passing through a single intersection point. This intersection point is later refined through a trial-based parameter, $\mu^{1/4}$, allowing it to vary with species and collision partner.

Although informed by theoretical considerations, the Millikan–White correlation is inherently semi-empirical and exhibits an uncertainty of approximately ±50%, with deviations of up to a factor of five reported under certain conditions. Shock-tube measurements conducted by Owen et al. (2016) demonstrated excellent agreement with the Millikan–White model for oxygen over the temperature range 1000–4000 K. In contrast, ultraviolet laser absorption spectroscopy measurements in O_2/N_2 mixtures revealed discrepancies of up to 70% in the temperature range 2000–4000 K (Streicher et al., 2020a).

Recognising these limitations, Park (1984) showed that the Millikan–White model increasingly underpredicts vibrational relaxation rates at higher temperatures. To address this shortcoming, Park introduced a correction factor based on an effective excitation cross-section, initially assumed to be temperature-independent. This assumption was later relaxed by Park (1987), who introduced a temperature-dependent cross-section to account for the diffusion-like nature of vibrational energy transfer in energy space. Further refinements were presented by Park (1993), who updated the model coefficients using more recent experimental data and improved the original correction formulation. As a consequence, the predicted vibrational relaxation times for certain species, including nitric oxide (NO), differ substantially from earlier formulations.

2.3.1 Zero-Dimensional Energy Exchange

The total vibrational energy per unit volume of the mixture is defined as

$$\rho e_v = \sum_{s \in \text{mol}} \rho_s e_{v,s} \quad , \tag{2.63}$$

where $\text{mol} = \text{N}_2, \text{O}_2, \text{NO}$ denotes the set of molecular species.

The vibrational energy conservation equation for an individual species is given in Equation 2.10 and is reiterated here for clarity.

$$\frac{\partial}{\partial t}\left(\rho_s e_{v,s}\right) + \frac{\partial}{\partial x_j}\left(\rho_s e_{v,s} u_j\right) = \frac{\partial}{\partial x_j}\left(K_{v,s}\frac{\partial T_v}{\partial x_j}\right) + \frac{\partial}{\partial x_j}\left(\rho_s e_{v,s} D_s \frac{\partial X_s}{\partial x_j}\right) + \frac{\rho_s(e^*_{v,s} - e_{v,s})}{\tau_s} + \dot{\omega}_s \hat{D}_s \tag{2.10}$$

At a single spatial location, that is, under zero-dimensional conditions, Equation 2.10 reduces to

$$\frac{\partial}{\partial t}\left(\rho_s e_{v,s}\right) = \underbrace{\frac{\rho_s(e^*_{v,s} - e_{v,s})}{\tau_s}}_{(1)} + \underbrace{\dot{\omega}_s \hat{D}_s}_{(2)} \quad , \tag{2.64}$$

where $e^*_{v,s}$ denotes the equilibrium vibrational energy of species s, $e_{v,s}$ is the instantaneous vibrational energy, $\dot{\omega}_s$ is the rate of production of species s per unit volume, and $\hat{D}_s$ represents the average vibrational energy per unit mass. Term (1) corresponds to the energy exchange arising from vibrational–translational relaxation due to molecular collisions within the control volume. Term (2) accounts for changes in vibrational energy associated with chemical reactions, either through energy loss during dissociation or energy gain during recombination processes (Gnoffo et al., 1989).

2.3.2 Vibrational Relaxation Time

The vibrational relaxation term includes the vibrational relaxation time, τ_s, for which a semi-empirical correlation was proposed by Millikan and White (1963). This model is applicable over the temperature range 300–8000 K and is given in Equation 2.65, with units of $\text{atm} \cdot \text{s}$.

$$\tilde{p}\tau^{MW} = \exp\left[A(T^{-1/3} - B) - 18.42\right] \quad , \tag{2.65}$$

In this formulation, $\tilde{p} = p/101325.0$ denotes the non-dimensionalised pressure, and A and B are empirical constants. The parameter A is defined as a product of reduced-mass and characteristic-temperature powers, $A = \mu^m \Theta_v^n$, while B is expressed as a function of

the reduced mass. These quantities may alternatively be evaluated using the relations

$$A = 0.00116\,\mu^{0.5}\Theta_v^{1.333}$$
$$B = 0.015\,\mu^{1/4}$$

where μ is the reduced mass of the colliding pair, defined as $\mu_{sj} = \frac{M_s M_j}{M_s + M_j}$, and Θ_v is the characteristic vibrational temperature of the mode under consideration.

As discussed previously, Park (1993) updated the Millikan–White correlation using revised experimentally derived constants to improve its accuracy at elevated temperatures. These updated coefficients are now widely adopted in the literature.

Since each species s undergoes collisions with a mixture of other heavy species, the vibrational relaxation time must be averaged accordingly. A commonly employed approach is the weighted harmonic mean, which has been used in studies such as Lee (1984), Park (1984), and more recently Miró Miró (2020); Passiatore (2021), defined as

$$\tau_j^{MW} = \frac{\sum_{s=1}^{N} \rho_s / M_s}{\sum_{s=1}^{N} \tau_s^{MW}\ \rho_s / M_s} \quad , \tag{2.66}$$

where ρ_s is the density of species s, M_s is the molecular weight of species s, and the subscript j denotes the collision partner contributing to vibrational relaxation.

To further reduce computational cost, Gnoffo et al. (1989) proposed an approximation in which a weighted arithmetic average is applied over species, combined with a harmonic average over molecular collision pairs

$$\tau_j^{MW} = \frac{\sum_{s=1}^{N} \tau_s^{MW}\ \rho_s / M_s}{\sum_{s=1}^{N} \rho_s / M_s} \quad , \tag{2.67}$$

This approximation has been widely adopted in practical modelling, although its accuracy is problem dependent. The influence of the averaging method and the associated modelling errors are examined in the following chapter.

It was noted by Park (1984) that Equation 2.65 significantly overpredicts vibrational relaxation times at temperatures above 8000 K. To address this limitation, Park reformulated the relaxation process in terms of an effective excitation cross section, σ_v. The most recent version of this model is given by Park (1993) as

$$\tau_j^{Park} = [n_t \sqrt{(8kT/\pi m)}\sigma_v]^{-1} \quad , \tag{2.68}$$

where n_t is the total number density of colliding particles, k is the Boltzmann constant, m is the average molecular mass of the mixture, and σ_v is the excitation cross section,

expressed in m^2, given by

$$\sigma_v = 3 \times 10^{-21}(50,000/T)^2 \quad . \tag{2.69}$$

A blended formulation is then introduced to ensure accuracy across a wide temperature range by combining the low-temperature behaviour of Equation 2.65 with the high-temperature formulation given in Equation 2.68

$$< \tau_j >= \tau_j^{MW} + \tau_j^{Park} \tag{2.70}$$

This blended model has been shown to provide improved agreement with experimental measurements for O_2 over the temperature range 5000–8000 K. The correction accounts for two key effects at elevated temperatures. First, the Millikan–White formulation implies unrealistically large excitation cross sections as temperature increases. Second, vibrational relaxation does not proceed as a strictly linear process; instead, it exhibits diffusion-like behaviour in vibrational energy space, in contrast to the assumptions underlying the Landau–Teller model (Park, 1988).

From a theoretical standpoint, two important observations emerge regarding vibrational relaxation. First, depending on the system conditions, relaxation may occur in a quasi-steady manner in which higher vibrational energy levels equilibrate more rapidly than lower levels, as also observed by Kim and Boyd (2012). Second, the characteristic relaxation timescale is strongly dependent on the initial vibrational population, commonly represented by the vibrational temperature. This dependence is not captured by empirical models such as that of Millikan and White (1963), which assume relaxation times independent of the initial vibrational state. This limitation introduces uncertainty when simplified Landau–Teller-based energy exchange models are applied and highlights the extent to which compressibility and non-equilibrium effects can significantly alter vibrational energy distributions.

2.3.3 Molecular Production/Depletion

The term $\dot{\omega}_j \hat{D}_j$ appearing in the governing equations represents the creation or destruction of vibrational energy within species j due to vibrational excitation and dissociation processes occurring at high vibrational quantum levels. Here, $\dot{\omega}_j$ denotes the net rate of production of species j as determined by the chemical reaction rates, while $\hat{D}_j$ represents the vibrational energy per unit mass associated with the dissociation or recombination of a diatomic molecule.

According to Gnoffo et al. (1989), the form of $\hat{D}_j$ depends on whether dissociation at high temperatures is assumed to be preferential or non-preferential. In the case of preferential

TABLE 2.2: Constants used in the calculation of the vibrational depletion/production term.

	N_2	O_2	NO
$\tilde{D}_s$ (eV)	9.759	5.115	6.496

dissociation, two commonly used formulations are reported

$$\hat{D}_s = \hat{c}_1 \tilde{D}_s \tag{2.71}$$

$$\hat{D}_s = \tilde{D}_s - kT \tag{2.72}$$

where $\tilde{D}_s$ is a constant representing the vibrational energy depletion potential. In Equation 2.71, the coefficient $\hat{c}_1$ is a scaling factor typically less than unity, indicating that the vibrational energy removed per dissociation event exceeds the mean vibrational energy of the molecule. In contrast, the formulation given in Equation 2.72, proposed by Park (1988), assumes that the vibrational energy removed during dissociation is partially offset by the average translational energy, kT, resulting in a reduced effective depletion term relative to $\tilde{D}_s$.

The values of the constants $\tilde{D}_s$ employed in these formulations are listed in Table 2.2 where $1, \text{eV} = 9.65 \times 10^7, \text{J/kg-mole}$. A more moderate formulation is also presented by Gnoffo et al. (1989), in which $\hat{D}_s$ is defined as

$$\hat{D}_s = \hat{c}_2 e_{v,s} \quad , \tag{2.73}$$

with $\hat{c}_2 > 1$ corresponding to preferential dissociation and $\hat{c}_2 = 1$ representing non-preferential dissociation. In this model, the depletion term scales with the instantaneous vibrational energy of the species rather than a fixed depletion constant.

Furthermore, Jaffe (1986) noted that, for non-preferential dissociation, in addition to setting $\hat{c}_2 = 1$, the reaction temperature T_q should be defined as a weighted average of all available energy modes. In this approach, T_q is expressed as a function of the mode-specific energies, $T_q = f(\tilde{e}_t, \tilde{e}_v, \tilde{e}_{tr})$. This weighted-temperature formulation was not implemented in the present study.

2.3.4 Thermal Equilibrium Chemically Reacting Flow

In a thermally equilibrated reacting flow, all internal energy modes, including vibrational modes, are assumed to be in equilibrium with the translational mode and are therefore described by a single temperature. Under this assumption, the vibrational temperature becomes a function of the translational temperature, and a separate vibrational energy transport equation is no longer required.

Imposing this thermal equilibrium assumption on the governing equations defined in Equation 2.1 through Equation 2.4 yields a reduced system of equations for a chemically reacting gas mixture

$$\frac{\partial}{\partial t}\left(\rho_s\right) + \frac{\partial}{\partial x_j}\left(\rho_s u_j\right) = \frac{\partial}{\partial x_j}\left(\rho D_s \frac{\partial X_s}{\partial x_j}\right) + \dot{w}_s + \rho_s \sum_{s=1}^{N} D_s \frac{\partial X_s}{\partial x_j} \quad , \tag{2.74}$$

$$\frac{\partial}{\partial t}\left(\rho u_i\right) + \frac{\partial}{\partial x_j}\left(\rho u_i u_j\right) = -\frac{\partial p}{\partial x_i} + \frac{\partial}{\partial x_j}\left[\mu\left(\frac{\partial u_i}{\partial x_j} + \frac{\partial u_j}{\partial x_i}\right) - \frac{2}{3}\mu\frac{\partial u_k}{\partial x_k}\delta_{ij}\right] \quad , \tag{2.75}$$

$$\begin{aligned}\frac{\partial}{\partial t}\left(\rho E\right) + \frac{\partial}{\partial x^j}\left(\rho H u^j\right) = \frac{\partial}{\partial x^j}\left(K\frac{\partial T}{\partial x^j}\right) + \frac{\partial}{\partial x^j}\left(\rho\sum_{s=1}^{N} h_{v,s} D_s \frac{\partial X_s}{\partial x^j}\right) \\ + \frac{\partial X_s}{\partial x^j}\left[u^i\mu\left(\frac{\partial u^i}{\partial x^j} + \frac{\partial u^j}{\partial x^i}\right) - \frac{2}{3}u^i\mu\frac{\partial u^k}{\partial x^k}\delta^{ij}\right] \quad .\end{aligned} \tag{2.76}$$

Within this formulation, the energy conservation equation given in Equation 2.18 must be restructured to solve directly for the translational temperature. The absence of an explicit vibrational energy equation, however, complicates this process. To address this, the translational temperature T is obtained using a Newton–Raphson iterative procedure, expressed as

$$T_{n+1} = T_n - \frac{f(T)}{f(T)'} \tag{2.77}$$

$$f(T) = \frac{\rho E - \frac{1}{2}\rho u_i u_i - \mathscr{R}\sum\limits_{\text{mol}} \frac{\rho_s \Theta_{v,s}}{M_s(\exp(\Theta_{v,s}/T)-1)} - \sum \frac{\rho_s h_{f,s}}{\rho}}{\beta} - T \tag{2.78}$$

$$f(T)' = -\frac{\mathscr{R}}{T^2\beta}\sum_{mol}\frac{\rho_s \Theta_{v,s}^2 \exp\left(\Theta_{v,s}/T\right)}{M_s(\exp\left(\Theta_{v,s}/T\right)-1)^2} - 1 \tag{2.79}$$

where the term β is defined as

$$\beta = \mathscr{R}\left[\sum_{s=\text{N,O}}\frac{3}{2}\frac{\rho_s}{M_s} + \sum_{s=\text{mol}}\frac{5}{2}\frac{\rho_s}{M_s}\right]. \tag{2.80}$$

This iterative method enables a consistent determination of the equilibrium temperature while accounting for vibrational energy contributions from diatomic species in the total energy balance, without the need to solve an additional vibrational energy transport equation.

2.4 Transport Properties

An accurate description of momentum, energy, and mass transport is essential for characterising high-temperature flow environments. In multi-component flow formulations, transport fluxes are expressed in terms of transport coefficients and gradients of macroscopic variables. These coefficients are not provided explicitly by the kinetic theory of gases (Giovangigli, 1999). Instead, they may be derived from Chapman–Enskog solutions of the Boltzmann equation. By employing Sonine polynomial expansions of sufficiently high order, transport coefficients can be evaluated with negligible error, as demonstrated in a number of detailed studies (Loyalka et al., 2007; Tipton et al., 2009a,b; Tompson et al., 2009, 2010). Despite their accuracy, such approaches are computationally prohibitive for use in large-scale CFD simulations. Consequently, simplified or approximate transport models are typically adopted in practical applications. These approximate models may generally be divided into two components. The first concerns the evaluation of transport properties for individual species within the flow, while the second addresses the determination of mixture-averaged transport properties through appropriate mixing rules.

From a physical standpoint, the presence of internal molecular energy modes does not alter the fundamental expressions for diffusion and viscosity, which depend solely on the molecular velocity distribution function. In contrast, thermal conductivity is directly influenced by internal molecular degrees of freedom, as these modes contribute to energy transport (Hirschfelder et al., 1954). While mass transport is driven by concentration gradients and energy transport by temperature gradients, the present study neglects mass diffusion induced by temperature gradients (the Soret effect) and heat flux induced by concentration gradients (the Dufour effect).

2.4.1 Collision Integrals

Transport fluxes derived from Enskog's solution of the Boltzmann equation are expressed in terms of transport coefficients. These coefficients arise from Sonine polynomial expansions of the velocity distribution function; however, the resulting polynomial coefficients involve a set of complex integrals (Hirschfelder et al., 1954). Chapman and Cowling showed that these integrals can be reduced to linear combinations of a specific family of collision integrals, denoted by $\Omega^{(l,s)}$. For collisions between molecules of species i and j, these integrals are defined as

$$\Omega_{ij}^{l,s} = \sqrt{\frac{2\pi kT}{\mu_{ij}}} \int_0^\infty \int_0^\infty e^{-\gamma_{ij}^2} \gamma_{ij}^{2s+3} (1 - cos^l \chi) b \, db \, d\gamma_{ij} \quad , \tag{2.81}$$

where the original notation of the source is retained[1]. Here, μ_{ij} denotes the reduced mass of the colliding molecular pair, γ_{ij} is the reduced initial relative speed, χ is the molecular deflection angle, and b represents the impact parameter (Hirschfelder et al., 1954). This formulation allows transport phenomena to be expressed explicitly in terms of the collision integrals $\pi\bar{\Omega}_{ij}^{(l,s)}$. Consequently, the accuracy of the computed transport properties is directly dependent on the accuracy of these collision integrals. The evaluation of these integrals may be carried out either through theoretical representations or empirical approaches (Vincenti and Kruger, 1965).

At lower temperatures, based on the theoretical definition of the intermolecular potential function—which depends on the modelling of individual species—accurate analytical expressions for collision cross sections can be derived. Such analytical models include the rigid elastic sphere and the Sutherland model, as well as more sophisticated formulations such as the Lennard-Jones potential and the modified Buckingham potential. The latter two are generally regarded as providing the most accurate representations of intermolecular interactions (Hirschfelder et al., 1954). However, for the conditions considered in this thesis, these models are not well suited to high-enthalpy states, where intermolecular forces become more complex and additional physical effects become significant.

At high temperatures, collision cross sections are typically obtained empirically. In hypersonic-flow simulations, the majority of available data is derived from the work of Gupta et al. (1990), which provides polynomial fits based on earlier datasets compiled by Yos (1963). The collision integrals reported by Yos were originally derived from the work of Mason (Yun et al., 1962), incorporating experimental measurements reported in Yun and Mason (1962). For interactions not included in Mason's dataset—specifically N-O_2 and N-NO collisions—Yos (1963) approximated the corresponding cross sections using data from similar neutral-neutral interactions. For temperatures exceeding 15,000 K, several collision cross sections were extrapolated. Further details regarding these approximations and extrapolation procedures are provided in Yos (1963).

The collision integrals $\pi\bar{\Omega}_{ij}^{(1,1)}$ and $\pi\bar{\Omega}_{ij}^{(2,2)}$ are represented using polynomial curve fits of the form

$$\pi\bar{\Omega}_{ij}^{(1,1)} = \exp\left(D_{11}\right) T^{\left[A_{11}\ln(T)^2 + B_{11}\ln(T) + C_{11}\right]} \quad , \tag{2.82}$$

$$\pi\bar{\Omega}_{ij}^{(2,2)} = \exp\left(D_{22}\right) T^{\left[A_{22}\ln(T)^2 + B_{22}\ln(T) + C_{22}\right]} \quad , \tag{2.83}$$

where T is the translational temperature, and the coefficients A_{11}, B_{11}, C_{11}, D_{11}, A_{22}, B_{22}, C_{22}, and D_{22} are provided by Gupta et al. (1990). These coefficients are listed in Appendix A.3.1.

[1] Equations (7.4-34) in Hirschfelder et al. (1954)

2.4.2 Viscosity and Thermal conductivity

In studies of high-enthalpy and thermo-chemically reacting flows, a range of models has been employed to evaluate viscosity and thermal conductivity, each presenting distinct advantages and limitations. The formulations of several commonly used models are presented in the following sections. The selection of models presented here, include those evaluated based on analytical approaches which are defined for low temperatures and those evaluated based on empirical methods for high, where the definition of such models are required for the detailed comparative analysis provided in subsequent chapters (Chapter 5).

2.4.2.1 Hirschfelder-Lennard-Jones (HLJ)

A commonly adopted approach for evaluating transport properties is based on the Lennard–Jones (LJ) intermolecular potential. Within the context of molecular kinetic theory, the Lennard–Jones model provides a more realistic description of intermolecular interactions for non-polar molecules than simpler representations such as the rigid-sphere or Sutherland potentials.

According to the formulation presented by Hirschfelder et al. (1954), which is applicable primarily to low-temperature regimes, the viscosity of a single species s and that of a gas mixture may be expressed, respectively, as

$$\mu_s = 266.93 \left(\frac{\sqrt{M_s T}}{\sigma_s^2 \Omega^{(2,2)}(T_s^*)} \right) \times 10^{-8} \tag{2.84}$$

$$\mu = 10^{-8} \sum_{i=1} \frac{X_i^2}{X_i^2/\mu_i + 2.308 \sum_{k \neq i} \frac{X_i X_k}{A_{ik}^\star \mu_{ik}} \frac{M_k}{(M_i + M_k)}}, \tag{2.85}$$

where the corresponding binary viscosity is given by

$$\mu_{ik} = 266.93 \left(\frac{\sqrt{2 M_i M_k T/(M_i + M_k)}}{\sigma_{ik}^2 \Omega_{ik}^{(2,2)}(T_{ik}^*)} \right) \times 10^{-8},$$

Here, μ_s and μ denote the viscosities of a pure gas and a gas mixture, respectively, expressed in kg/m · s (Hirschfelder et al., 1954). The Lennard–Jones parameters ϵ and σ are determined from experimental viscosity measurements, together with the interaction parameter $A^\star$. The quantity X_s denotes the mole fraction of species s, M_s is its molecular mass expressed in grams, and $\Omega_{ik}^{(2,2)}(T_{ik}^\star)$ is the collision integral evaluated at the reduced temperature $T_{ik}^\star$.

The simplified mixture expression given in Equation 2.85 is derived under the assumption that off-diagonal terms in the full multicomponent viscosity formulation are negligible.

Hirschfelder et al. (1954) demonstrated that this approximation yields results that closely match those obtained from the full Chapman–Enskog solution.

The Lennard–Jones potential is therefore regarded as a highly accurate model for computing viscosity in non-polar gases. Collision integrals, $\Omega^{(i,j)}$, have been tabulated as functions of the reduced temperature $T^\star$ (Hirschfelder et al., 1954). Interaction parameters for unlike molecular pairs may be estimated using empirical combining rules.

$$\sigma_{ij} = 0.5(\sigma_i + \sigma_j) \tag{2.86}$$

$$\epsilon_{ij} = \sqrt{\epsilon_i \epsilon_j} \tag{2.87}$$

Extensive comparisons with experimental data have shown that the Lennard–Jones model provides excellent agreement for viscosity predictions. In particular, Hirschfelder et al. (1954) reported the most accurate results among several tested models for temperatures up to approximately 950 K, provided that appropriate force constants are selected for the relevant temperature range.

The thermal conductivity may be formulated in a manner analogous to viscosity. For monatomic species, the thermal conductivity of a pure gas and that of a binary mixture may be expressed, respectively, as

$$\begin{aligned} K &= 1989.1 \frac{\sqrt{T/M}}{\sigma^2 \Omega^{(2,2)\star}(T^*)} \times 418.4 \times 10^{-7} \quad , \\ K &= \frac{15}{4} \frac{\mathscr{R}}{M} \mu \quad , \end{aligned} \tag{2.88}$$

For binary mixtures, the corresponding thermal conductivity is given by

$$K_{12} = 1989.1 \left(\frac{\sqrt{T(M_1 + M_2)/(2M_1 M_2)}}{\sigma_{12}^2 \Omega_{12}^{(2,2)\star}(T_{12}^*)} \right) \times 418.4 \times 10^{-7} \quad , \tag{2.89}$$

where K and K_{12} denote the thermal conductivities of a pure gas and a binary mixture, respectively, expressed in $\mathrm{W/m \cdot K}$.

For polyatomic species, Eucken's correction must be applied to account for energy exchange between translational and internal molecular degrees of freedom. Under this correction, the thermal conductivity is written as

$$K = \frac{15}{4} \frac{\mathscr{R}}{M} \mu \left(\frac{4}{15} \frac{C_v}{\mathscr{R}} + \frac{3}{5} \right) \tag{2.90}$$

where C_v is the specific heat at constant volume (Hirschfelder et al., 1954).

The evaluation of thermal conductivity for mixtures containing polyatomic species requires a semi-empirical approach, as the thermal conductivity of mixtures does not scale proportionally with mixture viscosity, unlike the case for pure monatomic gases. This is addressed by first computing the thermal conductivity using the monatomic

formulation and subsequently applying a correction based on experimental data for each species. The full expression for the monatomic mixture thermal conductivity, denoted as $[K_{\mathrm{mix}}]_{\mathrm{mon}}$, is provided by Hirschfelder et al. (1954). For each species, the ratio between experimentally measured thermal conductivity and the theoretical prediction obtained from Equation 2.88 is evaluated. These ratios are then used to correct the mixture thermal conductivity according to

$$K_{mix} = [K_{mix}]_{mon}[X_1 R_1 + X_2 R_2], \tag{2.91}$$

with

$$R_i = \frac{(K_i)_{exp}}{(K_i)_{mon}}. \tag{2.92}$$

In this expression, K_{mix} denotes the corrected thermal conductivity of the polyatomic mixture, $[K_{\mathrm{mix}}]_{\mathrm{mon}}$ is the uncorrected value obtained under monatomic assumptions, and R_i represents the ratio of experimental to theoretical thermal conductivity for species i (Hirschfelder et al., 1954). The experimental data employed in this study are taken from Hilsenrath and Touloukian (1954), which show good agreement with fully experimental datasets such as those reported by Johnston and Grilly (1946) for O_2.

The computation of viscosity and thermal conductivity using the Lennard–Jones framework requires specification of the force constants σ and ϵ/k. These parameters are typically calibrated using experimental measurements at two distinct temperatures. Numerous studies have reported Lennard–Jones parameters for individual air species and for air as a whole (Hirschfelder et al., 1954; Chapman and Cowling, 1970; Matyushov and Schmid, 1996; Poling et al., 2000; Lemmon and Jacobsen, 2004).

For lower temperature ranges, up to approximately 2000 K, the force constants reported by Poling et al. (2000) and Hirschfelder et al. (1954) show good agreement with the Yos–Gupta transport data, which are generally considered reliable in this regime. In contrast, the constants reported by Childs and Hanley (1966) and Lemmon and Jacobsen (2004) yield slightly higher viscosity values, although these datasets remain mutually consistent.

In the present study, the Lennard–Jones force constants reported by Hirschfelder et al. (1954) are adopted. This dataset provides two sets of parameters, optimised for temperatures below 300 K and for temperatures up to 1000 K, respectively. A summary of Lennard–Jones parameters from the various literature sources considered is provided in Table 2.3.

TABLE 2.3: Force constants for the Lennard-Jones potential.

Species	ϵ/k (K)	σ ($\AA$)	Data Range	Reference
N_2	91.5	3.681	80K–300K	Hirschfelder et al. (1954)
	79.8	3.749	300K–1000K	Hirschfelder et al. (1954)
	98.94	3.656	100K–1000K	Lemmon and Jacobsen (2004)
	90.9	3.680	100K–1000K	Childs and Hanley (1966)
	71.4	3.798	NA	Poling et al. (2000)
	102.0	3.630	NA	Matyushov and Schmid (1996)
	91.46	3.680	NA	Chapman and Cowling (1970)
O_2	113.0	3.433	80K–300K	Hirschfelder et al. (1954)
	88.0	3.541	300K–1000K	Hirschfelder et al. (1954)
	118.5	3.428	100K–1000K	Lemmon and Jacobsen (2004)
	110.7	3.440	100K–1000K	Childs and Hanley (1966)
	106.7	3.467	NA	Poling et al. (2000)
	116.0	3.340	NA	Matyushov and Schmid (1996)
	113.2	3.430	NA	Chapman and Cowling (1970)
NO	119.0	3.470	80K–300K	Hirschfelder et al. (1954)
	91.0	3.599	NA	Hirschfelder et al. (1954)
	116.7	3.492	NA	Poling et al. (2000)
	119.0	3.470	NA	Chapman and Cowling (1970)
Air	103.3	3.600	100K–1000K	Lemmon and Jacobsen (2004)
	97.0	3.620	NA	Chapman and Cowling (1970)

2.4.2.2 Lemmon and Jacobsen

The formulations for viscosity, μ, and thermal conductivity, K, developed by Lemmon and Jacobsen (2004) are based on a combination of theoretically derived dilute-gas models and empirically fitted expressions representing residual contributions arising from intermolecular interactions. The dilute-gas component is derived using Chapman–Enskog theory, with collision integrals represented by polynomial fits calibrated against experimental data. The improved collision-integral model proposed by Olchowy and Sengers (1989) is employed, while the residual contribution follows an approach similar to that of Lemmon et al. (2000). This combined formulation is applicable across both liquid and vapour phases.

The reported model uncertainty is approximately 2% for nitrogen and 5% for oxygen and air, with somewhat larger deviations observed near the critical point. In their comprehensive study, Lemmon and Jacobsen (2004) compared model predictions against more than 150 independent experimental datasets, demonstrating robust agreement within the stated uncertainty bounds.

Within this framework, the viscosity is expressed as

$$\mu = (\mu_0 + \mu_r) \times 10^{-6} \quad , \tag{2.93}$$

where μ is given in $\mathrm{N \cdot s/m^2}$, μ_0 denotes the dilute-gas viscosity, and μ_r represents the residual viscosity contribution. The dilute-gas viscosity is given by

$$\mu_0 = \frac{0.0266958\sqrt{MT}}{\sigma^2 \Omega^\star} \quad , \tag{2.94}$$

$$\Omega^\star = \exp\left(\sum_{i=0}^{4} b_i [ln(T/(\epsilon/k))]^i\right) \quad , \tag{2.95}$$

where M is the molecular mass, T is the translational temperature, σ is the force constant, and $\Omega^\star$ is the reduced collision cross section fitted to experimental data, with coefficients provided in Appendix A.3.3. The residual viscosity contribution is expressed as

$$\mu_r = \sum_{i=1}^{n} N_i \left(\frac{T_c}{T}\right)^{t_i} \left(\frac{\rho}{\rho_c}\right)^{d_i} \exp\left(-\varsigma \left(\frac{\rho}{\rho_c}\right)^{l_i}\right) \quad , \tag{2.96}$$

where N_i, t_i, d_i, and l_i are empirical constants, ς is equal to zero when $l_i = 0$ and unity otherwise, and T_c and ρ_c are the critical temperature and density, respectively. The corresponding constants and reference parameters are listed in Appendix A.3.3.

The thermal conductivity is similarly expressed as

$$K = K_0 + K_r + K_c \quad , \tag{2.97}$$

where K_0 is the dilute-gas thermal conductivity, K_r is the residual contribution, and K_c represents the critical enhancement term. In the present study, the critical enhancement is assumed to be zero. The dilute-gas thermal conductivity is given by

$$K_0 = N_1 \left[\mu_0 \times 10^{-6}\right] + N_2 \left(\frac{T_c}{T}\right)^{t_2} + N_3 \left(\frac{T_c}{T}\right)^{t_3} \quad , \tag{2.98}$$

where T_c is the critical temperature, μ_0 is the dilute-gas viscosity expressed in $\mathrm{N \cdot s/m^2}$, and N_1, N_2, N_3, t_2, and t_3 are species-specific constants provided in Appendix A.3.3. The residual contribution to the thermal conductivity is expressed as

$$\boldsymbol{K}_r = \sum_{i=4}^{n} N_i \left(\frac{T_c}{T}\right)^{t_i} \left(\frac{\rho}{\rho_c}\right)^{d_i} \exp\left(-\varsigma \left(\frac{\rho}{\rho_c}\right)^{l_i}\right) \quad , \tag{2.99}$$

where N_i, t_i, d_i, and l_i retain the same definitions as in the residual viscosity formulation, and T_c and ρ_c again denote the critical temperature and density.

For dilute-gas conditions, in which intermolecular interactions are negligible—typically at low pressures and high temperatures—the residual and critical enhancement (see the work by Lemmon and Jacobsen (2004) for details) contributions become insignificant. In

the flow regimes considered in this study, these contributions were found to be minimal and have therefore been neglected.

2.4.2.3 Sutherland

The Sutherland model represents molecules as rigid spheres with the addition of a weak attractive force acting at distances beyond contact. While this model is relatively crude from a theoretical standpoint, it provides a more realistic representation of the temperature dependence of viscosity compared to the simpler rigid-sphere model (Vincenti and Kruger, 1965). The first-order approximation for the viscosity of a gas using this model is given by

$$\mu = \mu_{exp} \left(\frac{T}{T_{exp}} \right)^{3/2} \frac{T_{exp} + S}{T + S}, \tag{2.100}$$

where μ_{exp} is the experimentally determined viscosity at a reference temperature T_{exp}, and S is the Sutherland constant. This constant quantifies the strength of the intermolecular attractive forces and is related to the mutual potential energy between two molecules in contact (Chapman and Cowling, 1970).

By using experimental viscosity data at a second known temperature, an appropriate value of S can be fitted to reproduce the temperature-dependent behaviour of viscosity over a practical range. The Sutherland constants, along with their respective temperature ranges and references, are presented in Table 2.4. In the present work, the constants provided by Hirschel (2015) are used: $S = 110.4$, $\mu_{exp} = 1.846 \times 10^{-5}$ kg/(m · s), and $T_{exp} = 300, \mathrm{K}$.

Table 2.4: Sutherland constants and their respective temperature ranges.

Species	S	Temperature Range	Reference
Air	113.0	293K–373K	(Chapman and Cowling, 1970)
Air	110.4	—	(Hirschel, 2015)
N_2	104.7	292.8K–1098K	(Chapman and Cowling, 1970)
O_2	125.0	287.8K–1102K	(Chapman and Cowling, 1970)

2.4.2.4 Yos - Gupta

In many approximations to the Chapman–Enskog formulation, momentum transfer between different species is either neglected or represented using constant empirical parameters. In contrast, the model proposed by Yos (1963) introduces approximations

that explicitly account for interspecies momentum transfer effects. The corresponding mixing rule is expressed as

$$\mu \text{ or } K_{tr} = \frac{\sum_s X_s/(A_s + a_{av})}{1 - a_{av}\sum_s /(A_s + a_{av})} \quad , \tag{2.101}$$

where X_s denotes the mole fraction of species s, and a_{av} represents the average value of the non-diagonal matrix elements, defined as

$$a_{av} = \frac{\sum_{i,j} X_i X_j \left(\frac{1}{A_i} - \frac{1}{A_j}\right)^2 a_{ij}}{\sum_{i,j} X_i X_j \left(\frac{1}{A_i} - \frac{1}{A_j}\right)^2} \quad , \tag{2.102}$$

$$A_i = \sum_l X_l B_{il} \quad . \tag{2.103}$$

The parameters a_{ij} and B_{il} appearing in these expressions are evaluated differently depending on whether viscosity or thermal conductivity is being computed. The specific formulations used for each transport property are detailed in the following subsections.

Viscosity

For the evaluation of viscosity, the coefficients a_{ij} and B_{il} are defined as

$$a_{ij} = \frac{N_A}{(M_i + M_j)}\left[2\Delta_{ij}^{(1)} - \Delta_{ij}^{(2)}\right] \quad , \tag{2.104}$$

$$B_{il} = \frac{N_A}{N_i}\Delta_{il}^{(2)} \quad , \tag{2.105}$$

where N_A is Avogadro's number expressed in mole/g-mole and M_i is the molecular mass of species i in g/g-mole. In addition,

$$\Delta_{ij}^{(1)} = 8/3 \times (1.5460 \times 10^{-20})\left[\frac{2M_iM_j}{\pi\mathscr{R}T(M_i + M_j)}\right]^{1/2} \pi\bar{\Omega}_{ij}^{(1,1)} \quad , \tag{2.106}$$

$$\Delta_{ij}^{(2)} = 16/5 \times (1.5460 \times 10^{-20})\left[\frac{2M_iM_j}{\pi\mathscr{R}T(M_i + M_j)}\right]^{1/2} \pi\bar{\Omega}_{ij}^{(2,2)} \quad , \tag{2.107}$$

where $\mathscr{R}$ is the universal gas constant expressed in cal/g-mole $\cdot$ K. The collision integrals $\pi\bar{\Omega}_{ij}^{(1,1)}$ and $\pi\bar{\Omega}_{ij}^{(2,2)}$ required in this formulation are provided in Equation 2.82 and Equation 2.83, respectively.

Thermal conductivity

Assuming Eucken's approximation, the frozen thermal conductivity of the mixture, K_f, may be expressed as

$$K_f = K_{tr} + K_v \quad , \tag{2.108}$$

where K_{tr} denotes the translational contribution and K_v represents the internal (vibrational) contribution to the thermal conductivity. For the translational thermal

conductivity, K_{tr}, the coefficients a_{ij} and B_{il} are defined as

$$a_{ij} = (4.184 \times 10^7) \frac{2M_iM_j}{15k(M_i + M_j)^2} \left[\left(\frac{33}{2} - \frac{18}{5} B^*_{ij} \right) \Delta^{(1)}_{ij} - 4\Delta^{(2)}_{ij} \right] \quad , \tag{2.109}$$

$$B_{il} = \frac{2\ (4.184 \times 10^7)}{15k\ (M_i + M_j)^2} \times \left[8M_iM_l\ \Delta^{(2)}_{il} + (M_i - M_l)\,(9M_i - 15M_l/2 + 18\ B^*_{il}\ M_l/5)\ \Delta^{(1)}_{il} \right] \quad , \tag{2.110}$$

where k is the Boltzmann constant expressed in erg/K. As with the collision integrals, the ratio B^*_{ij} is represented using a curve-fit expression of the form

$$B^*_{ij} = \exp(C)\ T^{[A \ln(T) + B]} \quad , \tag{2.111}$$

with coefficients A, B, and C provided by Gupta et al. (1990) and listed in Appendix A.3.1. The contribution of the internal excitation energy of the molecules to the thermal conductivity is expressed as

$$K_v = 2.3901 \times 10^{-8} k \sum_{i=1}^{N} \left[\frac{(\frac{C_{p,i}}{\mathcal{R}} - \frac{5}{2}) X_i}{\sum_j X_j \Delta^{(1)}_{ij}} \right] \quad , \tag{2.112}$$

where the factor 5/2 separates the translational and rotational contributions from the frozen specific heat.

2.4.2.5 Yos - Gupta - Brokaw

By adopting the approximations proposed by Brokaw (1958), Hirschfelder (1957), and Peng and Pindroh (1962), the computational cost associated with the original Yos–Gupta transport model can be significantly reduced. Under these approximations, the mixing laws for both viscosity and thermal conductivity may be written as

$$\mu = \sum_{i=1}^{N} \left(\frac{\frac{M_i}{N_A} X_i}{\sum_j X_j \Delta^{(2)}_{ij}} \right) \quad , \tag{2.113}$$

where M_i is the molecular mass of species i expressed in g/g-mole, N_A is Avogadro's number in mole/g-mole, X_i denotes the mole fraction of species i, and $\Delta^{(2)}_{ij}$ is defined in Equation 2.106. The translational component of the mixture thermal conductivity is given by

$$K_{tr} = 2.3901 \times 10^{-8} \frac{15}{4}\ k \sum_{i=1}^{N} \left(\frac{X_i}{\sum_j \alpha_{ij} X_j \Delta^{(2)}_{ij}} \right) \quad , \tag{2.114}$$

where k is the Boltzmann constant expressed in erg/K and the parameter α_{ij} is defined as

$$\alpha_{ij} = 1 + \frac{[1 - (M_i/M_j)][0.45 - 2.54(M_i/M_j)]}{[1 + (M_i/M_j)]^2} \quad . \tag{2.115}$$

The internal component of the thermal conductivity, K_v, from the "Yos–Gupta" method is used as expressed in Equation 2.112. The approximations introduced in this model provide a computational savings of approximately a factor of two; however, the model remains valid only for non-ionised or weakly ionised flow conditions.

Thermal Non-Equilibrium

The Yos–Gupta–Brokaw model may be extended to a thermal non-equilibrium framework in which distinct temperatures are used to evaluate the contributions from different molecular energy modes. In flow models where ionisation effects are neglected and only thermo-chemical non-equilibrium is considered, the viscosity may continue to be evaluated using Equation 2.113. The thermal conductivity, originally defined by Equation 2.114, may be decomposed into contributions associated with individual energy modes according to

$$K_{tr} = 2.3901 \times 10^{-8} \frac{15}{4}\, k \quad \sum_{i=1}^{N} \left(\frac{X_i}{\sum_j \alpha_{ij} X_j \Delta_{ij}^{(2)}(T)} \right) \quad , \tag{2.116}$$

$$K_{rot} = 2.3901 \times 10^{-8}\, k \quad \sum_{i=1}^{N} \left(\frac{\left(\frac{(C_{p,i})_{rot}}{\mathcal{R}} \right) X_i}{\sum_j X_j \Delta_{ij}^{(1)}} \right) \quad , \tag{2.117}$$

$$K_v = 2.3901 \times 10^{-8}\, k \quad \sum_{i=1}^{N} \left(\frac{\left(\frac{(C_{p,i})_{vib}}{\mathcal{R}} \right) X_i}{\sum_j X_j \Delta_{ij}^{(1)}} \right) \quad , \tag{2.118}$$

where $(C_{p_i})_{\text{rot}}$ and $(Cp_i)_{\text{vib}}$ denote the rotational and vibrational components, respectively, of the total species-specific heat Cp_s. The collision cross sections appearing in the denominators of these expressions are evaluated using the translational temperature, based on the assumption that the diffusion rates of excited species are governed primarily by translational motion.

Under this formulation, the frozen thermal conductivity of the mixture is then expressed as

$$K_f = K_{tr} + K_{rot} + K_v \quad . \tag{2.119}$$

2.4.2.6 Blottner - Wilke

The method proposed by Blottner et al. (1971) evaluates the viscosity and thermal conductivity of gas mixtures using Wilke's semi-empirical mixing rule, with individual species viscosities provided through empirical curve fits. These curve fits are based on transport-property data originally reported by Yos (1963) and Yun and Mason (1962), and effectively represent simplified fits to the collision-integral-based data used in the Yos–Gupta formulation.

The curve-fit expression for the viscosity of an individual species is given by

$$\mu_s = 0.1\, e^{C_B}\, T^{[A_B \ln(T)+B_B]} \quad , \tag{2.120}$$

where A_B, B_B, and C_B are empirically determined coefficients provided by Blottner et al. (1971), T is the temperature in Kelvin, and the factor 0.1 serves as a unit conversion to SI units of $\mathrm{kg/m \cdot s}$.

The thermal conductivity of an individual species is related to its viscosity through the expression

$$K_s = \frac{\mu_s}{M_s}\left[C_{p,s}\frac{M_s}{\mathscr{R}} + 1.25\right] \quad , \tag{2.121}$$

where M_s is the molecular mass of species s, $C_{p,s}$ is the species-specific heat at constant pressure, and $\mathscr{R}$ is the universal gas constant.

Wilke's mixing rule is then applied to compute the mixture viscosity and thermal conductivity according to

$$\mu_s = \sum_{i=1}^{N} \frac{X_i \mu_i}{\sum_{j=1}^{N} X_j \phi_{ij}} \quad , \tag{2.122}$$

$$K_s = \sum_{i=1}^{N} \frac{X_i k_i}{\sum_{j=1}^{N} X_j \phi_{ij}} \quad , \tag{2.123}$$

where X_s denotes the mole fraction of species s, and the interaction parameter ϕ_{ij} is defined as

$$\phi_{ij} = \left[1 + \sqrt{\frac{\mu_i}{\mu_j}}\left(\frac{M_j}{M_i}\right)^{1/4}\right]^2 \left[\sqrt{8}\sqrt{1+\frac{M_i}{M_j}}\right]^{-1} \quad . \tag{2.124}$$

It is important to note that Wilke's mixing rule has been reported to yield inaccurate results in partially ionised flow regimes. Consequently, the Blottner–Wilke method is generally recommended only for non-ionised or weakly ionised flow conditions (Blottner et al., 1971).

2.4.3 Diffusion

The mass flux due to diffusion can arise from four distinct mechanisms: (1) diffusion driven by concentration gradients, (2) diffusion induced by pressure gradients, (3) diffusion resulting from external forces—such as those acting on electrically charged particles in an ionised gas moving through a magnetic field—and (4) diffusion driven by temperature gradients (Hirschfelder et al., 1954). The general formulation of the diffusive mass flux accounting for these mechanisms is given by (Hirschfelder et al., 1954)

$$\overline{\mathbf{V}}_\mathbf{i} = \frac{n^2}{\rho} \sum M_i M_j D_{ij} \mathbf{d_j} - D_i^T \frac{\partial ln T}{\partial x} \tag{2.125}$$

and

$$\mathbf{d_j} = \frac{\partial X_i}{\partial x} + \left(X_i - \frac{n_j M_j}{\rho} \right) \frac{\partial ln p}{\partial x} - \left(\frac{n_j M_j}{p\rho} \right) \left[\frac{\rho}{M_j} \zeta_j - \sum n_k \zeta_k \right]$$

where X_i is the mole fraction of species i, M_i is the molecular weight, n_i is the number density, and $n = \sum n_i$ is the total number density. The pressure is denoted by p, ζ_i is the external force acting on species i, and D_i^T is the thermal diffusion coefficient.

The driving force of mass diffusion due to pressure gradients is extremely small and is typically neglected. Diffusion driven by temperature gradients is based on the principle that lighter particles, having higher mean molecular velocities at a given temperature, tend to diffuse more rapidly toward regions of lower temperature (Anderson, 2019). However, this effect is also small for most applications and is often omitted. Since this study does not consider ionisation, diffusion due to external forces is likewise neglected. Notably, thermal diffusion was not known prior to the Chapman-Enskog theory and was originally predicted through theoretical derivations. Although thermal diffusion is zero for Maxwellian molecules and theoretically requires a second-order Sonine polynomial expansion, hence referred to as a "second-order" effect (Hirschfelder et al., 1954), its existence was later confirmed experimentally (Vincenti and Kruger, 1965).

By omitting the influence of external forces, pressure gradients, and thermal gradients, Equation 2.125 simplifies to the form

$$\overline{\mathbf{V}}_\mathbf{i} = \frac{n^2 M_i}{\rho} \left(\sum_{j=1} M_j D_{ij} \right) \frac{\partial X_i}{\partial x} \, . \tag{2.126}$$

In laboratory studies of non-reacting gas mixtures, simplified conditions are often applied: the system is free from external forces, maintained at constant pressure and temperature, and diffusion is considered in only one spatial direction. Under these assumptions, the diffusion equation becomes second-order in space and first-order in time. By expressing the continuity equation in terms of the number-averaged velocity and substituting the diffusion velocity, the resulting formulation is the multicomponent generalisation of Fick's

second law of diffusion[2]. For binary mixtures, assuming ordinary diffusion and a closed, stationary system without thermal gradients, the generalised form is expressed as (Sutton and Gnoffo, 1998)

$$\overline{\mathbf{V}}_\mathbf{i} = -\rho \mathscr{D}_{ij} \frac{\partial Y_i}{\partial x} = -\rho \frac{M_i M_j}{M^2} \mathscr{D}_{ij} \frac{\partial X_i}{\partial x} \, . \tag{2.127}$$

where $\mathscr{D}_{ij}$ is the binary diffusion coefficient between species i and j, and M is the mixture molecular weight. This equation is widely recognised as Fick's second law and is commonly used in reacting flow simulations.

Similar to viscosity and thermal conductivity, the full Chapman–Enskog derivation for multicomponent binary mass diffusion is discussed in detail by Hirschfelder et al. (1954). However, applying this rigorous formulation to continuum CFD simulations would require solving a system of equations for every grid point at every iteration, which is computationally intensive and challenging to linearise in implicit schemes (Boyd and Schwartzentruber, 2017). As a result, various simplifications have been introduced, such as self-consistent effective binary diffusion, polynomial curve fits, or the assumption of a constant diffusion coefficient across all species.

The following subsections describe the models implemented in this study. It is also worth noting that the Stefan-Maxwell equation, originally formulated to solve for mole fraction gradients, has been adapted for multicomponent diffusion using iterative numerical schemes[3].

2.4.3.1 Chapman-Enskog

For a multicomponent gas mixture, the generalised diffusion coefficient can be expressed in terms of the binary diffusion coefficients between each species pair [4]. This formulation is also applied in defining species diffusion within multicomponent gases. For a binary mixture, the diffusion coefficient is given by

$$\mathscr{D}_{12} = 0.0026280 \cdot \frac{\sqrt{T^3 \left(\frac{M_1+M_2}{2M_1M_2}\right)}}{p\sigma_{12}^2 \, \Omega_{12}^{(1,1)\star}(T_{12}^*)} \, , \tag{2.128}$$

where $\mathscr{D}_{12}$ is the diffusion coefficient in cm^2/sec, p is the pressure in atmospheres, T is the translational temperature, T_{12}^* is defined as kT/ϵ_{12}, M_1 and M_2 are the molecular weights, and σ_{12} and ϵ_{12}/k are the intermolecular potential parameters.

Using collision cross sections from experimental data suitable for high-temperature conditions, specifically those used by Yos (1963) and later presented in polynomial form

[2] See Equations (8.1-4) to (8.1-6) in Hirschfelder et al. (1954)
[3] For more details, see Bird et al. (2007); Sutton and Gnoffo (1998); Alkandry et al. (2014)
[4] See Equation $(7.4 - 44)$ given by Hirschfelder et al. (1954) or Curtiss and Hirschfelder (1949).

by Gupta et al. (1990), Equation 2.128 has been reformulated by Gupta et al. (1990) into a polynomial expression with coefficient fittings tailored for 11-species air. In this form, the binary diffusion coefficient is then expressed as

$$\mathscr{D}_{ij} = \frac{kT}{p\Delta_{ij}^{(1)}} = \frac{\mathscr{D}_{ij}^{G}}{p} \quad , \tag{2.129}$$

where $\Delta_{ij}^{(1)}$ is given as Equation 2.106, k is the Boltzmann constant and p is the pressure in atmospheres and

$$\mathscr{D}_{ij}^{G} = \frac{kT}{\Delta_{ij}^{(1)}} = \exp(D)\, T^{(A\ln(T)^2 + B\ \ln(T) + C)} \quad , \tag{2.130}$$

where the coefficients A, B, C, D are given in Appendix A.3.2.

For multicomponent gas mixtures, the diffusion coefficient is evaluated using the following relation

$$D_{ij} = \frac{1}{M_j}\left(\sum_k X_k M_k\right) \cdot \frac{K^{ji} - K^{ii}}{|K|} \, , \tag{2.131}$$

where $|K|$ is the determinant of K_{ij} and K^{ij} are the minors, defined as

$$\begin{aligned}
K_{ii} &= 0 \\
K_{ij} &= \frac{X_i}{\mathscr{D}_{ij}} + \frac{M_j}{M_i}\sum_{k\neq i}\frac{X_k}{\mathscr{D}_{ik}}, \quad i \neq j \\
K^{ji} &= (-1)^{i+j}\begin{vmatrix}
0 & \cdots & K_{1,i-1} & K_{1,i+1} & \cdots & K_{1,v} \\
\vdots & & \vdots & \vdots & & \vdots \\
K_{j-1,1} & \cdots & K_{j-1,i-1} & K_{j-1,i+1} & \cdots & K_{j-1,v} \\
K_{j+1,1} & \cdots & K_{j+1,i-1} & K_{j+1,i+1} & \cdots & K_{j+1,v} \\
\vdots & & \vdots & \vdots & & \vdots \\
K_{v,1} & \cdots & K_{v,i-1} & K_{v,i+1} & \cdots & K_{v,v}
\end{vmatrix} .
\end{aligned}$$

However, as shown, this formulation of diffusion results in an asymmetric diffusion matrix, for which $D_{ij} \neq D_{ji}$.

2.4.3.2 Self-Consistent Effective Binary Diffusion (SCEBD)

An alternative to the full Chapman–Enskog formulation is the Self-Consistent Effective Binary Diffusion (SCEBD) model given by Ramshaw and Chang (1996). In this approach, the diffusion velocity is treated as that of a binary mixture, where species i diffuses relative to a composite of all other species. This simplification reduces computational complexity while maintaining accuracy. The effective or average diffusion coefficient

representing the composite species is expressed as

$$D_{im} = (1 - X_i) \,/ \sum_{i \neq j} \frac{X_j}{\mathscr{D}_{ij}} \,. \tag{2.132}$$

Using this definition with Fick's second law of diffusion (Equation 2.127), the diffusion velocity can then be expressed as (Sutton and Gnoffo, 1998)

$$\overline{\mathbf{V}}_\mathbf{i} = -\rho D_{im} \frac{\partial Y_i}{\partial x} = -\rho \frac{M_i}{M} \left(\frac{1 - Y_i}{1 - X_i} \right) D_{im} \frac{\partial X_i}{\partial x} \,. \tag{2.133}$$

This formulation expresses the mass flux in a more computationally efficient yet sufficiently accurate form. For completeness, it should be noted that while the mass-fraction-based form in Equation 2.133 is common in literature, alternative formulations exist that use the mole fraction gradient instead (Gnoffo et al., 1989; Lee, 1985). In those cases, the effective diffusion coefficient incorporates the mass-to-mole conversion and is defined as

$$D_{im} = \frac{\gamma_t^2 M_i (1 - M_i \gamma_i)}{\sum_{i \neq j} \gamma_j / \mathscr{D}_{ij}} \quad , \tag{2.134}$$

where $\gamma_i = \frac{\rho_i}{\rho M_i}$ is the molar concentration of the species, $\gamma_t = \sum \gamma_i$ is the total molar concentration and $\mathscr{D}_{ij}$ is the binary diffusion coefficient given as Equation 2.129.

2.4.3.3 Constant Diffusion Coefficient

Finally, the diffusion coefficient can be approximated as a constant parameter based on characteristic flow properties, such as the Lewis number and the Schmidt number, which are defined as

$$Le_i = \frac{K}{\rho C_p D_i} \quad , \tag{2.135}$$

$$Sc_i = \frac{\mu}{\rho D_i} \quad , \tag{2.136}$$

where K is the mixture thermal conductivity, C_p is the mixture specific heat, and μ is the mixture viscosity. By assuming a constant Lewis or Schmidt number, the diffusion coefficient can be expressed as a single value applicable to all species in the flow. In the present study, when treating diffusion as a constant parameter, a Schmidt number of 0.71 is used.

2.4.3.4 Mass Diffusion Correction

When using Fick's form of the mass flux with models such as the SCEBD model, the sum of the diffusion mass fluxes does not inherently equal zero. To ensure mass conservation in computational models, Sutton and Gnoffo (1998) propose a correction factor. This

correction is now widely adopted in the literature (Giovangigli, 1999; Casseau et al., 2016b; Passiatore et al., 2024, 2023).

The correction is implemented using the closure equation from the Stefan-Maxwell iterative scheme, as outlined in Sutton and Gnoffo (1998), which ensures that the total diffusion mass flux sums to zero by redistributing the residual proportionally to the species mass fractions. The correction term is defined as

$$D_i^{cor} = Y_i \sum_{j=1} \overline{\mathbf{V}}_{\mathbf{j}} \quad , \tag{2.137}$$

where Y_i is the mass fraction of species i. For cases in which a constant diffusion coefficient is used for all species, this correction is not necessary.

2.5 Computational Model

High-fidelity, high-order, scale-resolved simulations—where a complex system of partial differential equations, namely the full Navier–Stokes formulation, is solved directly—have seen substantial advances over the past few decades through the development of diverse numerical approaches and computational methodologies. The successful execution of such simulations requires careful consideration of several key aspects, including the selection of appropriate numerical schemes for spatial and temporal discretisation, the treatment of wall boundary conditions, the application of numerical filtering for stability, and the mitigation of numerical errors or spurious oscillations. Equally critical is the availability of significant computational resources, as well as the ability to efficiently scale simulations to exploit modern high-performance computing architectures.

A wide range of mature computational frameworks is currently available for the simulation of complex compressible flows, each addressing these challenges through different numerical strategies. High-order finite-difference solvers such as OpenSBLI (Lusher et al., 2025), URANOS (De Vanna et al., 2023), and STREAmS (Bernardini et al., 2021) have been developed specifically for compressible flow applications. Finite-volume solvers operating on unstructured meshes, including UCNS3D (Antoniadis et al., 2022) and US3D (Candler et al., 2015), provide increased geometric flexibility and are widely used in industrial and research contexts. Spectral element method frameworks such as Nektar++ (Cantwell et al., 2015) and Nek5000 offer high accuracy for canonical configurations, while NEKO (Jansson et al., 2024) extends this approach to turbulent flows in moderately complex geometries. In addition, unstructured high-order solvers based on flux reconstruction techniques, including PyFR (Witherden et al., 2014) and ZEFR (Romero et al., 2020), have demonstrated strong scalability and accuracy for compressible flow simulations.

Since one of the primary objectives of this work is the implementation of a high-enthalpy thermo-chemical non-equilibrium model within the OpenSBLI framework (see objectives in Section 1.3), a detailed justification of the selection of OpenSBLI itself is beyond the scope of this thesis. Instead, the emphasis in the following sections is placed on reviewing alternative solvers that incorporate thermo-chemical non-equilibrium modelling capabilities and have been openly documented in the literature, providing relevant context for the modelling choices adopted in this work.

The following list summarises a selection of key flow solvers with built-in capabilities for high-enthalpy, thermo-chemically reacting flows:

- US3D (Candler et al., 2015) is considered a state-of-the-art solver for hypersonic and reacting flow simulations. While not open-source, it has been widely adopted in leading publications in the field. US3D is based on the Data-Parallel Line-Relaxation (DPLR) algorithm (Nompelis et al., 2004), which is an implicit method designed for solving the compressible Navier–Stokes equations on hybrid unstructured finite-volume meshes. The solver has evolved through several stages, including a parallel implicit version with finite-rate chemistry (Nompelis et al., 2005), and now features multidisciplinary physics capabilities. These include finite-rate gas-phase kinetics, internal energy relaxation, gas–surface interactions, turbulence transition modelling, shock–boundary layer interactions, and ablation/thermal response models suitable for aerothermodynamic analysis.

- HTR (Hypersonic Task-based Research) (Di Renzo et al., 2020) is an open-source solver targeting hypersonic aerothermodynamics. Developed at Stanford, it leverages the Legion task-based runtime environment (Bauer et al., 2012) to enable scalability for future exascale computing. HTR is written in Regent, a language designed to interface seamlessly with Legion, and its codebase can be automatically translated into OpenMP or CUDA kernels. The solver employs a sixth-order Targeted Essentially Non-Oscillatory (TENO) scheme for shock capturing, along with a third-order Runge–Kutta scheme and operator splitting for time integration. Recent updates have extended its combustion models and included new optimisations (Di Renzo and Pirozzoli, 2021), as well as applications involving external electric fields in turbulent combustion (Di Renzo, 2022).

- hy2Foam (Casseau et al., 2016b; Casseau, 2017) is an OpenFOAM extension incorporating a two-temperature thermo-chemical reacting model, developed for hypersonic applications and as a basis for coupling with DSMC methods. While primarily aimed at hybrid CFD–DSMC simulations, its integration into DNS modules of OpenFOAM such as dnsFoam remains limited. Furthermore, even within dnsFoam, its use is typically restricted to isotropic turbulence boxes and may not scale efficiently to complex geometries or flow configurations.

- LeMANS (Le Michigan Aerothermodynamic Navier–Stokes Solver) (Scalabrin and Boyd, 2005; Scalabrin, 2007) was similarly developed as a CFD module in hybrid DSMC–CFD codes to address regimes where continuum assumptions break down. It has since been extended with capabilities such as the SST turbulence model and a two-gas approach for modelling gas–particle thermodynamics in rarefied environments (Cross and Boyd, 2016).

- SU2-NEMO (Maier et al., 2021) is an extension of the open-source SU2 multiphysics suite that includes high-enthalpy flow modelling. It incorporates its own thermo-chemical library but can also interface with Mutation++ for more detailed chemical kinetics. However, SU2-NEMO is not designed for DNS; it employs RANS-based turbulence modelling.

- LAURA (Langley Aerothermodynamic Upwind Relaxation Algorithm) (Gnoffo et al., 1989; Gnoffo, 1989) is a viscous CFD solver developed by NASA Langley. It uses a block-structured finite-volume scheme and is widely validated for high-enthalpy and chemically reacting flows. References to this solver will be made in the validation chapter due to the robust thermo-chemical models it employs (Gnoffo et al., 1989).

- Mutation++ (Multicomponent Thermodynamic And Transport properties for IONized gases in C++) (Scoggins and Magin, 2014; Scoggins et al., 2020) is not a flow solver itself but provides a comprehensive library for evaluating thermodynamic and transport properties of partially ionised gases in thermal nonequilibrium. The library is open-source, written in C++, and can be coupled with external solvers, including SU2 and OpenFOAM, to handle complex thermo-chemical modelling.

As demonstrated by the examples above, publicly available DNS-capable flow solvers with embedded thermo-chemical nonequilibrium modelling remain relatively rare. Of the solvers discussed, US3D stands out as a mature and feature-rich platform, albeit proprietary. On the other hand, while HTR is open-source and under active development, it lacks some of the numerical flexibility and extensibility offered by OpenSBLI. Thus, OpenSBLI presents a valuable platform for implementing and testing high-order, scale-resolved nonequilibrium thermo-chemical models in a modular and scalable environment.

OpenSBLI is an explicit, high-order finite-difference solver designed for structured curvilinear meshes (Lusher et al., 2025). It is capable of generating CFD solvers using the Oxford Parallel Structured (OPS) domain-specific language. The OPS library, written in C, enables parallel execution of the generated code on a wide range of high-performance computing (HPC) architectures, including both CPUs and GPUs.

Originally introduced by Jacobs et al. (2017) as a proof of concept, OpenSBLI has since been restructured to incorporate shock-capturing capabilities, coordinate transformations

for complex geometries, and a variety of boundary conditions, including heat transfer modelling (Lusher et al., 2021, 2025). The fundamental rationale behind OpenSBLI is to allow users to concentrate on the mathematical formulation of the problem while automating the process of code generation and hardware optimisation.

Traditionally, setting up a numerical study would require both detailed mathematical derivations and considerable effort to manually optimise the solver for the specific hardware being used. This often involved explicit calls to parallelisation libraries such as MPI or OpenMP for CPUs, or CUDA/OpenCL for GPUs. In contrast, OpenSBLI uses source-to-source translation to automatically generate optimised code that can run efficiently across a variety of hardware platforms (Lusher et al., 2025).

A schematic of the code generation framework is presented in Figure 2.3. In the work conducted in this thesis, no modifications were required within the *source code generation* or the *OPS library*. Instead, the primary contribution lies in the formulation stage (i.e., the governing equations), along with the implementation of additional models, such as boundary conditions, to enable simulation of thermo-chemical non-equilibrium flows. Accordingly, only the core components of the code that were directly used or modified will be discussed in this thesis. Further details regarding the overall code generation framework can be found in Lusher et al. (2025, 2021).

2.5.1 Numerical Method

OpenSBLI offers a range of high-order accurate spatial and temporal discretisation schemes. These include WENO/TENO-based shock capturing, central differencing using split skew-symmetric forms for improved numerical stability, and low-storage explicit third- and fourth-order Runge–Kutta schemes for time integration. This section provides a brief overview of the spatial and temporal schemes employed, along with the form in which the q-vectors are defined.

Spacial & Temporal Discretisation

The governing equations are discretised using a finite difference scheme. Both the spatial and temporal discretisation are handled within OpenSBLI. In the simulations presented in this work, a fourth-order central finite difference scheme is employed for spatial derivatives. The discrete forms for the first and second derivatives are given by

$$\frac{\partial f}{\partial x} = \frac{-f_{i+2} + 8f_{i+1} - 8f_{i-1} + f_{i-2}}{12\Delta x} \quad , \tag{2.138}$$

$$\frac{\partial^2 f}{\partial x^2} = \frac{-f_{i+2} + 16f_{i+1} - 30f_i + 16f_{i-1} - f_{i-2}}{12\Delta x^2} \quad . \tag{2.139}$$

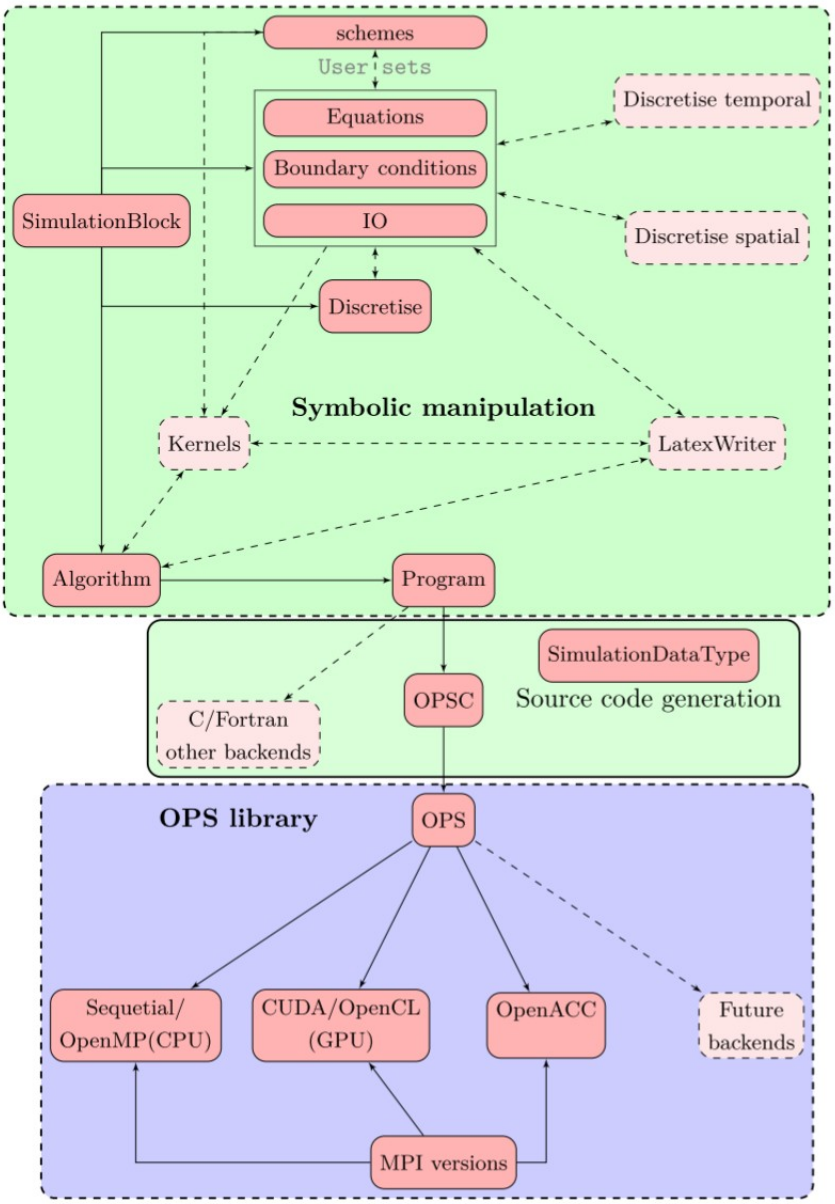

FIGURE 2.3: Schematic of OpenSBLI code generation framework (Lusher et al., 2021).

For time advancement, OpenSBLI provides both a third-order low-storage Runge–Kutta scheme and a classical fourth-order Runge–Kutta (RK4) method. Due to the presence of stiff source terms arising from fast chemical and vibrational processes, the RK4 method was selected to ensure temporal accuracy. All simulations in this study were therefore carried out using the fourth-order Runge–Kutta scheme.

Central finite-difference schemes are non-dissipative and are therefore capable of producing highly accurate solutions in smooth regions of the flow. However, the lack of inherent numerical dissipation can lead to numerical instabilities in the presence of steep gradients or shock-like structures. To ensure numerical stability, additional dissipation mechanisms are commonly introduced, including explicit artificial dissipation terms, selectively applied

filtering, or splitting approaches in central schemes following the methodology of Blaisdell and Feiereisen.

The non-linear convective terms appearing in the continuity, momentum, and total energy equations share the general conservative form $\frac{\partial(\rho\varphi u_j)}{\partial x_j}$ where the transported variable ϕ takes the values 1, u_i, e_v, and E for the continuity, momentum, vibrational energy, and energy equations, respectively. This formulation highlights the common structure of the advective fluxes and motivates the use of splitting forms to improve numerical stability while maintaining conservation properties.

For this thesis, three types of split formulations are considered. The first is the quadratic split form originally proposed by Feiereisen et al. (1981). This formulation is designed to preserve kinetic energy at the semi-discrete level and is known to be nonlinearly stable (Moser, 2022). The Feiereisen split is written as

$$\frac{\partial(\rho\phi u_j)}{\partial x_j} = \frac{1}{2}\frac{\partial(\rho\phi u_j)}{\partial x_j} + \frac{1}{2}\left(\rho u_j\frac{\partial\phi}{\partial x_j} + \phi\frac{\partial(\rho u_j)}{\partial x_j}\right) \quad . \tag{2.140}$$

Building on this work and the concept of secondary conserved quantities—where, in addition to the primary conservation laws, quantities such as kinetic energy or entropy are preserved—further split formulations were developed. One such formulation is the Blaisdell skew-symmetric form (Blaisdell, 1991; Blaisdell et al., 1993, 1996), along with several related variants (Honein and Moin, 2004; Jameson, 2008). This formulation rewrites the convective term as

$$\frac{\partial(\rho\phi u_j)}{\partial x_j} = \frac{1}{2}\left(\frac{\partial(\rho\phi u_j)}{\partial x_j} + u_j\frac{\partial(\rho\phi)}{\partial x_j} + \rho\phi\frac{\partial u_j}{\partial x_j}\right) \quad . \tag{2.141}$$

Both of the above formulations are classified as quadratic split forms and preserve kinetic energy at the semi-discrete level under periodic boundary conditions. For aperiodic boundary conditions, summation-by-parts operators are required to maintain this property (Moser, 2022; Strand, 1994). It should be noted that the term *skew-symmetric* is considered a misnomer by some authors (Moser, 2022), as true skew-symmetry is a strictly mathematical property. Convective splitting operators that rigorously satisfy skew-symmetry have been derived elsewhere (Morinishi, 2010).

Beyond quadratic formulations, cubic split forms have been proposed, including the Kennedy-Gruber-Pirozzoli (KGP) formulation (Kennedy and Gruber, 2008; Pirozzoli, 2010) and subsequent developments by Kuya et al. (2018). These formulations take the general form:

$$\frac{\partial(\rho\phi u_j)}{\partial x_j} = \frac{1}{4}\left(\rho\phi\frac{\partial u_j}{\partial x_j} + \rho u_j\frac{\partial\phi}{\partial x_j} + \phi u_j\frac{\partial\rho}{\partial x_j} + u_j\frac{\partial(\rho\phi)}{\partial x_j}\right) \quad . \tag{2.142}$$

Cubic split forms have been shown to provide additional robustness in flows exhibiting strong density fluctuations, particularly by reducing aliasing errors associated with non-linear interactions.

Overall, these split formulations introduce controlled numerical dissipation and improve stability while retaining the high accuracy of central differencing schemes. Further discussion of the specific split formulation adopted for each simulation configuration is provided in the relevant chapters that follow.

Conservation Computational Modelling

In terms of the numerical formulation of the governing equations defined in Equation 2.1 to Equation 2.4, the Navier–Stokes equations are expressed where the fluxes of mass, momentum, and energy are evaluated directly rather than the primitive flow variables. This formulation is the most commonly adopted approach in computational fluid dynamics (CFD) for supersonic and hypersonic flows (Anderson, 2019), due to its robustness in capturing shock waves and discontinuities. While the non-conservation form retains the same physical principles, it is generally less favoured for high-speed compressible flow simulations.

The vector of conserved variables is modelled as:

$$q = \begin{bmatrix} \rho_s \\ \rho u_i \\ \rho E \\ \rho_m e_{v_m} \\ \rho f \end{bmatrix} \quad . \tag{2.143}$$

Here, f is the passive scalar, which is defined in one of the following subsections.

2.5.2 Boundary Conditions

OpenSBLI provides a range of built-in boundary conditions. For this study, symmetry, periodic, and first-order extrapolation boundary conditions were employed. While documentation already exists elaborating on these standard conditions, a custom zero-pressure gradient wall boundary condition was implemented to account for the thermo-chemical non-equilibrium model. This is defined in Section 6.3.3. The boundary condition is enforced as a non-catalytic wall condition, thought due to not imposing a set species concentration, the wall chemistry can shift. Although wall catalysis is not fully explored in this study, it will be briefly discussed here.

Catalytic Wall Conditions

When accounting for chemical reactions at the wall in a non-ablative model, the wall can either be treated as non-catalytic, where the mass fraction of each species remains constant across the wall, or as reacting. For catalytic walls, three main modelling approaches can be employed (Anderson, 2019):

- **Equilibrium:** In this case, the fluid concentration modelled on the wall is assumed to be in its equilibrium state. While this requires evaluating the equilibrium composition of the mixture at the thermal state of the wall (T and p), for air species at wall temperatures below $3000K$, it can be reasonably assumed that the wall composition consists of N_2 and O_2 only.
- **Partially Catalytic:** In this case, the wall catalysis is defined by a specific model. Different models exist, such as the "gamma model" or the "finite reaction rate" model, which can be referred to in Bellas-Chatzigeorgis et al. (2017).
- **Fully Catalytic:** In this model, the wall is assumed to have no atomic species present and is solely composed of molecular species.

2.5.3 Miscellaneous

This section covers additional, less prominent considerations that were taken into account during the studies conducted as part of this thesis.

Grid Concentration

When setting up a computational domain, depending on the focus of the study and the overall configuration, it may be beneficial to apply a stretching factor in order to locally increase the grid density within specific regions of the domain. This approach allows enhanced resolution in areas of interest while maintaining a manageable total number of grid points. Domain stretching is typically implemented through a mapping function that defines the distribution of grid points.

Consistent with the types of simulations considered in this work, two different forms of grid refinement are required. The first corresponds to configurations where the centre of the domain is of primary interest and therefore requires a higher grid density, such as in temporally evolving mixing layers with freestream conditions at the boundaries. The second applies to cases where increased grid resolution is required near the outer regions of the domain, such as near solid walls in channel flow configurations.

To concentrate the grid towards the centre of the domain in the y-direction, a hyperbolic sine function is employed, given by

$$y_j = \frac{L_y}{2} \frac{\sinh\left(\beta \dfrac{j-(n_y-1)/2}{(n_y-1)/2}\right)}{\sinh(\beta)}, \tag{2.144}$$

where L_y is the domain length in the y-direction, n_y is the number of grid points, j is the grid index, and β is the stretching parameter controlling the degree of clustering towards the domain centre.

To concentrate the grid towards the outer regions of the domain in the y-direction, a hyperbolic tangent function is used, defined as

$$y_j = \frac{L_y}{2} \left[1 - \frac{\tanh\left(\beta \left(1 - 2\dfrac{j}{n_y - 1}\right)\right)}{\tanh(\beta)} \right] - \frac{L_y}{2}, \tag{2.145}$$

where the variables retain the same definitions, and the stretching parameter β controls the clustering of grid points towards the domain boundaries.

Passive Scalar

The passive scalar can be used as a visualisation tool to illustrate the evolution of the flow during the development of turbulence. This is achieved by solving a transport equation, as defined by (Ramaprian et al., 1989)

$$\frac{\partial(\rho f)}{\partial t} = \frac{\partial(\rho f u_j)}{\partial x_j} + \frac{1}{Sc}\frac{\partial}{\partial x_j}\left(\mu \frac{\partial f}{\partial x_j}\right) \quad , \tag{2.146}$$

where f is the passive scalar, and Sc is the Schmidt number, which is taken to be constant at 0.71.

Binomial Filter

Certain flow configurations, such as a temporally evolving mixing layer, require boundary conditions that emulate the free stream without generating acoustic or oscillatory feedback into the flow field. In the absence of characteristic boundary conditions, and in order to mitigate the response of acoustic waves in mixing layer cases, the computational domain is stretched in the far-field direction. Additionally, a filter is applied to suppress any feedback from the boundaries.

To damp oscillations within the flow field, an explicit filter is applied to a defined region of the domain, near the boundaries, at the end of each full time step. A filter strength f_{str} is introduced, and for a solution vector U, the filtered result is given by

$$U = (1 - f_{str})U + f_{str}U_f \quad , \tag{2.147}$$

where the averaged filtered solution U_f is defined as

$$U_f = (U_{fx} + U_{fy} + U_{fz})/3 \quad , \tag{2.148}$$

and U_{fx}, U_{fy}, and U_{fz} represent the explicit filters applied in each spatial direction. These filters are of order n, and the coefficients for the stencil points are taken from the expansion of $(a - b)^n/2^n$.

OpenSBLI Backend Modifications

The OpenSBLI Python front-end does not currently support the direct implementation of iterative procedures. Consequently, for certain transport property models—where matrices of constant coefficients are required—and for the Newton–Raphson iterative method employed to evaluate the vibrational and translational temperatures, manual modifications to the generated code are necessary.

Additionally, due to the form of the vibrational energy expression derived from the rigid-rotor harmonic-oscillator model, situations may arise in which the species-specific vibrational energy approaches zero. This can result in numerical failure during the evaluation of the vibrational temperature, owing to division-by-zero operations. To ensure numerical robustness, a hard safeguard is applied whereby any evaluation of the vibrational energy that results in NaN or infinite values is immediately reset to zero at each iteration. This procedure is purely numerical in nature and has no impact on the underlying physical modelling.

IRIDIS (UoS HPC)

The University of Southampton's High Performance Computing (HPC) system, IRIDIS, was employed for the computational work conducted in this thesis. IRIDIS is currently in its sixth generation (IRIDIS-6), featuring over 26,000 CPU cores. In addition, the IRIDIS facility includes IRIDIS-X, a high-performance GPU cluster comprising 26 × 80GB NVIDIA A100 graphics cards and 5,760 AMD CPU cores for batch computing.

The majority of the simulations were performed on the A100 and V100 GPUs, while some post-processing tasks were carried out on GTX 1080 Ti cards. Table 2.5 presents the technical specifications of the GPUs utilised in this work.

Table 2.5: GPU specification for NVIDIA A100, V100, and GTX 1080Ti.

Specification	**A100**	**V100**	**GTX 1080 Ti**
Architecture	Ampere	Volta	Pascal
CUDA Cores	6,912	5,120	3,584
Boost Clock	∼1,410 MHz	∼1,380 MHz	1,582 MHz
GPU Memory	80 GB HBM2e	16 GB HBM2	11 GB GDDR5X
Memory Interface	5,120-bit	4,096-bit	352-bit
Memory Bandwidth	> 2 TB/s	900 GB/s	484 GB/s
Peak FP32 Performance	19.5 TFLOPS	15.7 TFLOPS	∼11.3 TFLOPS
Peak FP64 Performance	9.7 TFLOPS	7.8 TFLOPS	∼0.35 TFLOPS
Tensor Cores	432 (3rd Gen)	640 (1st Gen)	—
NVLink Support	Yes (up to 600 GB/s)	Yes (SXM2: 300 GB/s)	No
TDP	400 W (SXM), 250-300 W (PCIe)	300 W (SXM2), 250 W (PCIe)	250 W
Use at Southampton	IRIDIS X	IRIDIS 5	IRIDIS

Scaling Thermo-chemical non-equilibrium

A vibrational Damköhler number is employed to quantify the relationship between the characteristic flow timescale and the vibrational relaxation timescale, and is defined as

$$Da_m = \frac{\tau_{flow}}{\tau_m} \quad , \qquad Da_v = \frac{\tau_{flow}}{\tau} \quad . \tag{2.149}$$

Here, τ_m denotes the vibrational relaxation time of molecule m, τ_{flow} is the characteristic flow timescale defined as $\theta_\circ/\Delta U$, and τ is the single vibrational relaxation time defined by Equation 2.67. Small values of the vibrational Damköhler number indicate that vibrational processes evolve on timescales much longer than the flow, and the flow may therefore be considered thermally frozen. Conversely, large values of the vibrational Damköhler number imply that vibrational relaxation occurs rapidly relative to the flow, corresponding to conditions closer to thermal equilibrium.

To facilitate a quantitative comparison between equilibrium and thermo-chemical non-equilibrium cases, the percentage difference of a generic quantity ϕ is defined as

$$\Delta\phi = \frac{(\phi_{TCNE} - \phi_{EQ}) \times 100}{\phi_{EQ}} \quad . \tag{2.150}$$

2.5.4 Grid Study

As required in any computational fluid dynamics (CFD) analysis, the grid-convergence study is performed using the concept of Richardson extrapolation. This approach allows an estimate of the exact solution of the underlying mathematical model to be obtained, provided that the formal order of convergence of the discretisation scheme is known and

that a sequence of systematically refined meshes is available (Richardson and Gaunt, 1927). In this context, knowledge of the formal convergence rate enables the extrapolation of discrete solutions toward the continuum limit, thereby permitting an assessment of the discretisation error. It should be noted that the validity of Richardson extrapolation relies on the assumption that the quantity being analysed—whether obtained directly from the solution or derived through post-processing operations such as integration or differentiation—exhibits the same order of accuracy as the underlying numerical discretisation.

For Richardson Extrapolation to be valid, several assumptions must be satisfied (Oberkampf and Roy, 2010):

- **Asymptotic convergence:** The solutions analysed must lie in the asymptotic range, meaning that the discretisation error decreases at the formal order of accuracy as the mesh is refined. This can be verified by computing the observed order of accuracy.
- **Uniform mesh spacing:** In the original Richardson formulation, discretisation error is defined using a single grid spacing Δx assumed to be uniform. For local quantities, local refinement factors may be used, assuming uniformity in the local region. While this is not directly applicable to global quantities, Celik and Karatekin (1997) showed that non-uniform grids can be included in the method if the grid distribution remains consistent (e.g., via power-law spacing). Thus, Celik et al. (2008) presents generalised cell representations defined here as Equation 2.152 and 2.153.
- **Smooth solution:** The solution must be free of discontinuities.
- **Systematic grid refinement:** Meshes must be refined systematically.
- **Negligible other numerical errors:** Other sources of numerical error must be at least two orders of magnitude smaller than the discretisation error.

The original Richardson extrapolation method was derived for second-order discretisation schemes employing a uniform refinement factor of two. However, the computational cost associated with such refinement levels—particularly for three-dimensional simulations—can be prohibitive for high-order methods. To address this limitation, a generalised formulation of Richardson extrapolation was introduced, allowing for arbitrary refinement ratios. This framework was subsequently extended by Richards (1997) to account for both spatial and temporal discretisation effects. Within this extended formulation, the temporal refinement factor is defined as

$$r_t = (r_x)^{P/q} \quad , \tag{2.151}$$

where r_x denotes the spatial refinement factor, P is the formal order of accuracy of the spatial discretisation, and q is the order of accuracy of the temporal integration scheme.

Procedure

The following steps outline the procedure adopted in this study. For further detail, see Celik et al. (2008) and Oberkampf and Roy (2010).

First, the grid must be represented by a characteristic size h. For local parameters, h is straightforward where it defines the length of a single cell. For global quantities, especially when grid refinement is not just done in one direction, a more global representation of the characteristic size can be expressed which is defined as

$$h = \left[\frac{1}{N}\sum_{i=1}^{N}(\Delta V_i)\right]^{1/3} \quad \text{(3D)} \ , \tag{2.152}$$

$$h = \left[\frac{1}{N}\sum_{i=1}^{N}(\Delta A_i)\right]^{1/2} \quad \text{(2D)} \ , \tag{2.153}$$

where N is the number of cells, ΔV_i is the cell volume, and ΔA_i is the cell area. Next, the grid refinement factor r is computed as

$$r = \frac{h_f}{h_c} = \frac{h_{i+1}}{h_i} \quad , \tag{2.154}$$

where h_c and h_f refer to the coarse and fine grid sizes, respectively. In most cases carried out in this thesis, the refinement factor will be constant.

Third, the observed order of accuracy P is calculated. For uniform refinement:

$$P = \frac{\ln\left(\frac{|\phi_i - \phi_{i+1}|}{|\phi_{i+1} - \phi_{i+2}|}\right)}{\ln(r)} \quad , \tag{2.155}$$

where ϕ is the parameter being evaluated and higher indices denote finer grids. For non-uniform refinement, the observed order of accuracy is defined as

$$P = \frac{1}{\ln(r_{(i+1),(i+2)})}\left[\ln\left(\frac{|\phi_i - \phi_{i+1}|}{|\phi_{i+1} - \phi_{i+2}|}\right) + \ln\left(\frac{r^P_{(i+1),(i+2)} - s}{r^P_{12} - s}\right)\right] \quad , \tag{2.156}$$

$$s = 1.sgn\left(\frac{\phi_i - \phi_{i+1}}{\phi_{i+1} - \phi_{i+2}}\right) \quad . \tag{2.157}$$

This nonlinear equation must be solved iteratively. If the sequential difference $|\phi_i - \phi_{i+1}|$ is close to zero, this approach is not valid.

The extrapolated value is then computed as

$$\phi_{ext} = \frac{(r^P_{(i+1),(i+2)}\phi_{i+2} - \phi_{i+1})}{(r^P_{(i+1),(i+2)} - 1)} \quad . \tag{2.158}$$

The relative errors are evaluated using

$$\epsilon_{abs} = \left| \frac{\phi_i}{\phi_{max}} \right| \tag{2.159}$$

$$\epsilon_a = \left| \frac{\phi_{i+1} - \phi_i}{\phi_{i+1}} \right| \tag{2.160}$$

$$\epsilon_{ext} = \left| \frac{\phi_{ext} - \phi_{i+2}}{\phi_{ext}} \right| \quad . \tag{2.161}$$

Finally, the Grid Convergence Index (GCI) is computed as an uncertainty metric

$$GCI = \frac{F\,|e_a|}{r^p - 1} \quad , \tag{2.162}$$

where F is a safety factor: $F = 1.25$ if the observed order P matches the formal order, otherwise $F = 3.0$ (Oberkampf and Roy, 2010; Pelletier and Roache, 2002).

This method provides a robust and widely accepted procedure for verifying mesh independence and estimating numerical uncertainty. It is also adopted as a standard by many computational journals (Celik et al., 2008).

Courant–Friedrichs–Lewy Stability Condition

Additionally, the Courant–Friedrichs–Lewy (CFL) stability condition is evaluated to ensure that the numerical domain of dependence encompasses the physical domain of dependence. The CFL number is defined as

$$\mathrm{CFL} = (u + a)\frac{\Delta t}{|\Delta h|_{min}} \quad , \tag{2.163}$$

where u denotes the local flow velocity, a is the speed of sound, Δt is the time step, and $|\Delta h|_{\min}$ represents the minimum grid spacing in the direction of u (Laney, 1998). The inclusion of the acoustic contribution through a accounts for wave propagation effects, which play a critical role in numerical stability.

Chapter 3

Model Evaluation and Selection

Before employing the thermo-chemical models presented in the previous chapter, it is essential to first validate the formulations and critically assess the various modelling components involved. These components may arise from physical phenomena or from assumptions and approximations introduced during model development.

The aim of this chapter is to evaluate elements of the thermo-chemical modelling framework and to assess the assumptions and modelling choices adopted in their development, with the objective of establishing a final, robust thermo-chemical model. To this end, the chapter presents a systematic verification of the models employed in the formulation of thermo-chemical non-equilibrium high-enthalpy flows through comparison with their original derivations or other authoritative references. In addition, individual components of the formulation are examined to quantify their influence on high-enthalpy behaviour. Where alternative modelling approaches exist for a given physical process, comparative analyses are performed to elucidate differences in predictive performance and the implications of the underlying assumptions.

3.1 Chemical Non-Equilibrium Model

The various approaches and models used to evaluate the chemical state of the flow have been introduced previously in Section 2.2. In the present study, emphasis is placed on the multi-temperature finite-rate chemical model, specifically the formulation originally proposed by Park (1985) and subsequently refined in later studies (Park, 1987, 1989, 1993; Park et al., 1994, 2001; Park, 1988). Two principal aspects of the multi-temperature model have undergone refinement. The first concerns the evaluation of the equilibrium air composition through modifications to the definition of the equilibrium constant. The second relates to the specification of chemical reaction rate coefficients, for which different parameters have been proposed across the literature.

The chemical model is governed by three key components that collectively determine its predictive behaviour. The first is the equilibrium constant, which defines the equilibrium composition of air at a given temperature and pressure. The second is the forward reaction rate coefficient, derived from experimental measurements and specified for individual reactions. The third is the backward reaction rate coefficient, which is computed as a function of the equilibrium constant and the corresponding forward rate. The remainder of this section examines each of these components in detail to assess their role within the overall chemical non-equilibrium framework.

3.1.1 Equilibrium Composition

As an initial step, a comparative study is conducted to evaluate the equilibrium composition of air over a range of temperatures using the principal formulations proposed by Park. To determine the final equilibrium mole fractions of each species at a prescribed temperature and pressure, a time-advancement procedure is required, starting from an initial chemical state and iterating until convergence is achieved.

A simple explicit forward Euler time-marching scheme was implemented, augmented with an additional relaxation term to facilitate convergence towards the reference chemical equilibrium state. The formulation is given by

$$\rho_s^{n+1} = \rho_s^n + \Delta t \left[\dot{\omega}_s + Y_s \frac{\phi_{ref} - \phi}{\tau} \right] \quad , \tag{3.1}$$

where ϕ denotes the total molar concentration, defined as $p\mathscr{R}/T$. Setting the relaxation time scale τ equal to the time step Δt was found to provide stable convergence to the equilibrium state. Convergence was monitored using the average iteration error across all species densities, defined as $\sum |\rho_s - \rho_s^{n-1}|$. For the present evaluation, a time step of $\Delta t = 10^{-8}$ was employed and an error tolerance of 10^{-9} was imposed. The models proposed by Park (1985, 1986); Gnoffo et al. (1989); Park (1987, 1989, 1990, 1993); Park et al. (2001) were implemented following the formulations described in Section 2.2 and iterated to convergence for air at atmospheric pressure over a temperature range of 1500 K to 9000 K.

Figure 3.1 presents the equilibrium air composition predicted by the different models. All simulations capture the progressive dissociation of molecular nitrogen and oxygen beginning at approximately 3000 K, with atomic species becoming dominant as the temperature approaches 9000 K. Notable discrepancies are observed in the earliest formulation, denoted here as “P1985” (Park, 1985), which deviates significantly from the later models. In contrast, good agreement is observed between the “P1986” (Park, 1986) and “P1989” formulations, while modest differences emerge when comparing the

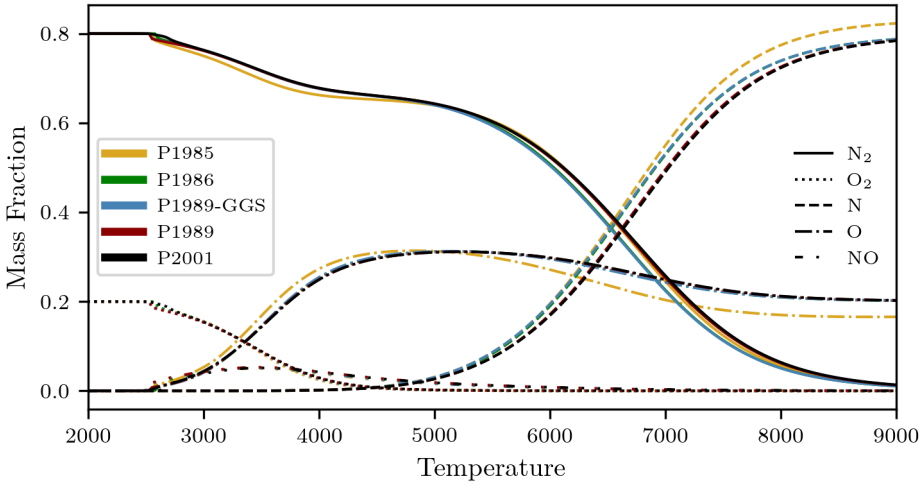

FIGURE 3.1: Comparison of equilibrium air composition obtained using different formulations of Park's model.

"P1989-GGS" model (Gnoffo et al., 1989) with the more recent "P2001" (Park et al., 2001) formulation. As these results represent converged, time-independent equilibrium states, the observed differences can be attributed solely to variations in the definition and evaluation of the equilibrium constants.

Although discrepancies are present among all formulations, the subsequent analysis focuses exclusively on the "P1989-GGS" and "P2001" models. This choice is motivated by the fact that the work presented by Park et al. (2001) provides the most recent parameter updates, while the formulation of Gnoffo et al. (1989) remains widely adopted within the literature.

The equilibrium composition is inherently dependent on both the set of chemical reactions considered and the corresponding equilibrium constants. The pronounced deviation of the Park (1985) model is expected, as it relies on older stoichiometric datasets. Of greater relevance, however, are the differences between the "P2001" formulation and the "P1989-GGS" model. In temperature ranges where substantial changes in species populations occur, particularly between 5000 K and 8000 K, the two formulations exhibit noticeable divergence in predicted equilibrium composition.

3.1.2 Equilibrium Constant

The equilibrium constant governs the equilibrium composition of air within chemical non-equilibrium models and is inherently dependent on both temperature and pressure. To assess the evaluation of the equilibrium composition, equilibrium constants derived from Park's formulations are compared with those obtained using the NASA-9 polynomial representation, as described in Section 2.2.1.

The computation of equilibrium constants using the NASA-9 formulation requires three distinct polynomial coefficient sets corresponding to the temperature ranges below 2000 K, between 2000–6000 K, and above 6000 K. For consistency in the present comparison, the equilibrium constants obtained from all approaches were converted to *cgs* units of cm^3/mol.

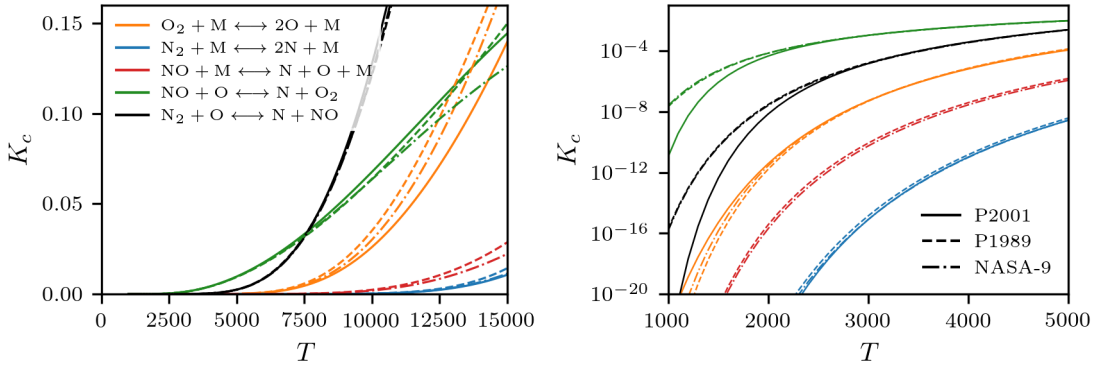

(a) Equilibrum constant evaluated up to 15,000 K.

(b) Equilibrium constant evaluated for lower temperatures in log scale.

FIGURE 3.2: Comparison of the equilibrium constant between different models (line styles) for different reactions (line colours).

Figure 3.2 presents the equilibrium constants evaluated up to 15,000 K. The full temperature range is shown in Figure 3.2a, while Figure 3.2b focuses on the lower-temperature regime using a logarithmic scale. Different colours correspond to individual chemical reactions, whereas line styles distinguish between the equilibrium constant formulations under consideration. At elevated temperatures, noticeable discrepancies between the models emerge from approximately 7500 K. Similar deviations are observed at lower temperatures, particularly below 2000 K, where the "P2001" formulation exhibits significant divergence.

For the equilibrium constants reported by Park et al. (2001), the lowest temperature at which values are evaluated is 3000 K, whereas the "P1989-GGS" formulation extends down to 2000 K. As a result, the representation of equilibrium constants at lower temperatures is less reliable in the "P2001" formulation. In contrast, the NASA-9 polynomial approach, provides a more accurate and continuous representation across the full temperature range. However, this increased fidelity comes at the expense of greater complexity, as three separate polynomial coefficient sets must be stored and evaluated to cover temperatures from 300 K to 9000 K. Park's formulation, while less accurate at low temperatures, offers a more compact representation with fewer coefficients and a simpler functional form.

It is also noted that the "P2001" model does not provide equilibrium constant data for the reaction $NO + M \leftrightarrow N + O + M$. Furthermore, inaccuracies in the low-temperature regime may introduce numerical errors when simulations involve wide temperature variations.

Based on these observations, it can be concluded that the equilibrium constant expressions proposed by Park et al. (2001) are insufficiently accurate below 2000 K and above 7500 K, while the NASA-9 polynomial approach, although accurate, introduces additional computational and storage overhead. This motivates the development of an alternative equilibrium constant formulation with tailored coefficients, capable of providing an accurate representation across the low-temperature regime while retaining a compact and efficient functional form.

Equilibrium Constant [Revised Model]

The NASA-9 database was employed to construct a revised representation of the equilibrium constant for each of the five chemical reactions considered. The functional form given by Equation 3.2, together with optimised coefficients, was selected to describe the equilibrium constant as a continuous function of temperature. This formulation was deliberately chosen to be consistent with the polynomial expressions adopted in the Park models discussed previously.

$$\ln(K_c) = a_i T^{-1.5} + b_i T^{-1} + c_i + d_i \ \ln(T) + e_i T + f_i T^2 \tag{3.2}$$

The logarithm of the equilibrium constant for each reaction was evaluated using the NASA-9 database over a temperature range from 200 K to 8000 K with increments of 10 K. Equation 3.2 was then adopted as the objective function, and an optimisation procedure was applied to determine the corresponding set of coefficients. The resulting coefficients for the revised model are listed in Table 3.1, where the subscript i denotes the individual reaction.

Table 3.1: Coefficients for the revised equilibrium constant formulation defined by Equation 3.2.

Reaction (i)	a	b	c	d	e	f
$O_2 + M \leftrightarrow 2O + M$	2.09180e+03	-1.13450e+05	3.76460e+00	1.56100e+00	-3.30080e-04	1.83680e-08
$N_2 + M \leftrightarrow 2N + M$	5.02970e+03	-7.59480e+04	5.16380e+00	1.18180e+00	-2.21420e-04	1.17870e-08
$NO + M \leftrightarrow N + O + M$	6.27520e+03	-6.01790e+04	7.48960e+00	1.09320e+00	-2.14740e-04	7.29820e-09
$NO + O \leftrightarrow N + O_2$	-2.93790e+03	-3.74970e+04	-1.39920e+00	3.79240e-01	-1.08650e-04	6.58020e-09
$N_2 + O \leftrightarrow N + NO$	-1.24550e+03	-1.57690e+04	-2.32590e+00	8.85260e-02	-6.68590e-06	4.48930e-09

To demonstrate the accuracy of the revised formulation, Figure 3.3a compares the equilibrium constants obtained from the NASA-9 database with those computed using Equation 3.2. Different colours correspond to individual reactions, while the markers represent values predicted by the revised model. Excellent agreement is observed across the entire temperature range, with the markers closely overlaying the reference curves. For a quantitative assessment, the relative percentage error between the two approaches is shown in Figure 3.3b.

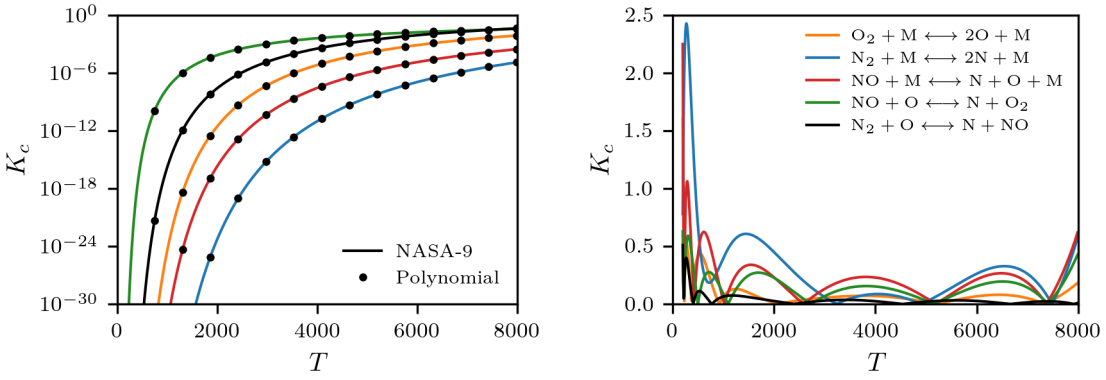

(a) Comparison between NASA-9 data and the revised polynomial formulation.

(b) Percentage error between NASA-9 data and the revised polynomial formulation.

FIGURE 3.3: Evaluation of the revised equilibrium constant formulation against the NASA-9 database. Different colours denote individual reactions, as indicated in the legend of (b).

As shown in Figure 3.3, the revised expression not only extends the valid temperature range beyond that of the Park polynomial formulations but also achieves improved accuracy, with a maximum deviation of approximately 2.5% relative to the NASA-9 database. Furthermore, unlike the NASA-9 approach, the revised model does not require piecewise definitions over multiple temperature intervals, thereby reducing both memory requirements and computational cost.

3.1.3 Forward and Backward Reaction Rate

As with the equilibrium constant, the reaction rate coefficients proposed in Park's formulations vary across publications due to successive updates to the fitted parameters. These coefficients play a critical role in governing the temporal evolution of species concentrations in chemically non-equilibrium flows. Figure 3.4 compares the forward and backward reaction rates predicted by the "P2001" and "P1989-GGS" models over a range of temperatures.

At elevated temperatures, the forward reaction rate for $O_2 + M \leftrightarrow 2O + M$ differs by several orders of magnitude between the two formulations. A similar level of discrepancy is observed at lower temperatures for the reaction $N_2 + O \leftrightarrow N + NO$. Of particular importance is the omission of the reaction $NO + M \leftrightarrow N + O + M$ in the "P2001" formulation. While this omission has a limited influence on the equilibrium composition, it can substantially affect the transient behaviour of chemically non-equilibrium states.

The backward reaction rate coefficients are computed from the corresponding forward rates and equilibrium constants. As shown in Figure 3.4b, the resulting backward reaction rates differ significantly between the two selected Park formulations. As noted in earlier sections, the temperature used in the evaluation of the forward reaction rates,

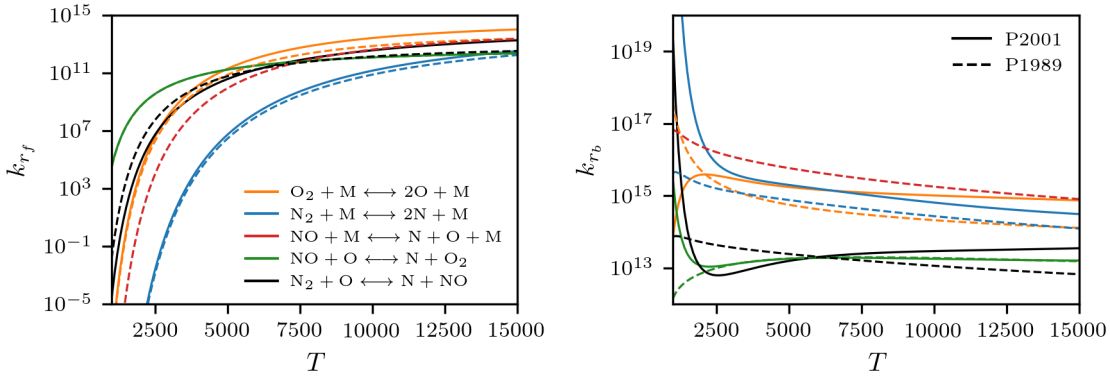

(a) Comparison of forward reaction rate coefficients.

(b) Comparison of backward reaction rate coefficients.

FIGURE 3.4: Evaluation of forward and backward reaction rates as functions of temperature.

and consequently in the backward rate expressions, corresponds to the translational temperature rather than the vibrational temperature in Park's two-temperature model.

It is worth noting that some chemical kinetics libraries, such as *Mutation++*, combine the most recent reaction rate coefficients reported by Park et al. (2001) with additional reactions sourced from earlier work Park (1993). In the present comparison, however, each model is implemented strictly according to its original publication in order to preserve consistency and allow for a clear assessment of the underlying modelling differences.

3.2 Thermal Non-Equilibrium Model

Within a multi-temperature framework, different energy modes are represented by their respective temperatures. In addition to the definition and evaluation of these modal temperatures, the exchange of energy between modes must also be modelled to accurately describe thermal non-equilibrium effects. This section examines these two aspects of the governing equations, along with the associated thermodynamic modelling required to represent non-equilibrium states.

3.2.1 Specific Heat Capacity at Constant Pressure

The specific heat capacity at constant pressure, C_p, plays a central role in the evaluation of thermal conductivity and, more fundamentally, in the definition of thermal modes within a flow. In high-enthalpy thermodynamic modelling, two principal approaches are commonly adopted. The first relies on thermo-chemical databases in which C_p is expressed as a polynomial function of temperature using empirically fitted coefficients. The second approach derives C_p from statistical thermodynamics by modelling molecular behaviour using the Rigid-Rotor and Harmonic-Oscillator (RRHO) approximations. The

validity, limitations, and suitability of these two methodologies are examined in this section. The corresponding formulations and databases are detailed in Section 2.1.4.

An air mixture in thermo-chemical equilibrium at atmospheric pressure was considered over a temperature range up to 9000 K. The equilibrium mole fractions of the constituent species are shown in Figure 3.5a, while Figure 3.5b presents the temperature dependence of the species-specific heat capacities computed using the different modelling approaches.

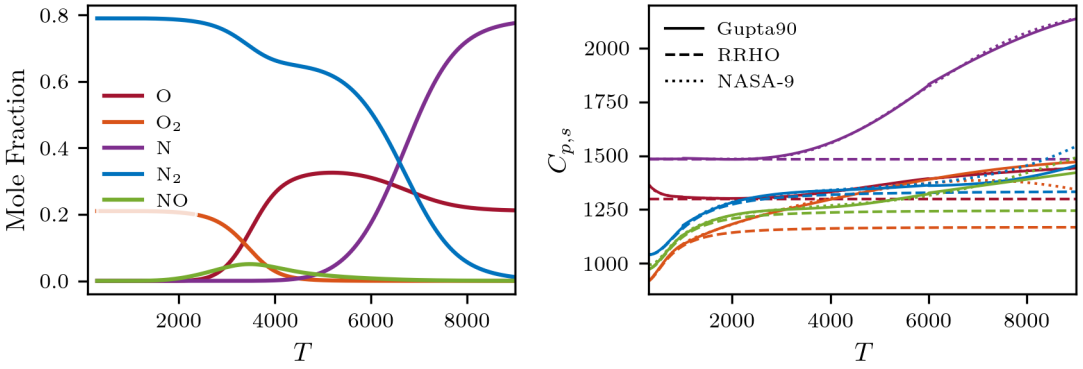

(a) Equilibrium species mole fractions as functions of temperature.

(b) Species-specific heat capacities as functions of temperature.

FIGURE 3.5: Thermodynamic properties of equilibrium air at varying temperatures.

The NASA database and Gupta polynomial formulations exhibit near-identical behaviour up to approximately 6000 K, with only minor deviations observed above 7000 K. In contrast, more pronounced differences arise when comparing these methods with the RRHO model. For atomic species, the RRHO formulation predicts a constant specific heat capacity, as only translational and rotational energy modes contribute, both of which depend solely on the gas constant and are independent of temperature. Molecular species, however, exhibit an increasing specific heat capacity with temperature due to the contribution of vibrational modes. Across all species, the RRHO approach tends to underpredict C_p, particularly at temperatures exceeding 4000 K. This discrepancy is attributed to the absence of electronic excitation contributions, as illustrated in Figure 2.2.

The mixture specific heat capacity is shown in Figure 3.6. When the contribution of chemical reactions is accounted for, as defined in Equation 2.28, the differences between the three modelling approaches are minimal over most of the temperature range considered. The divergence observed above 8000 K is associated with ionisation effects, which are not captured by the RRHO model and are not considered within the scope of this thesis. It is also noted that the Gupta model presented here corresponds to a direct polynomial representation of the air mixture, rather than being constructed from species-level contributions.

Figure 3.6 further demonstrates the suitability of the simplified RRHO model for evaluating vibrational energy contributions when compared with more detailed approaches. Alternative methods for modelling vibrational energy using specific heat formulations,

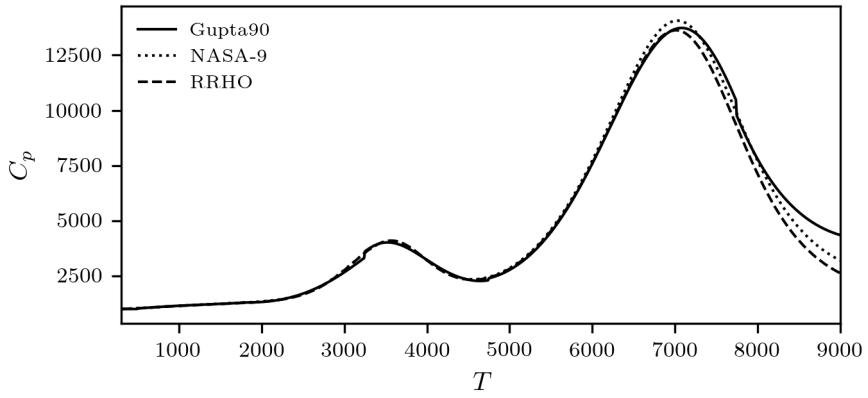

FIGURE 3.6: Mixture specific heat capacity of equilibrium air computed using three different models.

such as those proposed by Gnoffo et al. (1989), are available; however, the present results indicate that the RRHO approximation provides sufficient accuracy for temperatures up to approximately 8000 K. Beyond this range, the model becomes unsuitable for ionised flow conditions.

3.2.2 Park Relaxation Correction Term

The exchange of energy between the ro-translational and vibrational modes is commonly modelled using the formulation introduced by Landau and Teller (1936), which assumes a Boltzmann distribution of vibrational energy levels and incorporates a characteristic relaxation time. As discussed in earlier sections, a range of vibrational relaxation time models has been proposed in the literature, with notable discrepancies across different temperature regimes. Consequently, an assessment of the available formulations and associated correction factors is presented here.

Park (1984) demonstrated that the relaxation time expression proposed by Millikan and White (1963) significantly underpredicts vibrational relaxation rates at elevated temperatures, particularly for oxygen molecules. This behaviour was attributed to limitations in the original formulation, which assumes a temperature-independent excitation cross section. To address this deficiency, a correction factor based on an effective excitation cross section was introduced.

The correction factor defined in Equation 2.68 is applied here to examine its influence across different temperature regimes. Figure 3.7 compares three vibrational relaxation time models: the original Millikan–White (MW) formulation, the corrected model proposed by Park (1984), and the updated formulation presented by Park (1993), which incorporates revised coefficients together with the Park correction. As shown in Figure 3.7, the inclusion of the correction factor leads to pronounced deviations at higher temperatures. In the temperature range of approximately 8000 K to 10,000 K

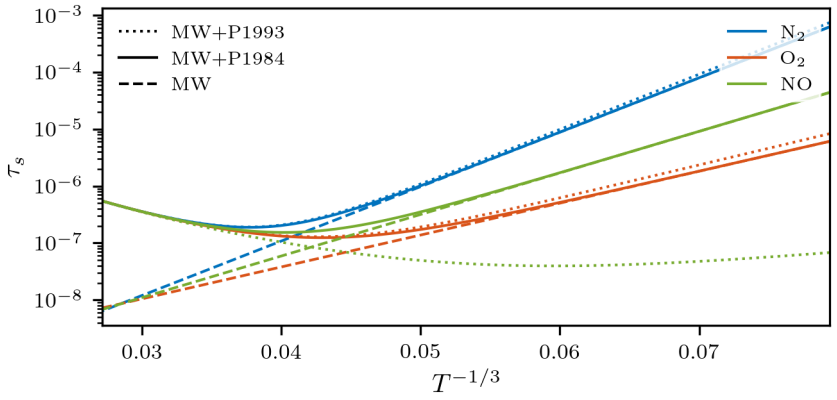

FIGURE 3.7: Effect of the Park correction on vibrational relaxation times derived from the Millikan–White formulation.

(corresponding to roughly 0.05–0.045), the oxygen relaxation time exhibits the largest divergence relative to the original Millikan–White model.

The correction proposed by Park (1984) is applied as an additive term to the Millikan–White formulation. As a result, the corrected model reproduces the Millikan–White behaviour at lower temperatures while diverging progressively at higher temperatures, where the original formulation becomes increasingly inaccurate.

In contrast, Park (1993) introduced updated coefficients within the Millikan–White framework to better match the experimental data available at the time. Notably, substantial modifications were made to the NO vibrational relaxation time, informed by shock-tube measurements reported in Wray (1962) and additional assumptions regarding NO collision processes. Smaller adjustments were also applied to the N_2 and O_2 relaxation times at lower temperatures, which explains the greater deviation of the dotted curves relative to the solid and dashed curves in Figure 3.7.

3.2.3 Single Vibrational Relaxation Time

Within the formulation of the vibrational energy exchange equation, a distinct relaxation timescale is defined for each molecular species. These molecular relaxation times are obtained by performing a weighted average over the collision-specific relaxation times associated with each species pair.

In addition, several studies propose a further averaging step in which a single effective relaxation time is computed for the entire mixture. This approximation is generally adopted to reduce computational cost while maintaining acceptable accuracy. Both weighted harmonic and weighted arithmetic averaging approaches have been reported in the literature (Lee, 1984; Gnoffo et al., 1989; Park, 1984), as defined by Equation 2.66 and Equation 2.67, respectively. Although limited attention has traditionally been paid

to the choice of averaging method, notable differences in the resulting relaxation times can arise, as illustrated in Figure 3.8.

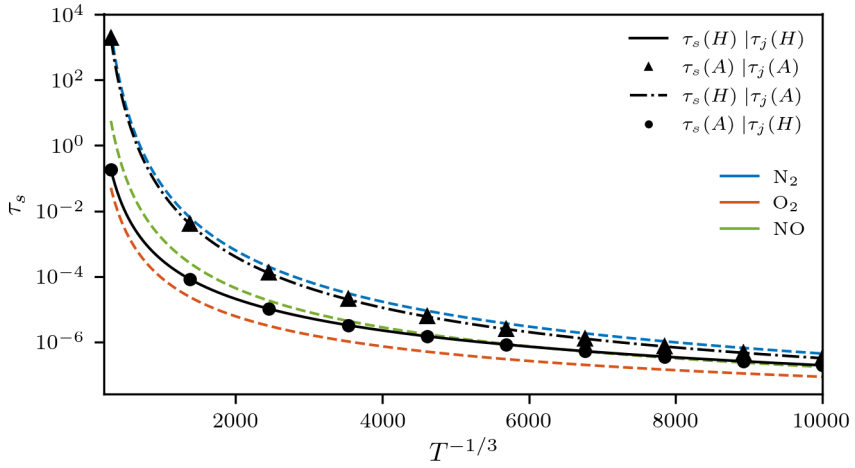

FIGURE 3.8: Comparison of vibrational relaxation time averaging methods.

Figure 3.8 demonstrates the extent to which the averaging strategy influences the relaxation time evaluated for individual molecular species and for the mixture as a whole. When averaging is performed only at the level of interspecies collisions, the choice between harmonic and arithmetic weighting has a negligible impact on the resulting molecular relaxation times. This is evident from the close agreement between the black markers and their corresponding solid black curves, particularly at lower temperatures.

In contrast, when a single effective relaxation time is adopted for the entire mixture, as proposed by Gnoffo et al. (1989), the predicted vibrational relaxation behaviour becomes strongly dependent on the averaging method. This sensitivity is reflected in the marked discrepancy between the solid and dashed black curves, indicating that the choice of averaging formulation can significantly influence the overall vibrational energy exchange when a mixture-level relaxation time is employed.

3.3 Thermo-Chemical Non-Equilibrium Model

Thus far, the multi-temperature formulation of gas dynamics has been examined by assessing the various components of the chemical and thermal models. In particular, the influence of key chemical parameters, such as the equilibrium constant and reaction rate coefficients, has been analysed, along with their variability across different modelling approaches. In addition, the thermal model has been evaluated with emphasis on the definition of thermodynamic properties and the modelling of energy exchange between modes. Given the wide range of available modelling options and possible combinations, it is necessary to define a single, consistent thermo-chemical non-equilibrium model for use throughout this thesis.

The final model adopted for the present thesis evaluates the thermodynamic state using the rigid-rotor harmonic-oscillator approximation. The chemical kinetics are based on reaction rate coefficients reported in one of Park's most recent formulations (Park et al., 2001), supplemented by parameters for the missing reaction $\mathrm{NO} + M \leftrightarrow \mathrm{N} + \mathrm{O} + M$ from Park (1993). This selection reflects the most up-to-date parameter set available for Park's two-temperature chemical model. The equilibrium constant is prescribed using the revised formulation introduced in Section 3.1.2. A single vibrational temperature, required for the chemical source terms, is obtained using the Newton–Raphson iterative method described in Section 2.1.3.

For the thermal model, vibrational relaxation rates are evaluated using the Millikan–White formulation (Millikan and White, 1963), with coefficients taken from Park (1993) to ensure consistency with the most recent experimental data compiled by Park. The Park correction factor for vibrational relaxation is omitted, since its influence was shown to be negligible for temperatures below 8000 K. In addition, the effects of molecular depletion and production are assumed to be non-preferential.

The remainder of this section evaluates the selected thermo-chemical non-equilibrium model through a series of controlled comparisons designed to isolate and assess the influence of individual modelling assumptions on the resulting flow behaviour.

3.3.1 Model Validation

To evaluate the thermo-chemical model defined above, a simplified numerical configuration was employed in which advection is neglected, resulting in a zero-dimensional heat-bath problem governed solely by the thermo-chemical formulation. The system is assumed to be adiabatic, with total energy conserved throughout the simulation. Under these assumptions, the vibrational energy transport equation reduces to Equation 2.64, which is reiterated below

$$\frac{\partial}{\partial t}\left(\rho_s e_{v,s}\right) = \frac{\rho_s (e^*_{v,s} - e_{v,s})}{\tau_s} + \dot{\omega}_s \hat{D}_s \quad . \tag{2.64}$$

Time integration was performed using a classical fourth-order explicit Runge–Kutta (RK4) scheme, in which the solution is advanced through four intermediate stages and updated as a weighted combination of the corresponding residual evaluations,

$$
\begin{aligned}
\mathbf{k}_1 &= \mathbf{R}(\mathbf{Q}^n)\,, \\
\mathbf{k}_2 &= \mathbf{R}(\mathbf{Q}^n + \Delta t/2 \quad \mathbf{k}_1)\,, \\
\mathbf{k}_3 &= \mathbf{R}(\mathbf{Q}^n + \Delta t/2 \quad \mathbf{k}_2)\,, \\
\mathbf{k}_4 &= \mathbf{R}(\mathbf{Q}^n + \Delta t \quad \mathbf{k}_3)\,, \\
\mathbf{Q}^{n+1} &= \mathbf{Q}^n + \frac{\Delta t}{6}\left(\mathbf{k}_1 + 2\mathbf{k}_2 + 2\mathbf{k}_3 + \mathbf{k}_4\right).
\end{aligned}
\tag{3.3}
$$

The thermo-chemical formulation may be implemented using either a single-e_v approach, in which vibrational energy is conserved through a single transport equation, or a multi-e_v formulation, in which separate vibrational energy equations are solved for each molecular species. As the single-e_v formulation is predominantly adopted in the literature, it is employed here to facilitate a focused assessment of differences arising from thermo-chemical model parameters, particularly those associated with reference data and fitted coefficients.

Reference solutions for comparison are taken from the study of Williamson and Wirtz (2021), in which the thermo-chemical modelling of the HTR flow solver is assessed. Additional reference data include results from the LeMANS solver (Scalabrin, 2007; Gimelshein et al., 2022) and the SU2-NEMO solver (Maier et al., 2021), which employs the *Mutation++* thermochemical library (Scoggins et al., 2020). Furthermore, a non-reacting reference case from Casseau et al. (2016a), involving results from MONACO, LeMANS, and hy2Foam, is also considered. In all cases, validation data were extracted from published figures and reconstructed using polynomial fits to provide a clear and consistent visual comparison. The corresponding polynomial expressions and coefficients are provided in Appendix B.2.

Three validation cases are examined. The first involves an air mixture composed of nitrogen and oxygen molecules, initially at a high translational temperature of 15,000 K with a vibrational temperature of 300 K, allowing relaxation towards equilibrium. The second case considers a single-species nitrogen flow with a higher initial translational temperature of 20,000 K. A third case examines a lower-temperature single-species configuration. The initial conditions for all cases are summarised in Table 3.2.

For the first two cases, the initial temperatures exceed 15,000 K, a regime in which the Park correction factor is known to have a significant influence. To ensure a consistent comparison with the reference data, the correction factor is therefore included in the present model for these cases. As demonstrated in subsequent sections, its influence is negligible for the temperature ranges relevant to the main simulations presented in this thesis.

Figure 3.9 presents the species mass fraction and temperature histories for Case A. Results from SU2-NEMO are identical to those obtained using the HTR solver and are

TABLE 3.2: Initial thermodynamic conditions and species mass fractions for the cases considered.

Case	T [K]	T_v [K]	P [atm]	Y_{O}	$Y_{\mathrm{O_2}}$	Y_{N}	$Y_{\mathrm{N_2}}$	Y_{NO}	dt
Case A	15,000	300	20.42	0.0	0.233	0.0	0.767	0.0	10^{-11}
Case B	20,000	300	27.25	0.0	0.0	0.0	1.0	0.0	10^{-11}
Case C	10,000	1000	1.0	0.0	0.0	0.0	1.0	0.0	10^{-9}

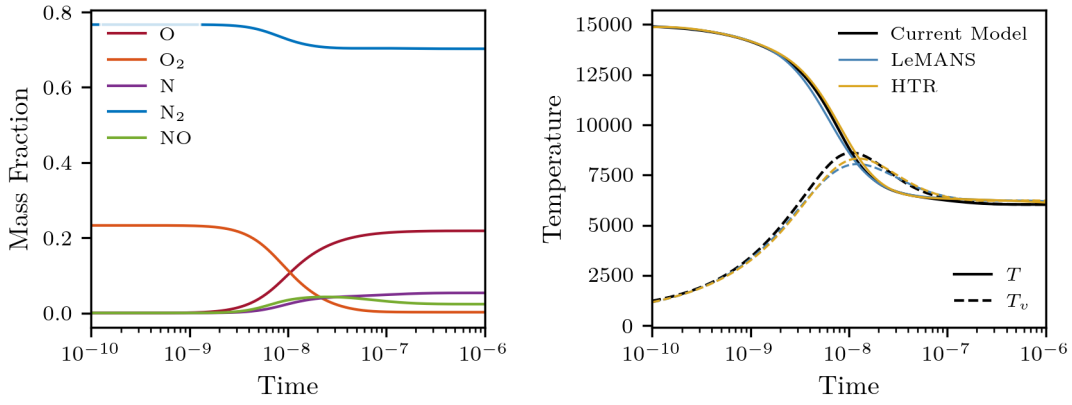

(a) Species mass fraction evolution during the simulation.

(b) Translational and vibrational temperatures during the simulation.

FIGURE 3.9: Thermo-chemical model validation for Case A using reference data from Williamson and Wirtz (2021). Results correspond to the non-preferential dissociation model.

therefore omitted for clarity. Figure 3.9a illustrates the evolution of species mass fractions during relaxation towards thermo-chemical equilibrium, showing complete dissociation of molecular oxygen into atomic oxygen and partial dissociation of molecular nitrogen accompanied by nitric oxide formation. The corresponding temperature histories in Figure 3.9b indicate strong initial thermal non-equilibrium, followed by relaxation of both translational and vibrational temperatures towards an equilibrium value of approximately 6200 K. The non-preferential dissociation model employed here produces a characteristic overshoot of the vibrational temperature above the translational temperature, a feature absent in preferential dissociation formulations. Minor discrepancies in peak vibrational temperature and final equilibrium temperature are attributed to differences in reaction rate coefficients and equilibrium constants between the present model and the reference implementations. Overall, however, strong qualitative agreement is observed.

Results for Case B are shown in Figure 3.10. In this configuration, the flow consists solely of nitrogen at a higher initial translational temperature. Figure 3.10a demonstrates the dissociation of molecular nitrogen into atomic nitrogen, while Figure 3.10b shows that the present model predicts a higher peak vibrational temperature compared to the HTR and LeMANS solvers, which exhibit a more gradual relaxation following the overshoot.

Finally, a single-species non chemically reacting nitrogen case is considered, following the

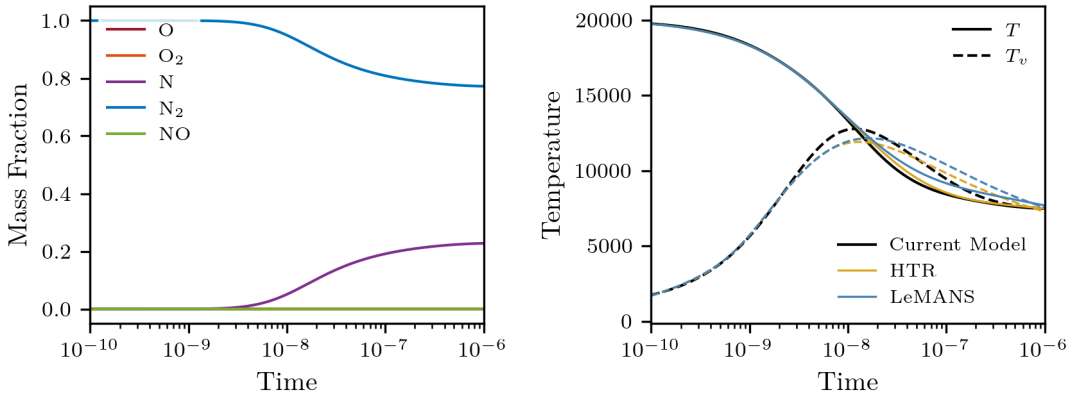

(a) Species mass fraction evolution during the simulation.

(b) Translational and vibrational temperature during the simulation.

FIGURE 3.10: Thermo-chemical model validation for Case B using reference data from Williamson and Wirtz (2021). Results correspond to the non-preferential dissociation model.

approach of Casseau et al. (2016a). The initial translational and vibrational temperatures are set to 10,000 K and 1000 K, respectively. As demonstrated in the reference study, results from MONACO, LeMANS, and hy2Foam are indistinguishable and are therefore represented using a single marker.

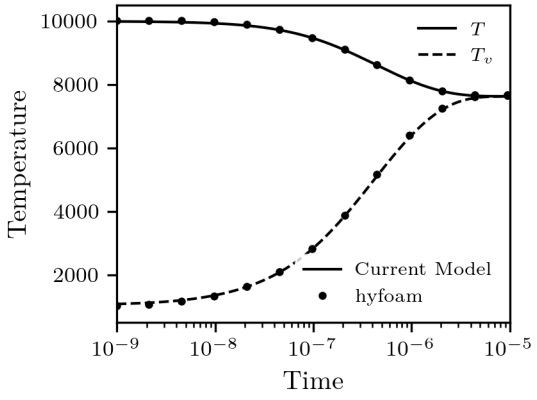

FIGURE 3.11: Translational and vibrational temperature evolution as functions of time for Case C. Validation against reference data from Casseau et al. (2016a).

Figure 3.11 shows excellent agreement between the present model and the reference data. The vibrational relaxation timescale is accurately captured, with the solutions converging at approximately 10^{-5}, s. As the reference case assumes a non-reacting gas, no further change in vibrational energy occurs once equilibrium is reached.

3.3.2 Multi-e_v Versus Single-e_v

In the formulation of vibrational energy transport, energy exchange occurs not only through vibrational–translational (V–T) relaxation, which is commonly modelled using

the Landau–Teller expression, but also through vibrational–vibrational (V–V) energy transfer between molecular species. As discussed in Section 2.1.1, the latter is almost universally assumed to be infinitely fast, effectively implying complete coupling between the vibrational modes of all species. While this assumption is generally valid at lower temperatures and higher pressures, it becomes questionable in regimes characterised by very high temperatures and low pressures. Ideally, V–V energy exchange should be modelled explicitly; however, due to the absence of a comprehensive and well-established model, two limiting cases are considered here. The first assumes fully coupled vibrational modes, while the second assumes that V–V energy exchange is infinitely slow.

Although this modelling aspect is examined in detail in Section 4.4.1, the present section focuses on a zero-dimensional heat-bath configuration with strongly non-equilibrium initial conditions, using the thermo-chemical model defined earlier. The simulation is initialised with a translational temperature of 9000 K and a vibrational temperature of 300 K. The corresponding initial conditions are summarised in Table 3.3.

TABLE 3.3: Initial thermodynamic conditions and species mass fractions for the simulation.

T [K]	T_v [K]	P [atm]	Y_{O}	$Y_{\mathrm{O_2}}$	Y_{N}	$Y_{\mathrm{N_2}}$	Y_{NO}	dt [s]
9000	300	1.0	0.0	0.233	0.0	0.767	0.0	1.0e-9

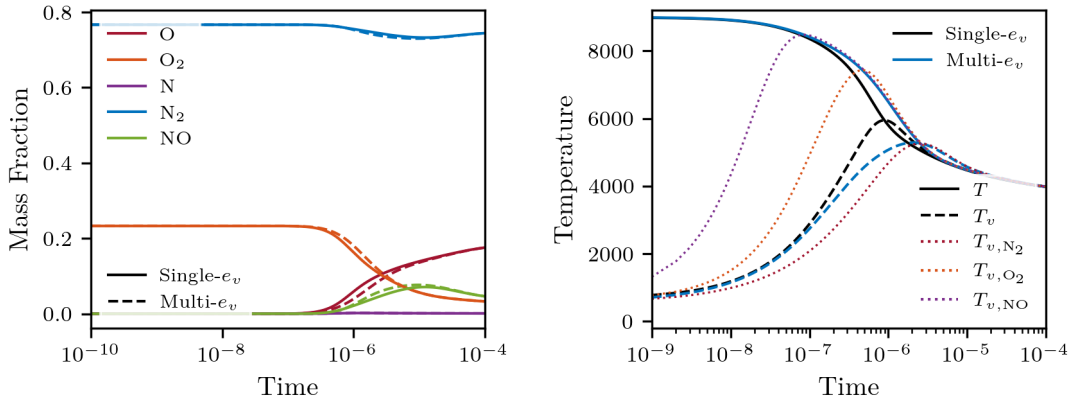

(a) Species mass fraction evolution during the simulation.

(b) Translational and vibrational temperatures during the simulation.

FIGURE 3.12: Zero-dimensional heat-bath case comparing single-e_v and multi-e_v formulations for vibrational energy transport.

Figure 3.12 presents the species mass fraction and temperature histories obtained using the two formulations. Figure 3.12a shows the evolution of species mass fractions, indicating substantial dissociation of molecular oxygen into atomic oxygen, along with smaller changes in nitrogen and nitric oxide concentrations. The corresponding temperature histories in Figure 3.12b illustrate relaxation from an initially strong thermal non-equilibrium state towards equilibrium.

A clear distinction is observed between the single-e_v and multi-e_v formulations (black and blue curves, respectively). The single-e_v model exhibits significantly faster relaxation, effectively corresponding to a shorter vibrational relaxation timescale. In contrast, the multi-e_v formulation accounts for species-dependent vibrational temperatures. In this case, the vibrational modes of O_2 and NO relax more rapidly than that of N_2. As nitrogen constitutes the dominant mass fraction in the mixture, its slower vibrational relaxation governs the overall relaxation behaviour, resulting in a delayed approach to equilibrium compared to the single-e_v model.

3.3.3 Park Relaxation Correction Term

An additional set of tests is presented to assess the influence of the Park correction factor for vibrational relaxation time in highly non-equilibrium conditions, within the temperature ranges relevant to this thesis. The objective is to quantify the impact of this correction and to determine its significance for the simulations conducted herein.

Two zero-dimensional heat-bath cases were evaluated at atmospheric pressure, each corresponding to equilibrium air composition under standard conditions. The cases differ only in their initial translational temperatures, which are set to 15,000 K and 8000 K, respectively. In both cases, the vibrational temperature is initially set to 300 K. The simulations employ the multi-vibrational energy transport formulation. The corresponding initial conditions are summarised in Table 3.4.

Table 3.4: Initial thermodynamic conditions and species mass fractions for the cases considered.

Case	T [K]	T_v [K]	P [atm]	Y_O	Y_{O_2}	Y_N	Y_{N_2}	Y_{NO}	dt [s]
Case A	15,000	300	1.0	0.0	0.233	0.0	0.767	0.0	10^{-10}
Case B	8000	300	1.0	0.0	0.233	0.0	0.767	0.0	10^{-9}

Figure 3.13 shows the translational and vibrational temperature evolution for both cases. In each simulation, the system relaxes towards thermal equilibrium, as indicated by convergence of the translational and vibrational temperatures. For the higher-temperature case shown in Figure 3.13a, only minor differences are observed during the early stages of relaxation when the Park correction factor is applied. In contrast, the lower-temperature case shown in Figure 3.13b exhibits no discernible difference in temperature evolution, indicating that the correction factor has a negligible effect in this regime.

These observations are consistent with the analysis presented in Section 3.2.2, which demonstrated that the Park correction factor introduces minimal changes for temperatures below 8000 K. Accordingly, the correction factor is omitted from the simulations presented in this thesis unless explicitly stated otherwise.

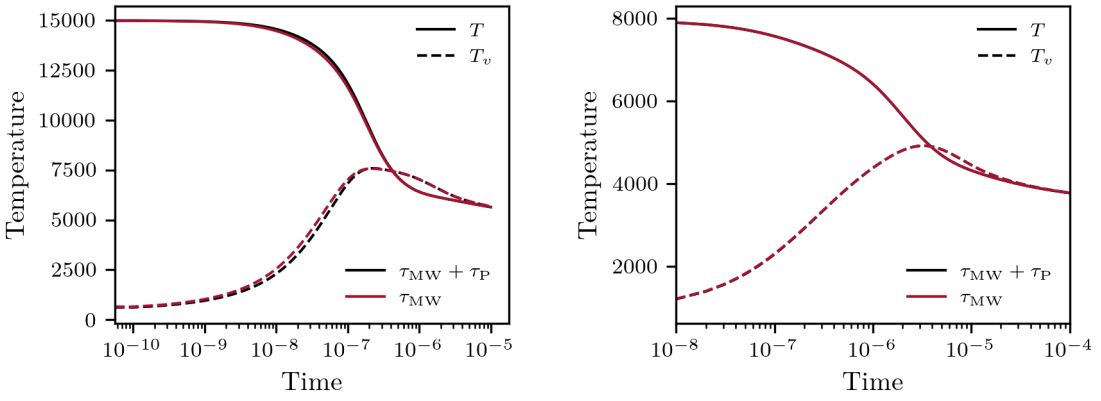

(a) Thermal relaxation with an initial translational temperature of 15,000 K.

(b) Thermal relaxation with an initial translational temperature of 8000 K.

FIGURE 3.13: Zero-dimensional heat-bath simulations evaluating the effect of the Park relaxation correction factor.

3.3.4 Relaxation Time Averaging

As discussed in Section 2.3.2, several approaches exist for averaging relaxation times when a single effective vibrational relaxation timescale is required across all species. These averaging strategies, commonly adopted in the literature (Park, 1985; Gnoffo et al., 1989), influence the evaluation of molecular relaxation times and, consequently, the overall vibrational energy exchange. In this section, a comparative case study is conducted to assess the impact of the averaging method used within a single-e_v formulation. Specifically, the weighted harmonic averaging approach used by Gnoffo et al. (1989) is compared with a weighted arithmetic averaging formulation.

For this investigation, the single-e_v formulation is employed without the Park relaxation correction factor. The original Millikan–White relaxation expression and coefficients are used consistently across all cases, with the averaging procedure being the sole difference. Referring to Figure 3.8, two configurations are considered: one in which both species-level and mixture-level averaging are performed using an arithmetic mean, and another in which both are performed using a harmonic mean. The initial conditions for the simulations are provided in Table 3.5.

TABLE 3.5: Initial thermodynamic conditions and species mass fractions for the simulation.

T [K]	T_v [K]	P [atm]	Y_O	Y_{O_2}	Y_N	Y_{N_2}	Y_{NO}	dt [s]
8000	300	1.0	0.0	0.233	0.0	0.767	0.0	1.0e-9

Figure 3.14 presents the time evolution of species mass fractions and temperatures for the two averaging approaches. In both figures, the harmonic averaging method yields shorter relaxation times, resulting in more rapid thermal equilibration and accelerated chemical reactions. The pronounced differences between the two approaches highlight

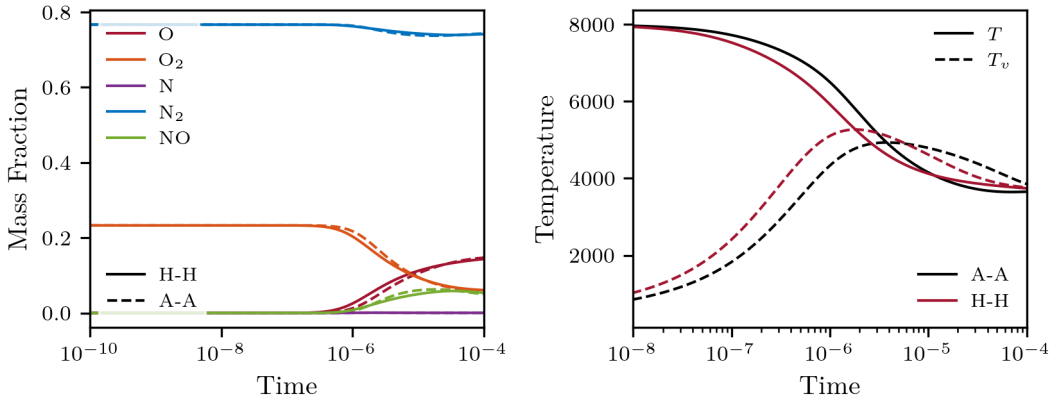

(a) Species mass fraction evolution during the simulation.

(b) Translational and vibrational temperature evolution.

FIGURE 3.14: Comparison of vibrational relaxation time averaging methods in a single-e_v formulation.

the sensitivity of the solution to the manner in which vibrational relaxation times are averaged.

The harmonic averaging formulation provides a more balanced weighting across species, whereas arithmetic averaging tends to bias the effective relaxation time towards species with larger mass fractions. In the present mixture, this behaviour is dominated by molecular nitrogen, which exhibits comparatively slower vibrational relaxation than oxygen-containing species. Historically, harmonic averaging has been widely adopted for rate-related quantities, and accordingly, it is employed in the simulations presented in this thesis when a single vibrational energy transport equation is used, unless stated otherwise.

3.4 Conclusion

Following the detailed formulation of a continuum flow model incorporating reacting thermo-chemical effects, it is necessary to evaluate the underlying assumptions and modelling choices adopted. Accordingly, the objective of this chapter was to examine key components of the thermo-chemical model and to assess their influence in order to establish a final, consistent modelling framework.

The chemical model was first investigated through a comparative assessment of several Park multi-temperature formulations. Across the different publications, discrepancies were identified in two principal areas: the evaluation of the equilibrium constant, where both the functional form and reference data vary, and the specification of forward reaction rate coefficients, which depend on the experimental datasets used for calibration. To address the former, a revised equilibrium constant formulation was developed based on the NASA-9 database, achieving a maximum deviation of approximately 2.5% while

avoiding the need to store multiple temperature-dependent polynomial coefficient sets. For the chemical kinetics, the most recent Park formulations were adopted, resulting in a combined parameter set sourced from multiple publications.

The thermal model was subsequently assessed through evaluation of the specific heat capacity and vibrational relaxation processes. Comparison of different C_p formulations demonstrated that the rigid-rotor harmonic-oscillator model provides sufficient accuracy for temperatures below 8000 K, which encompasses the conditions considered in this thesis. In addition, vibrational relaxation times derived from the original Millikan–White formulation were compared with updated coefficient sets, leading to the selection of Park's revised coefficients for the final thermal model. The influence of relaxation time averaging strategies was also examined, highlighting their impact on predicted relaxation behaviour.

Based on these analyses, the final thermo-chemical model adopted in this work employs Park's most recent chemical reaction rate coefficients (Park et al., 2001; Park, 1993), together with the revised equilibrium constant formulation introduced in this chapter. The thermal relaxation model is defined using the Millikan–White formulation with coefficients taken from Park (1993). This combined framework was subsequently validated against reference solutions from the literature, demonstrating good agreement across a range of non-equilibrium conditions.

Finally, a preliminary assessment of single-e_v and multi-e_v vibrational energy transport formulations was conducted, illustrating the two limiting assumptions associated with vibrational–vibrational energy exchange. The results highlight the sensitivity of thermal relaxation behaviour to these modelling choices and provide insight into their implications for highly non-equilibrium flows.

Overall, this chapter has systematically examined the key components of the thermo-chemical model, establishing a robust and consistent framework for the simulations presented in subsequent chapters. The comparative studies performed here provide a foundation for extending the modelling approach to more complex flow configurations in which additional physical phenomena, such as turbulence, play a dominant role.

3.5 Future Work

Several avenues for future work arise from the findings presented in this chapter:

- **Extension to multi-species air with ionisation:** The present model is formulated for a five-species air mixture and neglects ionisation effects. Future work could extend the framework to seven- or eleven-species air models to include charged species and electronic energy modes. Such an extension would enable

systematic assessment of ionisation effects and the relative importance of electronic versus vibrational energy contributions.

- **Explicit modelling of V-V energy exchange:** Inclusion of vibrational–vibrational (V-V) energy transfer in the vibrational energy transport equations would allow direct evaluation of its influence on relaxation behaviour. While full vibrational coupling is often assumed to be valid at lower temperatures, the temperature and pressure regimes over which this assumption breaks down remain uncertain. Existing studies suggest that V-V relaxation may be significantly slower than V-T relaxation at very low pressures, or may enhance overall relaxation rates for certain species. A systematic investigation of these effects would be particularly relevant for higher-temperature and multi-species flows.

- **Thermodynamic databases for vibrational energy modelling:** Instead of relying on RRHO-based statistical formulations, vibrational energy could be evaluated using thermo-chemical databases such as NASA-9 or polynomial expressions proposed by Gupta et al. (1990). Although the RRHO model was shown to be adequate below 8000 K, database-driven approaches become essential for ionised flows and may also improve accuracy in strongly non-equilibrium conditions.

- **Modelling of Mars atmospheric entry conditions:** An extension of the present framework to Mars atmospheric entry flows would require modelling CO_2-dominated mixtures, where different chemical reactions and relaxation mechanisms prevail. While a preliminary study on modelling such compositions has been done (see Appendix C), comprehensive simulations incorporating turbulence and thermo-chemical non-equilibrium effects remain limited and represent a promising direction for future research.

- **More complete thermo-chemical representation of the flow:** A more fundamental extension involves the adoption of advanced thermo-chemical modelling frameworks, such as the Marrone–Treanor model for chemical reaction rates or state-to-state formulations for the explicit resolution of vibrational energy levels. These approaches enable a more detailed representation of non-equilibrium effects by relaxing many of the simplifying assumptions inherent in multi-temperature models, and would be particularly beneficial for high-temperature and strongly non-equilibrium flow regimes.

Chapter 4

Compressible Mixing Layer

4.1 Introduction

Driven by the growing interest in hypersonic flight, considerable advancements have been made in understanding high-enthalpy flow regimes. Nevertheless, fundamental gaps remain in the understanding of the interactions between fluid dynamics and high-enthalpy phenomena, particularly regarding the coexistence of turbulence with chemical and thermal processes. Moreover, many of the approximations and assumptions employed in modelling high-enthalpy effects have yet to be subjected to rigorous scrutiny or validation.

Relatively few studies to date have exploited developments in high-performance computing to apply direct numerical simulation (DNS) to non-equilibrium phenomena in turbulent flow regimes (Volpiani, 2021). Examples of this approach include investigations of thermo-chemical non-equilibrium boundary layers using a multi-temperature framework, which demonstrated that turbulence–chemistry interactions lead to compositional variations across the boundary layer (Williams et al., 2025) and that chemical non-equilibrium has a stabilising effect on secondary instabilities (Passiatore et al., 2024). Other studies have shown that turbulence–thermal interactions can sustain thermal non-equilibrium through turbulent mixing (Passiatore et al., 2022, 2023). Further investigations have examined the effects of high-enthalpy conditions on decaying isotropic turbulence using DNS (Kerkar and Ghosh, 2019; Khurshid and Donzis, 2019). Additionally, research into vibrational relaxation effects has highlighted both the damping of temperature fluctuations and the role of acoustic waves in their generation (Neville et al., 2015). Fiévet et al. (2019) investigate turbulent thermal non-equilibrium flows using DNS, demonstrating the coupling between turbulence and vibrational relaxation through the use of a state-specific model. These simulations reveal that translational energy evolves through compressible fluid dynamics, while vibrational energy develops on its own relaxation timescale, thereby inducing local vibrational non-equilibrium.

Both theoretical and numerical investigations have demonstrated that finite-rate chemical processes influence the laminar-to-turbulent transition in hypersonic boundary layers. Experiments such as those conducted by Adam and Hornung (1997) and Germain and Hornung (1997) at the California Institute of Technology T5 shock tunnel show that the relaxation of vibrational modes of CO_2 can dampen instability growth, resulting in delayed transition. Likewise, linear stability theory applied under these experimental conditions indicates that vibrational energy relaxation and chemical reactions reduce instability growth rates. Furthermore, numerical studies have shown that exothermic reactions tend to increase instability growth rates, whereas endothermic reactions suppress them (Candler, 2019).

Various numerical simulation frameworks have been developed to study turbulent flows; however, mixing layers are widely regarded as an archetypal configuration for the development of compressible turbulence in high-speed free-shear flows, with significant implications for understanding such flow conditions. Mixing layers have therefore been extensively employed for the development and validation of turbulence models, the analysis of organised motion and coherent structures in turbulent flows, and the evaluation of experimental measurement techniques (Lele, 1989).

Some early studies include the work of Moser and Rogers (1991), who investigated vortex pairing in mixing layers and its role in the transition to small-scale turbulence using DNS. This study examined the characteristics of transition while providing estimates of the degree of three-dimensionality required for pairing to initiate turbulence. Subsequently, Rogers and Moser (1992) performed DNS of three-dimensional, temporally evolving mixing layers, demonstrating Kelvin–Helmholtz roll-up and highlighting nonlinear effects such as the collapse of rib vortices and the formation of spanwise vortices, which were identified as precursors to transition. This was followed by the work of Rogers and Moser (1994), who conducted DNS of an incompressible, self-similar turbulent mixing layer, demonstrating the emergence of self-similarity, describing the dominant flow structures, and evaluating structural differences through the use of a passive scalar.

Early studies on compressible shear layers include the work of Lele (1989), who investigated both temporally and spatially developing mixing layers, examining vortex roll-up, pairing, convective Mach number, and stability in relation to compressibility. When considering compressible mixing layers, the work of Sandham and Reynolds (1989) represents one of the most comprehensive early investigations into the effects of compressibility on mixing-layer instability and growth. Subsequently, Sandham and Reynolds (1990) demonstrated that three-dimensional modes dominate high-speed mixing layers ($M_c > 0.6$) and that linear stability theory accurately predicts growth rates arising from variations in velocity ratio, density ratio, and Mach number.

Further extending this work, Sandham and Reynolds (1991) examined the nonlinear evolution of a temporally evolving compressible mixing layer, highlighting how

Mach number influences instability and vortex structure. The study concluded that compressibility significantly alters the mixing layer structure, leading to highly three-dimensional eddies at high Mach numbers. Vreman et al. (1996) continued the investigation of compressibility effects by conducting simulations across a range of convective Mach numbers from 0.2 to 1.2. Their results showed that dilatational contributions have a negligible influence on dissipation, even in the presence of shocklets. Instead, reduced pressure fluctuations were identified as the primary mechanism responsible for changes in growth rate through the pressure–strain term. This was demonstrated by deriving an accurate relationship between the momentum-thickness growth rate and turbulent kinetic energy production using the integrated Reynolds stress tensor.

Further studies of compressible mixing layers in alternative configurations include the work of Freund et al. (2000a) and Freund et al. (2000b), who employed DNS of an annular mixing layer to investigate compressibility effects on turbulence, a configuration relevant to the early development of sound jets. Consistent with earlier findings, they observed a suppression of growth rates with increasing Mach number, while the dilatational contribution to the turbulent kinetic energy budget increased, though remaining small even in the presence of shocklets. Visualisations indicated that low-Mach-number mixing is dominated by large, azimuthally correlated rollers, whereas high-Mach-number flows exhibit smaller, streamwise-oriented structures. Their results suggest that the most characteristic effect of compressibility is the suppression of transverse turbulence length scales with increasing convective Mach number.

Similarly, Pantano and Sarkar (2002) conducted DNS of a turbulent shear layer to further evaluate compressibility effects. In addition to confirming the reduction in growth rate with increasing convective Mach number and the redistribution of energy from streamwise to cross-stream velocity fluctuations, they found that turbulent intensities, including shear stresses, decrease as the convective Mach number increases. Their study also examined the influence of varying density ratios between the two streams, demonstrating a substantial reduction in the momentum-thickness growth rate with increasing density contrast.

More recent studies include investigations into the effects of compressibility on turbulence statistics and flow structures near the interfaces of high- and low-speed large-scale motions (Wang et al., 2024); analyses of structural evolution and turbulence statistics in spatially developing mixing layers, which concluded that ring-like vortices significantly enhance mixing and prolong the transition stage (Zhang et al., 2019); and research examining the role of bulk viscosity in chemically reacting compressible shear layers developing through shock waves (Boukharfane et al., 2019).

Given the pronounced influence of high-enthalpy effects on flow characteristics, together with the pivotal role of mixing-layer simulations in advancing the understanding of

compressible turbulent flows, it is evident that investigating the impact of thermo-chemical non-equilibrium on turbulence within a direct numerical simulation (DNS) framework is of critical importance. Furthermore, careful consideration must be given to the assumptions and approximations employed in modelling high-enthalpy effects, as well as their physical implications within a non-equilibrium context. Accordingly, the primary objective of this chapter is to evaluate the extent to which thermal non-equilibrium influences turbulence properties in a compressible mixing-layer configuration, and to assess how selected modelling approximations affect the accuracy and reliability of the resulting simulations.

4.2 Canonical Flow Setup

Mixing layers have been a significant contributor to understanding the development of turbulence in external aerodynamics, particularly in atmospheric flows (Green, 1995). They arise from a Kelvin–Helmholtz instability caused by the inflectional nature of the initial velocity profile. The initial condition corresponds to two uniform flows in opposite directions, on which a hyperbolic profile of the form $[u \tanh(2y/\delta_\omega)]$ is imposed.

The temporal mixing layer is known to be an approximation of the spatial mixing layer when viewed in a Galilean frame of reference (four-dimensional, including time). This flow setup was first used by Riley and Metcalfe (1980) for a direct numerical simulation framework, where they demonstrated the formation of coherent vortices and examined the influence of forcing phase on vortex pairing. Rogers and Moser (1994) compared DNS of temporally and spatially evolving mixing layers and noted that there is no qualitative difference, and in most cases no significant quantitative difference either. Although minor differences exist — for example, the mixing spiral in spatially developing mixing layers is convected downstream in the physical frame — none of the physical parameters analysed in this thesis are affected by these distinctions.

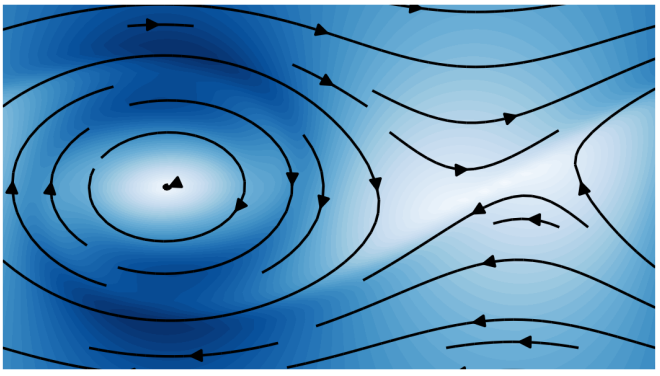

FIGURE 4.1: Instantaneous streamlines (black lines) in a 2D mixing layer superimposed on colour contours showing velocity magnitude, with white contour indicating zero velocity.

Figure 4.1 shows a schematic of a temporally evolving two-dimensional mixing layer, where the colour contours represent velocity magnitude. The bright region on the left marks the vortex core, while that on the right corresponds to the stagnation point. In a compressible flow, density, pressure, and temperature increase along streamlines approaching the stagnation point, while the opposite trend occurs along streamlines moving away from the stagnation point and subsequently entrained into the vortex core. Flow moving away from the stagnation region expands towards the vortex centre, while flow moving towards the stagnation point decelerates. In spatially developing mixing layers, the stagnation point is convected at the mean flow speed; thus, in the schematic representation of temporally developing layers, it appears stationary. When the densities of the two streams differ, baroclinic torque (vorticity generation due to misalignment of density and pressure gradients) becomes significant and modifies the vorticity distribution within the vortex. This conceptual picture (Figure 4.1) will prove useful when discussing the influence of thermo-chemical non-equilibrium.

To enable comparison with experimental configurations, several studies have examined the influence of splitter plates used in laboratory setups. Laizet et al. (2010) demonstrated that the trailing-edge geometry affects the spatial development of a mixing layer, highlighting discrepancies between numerical simulations and certain experimental observations. Additionally, Sandham and Sandberg (2009) showed that while an infinitely thin splitter plate does not induce a global mode, there exists a critical thickness above which the flow becomes globally unstable.

4.2.1 Flow Characteristics

To evaluate the flow characteristics of the mixing layer, suitable characteristic variables must be defined according to the flow configuration. Several canonical quantities commonly used in mixing-layer and shear-layer analysis are introduced in this subsection.

Papamoschou and Roshko (1988) introduced the convective Mach number to assess compressibility effects on mixing-layer growth. For instance, it has been shown that for $M_c < 0.4$, the instability remains predominantly two-dimensional; for $0.4 < M_c < 0.8$, the flow enters a moderately compressible regime where three-dimensional oblique waves appear; and for $M_c > 0.8$, the instability becomes fully three-dimensional (Zhang et al., 2019). The convective velocity is defined as

$$u_c = \frac{u_1 a_2 + u_2 a_1}{a_1 + a_2} \quad , \tag{4.1}$$

where a_i denotes the speed of sound in each free stream. The corresponding convective Mach numbers for each stream are

$$M_{c,1} = \frac{u_1 - u_c}{a_1} \quad , \qquad M_{c,2} = \frac{u_c - u_2}{a_2} \quad . \tag{4.2}$$

When both streams share the same specific heat ratio, the convective Mach number simplifies to

$$M_c = \frac{u_1 - u_2}{a_1 + a_2} \quad . \tag{4.3}$$

The vorticity thickness δ_ω, a key measure of shear-layer growth, is defined as (Cortesi et al., 1999)

$$\delta_\omega = \frac{\Delta u}{|d\bar{u}/dy|_{max}} \quad , \tag{4.4}$$

where Δu is the free-stream velocity difference and $\bar{u}$ is the mean streamwise velocity. The normalised growth rate of the vorticity thickness is given by

$$r_\omega = \frac{u_c}{\Delta u}\frac{d\delta_\omega}{dt} \quad , \tag{4.5}$$

where u_c is the convective velocity from Equation 4.1.

The momentum thickness θ, which is less sensitive to statistical noise than δ_ω due to it being an integral rather than a derivative quantity, is defined as (Rogers and Moser, 1994)

$$\theta = \int_{-\infty}^{+\infty} \left(\frac{1}{4} - \frac{\bar{u}^2}{(\Delta u)^2} \right) dy \quad , \tag{4.6}$$

where $\bar{u}$ is the mean streamwise velocity. For temporally evolving compressible mixing layers, the expression of Vreman et al. (1996) is adopted,

$$\theta = \frac{1}{\rho_\infty (\Delta u)^2} \int_{-\infty}^{+\infty} \bar{\rho}\,(u_1 - \bar{u_1})\,(\bar{u_1} - u_2)\,\frac{dy}{du} \quad , \tag{4.7}$$

where ρ_∞ is the free-stream density. The momentum-thickness growth rate is of importance as it is linked to the integrated turbulence production via (Vreman et al., 1996)

$$d\theta/dt = -\frac{2}{\rho_\infty (\Delta u)^2} \int \left(\overline{\rho u'' v''} \frac{\partial \tilde{u}}{\partial y} \right) dy \quad . \tag{4.8}$$

where $\tilde{u}$ is the Favre-averaged velocity. While this expression is for temporally developing mixing layers, it can be extended to spatially developing mixing layers as well (Vreman et al., 1996).

A dimensionless time is introduced as

$$\tau_\theta = \frac{t \Delta u}{\theta_\circ} \quad . \tag{4.9}$$

where $\theta_\circ$ is the initial momentum thickness. The dimensionless growth rate of the momentum thickness is then defined as

$$r_m = \frac{1}{\Delta u}\frac{d\theta}{dt} \quad . \tag{4.10}$$

4.2.2 Statistical Parameters

To characterise and compare the flow fields generated in various simulations, several parameters were computed and analysed using statistical methods. This section defines and explains these parameters.

4.2.2.1 Turbulence Intensity

Favre (mass-weighted) averaged quantities are defined as (Launder and Sandham, 2002)

$$\omega = \tilde{\omega} + \omega'' \quad , \qquad \text{and} \qquad \overline{\omega''} \neq 0 \quad , \tag{4.11}$$

where $\tilde{\omega}$ is the density-weighted average defined by $\overline{\rho\omega}/\bar{\rho}$, and averaging is carried out in the homogeneous x and z directions.

The stress components describe the intensity of turbulence across the shear layer. These are defined as

$$\bar{\rho}\widetilde{u''u''}/(\rho^\circ \Delta u^2) \quad , \qquad \bar{\rho}\widetilde{v''v''}/(\rho^\circ \Delta u^2) \quad , \qquad \bar{\rho}\widetilde{w''w''}/(\rho^\circ \Delta u^2) \quad , \tag{4.12}$$

where the dominant contributor to turbulence production is given by (Zhang et al., 2019)

$$\bar{\rho}\widetilde{u''v''}/(\rho^\circ \Delta u^2) \quad . \tag{4.13}$$

Here, ρ° is the reference density and Δu the stream velocity difference. Reynolds stresses of the form $\overline{u'u'}$, without favre averaging, are computed via the variance

$$\overline{u'u'} = \mathrm{var}(u) = \frac{\sum(u-\bar{u})^2}{n} \quad , \tag{4.14}$$

where $\bar{u}$ is the mean streamwise velocity and n is the number of data points. The root-mean-square (rms) velocity component is calculated as

$$u_{i,rms} = \sqrt{\frac{\sum_i u_{ij}^2}{n}} \quad , \tag{4.15}$$

with n being the number of points along axis i.

4.2.2.2 Turbulence Kinetic Energy

The Favre averaged Turbulent Kinetic Energy (TKE) is defined as half the trace of the stress tensors

$$\text{TKE} = \frac{1}{2}(\widetilde{u''u''} + \widetilde{v''v''} + \widetilde{w''w''}) \quad , \tag{4.16}$$

where u'', v'', and w'' are the fluctuating velocity components in each spatial direction. TKE quantifies the mean kinetic energy per unit mass contained in velocity fluctuations (Pope, 2000).

The integrated turbulent kinetic energy (ITKE) provides a better measure of the overall energy content in the flow and is given by

$$\text{ITKE} = \frac{1}{2}\int_{-\infty}^{\infty}(\widetilde{u''u''} + \widetilde{v''v''} + \widetilde{w''w''})dy \quad . \tag{4.17}$$

4.2.2.3 Vorticity - Circulation - Enstrophy

Vorticity quantifies the local rotation in the flow and is defined as the curl of the velocity vector. Its magnitude is given by

$$|\omega| = \sqrt{\omega_x^2 + \omega_y^2 + \omega_z^2} = \sqrt{\left(\frac{\partial w}{\partial y} - \frac{\partial v}{\partial z}\right)^2 + \left(\frac{\partial w}{\partial x} - \frac{\partial u}{\partial z}\right)^2 + \left(\frac{\partial v}{\partial x} - \frac{\partial u}{\partial y}\right)^2} \quad . \tag{4.18}$$

Circulation Γ is defined as the volume integral of the vorticity:

$$\Gamma = \iiint_v \omega dv \quad , \tag{4.19}$$

and enstrophy Ω is the integral of the squared vorticity:

$$\Omega = \iiint_v \omega^2 dv \quad , \tag{4.20}$$

4.2.2.4 Q-Criterion

The Q-criterion is used to visualise vortices and is defined as:

$$Q = \left[\left|\frac{\nabla\vec{V} - \nabla\vec{V}^T}{2}\right|^2 - \left|\frac{\nabla\vec{V} + \nabla\vec{V}^T}{2}\right|^2\right]/2 \quad , \tag{4.21}$$

where $\vec{V}$ is the velocity vector. The first term represents the rate of rotation and the second the rate of strain. Thus, $Q > 0$ indicates vortex-dominated regions where rotation exceeds strain (Cummings et al., 2015).

4.2.3 Energy Budget

Following the connection between the momentum-thickness growth rate and the integrated turbulence production in Equation 4.8, Vreman et al. (1996) employed the Reynolds stress transport equation for compressible flows to derive an energy budget for the mixing layer. The ij-component of the integrated Reynolds stress evolves according to

$$\frac{d}{dt}\int \overline{\rho\, u_i'' u_j''}\, dy = P_{ij} + \Pi_{ij} - \epsilon_{ij} \quad , \tag{4.22}$$

where P_{ij}, Π_{ij}, and ϵ_{ij} refer to the integrated production, pressure-strain, and dissipation tensors, respectively. These are defined as

$$P_{ij} = -\int \left(\overline{\rho u_i'' v''} \frac{\partial \tilde{u}_j}{\partial y} + \overline{\rho u_j'' v''} \frac{\partial \tilde{u}_i}{\partial y} \right) dy \, , \tag{4.23}$$

$$\Pi_{ij} = \int \overline{p \left(\frac{\partial u_i''}{\partial x_j} + \frac{\partial u_j''}{\partial x_i} \right)} dy \, , \tag{4.24}$$

$$\epsilon_{ij} = \int \left(\overline{\sigma_{ik} \frac{\partial u_j''}{\partial x_k}} + \overline{\sigma_{jk} \frac{\partial u_i''}{\partial x_k}} \right) dy \, , \tag{4.25}$$

For a fully self-similar mixing layer, both the growth rate and the integrated production become approximately constant, making Equation 4.22 independent of time and spatial scaling. However, reaching strict self-similarity in temporally evolving mixing layers is challenging due to the continual thickening of the layer and the limited spatial extent of the computational domain.

Despite these limitations, the expressions in Equation 4.22-4.25 provide a robust framework for evaluating the energy budget of the compressible mixing layers studied in this chapter. They enable quantification of how production, pressure-strain redistribution, and viscous dissipation contribute to the evolution of turbulent stresses, forming the basis for the subsequent analysis of thermo-chemical non-equilibrium effects.

4.2.4 Acoustic Waves

Colonius et al. (1997) investigated sound generation in mixing layers using direct numerical simulation. While their study focuses primarily on acoustic analogies and field prediction, it also reveals the presence of acoustic waves within temporally evolving mixing layers. In simulations with symmetric boundary conditions, wave reflections may interfere with solution accuracy near the roll-up region.

Dilatation is a useful indicator of acoustic waves in the far field, as it correlates directly with acoustic pressure. Additionally, its Discrete Fourier Transform (DFT) is less prone to contamination by low- and high-frequency noise (Colonius et al., 1997). Dilatation is

defined as

$$\nabla \cdot \mathbf{u} = \frac{\partial u_x}{\partial x} + \frac{\partial u_y}{\partial y} + \frac{\partial u_z}{\partial z} \quad . \tag{4.26}$$

4.3 Numerical Setup

This section describes the numerical aspects of the simulation framework, including the imposed initial disturbance used to trigger the Kelvin–Helmholtz instability, the boundary filtering applied at the outer limits of the computational domain, and the grid-resolution study undertaken to ensure numerical accuracy and stability.

4.3.1 Turbulence Transition

As discussed by Lele (1989), the inviscid vorticity equation for a two-dimensional compressible flow indicates that the rate of change of vorticity arises from three mechanisms: advection, dilatation (compression/expansion), and baroclinic torque. Among these, advection plays the dominant role in the classical incompressible shear-layer instability, as vorticity generated near the stagnation region is advected and accumulated towards the vortex centre, initiating the Kelvin–Helmholtz roll-up.

The dilatational term, associated with compressibility, has the opposite effect: expansion and compression across the flow field increase vorticity near the stagnation point and reduce it near the vortex core. This counteracting influence introduces a stabilising effect as the convective Mach number increases. Meanwhile, baroclinic torque arises from misalignment of pressure and density gradients and hence is an incompressible effect, becoming dynamically important in braided regions and near stagnation points where strong density gradients exist between the two free streams.

To trigger the transition process numerically, an initial disturbance must be imposed on the base flow. One possible approach is to refine the forcing using linear stability eigenfunctions computed from the inflow profiles. This method, originally proposed by Sandham and Reynolds (1989) for incompressible mixing layers, enables the introduction of the most unstable linear frequency to accelerate the transition to turbulence. However, for the present study, a simpler and widely adopted form of sinusoidal forcing is sufficient to initiate the Kelvin–Helmholtz instability.

The initial conditions for the velocity components, designed to generate vortex roll-up within the mixing layer, are defined as

$$u(x,y) = u_\infty \tanh\left(\frac{2y}{\delta_\omega}\right), \tag{4.27}$$

$$v(x,y) = A\,u_\infty \cos\left(\frac{2\pi x}{L_x}\right) \exp\left[-\frac{1}{10}\left(\frac{y}{\delta_\omega}\right)\right], \tag{4.28}$$

$$v(x,y,z) = A\,u_\infty \cos\left(\frac{2\pi x}{L_x}\right) \cos\left(\frac{2\pi z}{L_z}\right) \exp\left[-\frac{1}{10}\left(\frac{y}{\delta_\omega}\right)\right], \tag{4.29}$$

$$w(x,y) = 0 \quad , \tag{4.30}$$

where u_∞ is the free-stream velocity, δ_ω is the initial vorticity thickness, L_x is the domain length in the streamwise direction and L_z is the domain length in the spanwise direction, A is a constant determining the magnitude of the disturbance (usually set to 0.01), and (x, y, z) denote spatial coordinates within the computational domain. The streamwise domain length $L_x = 2\pi/\alpha$ was chosen using a wavenumber $\alpha\delta^0_\omega = 0.42$, sufficiently large to accommodate both K–H roll-up (2D) and oblique breakdown (3D). The imposed perturbation in v is localised near the shear layer and decays exponentially with y, ensuring that the disturbance remains confined to the mixing region while still effectively triggering the instability.

4.3.2 Filtering Acoustic Disturbances

The development of the mixing layer, initiated by the imposed disturbance used to trigger the Kelvin–Helmholtz instability, generates acoustic waves that propagate from the shear region towards the outer boundaries of the computational domain. The nature of acoustic waves in mixing layers has been examined by Lele (1989), who noted that acoustic waves generated during the initial roll-up consist of a compression wave followed by a spread out expansion wave, whereas pairing vortices tend to produce more symmetric compression–expansion waves.

In the absence of characteristic boundary conditions in OpenSBLI, a filtering strategy is required to prevent these acoustic waves from reflecting back into the shear region, which would otherwise contaminate the transition process. To address this, a binomial (explicit) filter is applied near the upper and lower boundaries of the domain, diffusing outgoing acoustic disturbances. However, excessive filtering may itself induce artificial reflections, while insufficient filtering fails to attenuate outgoing waves. Therefore, it is necessary to determine an appropriate filter strength and order for the present configuration.

The binomial filter used in this study, described in Section 2.5.3, is applied 30 stencil points away from both the upper and lower boundaries. The filter contains two tunable parameters: the filter order and the intensity factor. A series of numerical experiments

was carried out to identify suitable values for these parameters for the present mixing-layer configuration.

To assess filter performance, a two-dimensional simulation was conducted using the flow conditions listed in Table 4.1, with the flow assumed to be in thermo-chemical equilibrium. The mass fractions were set to [0.051, 0.139, 0.0, 0.772, 0.038] for O, O_2, N, N_2, and NO respectively. As a baseline, a simulation with an extended domain and no filtering was performed. The enlarged domain delays acoustic reflections significantly, allowing the mixing layer to evolve without interference, providing a reference case against which filtered cases may be compared. Subsequently, multiple simulations using different filter parameters were carried out, with symmetry boundary conditions applied at the upper and lower boundaries.

To illustrate the propagation of acoustic waves, the volumetric dilation defined in Equation 4.26 is displayed in Figure 4.2 for the unfiltered base case. The figure shows the acoustic pulse reaching the outer boundaries, reflecting from the symmetry boundary condition, and subsequently travelling back towards the mixing layer.

To quantify the influence of acoustic reflections, the mean turbulent kinetic energy and pressure fluctuations along the centreline were compared against the extended-domain

TABLE 4.1: Flow conditions for the 2D mixing-layer simulations.

u_∞ (m/s)	ρ (kg/m^3)	p (N/m^2)	δ°_ω (m)	L_x (m)	L_y (m)	Model
439.8	0.02	18142.48	0.003998	$15\delta^\circ_\omega$	$\frac{1000}{15}\delta^\circ_\omega$	TE-CF

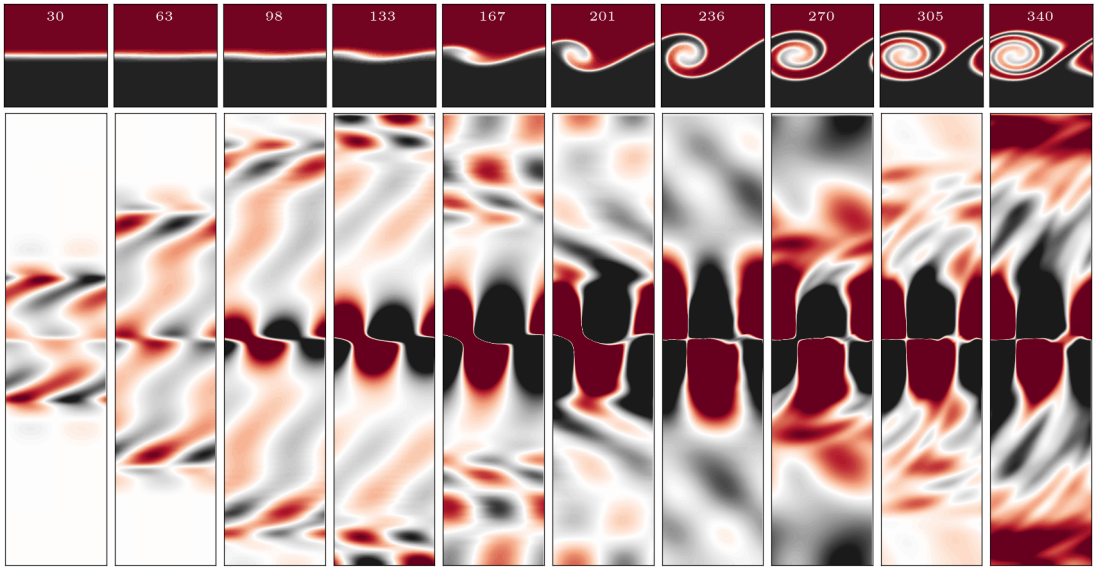

FIGURE 4.2: Volumetric dilation (defined by Equation 4.26) demonstrating acoustic-wave propagation and its reflection back towards the vortex roll-up region in the unfiltered case. The numbers above each column refers to the non-dimensional time (τ_θ).

base case. Figure 4.3 shows the percentage error of these quantities for different filter settings.

The results illustrate a balance between filtering strength and disturbance magnitudes. As seen in Figure 4.3a, stronger filters reduce acoustic amplitudes later in the simulation. However, they also introduce earlier deviations due to artificial reflections at the filter location. This behaviour is even more evident in the pressure fluctuations shown in Figure 4.3b. Based on these observations, an order of 2 with an intensity factor of 0.25 was found to provide an effective compromise between dissipation and reflection, and this

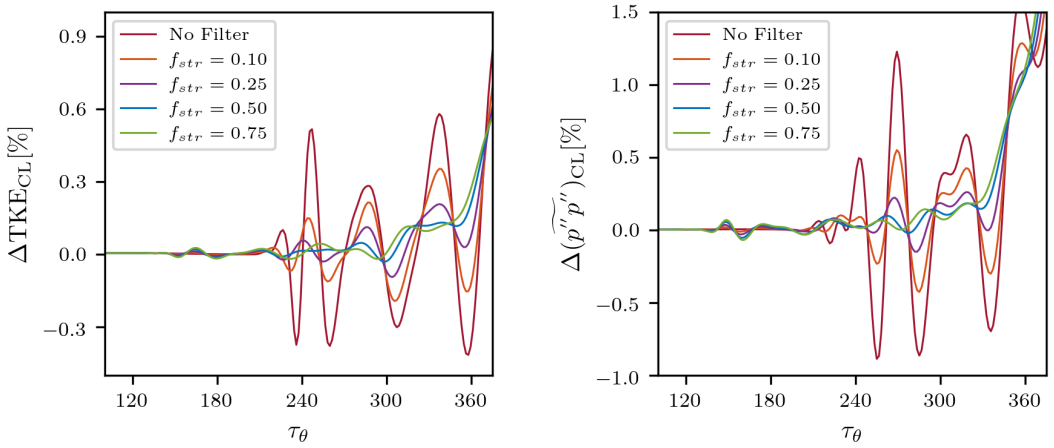

(a) Percentage error in centreline turbulent kinetic energy.

(b) Percentage error in centreline pressure fluctuations.

FIGURE 4.3: Deviation from the undisturbed extended-domain case for various binomial filter strengths.

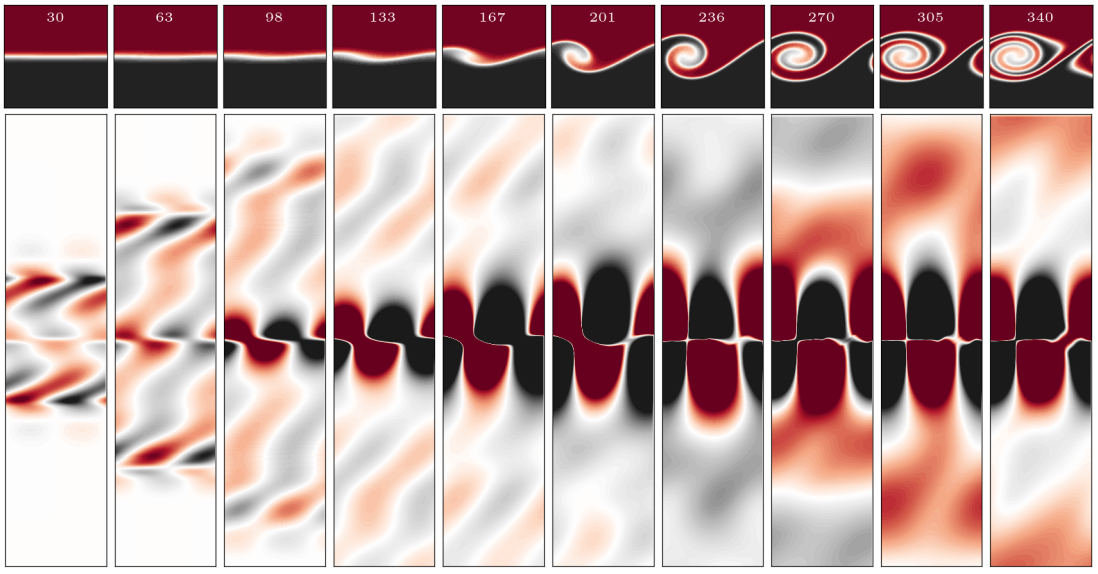

FIGURE 4.4: Propagation of the acoustic wave with the binomial filter applied and extrapolation boundary conditions. Reflections from the outer boundaries are effectively removed. The numbers above each column refers to the non-dimensional time (τ_θ).

configuration is employed for all mixing-layer simulations in this thesis unless otherwise stated.

The effectiveness of this filter configuration is demonstrated in Figure 4.4, which shows the same scenario as Figure 4.2, but with the binomial filter applied in conjunction with the extrapolation boundary condition. The reflection of acoustic waves from the outer boundaries is almost entirely eliminated.

Overall, the filtering strategy adopted here successfully suppresses acoustic reflections without introducing significant artefacts, thereby providing a reliable setup for analysing the subsequent evolution of the compressible mixing layer.

4.3.3 Grid Convergence

To conduct the grid-convergence study, two quantities were selected for evaluation: one global and one local parameter. Mesh refinements were performed along each coordinate direction separately, using a constant refinement factor, and a final case was computed with the maximum feasible number of grid points as an additional reference. Richardson extrapolation, as described in Section 2.5.4, was also employed to estimate the discretisation error. The same procedure was applied to both the two-dimensional and three-dimensional mixing-layer configurations.

Two-Dimensional Mixing Layer

For the two-dimensional simulations, a single-e_v thermal non-equilibrium model without chemical reactions was used. The flow conditions are summarised in Table 4.2, and were held constant across all cases considered. The flow is chemically frozen with mass fractions of 0.05, 0.14, 0.00, 0.77, and 0.04 for O, O_2, N, N_2, and NO respectively. Since there is no chemical diffusion, a constant Schmidt number model was employed for the diffusion coefficient in order to reduce computational cost. The stretching factor (β) of the grid in the y-direction was set to 3.0 for the simulations reported here.

Table 4.2: Flow conditions for the 2D mixing-layer simulations.

u_∞ (m/s)	ρ (kg/m^3)	p (N/m^2)	δ°_ω (m)	L_x (m)	L_y (m)	Model
438.02	0.02	18124.5	0.003958	$15\delta^\circ_\omega$	$\frac{1000}{15}\delta^\circ_\omega$	single-e_v (TNE-CF)

The grid parameters corresponding to each refinement level are listed in Table 4.3. Three refinement sets were considered. In the first two sets, the y- and x-directions were refined independently (with the other direction held at a refinement factor of 1.0), while in the third set both directions were refined simultaneously. Two parameters were selected to assess convergence: a global quantity, ϕ_1, defined as the integral turbulent

TABLE 4.3: Grid specification for each refinement step (2D cases).

Refinement Factor	Δt	N_{iter}	N_x	N_y	Filter Index	Printout
0.66	5.103×10^{-7}	1600	80	121	7	80
1.0	3.402×10^{-7}	2400	120	181	9	120
1.5	2.268×10^{-7}	3600	180	271	12	180
2.25	1.512×10^{-7}	5400	270	405	20	270
3.375	1.008×10^{-7}	8100	404	607	29	405
6.75	0.504×10^{-7}	16200	810	1213	58	810

kinetic energy (ITKE) over the flow field, and a local quantity, ϕ_2, defined as the mean translational temperature along the centreline. For both parameters, a single output time was used for comparison, corresponding to the eighth printout (where 'printout' denotes the number of time steps between outputs). This printout occurs near the end of the linear growth phase of the momentum thickness. Since the time step changes with grid refinement for numerical stability, the iteration number associated with a given physical time differs between cases; these values are listed in Table 4.3. Figure 4.5 summarises the grid-convergence behaviour of the two parameters. The markers labelled "y" (triangles) denote refinement in the y-direction only, "x" (crosses) denote refinement in the x-direction only, and "x, y" (circles) denote simultaneous refinement in both directions. Figure 4.5a and Figure 4.5b show the normalised values of the global and local parameters, while Figure 4.5c and Figure 4.5d display the approximated error as defined in Equation 2.160. Both the integral turbulent kinetic energy and the centreline temperature exhibit clear convergence behaviour: the error decreases as the grid is refined and the solutions approach one another. This trend becomes less pronounced beyond a refinement factor of 1.5, indicating that further refinement offers diminishing returns. In particular, refinement in the x-direction has only a minor effect on the solution, whereas refinement in the y-direction leads to clear improvements; simultaneous refinement of both directions follows a similar trend. These results indicate that refinement beyond a factor of 1.5 in the x-direction is unnecessary.

Figure 4.5e and Figure 4.5f show the extrapolated error estimated using the observed order of accuracy. The global parameter exhibits an order of accuracy within approximately 10% of the nominal scheme order, whereas the local parameter shows a less consistent trend. As discussed earlier, this discrepancy is attributed to the relative error for ϕ_2 being very small, which can affect the robustness of the order-of-accuracy estimate.

The observed orders of accuracy and grid-convergence indices (GCI) for the "x, y" refinement set are summarised in Table 4.4. The GCI values are small for both parameters over the tested refinement factors, indicating low discretisation uncertainty.

Overall, the 2D grid study indicates that increasing the resolution beyond a refinement factor of 1.5 in the x-direction and 2.25 in the y-direction yields negligible improvements.

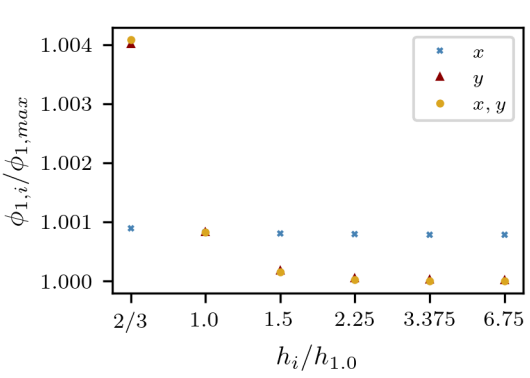

(a) Normalised global parameter where $\phi_1 = \text{ITKE}$.

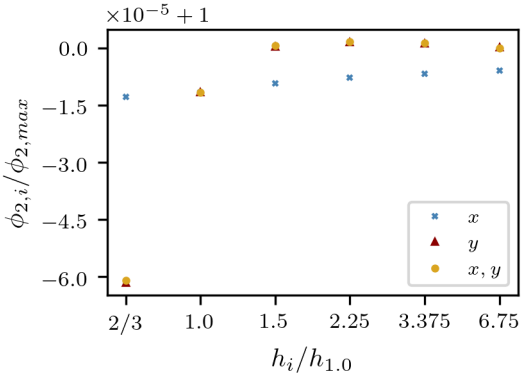

(b) Normalised local parameter where $\phi_2 = \overline{T}_{\text{Centreline}}$.

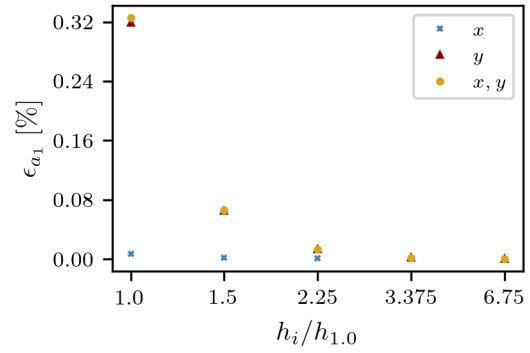

(c) Approximated error for ϕ_1 in percentage.

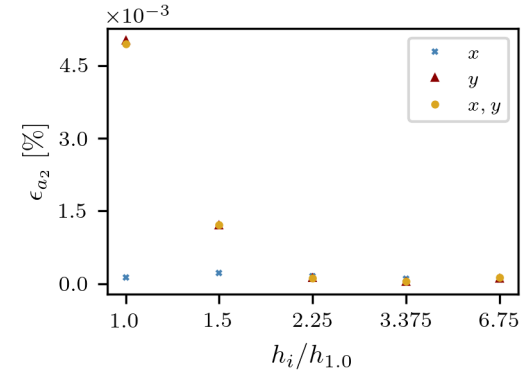

(d) Approximated error for ϕ_2 in percentage.

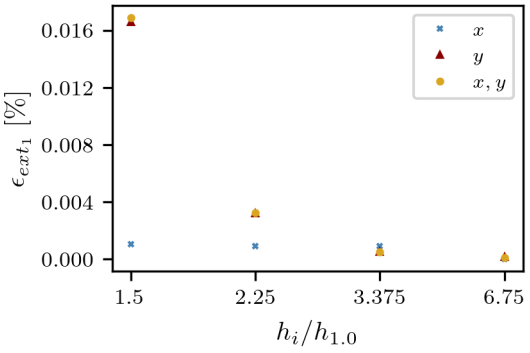

(e) Extrapolated error for ϕ_1 in percentage.

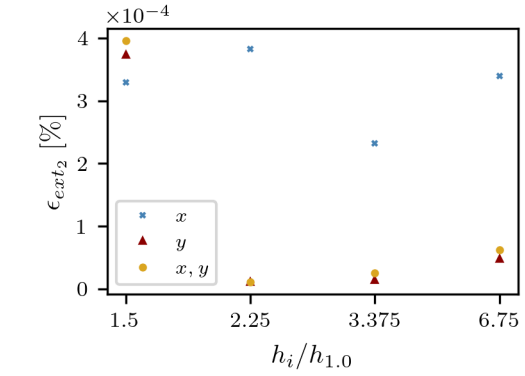

(f) Extrapolated error for ϕ_2 in percentage.

FIGURE 4.5: Grid refinement effects on the global and local parameters. ϕ_1 is the integral turbulent kinetic energy and ϕ_2 is the mean translational temperature along the centreline. The formulations used in (c)–(f) are defined in Equation 2.159–2.161.

A grid of $N_x = 180$ and $N_y = 405$ is therefore adopted for the two-dimensional simulations presented in the following sections.

TABLE 4.4: Observed order of accuracy and GCI of refinement set "x, y" (2D).

Refinement Factor	P_1 (global)	GCI_1 (global)	P_2 (local)	GCI_2 (local)
0.66	–	–	–	–
1.0	–	–	–	–
1.5	3.930	2.1130×10^{-4}	3.462	3.8746×10^{-6}
2.25	3.989	4.0701×10^{-5}	5.877	3.4698×10^{-7}
3.375	4.297	6.2586×10^{-6}	2.421	1.1364×10^{-7}
6.75	2.511	1.0714×10^{-6}	1.619	3.4416×10^{-7}

4.3.3.1 Three-Dimensional Cases

A similar grid-convergence study was conducted for the three-dimensional simulations. As in the 2D case, a single-e_v thermal non-equilibrium model without chemical reactions was used. The flow is chemically frozen with mass fractions of 0.05, 0.14, 0.00, 0.77, and 0.04 for O, O_2, N, N_2, and NO respectively. The stretching factor in the y-direction was set to 2.2. The flow conditions are listed in Table 4.5. A constant refinement

TABLE 4.5: Flow conditions for the 3D mixing-layer simulations.

u_∞ (m/s)	ρ (kg/m^3)	p (N/m^2)	δ°_ω (m)	L_x (m)	L_y (m)	L_z (m)	Model
438.02	0.02	18124.5	0.003958	$15\delta^\circ_\omega$	$\frac{1000}{15}\delta^\circ_\omega$	$15\delta^\circ_\omega$	single-e_v (TNE-CF)

factor was employed, with refinements performed independently along each of the three coordinate directions, while the remaining directions were held at a factor of 1.0. A final "max" case with all directions refined to a factor of 3.6 was also computed. The grid parameters for each refinement level are provided in Table 4.6. The final refinement factor was set to 1.6 rather than 1.5 for practical reasons. Furthermore, because the binomial filter is used to attenuate acoustic reflections, the filter index must be adjusted with refinement to maintain a fixed physical location of the filtering region and avoid introducing grid-dependent artefacts.

TABLE 4.6: Grid specification for each refinement step (3D cases).

Refinement Factor	Δt	N_{iter}	N_x	N_y	N_z	Filter Index	Printout
0.66	2.250×10^{-7}	1800	120	121	120	8	120
1.0	2.250×10^{-7}	2700	180	181	180	13	180
1.5	1.500×10^{-7}	4050	270	271	270	17	270
2.25	1.000×10^{-7}	6075	404	405	404	26	405
3.6	0.625×10^{-7}	9720	648	647	648	38	648

As in the 2D study, one global and one local parameter were selected for assessment, and the ninth printout was used for comparison, corresponding to the end of the initial linear growth stage of the momentum thickness.

Figure 4.6 shows the convergence behaviour of the chosen parameters. The markers labelled "y" (triangles) denote refinement in the y-direction only, "x" (crosses) represent refinement in the x-direction only, and "z" (circles) indicate refinement in the z-direction only. Figure 4.6a and Figure 4.6b display the normalised values of the global and local parameters, while Figure 4.6c and Figure 4.6d show the approximated error, and Figure 4.6e and Figure 4.6f the extrapolated error. Both absolute and relative errors decrease with refinement, indicating convergence. This trend is most evident for refinements in the y-direction; the x- and z-directions appear to have largely converged already at lower refinement levels.

The extrapolated error for the global parameter becomes very small by a refinement factor of 2.25, while the local parameter shows consistently low errors for both intermediate and fine grids. As in the two-dimensional case, the extrapolated error for the local quantity should be interpreted with care when the relative differences $|\phi_i - \phi_{i+1}|$ are close to zero.

The observed order of accuracy and GCI values for the "y" refinement set are summarised in Table 4.7. Since the observed orders do not match the nominal scheme order, a safety factor of 3.0 was used in the GCI evaluation instead of 1.25. The change in refinement ratio in the final case also contributes to the variation in the estimated order. Nonetheless, the GCI values remain small for the refinement levels considered.

TABLE 4.7: Observed order of accuracy and GCI of refinement set "y" (3D).

Refinement Factor	P_1 (global)	GCI_1 (global)	P_2 (local)	GCI_2 (local)
0.66	–	–	–	–
1.0	–	–	–	–
1.5	1.226	5.4151×10^{-2}	4.442	6.4605×10^{-4}
2.25	7.995	5.7742×10^{-5}	2.660	5.9170×10^{-6}
3.6	6.977	5.3417×10^{-4}	3.131	1.2882×10^{-6}

The 3D grid study demonstrates that increasing resolution in the x- and z-directions beyond a refinement factor of 1.5 brings little additional benefit, indicating that $N_x = N_z = 270$ is sufficient. In contrast, the y-direction shows a stronger influence on the solution. A refinement factor of 2.25 yields near-perfect grid convergence, while a factor of 1.5 still results in very small errors (of order 0.08%) and significantly reduces computational cost. Accordingly, a compromise grid with $N_y = 271$ and $N_x = N_z = 270$ is adopted for the three-dimensional simulations presented in the remainder of this chapter.

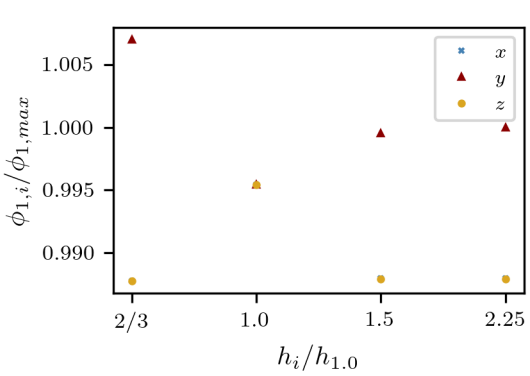

(a) Normalised global parameter where $\phi_1 = \text{ITKE}$.

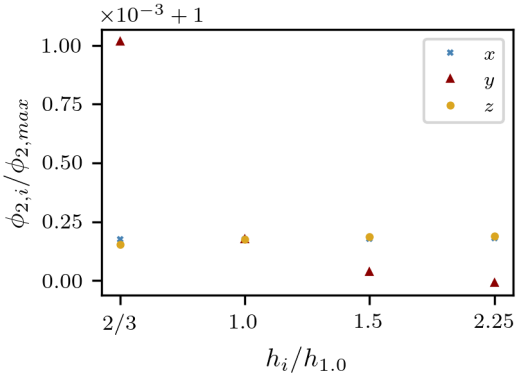

(b) Normalised local parameter where $\phi_2 = \overline{T}_{\text{Centreline}}$.

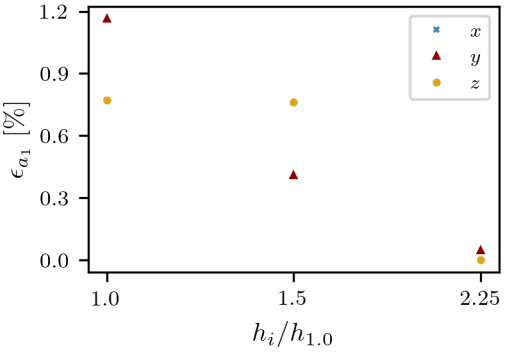

(c) Approximated error for ϕ_1 in percentage.

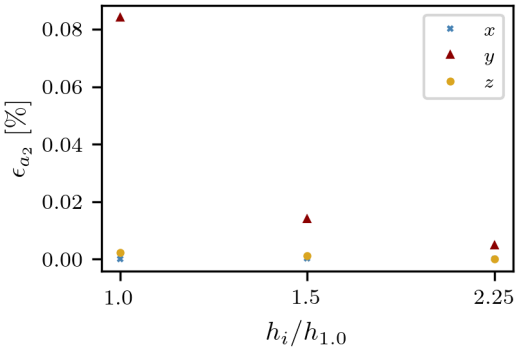

(d) Approximated error for ϕ_2 in percentage.

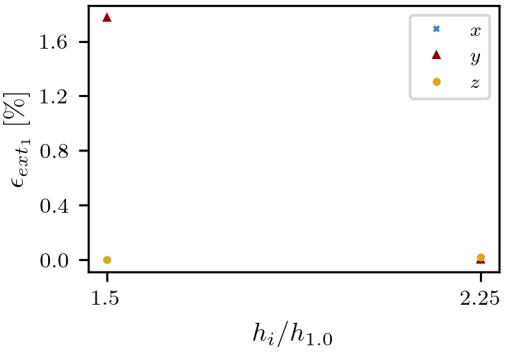

(e) Extrapolated error for ϕ_1 in percentage.

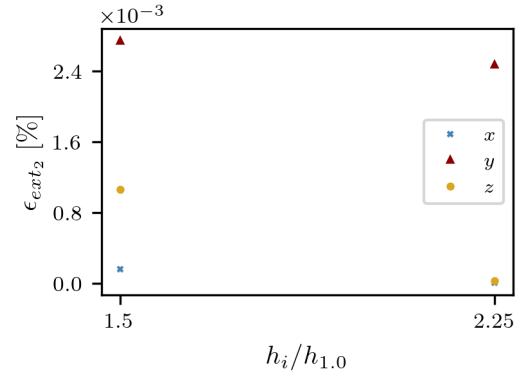

(f) Extrapolated error for ϕ_2 in percentage.

FIGURE 4.6: Grid refinement effects on the global and local parameters for the 3D cases. ϕ_1 is the integral turbulent kinetic energy and ϕ_2 is the mean translational temperature along the centreline. Formulations for (c)–(f) are defined in Equation 2.159–2.161.

4.3.3.2 Symmetry Evaluation

In evaluating the influence of thermo-chemical non-equilibrium in this chapter, the statistical state of the flow plays a crucial role in shaping the conclusions drawn. A symmetry analysis provides insight into the duration over which the turbulence remains symmetric and, in this context, indicates whether the flow is in a deterministic or non-deterministic state. If symmetry is preserved, the flow may be regarded as largely deterministic and repeatable for a given set of initial conditions. Conversely, a loss of symmetry signifies the onset of non-deterministic turbulent behaviour indicating a highly sensitive state, which has important implications for how the flow characteristics should be interpreted.

From the perspective of grid-convergence analysis, non-deterministic turbulence implies that small variations in the grid or initial conditions can lead to noticeable differences in the instantaneous flow fields. In such regimes, time-dependent quantities cannot be used directly for strict pointwise grid-convergence assessment, and care must instead be taken to focus on statistically converged quantities. The significance of this behaviour in relation to the thermo-chemical state of the flow will be further discussed in the following sections.

Figure 4.7 presents the symmetry analysis for the 2D simulations. The quantities examined are the velocity components u and v, the pressure p, and the density ρ. Symmetry is evaluated across the flow domain as indicated in Figure 4.7b, for the case with a refinement factor of 3.375. Three main observations can be made. First, immediately after the initial disturbance is applied, there is a noticeable increase in symmetry error associated with the development of the primary vortex structures. Second, as the grid is refined, the symmetry error decreases slightly, indicating improved numerical accuracy. Third, a comparison between simulations with and without the binomial filter shows that the presence of the filter introduces an additional source of asymmetry.

Figure 4.7c shows the symmetry error of the aforementioned quantities along the y-axis for the first five output times (corresponding to the first five markers in Figure 4.7a), with non-dimensional times of [0.089, 36.1, 72.3, 108.4, 144.5]. In addition to the error introduced by the wall boundary, a distinct kink appears at the location where the binomial filter is applied. This kink represents a discontinuity that propagates through the shear layer. The results clearly show that this discontinuity is the source of the increased symmetry error in the filtered cases when compared with the unfiltered reference (see Figure 4.7a). In all variables, the highest errors occur in the vicinity of the shear layer.

A similar symmetry analysis was conducted for the three-dimensional simulations, using flow conditions consistent with those employed in the 3D grid-convergence study. The results are shown in Figure 4.8.

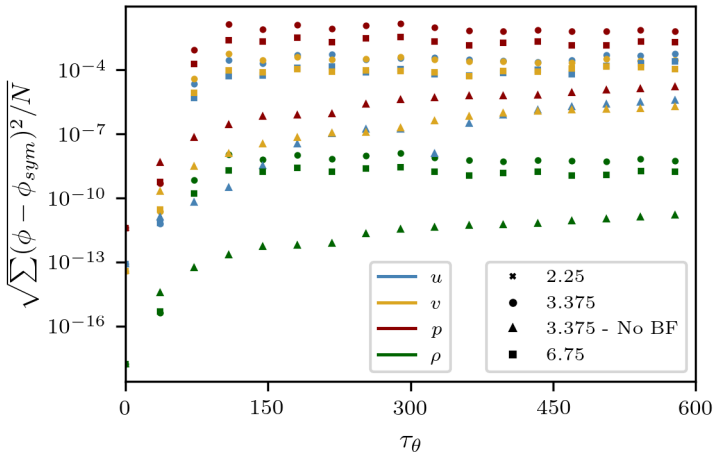

(a) Symmetry analysis across the whole grid.

(b) Sketch of the evaluated regions.

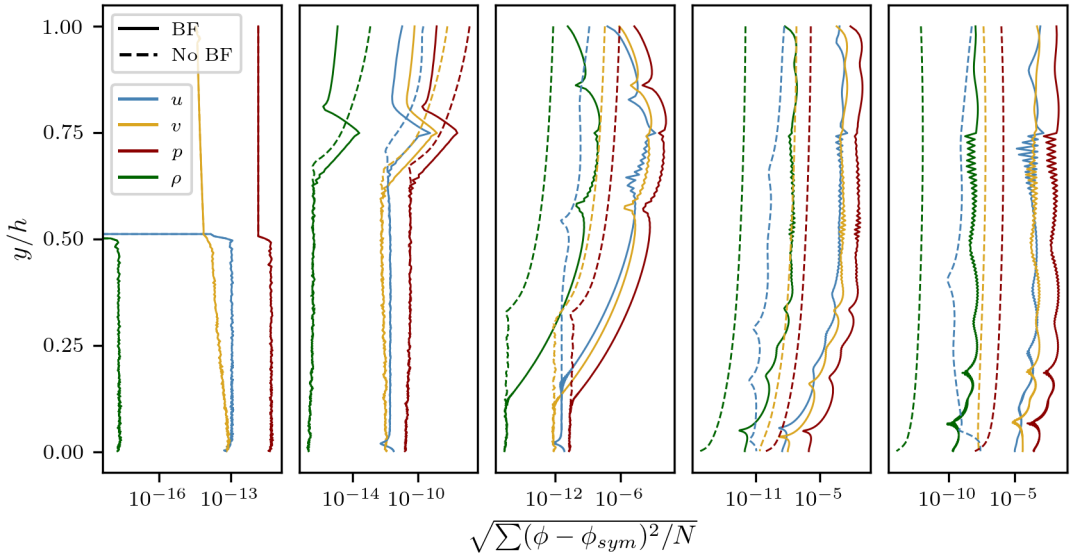

(c) Symmetry analysis along the y-direction for the first five markers in Figure 4.7a.

FIGURE 4.7: Symmetry analysis for the two-dimensional mixing layer cases.

Figure 4.8a shows an initial deviation from a perfectly symmetric state, again associated with the imposed disturbance and the formation of vortex tubes. Following the initial peak in momentum thickness, these large-scale structures begin to break down, leading to a marked increase in asymmetry. As in the 2D case, the difference between filtered and unfiltered simulations is evident: cases without the binomial filter exhibit lower symmetry error, and higher-resolution grids display reduced error compared with coarser grids.

The magnitude of the error also reflects the role of numerical precision. Since the simulations are performed in double precision, quantities with larger absolute values (such as velocity) exhibit higher absolute symmetry errors than quantities like density and pressure. Figure 4.8c confirms that, for the filtered cases, the error across the shear layer is significantly higher, primarily due to the discontinuity introduced at the filter

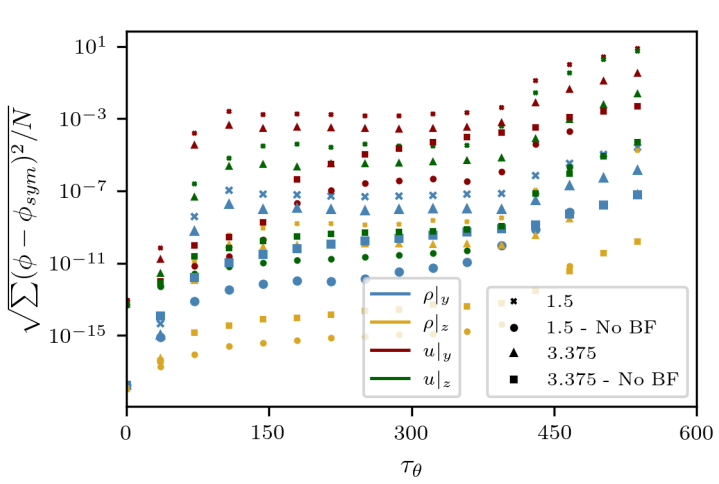

(a) Symmetry analysis across the whole grid.

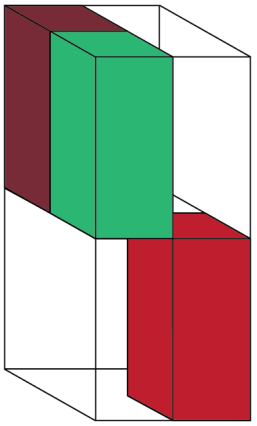

(b) Sketch of the evaluated regions.

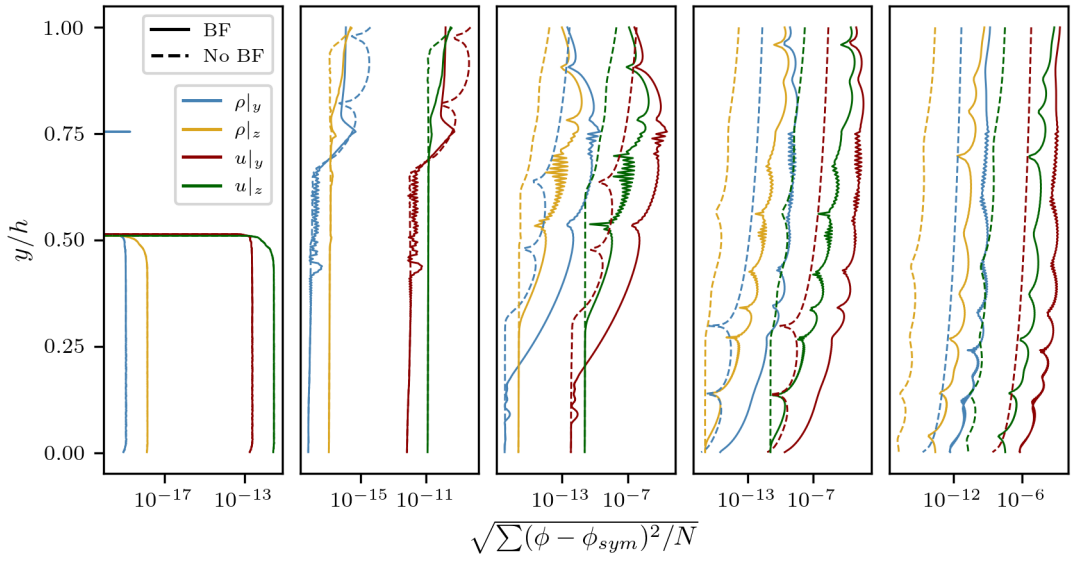

(c) Symmetry analysis along the y-direction for the first five markers in Figure 4.8a.

FIGURE 4.8: Symmetry analysis for the three-dimensional mixing layer cases.

location. Figure 4.8b illustrates the regions used in the evaluation: the green region against the dark red region represents symmetry about the z-axis, while the green region against the lighter red region corresponds to symmetry about the y-axis.

After the initial deviation associated with vortex formation and the binomial filter, the symmetry is further broken at non-dimensional times $\tau_\theta > 400$. This marks the onset of the breakdown of large-scale vortices into smaller turbulent structures and indicates a transition in the character of the turbulence, from a quasi-deterministic to a fully non-deterministic state.

As demonstrated, there are two main sources of the symmetry error observed. The first stems from numerical accuracy, arising from errors in the evaluation of small quantities.

These errors are associated with the application of the binomial filter and the numerical inaccuracies introduced by its use. The second source is the inherently asymmetric nature of turbulence, which is characterised by the flow being in either a deterministic or non-deterministic state.

In summary, the symmetry analysis leads to two main conclusions:

1. The evolution of the mixing layer can be divided into two phases. In the first phase, the turbulent structures are largely deterministic, as indicated by the near-symmetric nature of the flow. In the second phase, once the large-scale structures begin to break down and symmetry is lost, the turbulent flow becomes non-deterministic, meaning small changes in initial conditions or grid resolution can alter the detailed time-dependent behaviour of the flow.

2. For grid-convergence assessment, direct comparison of instantaneous, time-dependent quantities is not meaningful in the non-deterministic phase. As illustrated in Figure 4.8a, deviations in both global and local parameters are expected after the onset of breakdown, irrespective of how fine the grid is.

Mitigating the Error

For simulations in which maintaining symmetry is particularly important, and where the use of a binomial filter is nevertheless required, a modification of the filtering strategy can be employed to reduce the artificial discontinuity. Specifically, the filter can be applied with a spatially varying intensity, forming a smooth gradient rather than a sharp transition. This approach reduces the local discontinuity introduced by finite numerical precision and leads to weaker spurious fluctuations.

To impose the gradient, the filter frequency is multiplied by a spatially varying factor,

$$\eta = 1 - \exp\left(-\left[\frac{y}{a\,\delta_\omega^\circ}\right]^b \Big/ 10.0\right) \quad , \tag{4.31}$$

where a controls the location of the gradient and b determines its sharpness. In the case considered here, $a = 23$ and $b = 16$. Figure 4.9 compares three two-dimensional simulations with a refinement factor of 3.375: one without a binomial filter, one with the standard binomial filter as implemented in OpenSBLI, and one with the binomial filter applied using the gradient factor η. The symmetry error clearly shows that the discontinuity arising from the limitation of numerical precision is substantially mitigated when the gradient formulation is employed (dotted lines). In particular, the initial kink around $y/h \approx 0.75$ observed in the standard filtered case (solid line) is significantly reduced with the gradient approach. Further into the simulation, the symmetry errors across the shear layer in the gradient-filtered case become comparable to those of the unfiltered case (dashed line). The right-hand panel of Figure 4.9 shows the distribution

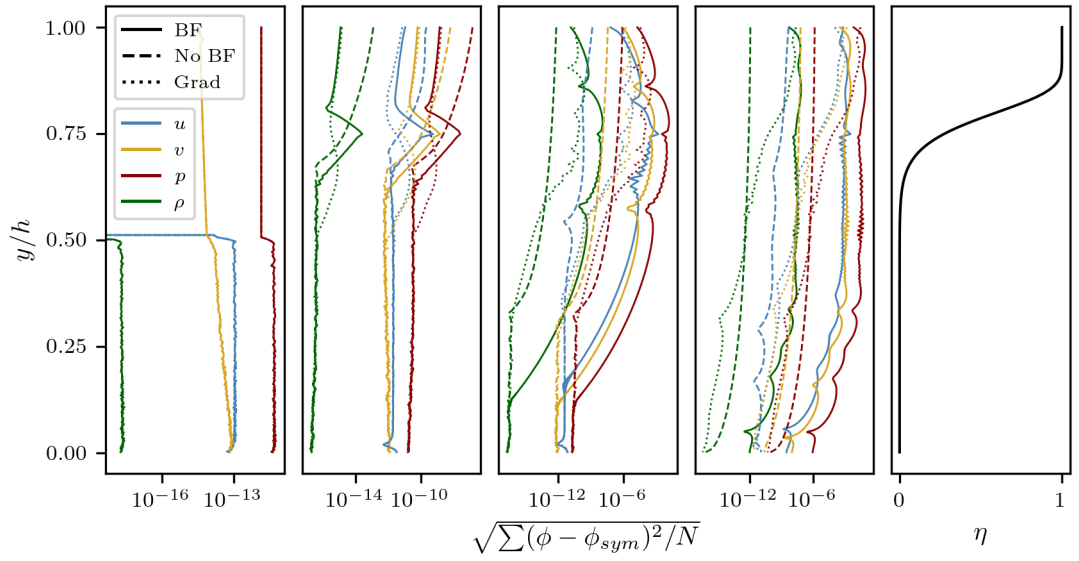

FIGURE 4.9: Symmetry analysis along the y-direction showing the first four output times of a 2D simulation with no binomial filter (dashed), with a standard binomial filter (solid), and with a gradient-applied binomial filter (dotted).

of η across the domain, illustrating the spatial location and magnitude of the modified filter intensity.

Although the gradient method reduces the symmetry error, the small differences observed here have minimal impact on the global characterisation of the flow in the cases considered in this chapter (as will be discussed later). For this reason, and to remain consistent with the default OpenSBLI formulation and facilitate reproducibility, the gradient-based modification was not adopted in the simulations presented in the remainder of this work.

4.4 Simulations

Direct numerical simulations are performed using the flow configurations described in Section 4.2, for two distinct post-shock flow conditions. The first corresponds to a Mach 10 flow under atmospheric conditions at an altitude of 40 km, downstream of a normal shock, yielding a post-shock temperature of 3000 K. In this case, the flow consists of a mixture of diatomic and atomic air species. The second configuration considers a higher post-shock temperature of 6000 K while maintaining the same freestream density. This latter case represents a regime in which vibrational energy is carried predominantly by a single molecular species (N_2).

Both flow conditions are modelled as thermally and chemically reacting mixtures, initialised close to their respective thermal and chemical equilibrium states. Table 4.8 summarises the initial conditions for the low-temperature (LT, $T_\infty = 3000\,\mathrm{K}$) and high-temperature (HT, $T_\infty = 6000\,\mathrm{K}$) cases. The freestream compositions are specified

as [0.053, 0.137, 0.00, 0.772, 0.038] and [0.208, 0.00, 0.227, 0.562, 0.003] for the mass fractions [Y_O, Y_{O_2}, Y_N, Y_{N_2}, Y_{NO}] in the LT and HT cases, respectively. In all simulations, the diffusion model defined in Section 2.4.3.2 and the transport property model defined in Section 2.4.2.4 is employed.

In thermally non-equilibrium flows, the relaxation time governing energy exchange between translational and vibrational modes is the primary factor determining the thermal state of the gas. A longer relaxation time delays vibrational equilibration, while a shorter relaxation time promotes a more rapid return to equilibrium. For the flow conditions considered here, the characteristic flow timescale is small or comparable to the vibrational relaxation timescales. As a result, regions of the mixing layer remain out of equilibrium between translational and vibrational modes throughout its evolution. In contrast, the chemical relaxation timescales are significantly shorter than the flow timescale, meaning that chemical reactions adjust rapidly and the mixture remains close to chemical equilibrium during the development of the mixing layer.

TABLE 4.8: Initial conditions for the low-temperature (LT) and high-temperature (HT) cases.

Case	u_∞ (m/s)	T_∞ (K)	ρ_∞ (kg/m^3)	p_∞ (N/m^2)	dt (s)	δ°_ω (m)	$Re_{\delta^\circ_\omega}$	M_c	Model
LT	439	3000	0.02	18173.66	1.2×10^{-7}	0.004014	400	0.4	TCNE
HT	752	6000	0.02	49271.14	7.0×10^{-8}	0.004170	400	0.4	TCNE

4.4.1 Two-Dimensional Mixing Layer

For each of the specified flow conditions in Table 4.8, two simulations were conducted: one under thermal equilibrium and the other under thermal non-equilibrium, with both simulations incorporating chemical reactions. Figure 4.10 illustrates the two-dimensional mixing layer for the high-temperature flow condition. Each square depicts the same region of the domain, with each row representing different flow properties and each column corresponding to a distinct time of the simulation, shown as the non-dimensional time on the first row. Row (a) displays the passive scalar, a quantity ranging between 1 (upper stream) and -1 (lower stream). The passive scalar serves as an effective tool for observing the progression of the vortex roll-up. Rows (b), (c), and (d) show the pressure, translational temperature, and vibrational temperature, respectively. As the vortex develops, a reduction in pressure and temperature is observed at the vortex core, accompanied by an increase in temperature at the stagnation point.

As sketched in Figure 4.1, regions of expansion and compression emerge within the flow field that can affect the thermal response. Row (e) of Figure 4.10 presents the difference between vibrational and translational temperatures, $T_v - T$, indicating the degree of thermal non-equilibrium in K. As the vortex develops, the core experiences a drop in translational temperature, while the stagnation point exhibits an increase.

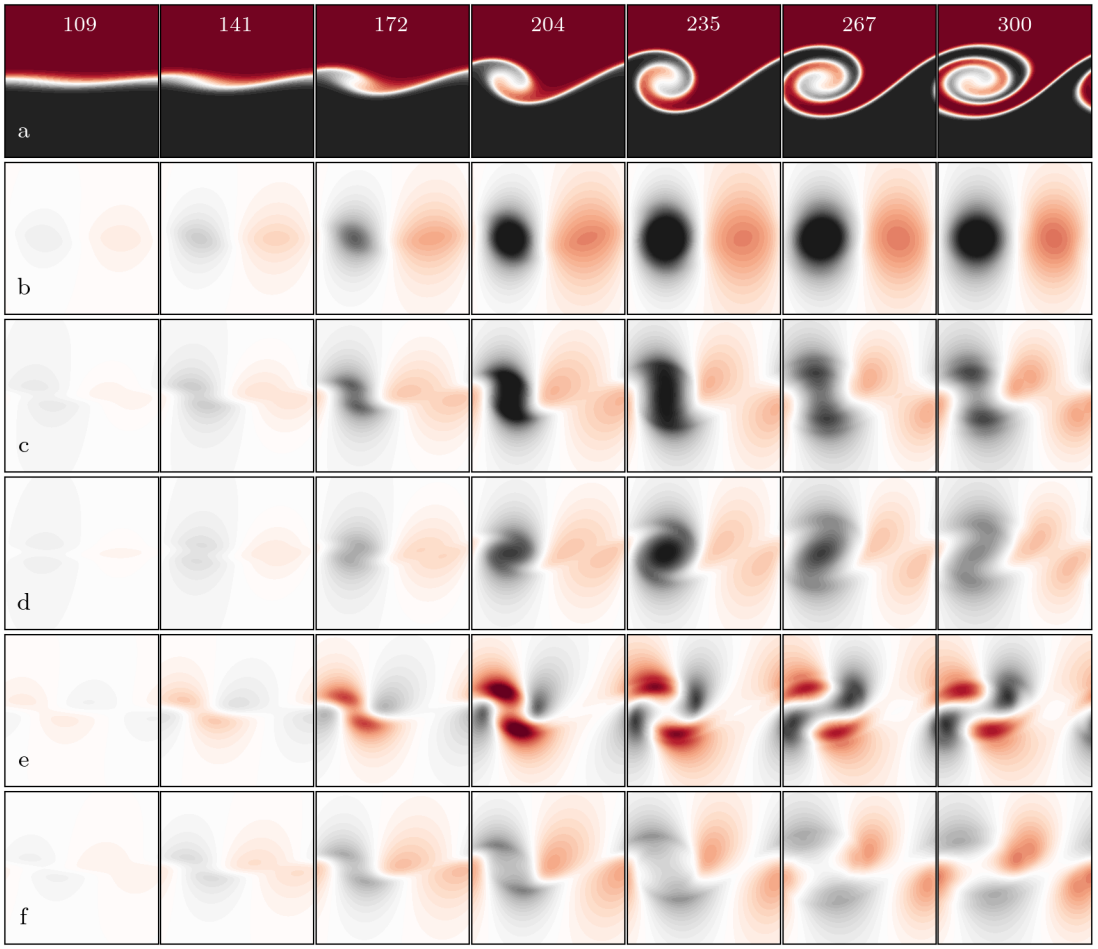

FIGURE 4.10: Two dimensional temporal mixing layer with thermo-chemical non-equilibrium for the HT case, with non-dimensional time τ_θ displayed in the first row. a) passive scalar [min:-1, max:+1], b) pressure in Pa [min:39139, max:59139], c) translational temperature in Kelvin [min:5750, max:6250], d) vibrational temperature in Kelvin [min:5750, max:6250], e) thermal non-equilibrium ($T_v - T$) in Kelvin [min:-130, max:130], f) percentage chemical non-equilibrium of Nitrogen molecules (N_2) [min:-0.004, max:0.004].

Due to the finite energy exchange timescales between translational and vibrational modes, a lag occurs in the vibrational temperature response. This results in regions of hot thermal non-equilibrium, highlighted by red contours, where the vibrational temperature lags behind a reduction in translational temperature, and regions of cold thermal non-equilibrium where it lags behind an increase in translational temperature. Areas of flow expansion (associated with decreasing translational temperature) are associated with a hot thermal non-equilibrium, while areas of compression exhibit a cold thermal non-equilibrium. In this high-temperature case, the vibrational mode is governed solely by Nitrogen molecules. Finally, row (f) depicts the extent of chemical non-equilibrium for Nitrogen molecules, expressed as a percentage (using Equation 2.150). As previously noted, chemical non-equilibrium remains minimal throughout the vortex development due to the significantly shorter timescales of chemical reactions.

Modelling of Vibrational Energy: Single vs. Multi-Species Formulation

A focus of this study is to critically evaluate certain approximations commonly employed in hypersonic flow modelling and to demonstrate the extent to which these simplifications influence the final solution. One such approximation concerns the modelling of vibrational energy in computational simulations, where the transport of vibrational energy is aggregated across all molecular species within the mixture and represented by a single conservation equation. This approach effectively assumes full coupling between vibrational modes, removing the vibrational-vibrational relaxation term, and fundamentally relies on a single approximate relaxation time for translational-vibrational energy exchange. Although this method offers advantages in terms of computational efficiency, it introduces significant approximations into the underlying molecular kinetic theory.

To highlight the differences between employing a single vibrational energy conservation equation and a formulation that accounts for the conservation of vibrational energy for each molecular species individually, the low-temperature flow condition is used, as described in Table 4.8. In this case (in contrast to the HT case) the contribution to the internal energy modes arises from N_2, O_2 and NO molecules. Under these conditions, the impact of averaging relaxation times becomes more pronounced.

Figure 4.11 illustrates the differences between the two kinetic models (single-e_v vs. multi-e_v) in terms of the temperature difference between the translational and vibrational modes. Row (a) presents the passive scalar, while (b) depicts the extent of thermal non-equilibrium for the single-e_v model, and (c) shows the corresponding non-equilibrium $T_v - T$ for the multi-e_v model. The relaxation timescales of the two models differ significantly. The multi-e_v model results in a more highly concentrated non-equilibrium region at the centre of the roll-up, mimicking a thermally frozen state.

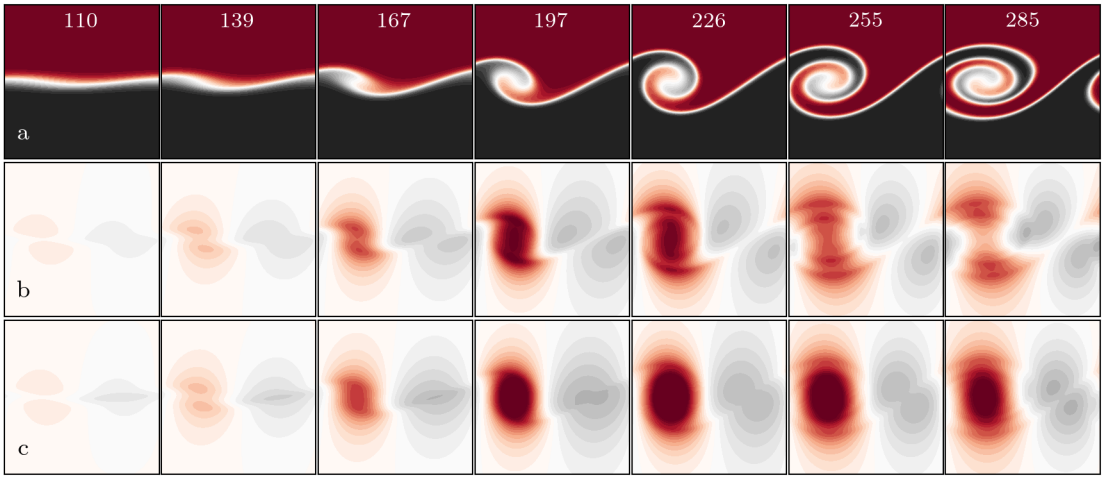

FIGURE 4.11: Mixing layer simulation for the lower temperature (3000 K) case comparing the single to multi vibrational energy conservation equation. a) passive scalar [min:-1, max:+1], b) $T_v - T$ for single-e_v model in K [min:-130, max:130], c) $T_v - T$ for multi-e_v model in K [min:-130, max:130].

This difference in relaxation behaviour arises from how the relaxation time is considered within each model. The multi-e_v model captures the contribution of the slower relaxation associated with N_2, whereas the single-e_v model, due to averaging, skews the relaxation time towards the faster relaxation characteristic of O_2. When considering the higher mass fraction of N_2, this averaging approach leads to an underestimation of Nitrogen's contribution to the energy exchange between translational and vibrational modes. It should be noted that the governing equations defined for the multi-e_v model do not account for vibrational-vibrational energy exchange. Therefore, the differences observed reflect a scenario in which inter-species relaxation is considerably slower relative to translational-vibrational modes. In this scenario, the discrepancies are significant. In terms of computational cost, the single-e_v model was found to provide savings of less than $\sim 3\%$ in run time compared to the multi-e_v model, so the only drawback of the multi-e_v model is the increased storage associated with having a transport equation for each molecular species. In the present cases this increases the number of equations (including the passive scalar) from 11 to 13.

While the qualitative description of thermal non-equilibrium for the LT case (Figure 4.11) with the single-e_v model is closer to that described earlier for the high-temperature case (Figure 4.10e), the development is distinct. Following the initial departure from equilibrium at the core and stagnation point, the non-equilibrium state persists and intensifies as the vortex continues to roll up. This leads to a higher region of hot non-equilibrium within the vortex core, alongside a cold non-equilibrium state in the stagnation region. This is consistent with the previous comments that the use of a single vibrational energy conservation equation in this case results in a faster overall relaxation timescale, leading to an underestimation of the influence of thermal non-equilibrium.

Qualitative and Quantitative Analysis

The two flow conditions examined (LT and HT, comparing Figure 4.10 and Figure 4.11) demonstrate distinct qualitative characteristics of thermal non-equilibrium within the flow field. In one case (Figure 4.10e), a mixture of cold and hot non-equilibrium regions forms a quadrupole-like pattern around the vortex, where the thermal state responds to flow kinetics by reacting to compression and expansion, respectively. In contrast, Figure 4.11c shows that the thermal energy exchange is too slow to respond effectively to regions of compression and expansion within the flow field, resulting in a thermally hot vortex core, i.e. the free-stream flow is fully entrained before it is able to relax to match the translational temperature. Across the simulated cases, three primary regions can be identified where the flow departs from equilibrium: the entrainment region, the vortex core, and the stagnation point. When the relaxation time is shorter, these regions tend towards equilibrium. Conversely, when the relaxation time is sufficiently long to induce a thermally frozen state, these regions remain in a non-equilibrium condition throughout the flow evolution.

TABLE 4.9: Vibrational Damköhler numbers for molecules and for the mixture.

	Da_{O_2}	Da_{N_2}	Da_{NO}	Da_v
LT	0.1169	0.0028	0.0238	0.0187
HT	1.0931	0.0909	0.3811	0.0909

Vibrational Damköhler numbers based on the initial mixing layer momentum thickness (see Section 2.5.3) are shown in Table 4.9. The absolute values are not as important as the relative magnitudes. For example, if we used a characteristic roll-up time of the vortex, from the start of non-linear growth of disturbances up to non-linear saturation, the numbers would be two orders of magnitude higher. For the most important molecular contributor, Da_{N_2} is a factor of 30 higher for the HT case. It can also be seen that the mixture Da is also much higher for the HT case. These relative values are consistent with the HT case being in non-equilibrium and the LT case (with the multi-e_v model) being closer to frozen.

Overall, the effects of free stream temperature and thermal non-equilibrium on the mixing layer evolution are not large. Figure 4.12a shows the momentum thickness (normalised

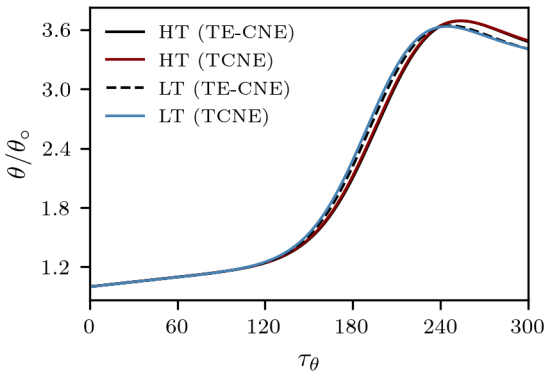

(a) Normalised momentum thickness as a function of non-dimensional time.

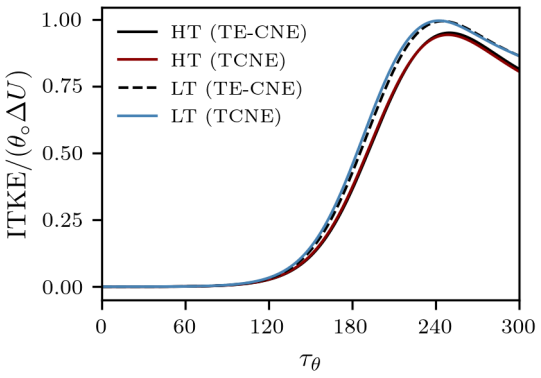

(b) Integral of turbulent kinetic energy as a function of non-dimensional time.

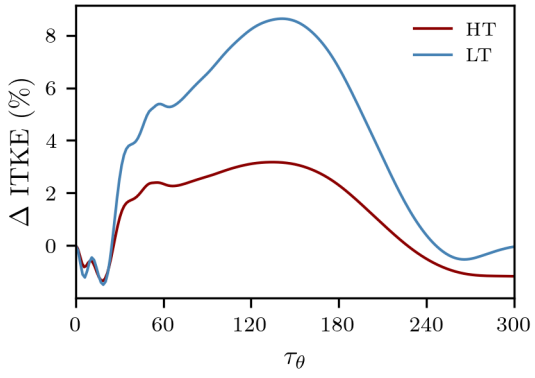

(c) Difference in ITKE between equilibrium and non-equilibrium cases.

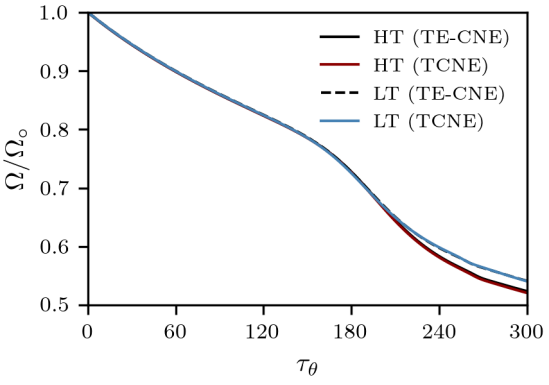

(d) Normalised integral of enstrophy (Ω) as a function of non-dimensional time.

FIGURE 4.12: Flow properties of the two-dimensional LT and HT cases.

with its initial value) as a function of the normalised time given by Equation 4.9 for the LT and HT cases, each carried out for thermal equilibrium (TE-CNE) and thermo-chemical non-equilibrium (TCNE) conditions. Both conditions use the multi-e_v formulation as defined in Section 2.1.1. The HT case shows a slightly delayed increase in mixing layer thickness due to vortex roll-up. Figure 4.12c shows the percentage difference in the spatial integral of turbulence kinetic energy (ITKE) between the equilibrium (TE-CNE) and thermal non-equilibrium (TCNE) flow states, as defined in Section 2.5.3 — showing an increase of approximately 4% for the HT case and 8% for the LT case. Thermal non-equilibrium causes an increase in turbulence kinetic energy (TKE) relative to equilibrium state, consistent with the slightly earlier rise in momentum thickness. It should be noted, however, that the reduction in TKE after the momentum thickness peak where the vortex breakdown starts may not be fully representative in a two-dimensional simulation due to confinement in the z-axis. This aspect is therefore examined further in the three-dimensional simulations.

4.4.2 Three-Dimensional Mixing Layer

Three-dimensional (3D) simulations were conducted for the same flow conditions specified in Table 4.8 to assess whether the conclusions drawn in the previous section regarding thermal non-equilibrium extend to fully three-dimensional flows. All cases employed the multi-e_v formulation, with initial conditions consistent with those defined earlier. Periodic boundary conditions were applied along the lateral (homogeneous) directions, while first-order extrapolation boundary conditions combined with a binomial filter were imposed at the top and bottom boundaries to prevent acoustic waves from reflecting back into the shear layer. The filter strength was set to $\beta = 0.25$, and a second-order binomial filter was used.

Figure 4.13 illustrates the flow development in the three-dimensional domain. The top row corresponds to the LT case, the bottom row to the HT case, and each column to a different stage in the vortex roll-up, at non-dimensional times $\tau_\theta = 200,\ 300$, and 500. Iso-surfaces of the Q-criterion at 1.0×10^{10} and 2.0×10^{10} are shown, coloured by $T_v - T$ to indicate the local degree of thermal non-equilibrium (in K).

Following the introduction of the initial disturbance, oblique-mode instabilities give rise to the formation of vortical tubes within the shear layer. These inclined vortex tubes deform into hairpin-like vortices (Moin et al., 1986), with the same structure on the lower side due to a cross-stream symmetry of the initial disturbance. The evolution of the vortices is accompanied by regions of thermal non-equilibrium. Consistent with the two-dimensional simulations, the slower thermal relaxation in the LT case results in persistent regions of hot thermal non-equilibrium throughout the vortex roll-up, extending from the core to the point of breakdown. In contrast, the faster relaxation in the high-temperature case produces a combination of cold and hot thermal non-equilibrium around the vortical

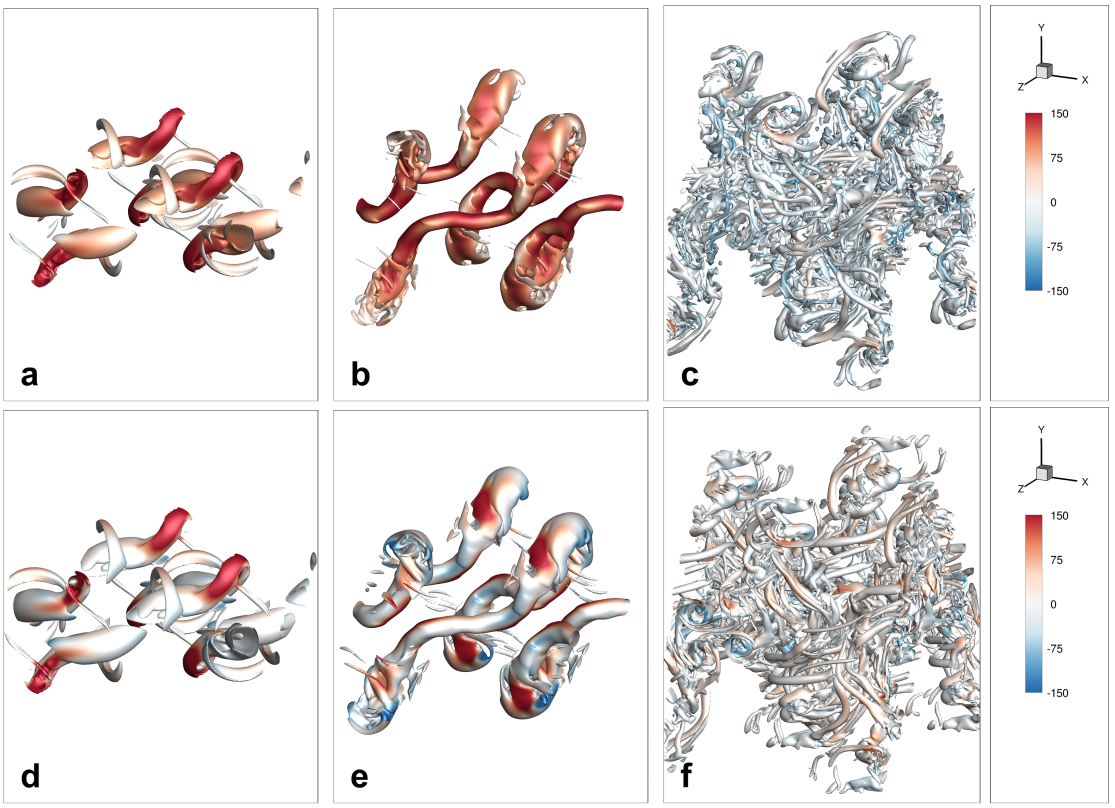

FIGURE 4.13: Iso-surfaces of the Q-criterion for a three-dimensional, temporally developing mixing layer, coloured by $T_v - T$. (a)–(c) correspond to the LT case and (d)–(f) to the HT case, at $\tau_\theta = 200,\ 300$, and 500, respectively.

tubes. As the hairpin head develops, flow is accelerated and the translational temperature reduces, generating a hot thermal non-equilibrium region, while compression on the lower side leads to the formation of a cold non-equilibrium, shown in blue on Figure 4.13(e).

Quantitative Analysis

These observations extend the findings from the two-dimensional simulations, indicating that the formation of non-equilibrium regions is strongly governed by local compression and expansion, whereas the persistence of these regions within the flow depends on the thermal relaxation time. This behaviour is consistent with the results of Fiévet et al. (2019), who showed that vibrational non-equilibrium can be driven by compressibility effects, although the authors also showed thermal relaxation does not always follow the Landau-Teller model. Similar behaviour, in which thermal non-equilibrium is sustained by turbulence, has been reported in other flows (Passiatore et al., 2023, 2022; Khurshid and Donzis, 2019). According to the Kolmogorov cascade, one can speculate that the small-scale motions would have shorter time scales and become more thermally frozen, but this is not seen in the present low Reynolds number simulations. Instead, following the development of the hairpin vortex head, the vortices break down and small-scale

structures continue to exhibit varying non-equilibrium states, maintaining the qualitative characteristics identified earlier.

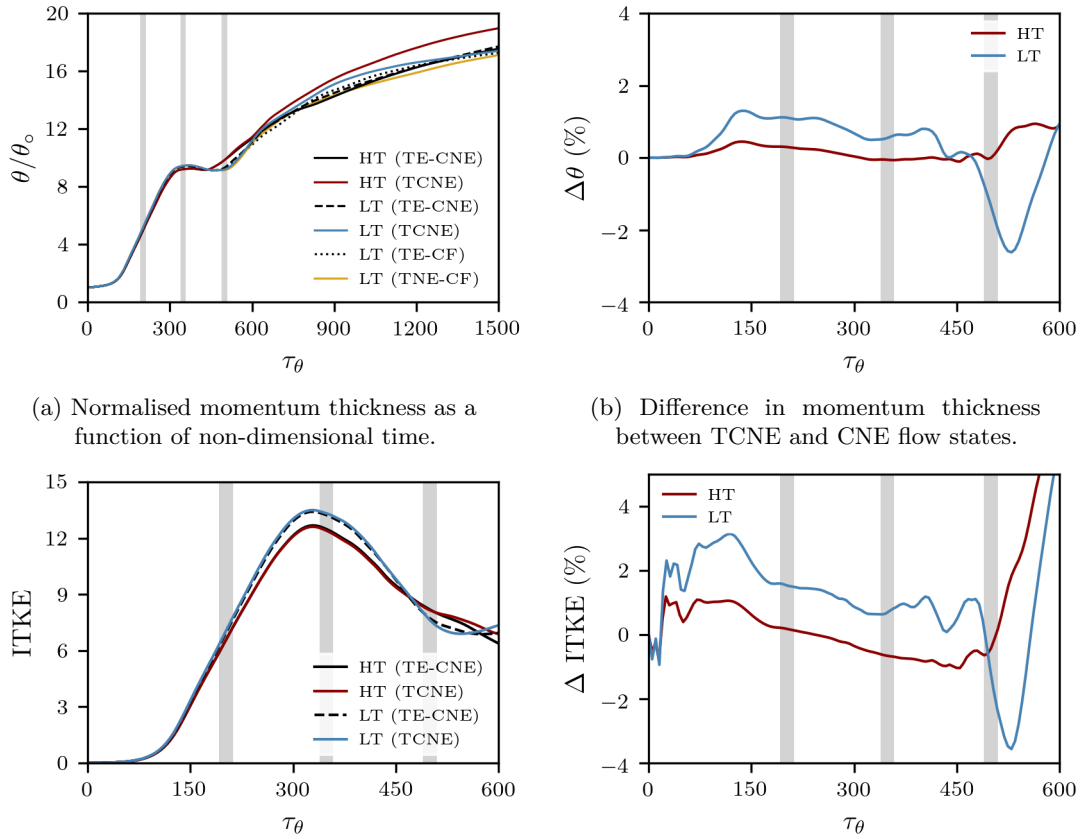

(a) Normalised momentum thickness as a function of non-dimensional time.

(b) Difference in momentum thickness between TCNE and CNE flow states.

(c) Integral of turbulent kinetic energy as a function of non-dimensional time.

(d) Difference in ITKE between TCNE and CNE flow states.

FIGURE 4.14: Flow properties for the three-dimensional LT and HT cases under CNE and TCNE conditions.

Figure 4.14a shows the evolution of momentum thickness for the three-dimensional cases, with vertical bars used to identify averaging zones to be discussed later. As observed in previous studies (Rogers and Moser, 1994; Pantano and Sarkar, 2002; Vreman et al., 1996), the momentum thickness exhibits an initial region with a high growth rate. The peak in momentum thickness at $\tau_{\theta_0} \approx 350$ is associated with the non-linear saturation of the hairpin vortex. Subsequently, the momentum thickness starts to grow again, driven only by small-scale structures, since the shear layer has grown and the relative size of the computational box is no longer large enough to sustain oblique-mode instabilities at large scale. The influence of thermal non-equilibrium in the early stages of hairpin vortex development is small.

The divergence of the curves at later times is partly due to the amplification of small differences in initial conditions, which leads to distinct trajectories in the phase space of the non-linear system. That the present system behaves in this manner was demonstrated by the symmetry breaking discussed in Section 4.3.3.2. In addition, for the LT case, the flow is sensitive to the chemical modelling (frozen versus non-equilibrium), and the

chemistry itself is sensitive to the thermal state (equilibrium versus non-equilibrium). Improved statistical convergence could be obtained either by ensemble-averaging over multiple simulations with slightly perturbed initial conditions, or by running simulations in larger domains with randomised initial disturbances. The former is not pursued here, while the latter is investigated in Section 4.4.3.

Figure 4.14d presents the percentage difference in the integral of turbulent kinetic energy (ITKE) between the equilibrium and non-equilibrium simulations. As in the two-dimensional cases, ITKE increases during the development of the mixing layer, although the magnitude of the CNE-TE and TCNE differences is smaller. At later times ($\tau_\theta > 500$), larger variations appear. As with the momentum thickness, these are attributed to the non-linear amplification of small discrepancies from earlier stages of the evolution. While the magnitude and intensity observed in Figure 4.14d do not match those of the two-dimensional counterpart (Figure 4.12c), this is expected due to the differing nature of the flow structures. In the two-dimensional case, the flow is confined to a plane, with the entire core and entrainment contributing to the mixing process. In contrast, the three-dimensional case involves vortex tubes with associated upwash and downwash regions, leading to a more complex redistribution of energy and momentum.

Statistical Analysis

Turbulence statistics are shown in Figure 4.15. To obtain smoother profiles, averages were computed using six flow fields within three time intervals, centred at $\tau_\theta = 200,\ 350,$ and 500, corresponding to the shaded regions in Figure 4.14a and Figure 4.14d.

Figure 4.15a–4.15d present the non-dimensional Reynolds stresses corresponding to the normal and shear components arising from momentum transfer by the fluctuating velocity field. The normal stresses exhibit increased fluctuations in the central region of the shear layer, associated with the formation of vortex tubes. As the hairpin vortex heads develop, a splitting of the peak in $\bar{\rho}\,\widetilde{u'u'}/(\rho_\infty \Delta u_\infty^2)$ is observed. By contrast, a strong single peak along the centreline is seen in $\bar{\rho}\,\widetilde{v'v'}/(\rho_\infty \Delta u_\infty^2)$ in Figure 4.15b, whereas $\bar{\rho}\,\widetilde{w'w'}/(\rho_\infty \Delta u_\infty^2)$, shown in Figure 4.15c, exhibits a transient reduction in lateral fluctuations.

The shear stress (Figure 4.15d) spreads progressively in the y-direction and decreases as the shear layer grows. The influence of thermal non-equilibrium on the Reynolds stresses is minimal during the vortex development and the initial peak in momentum thickness (up to $\tau_\theta = 350$). Although the effects are small in the present case, experimental studies of channel flows with plasma heating have reported reductions of up to 50% in Reynolds stress (Fuller et al., 2014). In flows where higher vibrational modes are significantly excited, more sophisticated relaxation models (Fiévet et al., 2019) are therefore likely to be required.

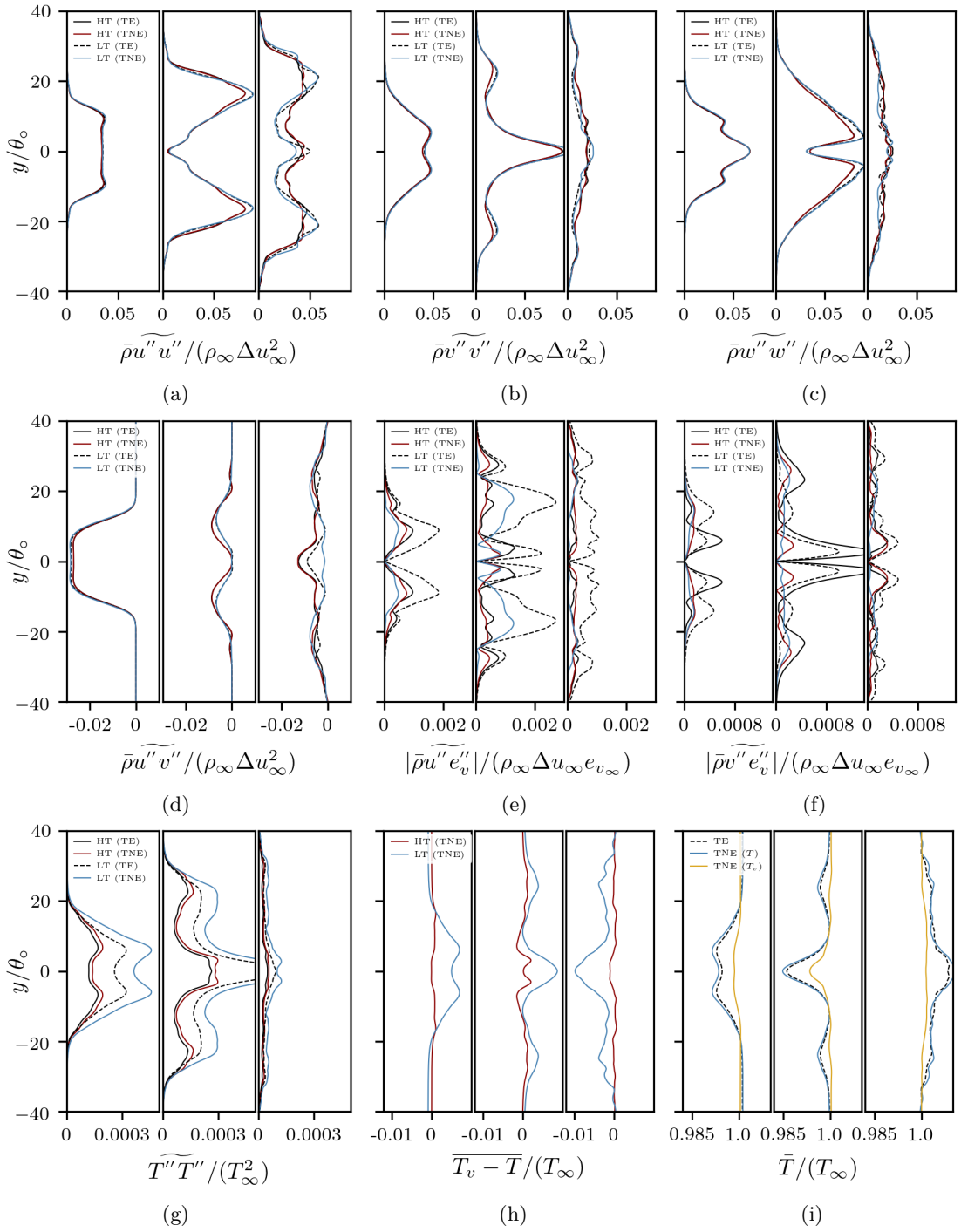

FIGURE 4.15: Turbulence statistics for the three-dimensional mixing layer, showing Reynolds stresses, vibrational energy fluxes, temperature fluctuations and mean temperatures across the shear layer. All cases are chemically reacting (CNE).

Turbulence introduces additional flux terms in the vibrational energy equation. Figure 4.15e and Figure 4.15f show two such fluxes, for which clear differences emerge between the equilibrium and non-equilibrium cases. In both, thermal non-equilibrium reduces vibrational fluctuations across the shear layer. This behaviour can be interpreted as a damping of peak fluctuations due to the weaker coupling of the vibrational mode relative to the translational mode, such that the vibrational temperature does not fully inherit the variability present in the translational temperature field. Figure 4.15g presents the translational temperature fluctuations, $\widetilde{T'T'}/T_\infty^2$, which increase in the presence of thermal non-equilibrium.

In the present mixing-layer configuration, the vortex core is characterised by a reduced translational temperature, and this cooling is amplified under non-equilibrium conditions. The resulting stronger gradients in translational temperature play a role in enhancing transport by fluctuating terms. Thermal non-equilibrium within the flow field has previously been attributed to translational temperature fluctuations (Fiévet et al., 2019; Passiatore et al., 2022; Williams et al., 2025; Neville et al., 2015). This is confirmed by comparing Figure 4.15g and Figure 4.15h, where the profiles of the averaged non-equilibrium correlate closely with those of the temperature fluctuations. In Figure 4.15h, the high-temperature case exhibits steeper gradients across the shear layer, which may be associated with the coexistence of hot and cold non-equilibrium regions that partially offset one another when averaged.

Figure 4.15i shows the mean translational and vibrational temperatures across the shear layer for the low-temperature case. As expected, the mean translational temperature is reduced in the central region, reflecting cooling in the vortex cores. Comparing equilibrium and non-equilibrium cases reveals a further reduction in the mean translational temperature under non-equilibrium conditions, together with a corresponding increase in the mean vibrational temperature (in TE, $T_v = T$). This behaviour is attributed to the slower vibrational relaxation in the LT case, which prolongs energy exchange between translational and vibrational modes. As a result, the vibrational mode retains a larger fraction of the total energy, further lowering the translational temperature relative to its equilibrium counterpart. Reductions in mean translational temperature have also been reported in other studies of compressible shear layers (Neville et al., 2015); however, in that case the central region of the mixing layer was hotter than the free stream, whereas here it is cooler. Consequently, in the present case the temperature difference between the centre and the free stream is increased, whereas in Neville et al. (2015) it is reduced. In both scenarios, the temperature fluctuations scale with the magnitude of the temperature difference between the mixing-layer centre and the free stream. Both behaviours are physically plausible, for instance depending on whether the mixing layer develops behind a splitter plate with adiabatic or cooled-wall conditions.

While the emergence of non-equilibrium states is inherently governed by the relative timescales of the flow and the internal energy modes, the present findings highlight an

additional mechanism: the coupling between thermal non-equilibrium and turbulent fluctuations. This source is fundamentally distinct from other well-documented non-equilibrium scenarios, such as post-shock relaxation, where the timescale misalignment arises from the near-instantaneous change in the flow state imposed by the shock. In the present configuration, non-equilibrium is instead sustained and amplified by the fluctuating velocity and temperature fields associated with turbulence, representing a turbulence-driven pathway to non-equilibrium that warrants separate consideration.

Energy Budget

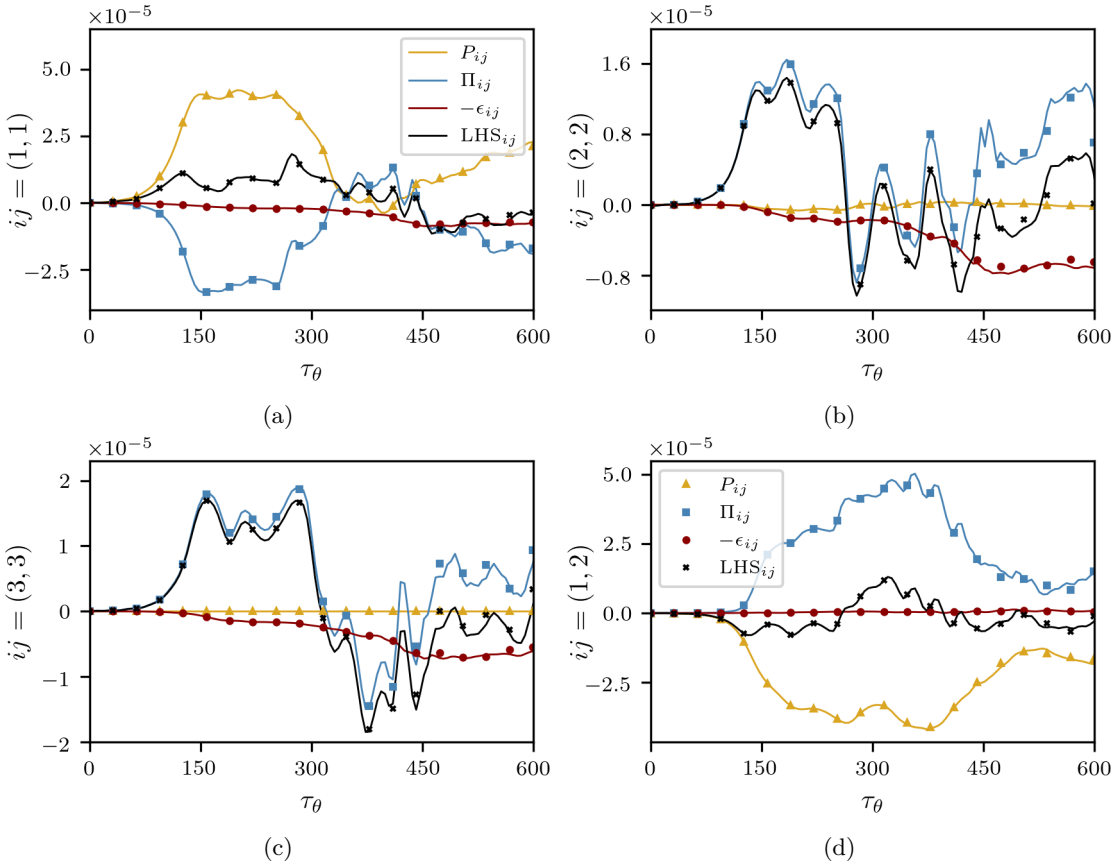

FIGURE 4.16: Energy budget for the LT case. Solid lines denote the CNE case and markers denote the TCNE case. P_{ij} is the integrated production, Π_{ij} is the pressure-strain term, $-\epsilon_{ij}$ is the dissipation, and LHS is the integrated Reynolds stress, $\frac{d}{dt}\int \overline{\rho u_i'' u_j''}\, dy$.

Figure 4.16 shows the temporal evolution of the terms in the energy budget for the LT case, using the formulation given in Equation 4.22–Equation 4.25. Each subfigure corresponds to a different Reynolds-stress component; the $(1,3)$ and $(2,3)$ components are omitted as they are negligible for the present configuration. Colours denote the contributions of different terms to the integrated Reynolds stresses, while markers indicate the corresponding quantities for the TCNE case.

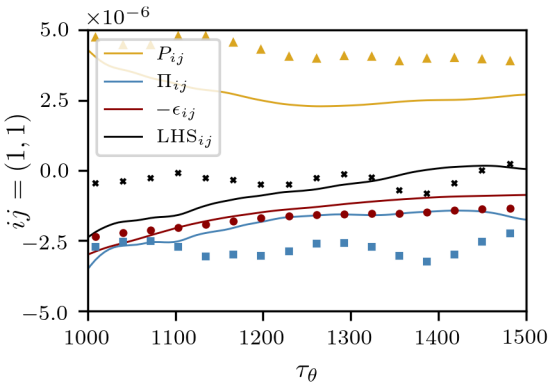

FIGURE 4.17: Energy budget for the $(1,1)$ component at later times in the LT case.

During the initial growth of the momentum thickness ($\tau_\theta \approx 150$–300), both the growth rate and the integrated production remain approximately constant, consistent with the self-similar regime implied by Equation 4.8. In this stage, the differences between CNE and TCNE are small, mirroring the modest differences observed in ITKE (Figure 4.14d). The pressure–strain term is negative for the $(1,1)$ component and positive for the $(2,2)$ and $(3,3)$ components, indicating redistribution of turbulent kinetic energy from the streamwise fluctuations into the cross-stream and spanwise components (Vreman et al., 1996).

As the flow evolves beyond $\tau_\theta \gtrsim 300$, small-scale turbulence develops and the layer departs from the near-linear growth regime. The direct link between growth rate and integrated production then weakens, and the influence of non-linear interactions becomes more pronounced. This is reflected in the gradual divergence between the CNE and TCNE curves, again consistent with the sensitivity to initial conditions and symmetry breaking discussed in Section 4.3.3.2. In the later stages of the simulation ($\tau_\theta \approx 1200$–1500), dissipation becomes comparable in magnitude to production and pressure–strain, signalling a regime dominated by small-scale motions and enhanced viscous and thermal effects.

Figure 4.17 focuses on the $(1,1)$ component in the late-time regime. The figure shows that, at these times, the dissipation term makes a substantial contribution to the balance of the streamwise Reynolds stress, approaching the combined magnitude of production and pressure–strain. This behaviour is characteristic of a flow in which large-scale structures have largely broken down, and the remaining dynamics are governed by the cascade of energy to the smallest dynamically relevant scales, where viscous dissipation ultimately dominates.

4.4.3 Three-Dimensional Large-Domain Pairing Mixing Layer

When studying mixing layers, as discussed at the beginning of this chapter, simulations of vortex pairing have been carried out since the early DNS studies (Moser and Rogers,

1991). While the focus so far has been on the development of a single vortex, a pairing case complements the previous results by providing a slightly different route to turbulence. The larger-scale interaction between individual vortices leads to a more coherent transition to small-scale turbulence and, for a sufficiently large domain (enhancing the degree of random interaction), to a more statistically homogeneous and well-spread turbulent field.

Most importantly, pairing shear-layer simulations allow the flow to become closer to a self-similar phase, characterised by the absence of large-scale organised pairings, the absence of strong streamwise vortices in the braid region, and a sustained linear growth of the mixing layer (Rogers and Moser, 1994). These features lead to smoother averaged profiles, which in turn provide a cleaner and less noisy basis for statistical evaluation across the shear layer.

Only the low-temperature flow condition was considered for this configuration, as it is more susceptible to thermo-chemical non-equilibrium effects. Table 4.10 summarises the domain parameters for the simulation. Compared with the earlier three-dimensional setup, the streamwise extent L_x is increased by a factor of four and the spanwise extent L_z by a factor of two, allowing approximately eight primary vortices to develop within the domain. The grid resolution (N_x, N_y, N_z) was selected based on the grid studies presented in Section 4.3.3.1, where the number of grid points in the x- and z-directions was increased by factors of four and two, respectively, relative to the acceptable resolution for a single vortex roll-up, consistent with the number of vortices initially designed to form. The multi-e_v model is employed for all cases; for chemically reacting simulations, the SCEBD diffusion model is used, while the newly developed efficient transport-property model (discussed in Chapter 5) is adopted to mitigate the increased computational cost associated with the larger domain.

Table 4.10: Domain properties for the three-dimensional pairing cases.

$N_x \times N_y \times N_z$	β	$L_x \times L_y \times L_z$
800×875×400	2.0	$60\delta^\circ_\omega \times 90\delta^\circ_\omega \times 30\delta^\circ_\omega$

To promote vortex pairing and generate the desired small-scale turbulence, the initial disturbance was modified. In addition to the base perturbation used previously to generate a well-defined primary roll-up, subharmonic disturbances were introduced to trigger pairing, and random waves were superimposed to prevent the persistence of large, coherent structures and strongly organised pairings. The initial normal velocity containing the disturbance was defined as

$$v = a\, u_\infty\, \zeta_{KH} + b\, u_\infty\, \zeta_{Rand} \quad , \tag{4.32}$$

where a and b are constants defining the magnitude of the disturbance defined in percentage of the free-stream, ζ_{KH} represents the Kelvin–Helmholtz instability with

added subharmonics, and ζ_{Rand} is the random phase field, given by

$$\zeta_{KH} = \exp\left(-\frac{(y/\delta_\omega)^2}{10}\right)\left[\sum_{n\in\{2,4,8\}}\sin\left(\frac{2\pi nx}{L_x}\right)\sum_{m\in\{2,4\}}\sin\left(\frac{2\pi mz}{L_z}\right)\right] \quad , \tag{4.33}$$

$$\zeta_{Rand} = \exp\left(-\frac{(y/\delta_\omega)^2}{8}\right) \times\left[\sum_{n\notin\{2,4,8\}}\sum_{m\notin\{2,4\}}A_{nm}\cos\left(\frac{2\pi nx}{L_x}+\phi_{nm}\right)\cos\left(\frac{2\pi mz}{L_z}+\theta_{nm}\right)\right] \quad , \tag{4.34}$$

where ϕ_{nm} and θ_{nm} are random phases. The wavenumbers m and n for the random disturbance were chosen to exclude those used in ζ_{KH}, in order to avoid contaminating the primary roll-up. By varying the combinations of the disturbance magnitude used (a and b), the degree to which the flow is shifted out of equilibrium during the initial development can be controlled. The larger a is (for ζ_{KH}), the higher the inertial motion is and hence it encourages the development of non-equilibrium regions throughout the flow field. On the other hand, if b is dominating (for ζ_{Rand}), the sooner random disturbances start to devolve and hence the weaker the inertial forces for the vortex tubes are to take the flow out of equilibrium.

To evaluate this, two cases were conducted in which the same initial disturbance configuration was imposed, with only the disturbance magnitude varied. Both cases were simulated under thermo-chemical non-equilibrium conditions using the same configuration described earlier. Figure 4.18 presents the momentum thickness for each case, overlaid with the difference in the degree to which the flow departs from equilibrium throughout the simulation.

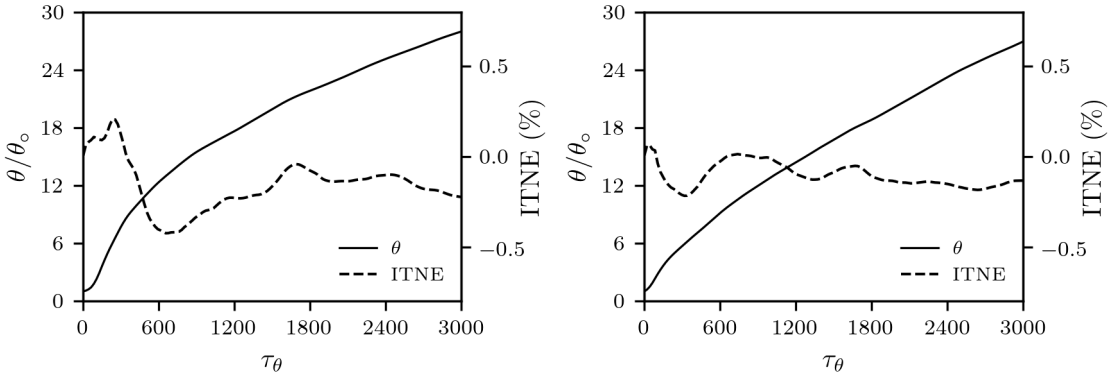

(a) Integral of thermal non-equilibrium across the simulation for Case A ($\zeta_{KH} = 0.05$).

(b) Integral of thermal non-equilibrium across the simulation for Case B ($\zeta_{KH} = 0.02$).

FIGURE 4.18: Momentum thickness evolution over the simulation, overlaid with the degree of thermal non-equilibrium, for two pairing cases with different initial disturbance magnitudes.

When comparing Figure 4.18a (hereafter Case A) and Figure 4.18b (hereafter Case B), clear differences are observed in the momentum-thickness evolution. For Case A, the

initial stage is characterised by the development of large-scale vortex tubes driven by the Kelvin–Helmholtz instability, during which a linear growth is observed ($50 < \tau_\theta < 400$). This is followed by a breakdown of the large-scale structures, where an approximately linear growth persists but at a reduced rate ($400 < \tau_\theta < 800$). The growth rate then gradually stabilises as the large-scale structures fully disintegrate, leading towards a more homogeneous small-scale turbulent state. Based on a preliminary assessment using momentum thickness alone, the fully self-similar region appears to be reached at approximately $\tau_\theta > 1800$. The thermal state of the flow exhibits a strong correlation with the momentum-thickness evolution, similar to that observed in the single-vortex simulations discussed in Section 4.4.2. During the initial stages, where inertial effects are dominant ($50 < \tau_\theta < 400$), the flow is driven out of thermal equilibrium. As the large-scale structures break down and dissipate, energy is transferred from the vibrational mode to the translational mode, resulting in a clear change in the sign of the thermal non-equilibrium indicator. Beyond this stage, the flow predominantly resides in a thermally cold state.

For Case B, in which random disturbances dominate, the initial phase of large-scale structure development is considerably shorter, lasting only for $\tau_\theta < 150$. This is followed by an extended breakdown phase of these structures ($150 < \tau_\theta < 700$). Subsequent growth continues at a more constant rate compared with Case A. A comparison of the momentum-thickness evolution between the two cases suggests that a rough self-similar state is reached earlier in Case B. In contrast, examination of the thermal state indicates that Case A is driven further out of equilibrium than Case B. This difference is attributed to the stronger initial inertial motion of the vortices in Case A and their enhanced ability to shift the flow field away from thermal equilibrium.

In view of these observations, the statistical analysis presented in this section is based on the second configuration (Case B), which corresponds to the lower Kelvin–Helmholtz disturbance magnitude, ζ_{KH}. Although thermo-chemical effects are weaker in this case (see Figure 4.18b), the earlier onset and clearer manifestation of self-similar behaviour provide a more robust and interpretable statistical basis for assessing the influence of thermal non-equilibrium on the mixing layer. Overall, the larger pairing domain yields smoother and more consistent statistics than the single-vortex configuration, while the lower-ζ_{KH} case remains closer to a fully self-similar state.

When conducting the simulations, all statistical evaluations and analyses for this configuration follow the same procedures as those employed for the three-dimensional cases described in Section 4.4.2. To isolate the effects of thermal non-equilibrium, and to provide a contrast with the single-vortex simulations presented earlier, the pairing simulations examined here are restricted to thermal non-equilibrium while remaining chemically frozen. The initial conditions for the simulations are summarised in Table 4.11.

TABLE 4.11: Initial conditions for the low-temperature (LT) pairing case.

Case	u_∞ (m/s)	T_∞ (K)	ρ_∞ (kg/m^3)	p_∞ (N/m^2)	dt (s)	δ°_ω (m)	$Re_{\delta^\circ_\omega}$	M_c	Model
LT	440	3000	0.02	18142.5	1.2×10^{-7}	0.003998	400	0.4	TCNE

Figure 4.19 illustrates the flow development within the three-dimensional large-domain configuration, where each sub-figure corresponds to a different stage of vortex evolution at $\tau_\theta = 100$, 500, and 2400, respectively. Iso-surfaces of the Q-criterion at 4.0×10^9 are shown, overlaid with colour contours of $T_v - T$ indicating the magnitude of thermal non-equilibrium (in K). Following the initial disturbance, and similarly to the single-vortex simulations, large-scale vortex tubes develop in the form of horseshoe vortices (Figure 4.19a), around which regions of thermal non-equilibrium emerge. At later times (Figure 4.19b), the vortices begin to shed and break down, while the initially strong non-equilibrium regions progressively relax and evolve towards an overall thermally cold state across the flow field. By the end of the simulation ($\tau_\theta \sim 2400$), the small-scale vortices have largely dissipated and only weak, localised non-equilibrium pockets remain (Figure 4.19c).

Overall, the dominance of small-scale random turbulent structures is more pronounced in this configuration than in the single-vortex case, providing a clearer distinction between the large-scale roll-up phase and the subsequent breakdown process. The pairing configuration also exhibits a less intense thermal non-equilibrium state throughout its evolution, consistent with the weaker vortices generated by the imposed disturbance. Increasing the magnitude of the Kelvin–Helmholtz component ζ_{KH} in the initial condition enhances the formation of non-equilibrium regions but simultaneously delays the transition to small-scale turbulence. This behaviour is illustrated in Appendix B.1, which is strongly recommended for reference. As discussed therein, such cases would require a substantially longer simulation time and a larger domain size for the flow to reach a fully self-similar regime.

Quantitative Analysis & Self-Similarity

Figure 4.20a illustrates the evolution of the momentum thickness for the three-dimensional pairing cases. The vertical bars indicate the times corresponding to the flow visualisations shown in Figure 4.19 and the statistical results presented in Figure 4.23. These bars also denote the three instantaneous fields used for time averaging in the statistical analysis that follows. Unlike the single-vortex cases, no distinct peak followed by a pronounced dip in momentum thickness is observed during the breakdown of large-scale vortices. Nevertheless, within the interval $0 < \tau_\theta < 150$, an approximately linear growth rate is evident, associated with the non-linear dynamics of the developing vortices induced by the Kelvin–Helmholtz disturbance ζ_{KH}. During this phase, energy is transferred from the mean flow to the inertial modes associated with vortex development. In the

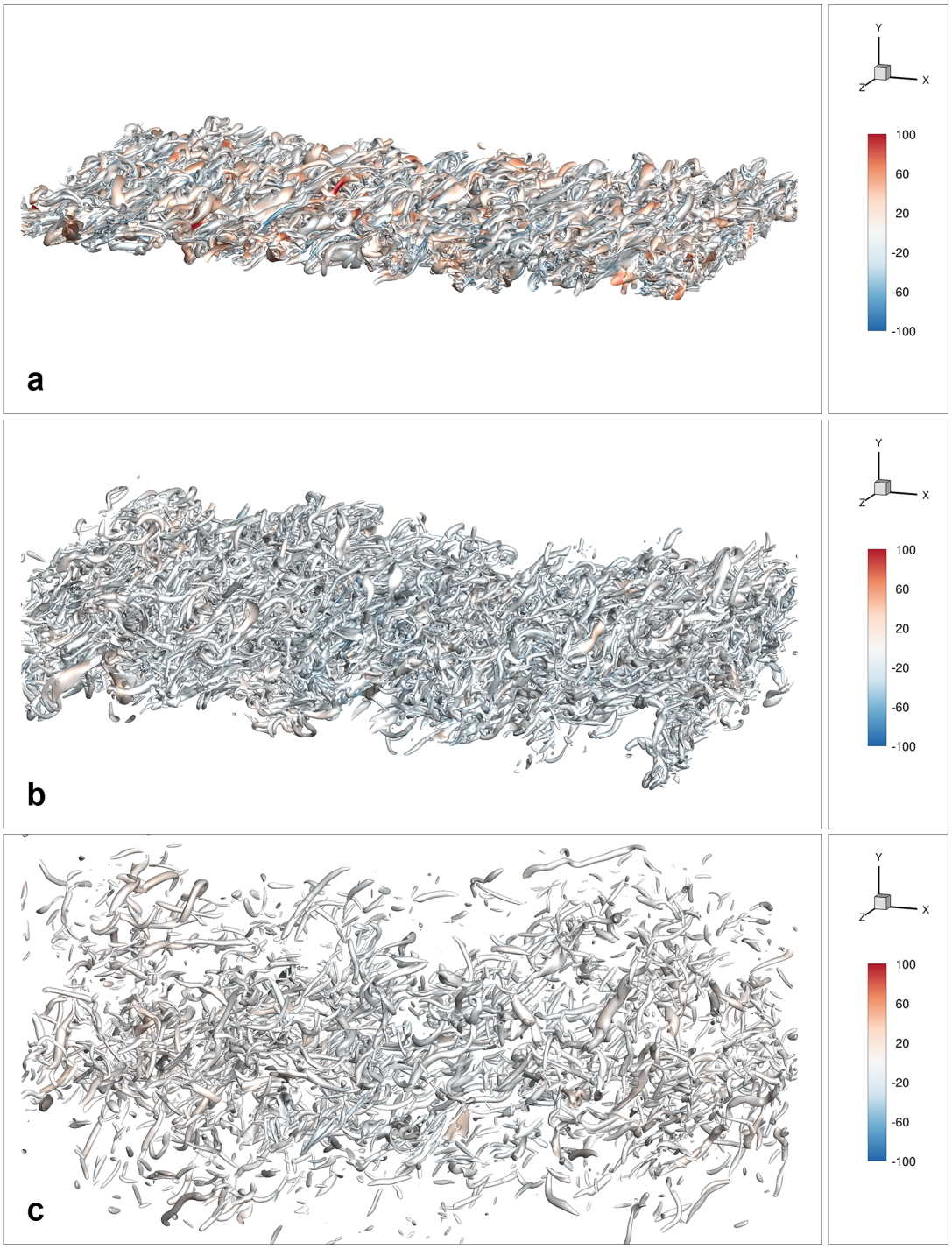

FIGURE 4.19: Iso-surfaces of the Q-criterion for a three-dimensional, temporally developing mixing layer, coloured by $T_v - T$. (a)–(c) correspond to $\tau_\theta = 100,\ 500$, and 2400, respectively.

subsequent interval $150 < \tau_\theta < 800$, the large-scale structures progressively break down into smaller-scale turbulence. This transition is accompanied by a change in the direction of energy transfer within the flow. This behaviour correlates well with the thermal non-equilibrium trends shown in Figure 4.18b, where, for $\tau_\theta > 150$, the flow transitions from having regions of thermally hot and cold non-equilibrium states to a thermally cold

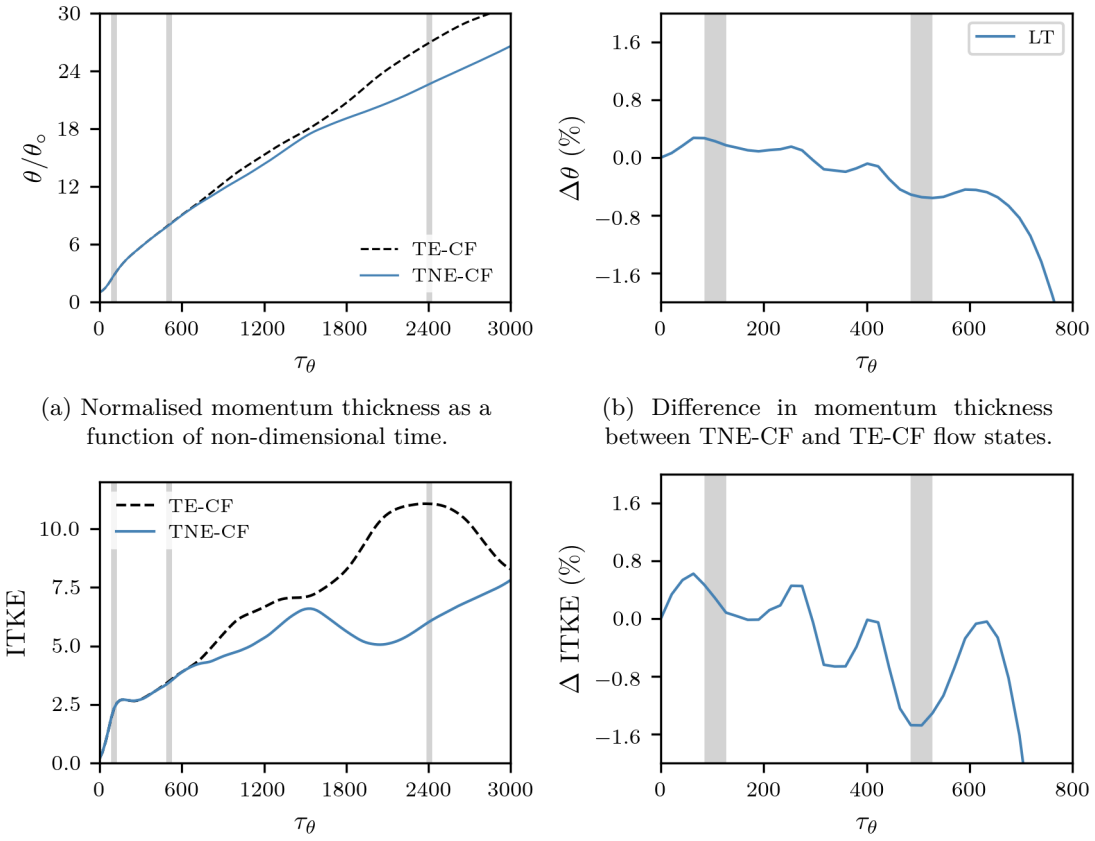

(a) Normalised momentum thickness as a function of non-dimensional time.

(b) Difference in momentum thickness between TNE-CF and TE-CF flow states.

(c) Integral of turbulence kinetic energy as a function of non-dimensional time.

(d) Difference in ITKE between TNE-CF and TE-CF flow states.

FIGURE 4.20: Flow properties of the three-dimensional large-domain pairing case under LT conditions, comparing thermo non-equilibrium (TNE) and thermal-equilibrium (TE) simulations, with both cases chemically frozen (CF).

non-equilibrium state.

Figure 4.20c presents the integral of turbulent kinetic energy (ITKE) for the two simulations, while Figure 4.20d shows the corresponding percentage difference. Consistent with the single-vortex case and with the momentum-thickness behaviour discussed earlier, an initial increase in ITKE is observed for the thermal non-equilibrium case. The corresponding percentage difference in momentum thickness between the thermal-equilibrium and non-equilibrium cases is shown in Figure 4.20b. As in the single-vortex configuration, the presence of thermal non-equilibrium leads to an increased momentum thickness during the early stages of flow development.

Comparison of Figure 4.20b and Figure 4.20d clearly indicates that the flow state for $\tau_\theta \gtrsim 800$ is highly non-deterministic, with small differences in the initial conditions giving rise to amplified discrepancies at later times. Consequently, as noted in the previous section, direct cross-comparison of the two cases in this regime becomes unreliable. Nevertheless, analysis of the statistical behaviour of the resulting random structures remains meaningful.

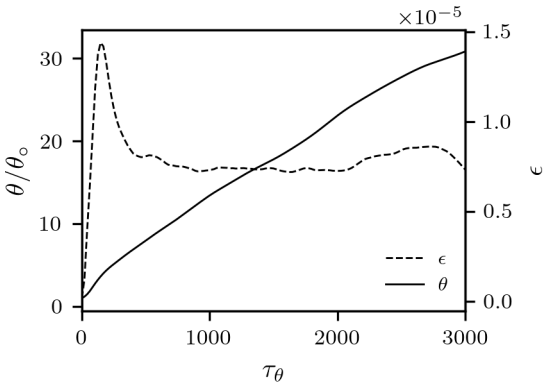

(a) Momentum thickness and scalar dissipation as functions of non-dimensional time.

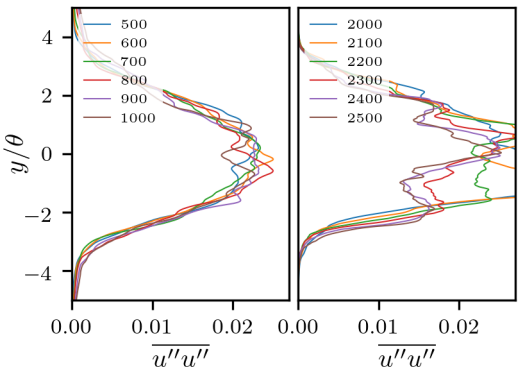

(b) Streamwise Reynolds stress at different non-dimensional times.

FIGURE 4.21: Evaluation of the self-similarity of the flow for the thermal equilibrium (TE-CF) case.

The evolution of turbulent mixing layers towards a self-similar state, characterised by linear growth of the momentum thickness, is well established (Rogers and Moser, 1994; Pope, 2000). Based solely on the linear portion of the momentum-thickness evolution shown in Figure 4.20a, it may be inferred that, in the equilibrium case, a state approaching self-similarity is reached for $\tau_\theta \gtrsim 600$, noting the inherent difficulty of achieving full self-similarity in finite-domain simulations (Rogers and Moser, 1994). A similar onset time is observed for the non-equilibrium case.

To assess more rigorously whether the flow has reached a self-similar regime, more sensitive indicators are required, such as Reynolds-stress components or vorticity profiles across the shear layer. In addition, self-similarity should be accompanied by an approximately constant dissipation rate. To evaluate this, flow profiles across the shear layer are rescaled using the local, time-dependent characteristic length scale defined by the momentum thickness. If the rescaled quantities collapse onto a single curve at different times, the flow may then be regarded as having attained a self-similar state (Rogers and Moser, 1994).

Figure 4.21 shows the scalar dissipation (defined as the trace of the dissipation tensor from Equation 4.25, i.e. $\epsilon_{11} + \epsilon_{22} + \epsilon_{33}$) overlaid with the momentum thickness, together with the streamwise Reynolds stress, which represents turbulent fluctuations in the u-direction. The results shown correspond to the thermal-equilibrium (TE-CF) simulation. As observed in Figure 4.21a, the scalar dissipation attains an approximately constant level over the interval $400 < \tau_\theta < 2000$, with noticeable departures towards the end of the simulation ($\tau_\theta > 2200$). This behaviour correlates well with the approximately linear growth of the momentum thickness over the same time range.

Figure 4.21b presents instantaneous profiles of the streamwise Reynolds stress at two different time intervals, $500 < \tau_\theta < 1000$ and $2000 < \tau_\theta < 2500$, sampled at intervals

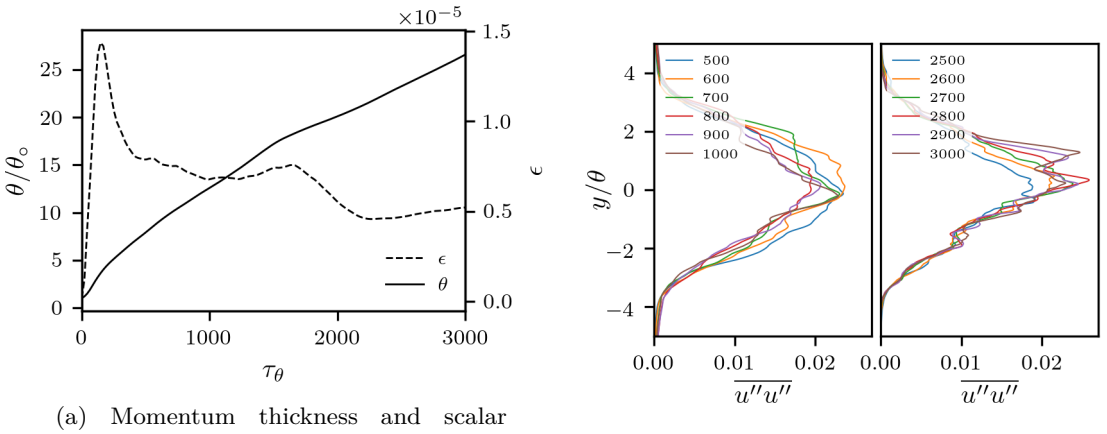

(a) Momentum thickness and scalar dissipation as functions of non-dimensional time.

(b) Streamwise Reynolds stress at different non-dimensional times.

FIGURE 4.22: Evaluation of the self-similarity of the flow for the thermal non-equilibrium (TNE-CF) case.

of 100 and scaled across the shear layer using the local momentum thickness. For the first interval ($500 < \tau_\theta < 1000$), the Reynolds-stress profiles exhibit a strong collapse, consistent with the results reported by Rogers and Moser (1994). This behaviour, together with the near-linear dissipation observed over the same period, supports the conclusion that the flow in this time range has reached a self-similar state.

For the second interval ($2000 < \tau_\theta < 2500$), the profiles collapse reasonably well on one side of the shear layer but exhibit differing decay rates on the opposite side. This asymmetry may be attributed to residual large-scale structures or localised vortical regions persisting in the area of poorer collapse, which are still undergoing breakdown into smaller scales. On this basis, it can be concluded that a fully self-similar state has not yet been achieved, as a complete collapse of the scaled Reynolds-stress profiles is not observed and the dissipation no longer remains approximately constant.

Figure 4.22 presents analogous quantities for the assessment of self-similarity in the thermal non-equilibrium case. As shown in Figure 4.22a, two time intervals exhibit approximately linear momentum-thickness growth accompanied by an approximately constant dissipation rate, namely $500 < \tau_\theta < 1100$ and $2400 < \tau_\theta < 3000$. Examination of the Reynolds-stress profiles, shown in Figure 4.22b, indicates that the profiles collapse well over the first interval, whereas in the second interval behaviour similar to that observed previously is present, with the stress decaying on one side of the shear layer.

Consistent conclusions can therefore be drawn for this case: the first interval demonstrates reasonable agreement with the expected characteristics of a self-similar flow, while the second interval does not. It should also be noted that the collapse of the Reynolds-stress profiles in the first interval is less pronounced than that observed for the thermal-equilibrium case. This may indicate the additional difficulty of attaining self-similarity under thermal non-equilibrium conditions, owing to the added dynamics of

energy exchange between the vibrational and translational modes, which may influence the dissipation rate. This aspect is examined further in the subsequent energy budget analysis.

Statistical Analysis

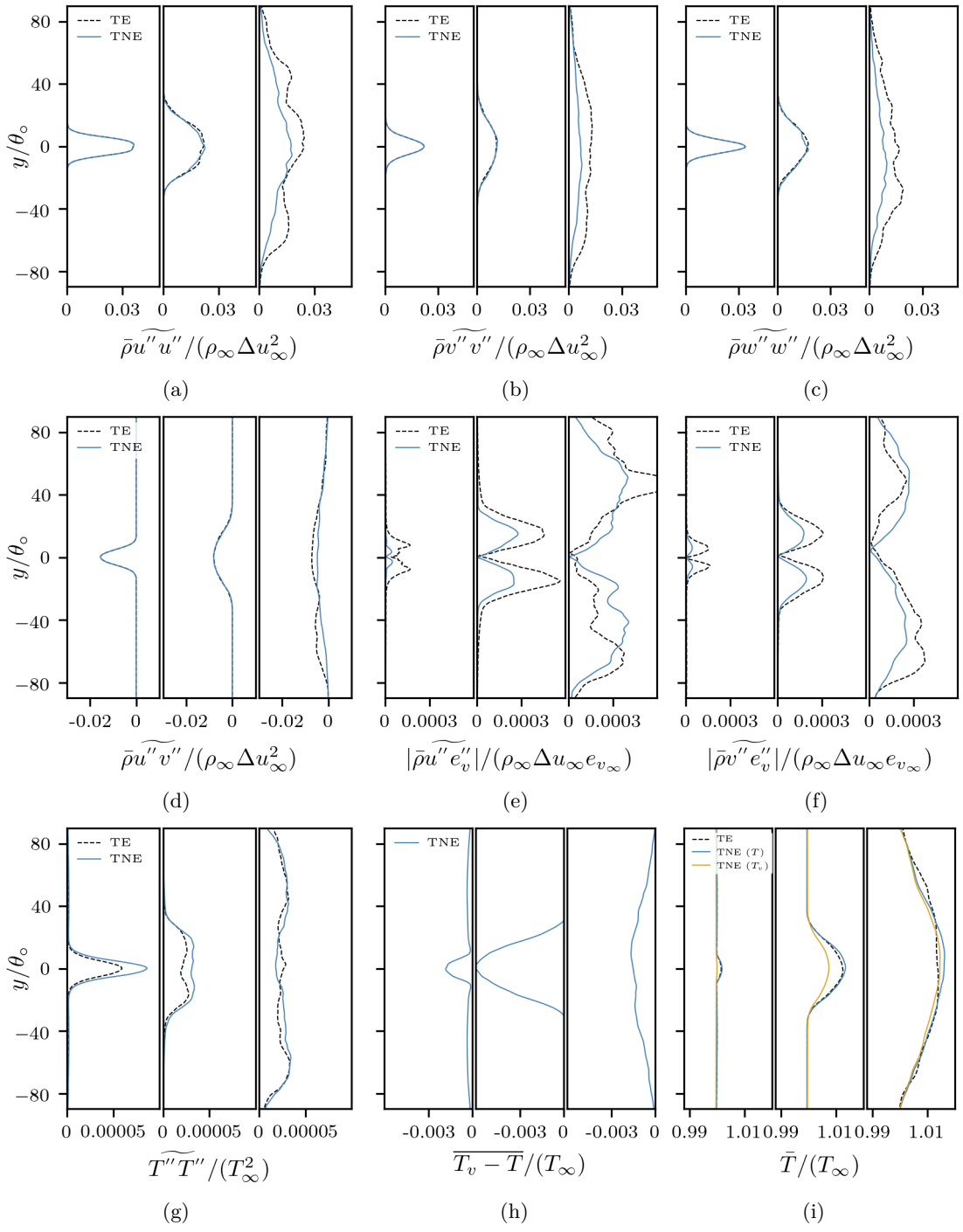

FIGURE 4.23: Statistical analysis of the three-dimensional pairing mixing layer across the shear layer for the low-temperature case showing non-dimensional times of $\tau_{\theta_\circ} = 100, 500, 2400$. All cases are chemically frozen (CF).

Figure 4.23 presents the statistical parameters across the shear layer for the pairing configuration. Both the thermal-equilibrium (TE-CF) and thermal non-equilibrium (TNE-CF) cases discussed earlier are shown, where the results are averaged over three instantaneous fields at non-dimensional times of $\tau_{\theta_\circ} = 100, 500$, and 2400. These sampling times, relative to the evolution of the momentum thickness and ITKE, are indicated in Figure 4.20 by the vertical markers superimposed on the curves.

Figure 4.23a–4.23d show the non-dimensional Reynolds stresses corresponding to the normal and shear stresses arising from momentum transfer by the fluctuating velocity field. The normal stresses exhibit increased fluctuations in the central region of the shear layer, associated with vortex formation. During the early vortex-development stage, the presence of elongated, domain-spanning hairpin vortices at $\tau_\theta = 100$ (see Figure 4.19a) results in smooth stress profiles with a single peak near the centre of the layer. As the larger scales spread and random disturbances become dominant, leading to continued growth of the momentum thickness, these structures begin to shed and break down. During this transition, the thermal state of the flow evolves from a mixture of thermally hot and cold regions to a predominantly thermally cold field (Figure 4.19b).

This change in thermal state is observed to have little influence on the Reynolds stresses at $\tau_\theta = 500$ in Figure 4.23a–4.23d, a region already associated with a self-similar regime. Further into the simulation ($\tau_\theta = 2400$), the small-scale structures progressively dissipate, and the domain becomes populated by longer, weaker streak-like structures that continue to break down and sustain the growth of the mixing layer (Figure 4.19c). The influence of thermal non-equilibrium is shown to be considerably weaker in the pairing case; this is most likely due to the reduced magnitude by which the flow is driven out of equilibrium. A more pronounced effect on the Reynolds stresses is observed when the flow is further from equilibrium, as demonstrated for the higher-disturbance case in Appendix B.1. Overall, the influence of thermal non-equilibrium is consistent with earlier observations: it has little impact during the initial vortex-development phase, while differences become more apparent once the flow is dominated by small-scale turbulent structures. At later times, quantitative comparisons between the two cases become less meaningful due to the increasingly non-deterministic nature of the flow. The differing behaviour of the flow in the deterministic and non-deterministic regimes of the mixing layer is examined further in the following section (Section 4.4.4).

The additional turbulent flux terms in the vibrational energy equation exhibit much smoother profiles in the pairing configuration (Figure 4.23e and 4.23f). These profiles provide insight into the underlying temperature fluctuations. In the equilibrium (TE-CF) case, the vibrational energy is fully coupled to the translational temperature, whereas in the TNE-CF case it follows the vibrational temperature and its coupling to the translational mode. The zero-crossing at the centre of the profiles is associated with the change in sign of the velocity fluctuations as the flow reverses direction across the shear layer. As in the single-vortex simulations, a reduction in the fluctuation levels of

these flux terms is observed under thermal non-equilibrium conditions, reflecting the breakdown of perfect synchronisation between the translational and vibrational modes.

The profiles linking translational temperature fluctuations, thermal non-equilibrium, and mean temperature (Figure 4.23g–4.23i) reaffirm trends identified earlier, but with smoother statistics. Temperature fluctuations (Figure 4.23g) exhibit weaker correlation with the local degree of thermal non-equilibrium (Figure 4.23h) than in the single-vortex case, which is expected given the averaged nature of the pairing configuration across multiple interacting vortex structures. The increased mean translational temperature in the TNE-CF case (Figure 4.23i) continues to correlate with larger temperature fluctuations and, consequently, with higher levels of thermal non-equilibrium, consistent with previous observations. As expected, the magnitudes of these effects are noticeably smaller than those reported for the single-vortex configuration, reflecting the weaker vortices and reduced departure from equilibrium in the pairing case.

Energy Budget

Figure 4.24 presents the temporal evolution of the terms in the Reynolds-stress energy budget for the pairing configuration. Each sub-figure corresponds to a different stress component; the $(1,3)$ and $(2,3)$ components are omitted, as they are negligible for this configuration. Colours denote the contributions of the different terms to the integrated Reynolds stresses, while markers indicate the corresponding quantities for the TNE-CF case. The results are broadly consistent with those presented earlier for the smaller-domain simulations; however, in the present configuration a clearer correlation between the budget terms is observed, owing to the more pronounced self-similar region characterised by approximately linear growth for $\tau_\theta \gtrsim 500$.

For the $(1,1)$ component (Figure 4.24), the approximately constant levels of production and dissipation over an extended interval ($400 < \tau_\theta < 1500$) are consistent with the expected characteristics of a self-similar mixing layer. As in the earlier cases, within the self-similar regime the turbulence is sustained by positive production, while the pressure–strain term, Π_{ij}, redistributes energy from the streamwise component $(1,1)$ into the lateral components $(2,2)$ and $(3,3)$. Across all components, a steady and nearly constant dissipation rate is observed, particularly for the TE-CF case.

Focusing on the non-dimensional time interval $500 < \tau_\theta < 1000$, during which both cases were shown to be close to self-similar, it is notable that the dissipation term exhibits almost no difference between the TE-CF and TNE-CF simulations. Since the quantity in this term, ϵ_{ij}, that is directly linked to the thermal state of the flow is the viscosity, and since the viscosity difference between the two thermal states is small under the present conditions, only minor variations in dissipation are expected and are indeed observed. By contrast, the pressure–strain term is more directly influenced by the thermal state of

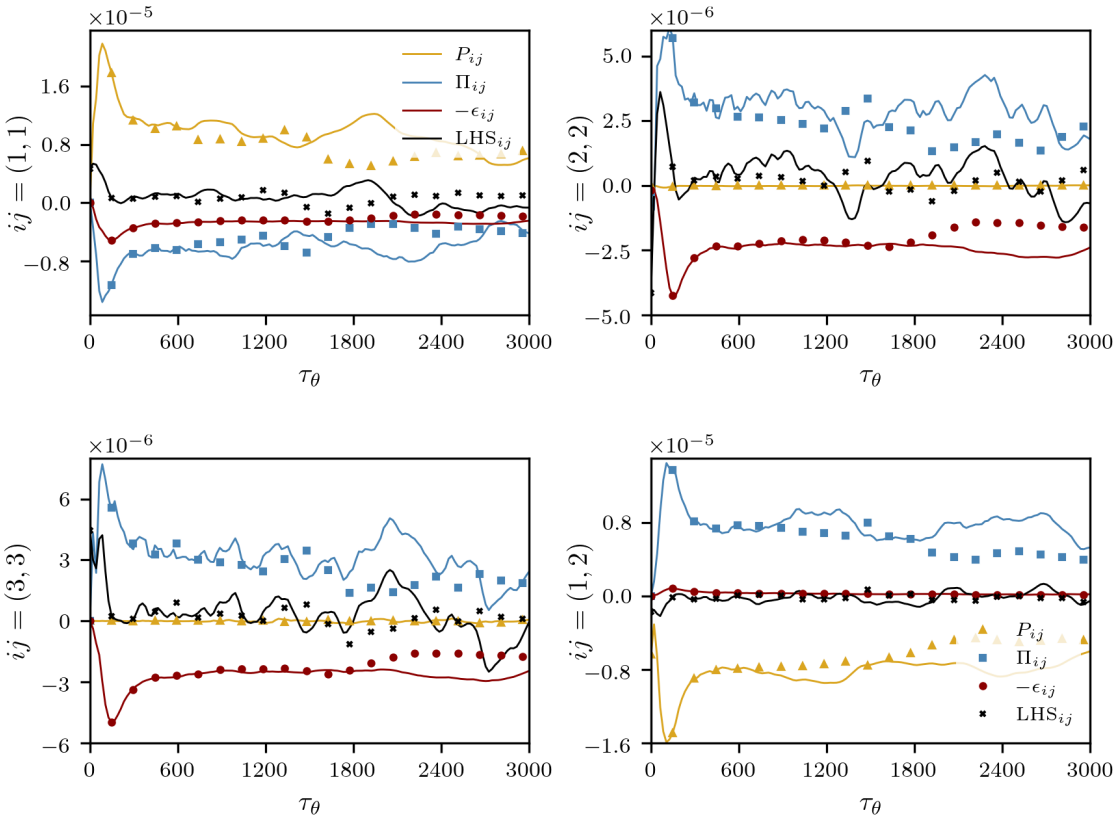

FIGURE 4.24: Energy budget of the lower-temperature pairing case. Solid lines refer to the TE-CF case, while markers denote the TNE-CF case. P_{ij} is the integrated production, Π_{ij} the pressure–strain contribution, $-\epsilon_{ij}$ the dissipation, and LHS the time derivative of the integrated Reynolds stress, $\frac{d}{dt}\int \overline{\rho u_i'' u_j''}\, dy$.

the flow, as pressure is coupled to the translational temperature through the perfect-gas assumption. Although differences between the TE-CF and TNE-CF cases are present, the relatively small departure from equilibrium in the TNE-CF simulation (approximately 0.5%) makes it difficult to draw strong quantitative conclusions.

Nevertheless, the results clearly demonstrate a relationship between thermal non-equilibrium and turbulent production. While dissipation remains approximately constant in both cases, a consistent correlation is observed between the pressure–strain term Π_{ij} and the production term P_{ij} across the components. This relationship is evident throughout the energy-budget results presented here.

The implication of this behaviour is that changes in the pressure–strain contribution modify the streamwise production term, and this modification correlates with the relaxation of thermally hot or cold non-equilibrium states and their influence on turbulent production. Specifically, when the flow relaxes from a vibrationally hot non-equilibrium state, turbulent production is enhanced, whereas relaxation from a vibrationally cold non-equilibrium state leads to a reduction in production.

4.4.4 Potential Hypothesis

When considering the analyses carried out so far, one can observe a possible link between the nature of turbulence and the influence of thermo-chemical non-equilibrium on the flow.

The symmetry analysis presented in Section 4.3.3.2 indicated two distinct dynamical states of the flow. In the first, the turbulent structures remain fully deterministic, preserving the inherent symmetry of the initial disturbance and retaining a significant amount of energy in large-scale coherent vortices. In the second, the domain is populated predominantly by small-scale turbulence arising from the breakdown and shedding of these vortex tubes. This latter stage was shown to exhibit non-deterministic behaviour, in the sense that instantaneous flow fields diverge due to the amplification of very small changes in initial or numerical conditions.

These two turbulent regimes can be related to the universal equilibrium range, consisting of the inertial subrange and the dissipation range (Pope, 2000). The inertial subrange is associated with Kolmogorov's second similarity hypothesis, in which the motion is governed primarily by inertial effects and viscous influences are negligible, whereas the dissipation range is characterised by motions strongly affected by viscosity.

If the initial, deterministic phase of vortex development is associated with the inertial range, and the later, non-deterministic phase with the dissipation range, a consistent picture emerges when considering the role of thermal non-equilibrium. In the first phase, the influence of thermal non-equilibrium on the flow appears to be negligible, while in the second phase, differences between the TE-CNE and TNE-CNE simulations become apparent, particularly in the energy budget analysis. This interpretation is supported by the observation that the pressure–strain term was seen to influence production in the self-similar regime of the pairing case (Section 4.4.3), while it had negligible impact during the earlier stages dominated by coherent vortex tubes.

The implication of this hypothesis is that the influence of thermal non-equilibrium on turbulent flows is weak when inertial effects dominate the motion (in the inertial range), but becomes more significant when the turbulence resides in the dissipation range, where viscous and thermal effects play a leading role. Further work, ideally involving higher-Reynolds-number simulations and more extensive ensemble averaging, would be required to confirm and generalise this proposed connection.

4.5 Conclusion

The objective of this chapter was to evaluate the extent to which thermo-chemical non-equilibrium influences turbulence and its characteristics, while simultaneously

assessing the significance of certain modelling approximations on the resulting outcomes. This investigation was conducted using a free shear mixing layer framework, where initially the development of a single vortex was examined by initiating a Kelvin–Helmholtz instability. Two flow conditions were defined: one representing a lower-temperature case, characterised by slower vibrational relaxation times due to the presence of multiple molecular species, and the other representing a higher-temperature case, in which the vibrational contribution arises solely from a single molecular species (N_2).

The two-dimensional simulations of thermal non-equilibrium revealed two distinct patterns of non-equilibrium formation within the flow field. The high-temperature case exhibited a flow state in which the thermal and flow timescales were comparable, leading to the formation of thermally hot and cold regions around the vortex entrainment during its development. In contrast, the low-temperature case demonstrated a flow where thermal relaxation timescales were significantly slower than the flow timescales, resulting in persistent thermal non-equilibrium within the vortex core. This region consistently remained out of equilibrium as the vortex evolved, effectively representing a thermally frozen state. Additionally, in both cases, the chemical timescales were shown to be significantly faster than the flow timescales, resulting in a chemically near-equilibrium state throughout the simulations.

For both the high- and low-temperature cases, only minor differences were observed in momentum thickness when comparing the thermal non-equilibrium simulations to their respective equilibrium counterparts. In contrast, a significant influence was noted on the turbulent kinetic energy (TKE), with differences exceeding 8% and 4% for the low- and high-temperature cases, respectively. These results suggest that the presence of thermal non-equilibrium causes an increase in turbulent kinetic energy.

When evaluating the modelling of high-enthalpy effects in a two-dimensional high-enthalpy flow with non-equilibrium reactions, a comparison was made between a model where the vibrational modes of all species are coupled and represented by a single transport equation, and a model in which the vibrational mode of each molecular species is governed by a separate transport equation. The results demonstrated that harmonic averaging of vibrational energy across multiple molecular species has a significant impact on the overall relaxation time, leading to a more balanced distribution despite substantial differences in species mass fractions. As a consequence, a pronounced difference was observed between the multi-e_v and single-e_v models. In the low-temperature case, where the mixture comprises Nitrogen and Oxygen, the single-e_v model produced a faster thermal relaxation time. This occurred because the single relaxation time leaned towards the faster relaxation rate of oxygen, despite oxygen constituting only 20% of the mixture. In contrast, for the high-temperature case, the differences between the two models were minimal, as the flow was predominantly composed of a single molecular species. Therefore, it was concluded that for flows involving mixtures of molecular species contributing to vibrational modes, the approximation of assuming complete coupling of vibrational

modes, by treating them collectively within a single transport equation, can lead to significant alterations in the thermal non-equilibrium state of the flow, depending on the temperature and pressure.

The two-dimensional cases were followed by a set of three-dimensional simulations, where similar thermal non-equilibrium patterns to those observed in the two-dimensional cases were identified. In the low-temperature case, large regions of thermally hot non-equilibrium were present, while in the high-temperature case, a combination of hot and cold regions was observed. The presence of upwash and downwash within the flow field led to the formation of vortex horseshoe structures alongside vortex tubes. The differences in turbulent kinetic energy between the equilibrium and non-equilibrium cases followed trends similar to those seen in the two-dimensional simulations, albeit with significantly reduced magnitudes. An increase in TKE was observed as the degree of thermal non-equilibrium in the flow field increased. However, the differences between the two- and three-dimensional results were clearly attributable to the distinct turbulent structures formed in each case. Additionally, small but measurable differences in momentum thickness were observed between the non-equilibrium and equilibrium cases, indicating that thermal non-equilibrium may influence characteristic length scales, particularly in flows where vibrational modes constitute a larger proportion of the total energy.

The statistical analyses of the domain, along with the observed flow characteristics across the shear layer, demonstrated minimal differences in Reynolds stresses due to the presence of thermal non-equilibrium during the initial stages of vortex development. The additional flux terms in the vibrational energy equation showed that, in the presence of thermal non-equilibrium, vibrational fluctuations are reduced due to a weaker coupling between the vibrational and translational modes, such that the vibrational mode does not fully inherit the variability of the translational temperature field. In the mixing layer configuration, a reduction in translational temperature in the vortex core was demonstrated, with an enhanced cooling observed when the flow was in non-equilibrium. The stronger temperature gradients were shown to play a role in increased temperature fluctuations and, while thermal non-equilibrium is often attributed to temperature fluctuations, it was here linked to the cause of the non-equilibrium state. The observations from the energy budget analysis highlighted that, with the emergence of small-scale turbulent structures in the single-vortex case, the link between growth rate and integrated production breaks down. This transition was shown to be consistent with the non-linear dynamics associated with the saturation and subsequent breakdown of the hairpin vortex.

This was followed by a larger-domain shear layer case designed to approach a self-similar state. Profiles derived from the pairing case showed statistically smoother behaviour, aligning with similar findings to those obtained in the single-vortex cases. The energy budget conducted on this case demonstrated clear regions correlating with self-similar mixing layers. Within the self-similar region, it was shown that the presence of thermal non-equilibrium has almost no effect on the dissipation due to the small difference

in viscosity between the two cases, while being directly linked to the pressure–strain term. Changes in the pressure–strain contribution modify the streamwise component of production, and this was found to correlate with the relaxation of thermally hot or cold non-equilibrium states and their influence on turbulent production. Hence, if the flow is relaxing from a vibrationally hot state the production is increased, and if the flow is relaxing from a vibrationally cold state the production is reduced.

From the observations made in the statistical analysis, a potential connection between the nature of the turbulent structures and the influence of thermal non-equilibrium was suggested. In particular, the influence of thermal non-equilibrium on turbulent flows appears to be negligible when inertial effects dominate the motion, whereas its effect becomes more pronounced when the turbulence resides in the dissipation range. While the evidence gathered aligns with this proposed picture, more extensive statistical analysis is required to strengthen and generalise the hypothesis.

In conclusion, this chapter provides insight into the influence of thermo-chemical non-equilibrium on turbulence development in a canonical temporally evolving mixing layer. Although further investigation is required to extend and generalise these findings, the present work establishes a solid foundation for the systematic study of high-enthalpy effects on turbulent flows.

4.6 Future Works

As part of future works related to this chapter, one could continue the work by looking into:

- **Further study in turbulence and non-equilibrium coupling:** Further investigation into how high-enthalpy effects influence different turbulent structures. Future work could include sensitivity studies targeting the two distinct turbulent configurations shown here, as well as simulations with higher ratios of vibrational to translational energy to enable a clearer and more systematic evaluation.
- **Shocklets in high-Mach-number mixing layers:** Investigating the presence of shocklets during the development of a mixing layer at higher Mach numbers. With shock capturing embedded in the simulation, one could evaluate the small discontinuities developed due to these shocklets, where regions of strong thermo-chemical non-equilibrium are present.
- **Compressibility effects on the formation of thermal non-equilibrium regions:** Investigating the effect of compressibility on the creation of thermal non-equilibrium regions in the flow field. Conducting a series of cases with increasing Mach number would allow evaluation of the influence of compressibility

on turbulence and whether similar conclusions can be drawn to those obtained under equilibrium conditions.

- **Effect of chemical reaction and turbulence coupling:** Investigating the effect of chemical reaction on turbulence where the chemical and flow timescales are more comparable. This could be extended by reproducing and validating experiments involving two streams with different compositions. Furthermore, the presence of different chemistries could generate density differences and hence baroclinic effects, which could be investigated. In addition, the chemical mixing of species can be examined where the streams are in thermo-chemical non-equilibrium.
- **Extension to ionisation and electronic energy:** Including ionisation and electronic energy effects. By extending the thermo-chemical model to incorporate ionisation and electronic energy, one could investigate the influence of ionisation on turbulence.

Chapter 5

Transport Property Formulation for Scale-Resolved Hypersonic Flow Simulations

5.1 Introduction

Hypersonic flight regime presents significant challenges for both experimental and numerical investigations. Experimental studies are limited by constraints in measurement techniques and difficulties in controlling background turbulence levels, while simulations are challenged by the presence of shock waves and steep temperature gradients near solid surfaces. As computational power continues to increase, scale-resolved simulations, such as direct numerical simulation (DNS) and large-eddy simulation (LES), have increasingly complemented experimental efforts and provided fundamental insights into hypersonic flow physics.

To date, much of the research has focused on so-called 'cold' or 'classical' hypersonic conditions, in which high-temperature effects are negligible. Under these assumptions, most simulations employ Sutherland's law to model viscosity and assume a constant Prandtl number to estimate thermal conductivity. However, such approximations break down under 'hot' or 'high-enthalpy' conditions, where a more fundamental treatment of gas dynamics is required (Lee, 1984; Gnoffo et al., 1989; Park, 1984, 1993). Current modelling approaches for these conditions are complex and computationally expensive. For example, the Yos-Gupta model (defined in Section 2.4.2.4) incorporates detailed mixing rules but is only valid for temperatures above 1000 K (Gupta et al., 1990), thereby excluding regions such as the flow near cooled walls. In this context, a DNS or LES framework would ideally avoid the use of conditional statements to switch between different formulations across temperature ranges, particularly when simulations may involve billions of grid points over millions of time steps. The objective of this chapter

is therefore to develop efficient modelling approaches that remain valid over a wide temperature range.

In strongly non-equilibrium flows, where characteristic flow timescales become comparable to those of internal relaxation processes, it is necessary to couple the governing equations of macroscopic flow variables with those describing physico-chemical kinetics. Under such conditions, transport coefficients, heat fluxes, and diffusion velocities are directly influenced by the non-equilibrium state of the gas (Nagnibeda and Kustova, 2009). Accurately capturing the effects of non-equilibrium kinetics on transport properties and their formulation is therefore essential. When the distribution function is obtained as a solution to the Boltzmann equation, expressions for the flux vectors are derived, and transport coefficients can be defined consistently in terms of these fluxes (Hirschfelder et al., 1954). Chapman and Enskog independently derived general expressions for transport coefficients, thereby providing closure to the transport equations (Chapman and Cowling, 1970; Nagnibeda and Kustova, 2009). The Chapman-Enskog kinetic theory of gases is strictly applicable to monatomic gases or species without internal degrees of freedom, for which the intermolecular interaction potential is spherically symmetric. Nevertheless, viscosity and diffusion are not influenced by the presence of internal degrees of freedom, allowing the theory to be applied to most polyatomic species (Hirschfelder et al., 1954). Since its original development, the Chapman-Enskog formulation has been extended to accommodate more general molecular models, including species with internal energy modes, ionised gases, and thermo-chemical non-equilibrium effects.

When deriving transport coefficients for flow simulations, two primary considerations must be addressed. The first concerns the evaluation of the Chapman-Enskog formulation for multi-species mixtures, which involves lengthy calculations and inverse matrix operations. The second is the determination of collision cross-section terms for all possible species pairs. While the complexity associated with the former is often reduced through the use of approximations that retain good accuracy, such as those proposed by Hirschfelder et al. (1954) and Yos (1963), the latter is addressed either by analytically modelling intermolecular potential functions—using, for example, rigid-sphere or Lennard-Jones potentials—or by utilising experimental data to infer intermolecular interactions (Yun and Mason, 1962; Yun et al., 1962). Furthermore, in high-enthalpy flows involving molecular species, the presence of internal degrees of freedom must be accounted for. Although viscosity is unaffected by internal energy modes, thermal conductivity depends strongly on the nature of these internal modes (Hirschfelder et al., 1954).

Recent studies on high-temperature transport properties include the work of Hao et al. (2017), which presents comparisons of transport property models for Mars entry conditions; Alkandry et al. (2014), which evaluates transport properties for ablative heat-shield flows; and Tian et al. (2021), which analyses diffusion theory for high-temperature multi-species gases. Each of these studies employs the Yos mixing rule (Yos, 1963, 1967) in conjunction with the collision integral method to derive accurate transport

properties, supplemented by collision integral data from sources such as Gupta et al. (1990, 1991) or more recent datasets provided by Wright et al. (2005, 2007). For air-specific species, Palmer and Wright (2003b) compare four different approaches for computing the viscosity of 11-species air mixtures at high temperatures, assessing both accuracy and computational efficiency. In addition, four distinct methods for calculating frozen thermal conductivity are evaluated in Palmer and Wright (2003a). Both studies compare the Yos formulation with first-order approximations for multi-component mixture viscosity and thermal conductivity, concluding that the Yos model provides excellent agreement for non-ionized or weakly ionized flows.

High-fidelity simulations of boundary-layer flows and the transition to turbulence under high-enthalpy conditions have seen significant contributions from Passiatore et al. (2024, 2023, 2022), who model viscosity and thermal conductivity following the approach proposed by Blottner et al. (1971). As previously defined, the mixing rule introduced by Wilke (1950), which is employed within this framework, requires embedded loops over all species. This procedure can become computationally expensive in large-scale simulations with grid resolutions on the order of 10^8–10^9 points.

Similarly, studies on high-enthalpy channel flows such as Chen et al. (2024), direct numerical simulations of transitional boundary layers under high-enthalpy conditions conducted by Di Renzo and Urzay (2021), and investigations of shock standoff distances in hypersonic flows around blunt bodies performed by Khatri and Zhang (2023) all apply Wilke's mixing rule in combination with various models for species-specific viscosity and thermal conductivity. Additional research on compressible isotropic turbulence with vibrational non-equilibrium includes the studies of Zheng et al. (2022, 2021), while chemically reacting hypersonic flow simulations conducted by Margaritis et al. (2022) model viscosity using Sutherland's law, originally proposed by Sutherland (1893), with updated constants.

The objective of this chapter is to develop and assess a computationally efficient formulation for viscosity and thermal conductivity, aimed at improving suitability for DNS and LES applications while maintaining a balance between accuracy and computational cost. The model will be based on a five-species air mixture (O, O_2, N, N_2, NO) and will be applicable over a temperature range of 100 K to 9000 K, within which ionization effects can be reasonably neglected. The formulation will be further examined through simulations of a thermally and chemically non-equilibrium free shear layer flow under high-enthalpy conditions.

5.2 Evaluation of Transport Property

While an extensive description of transport properties has already been provided (Chapter 2), this section focuses on the current state of the literature specifically addressing the evaluation of transport properties under high-enthalpy conditions.

5.2.1 Viscosity and Thermal Conductivity

High-enthalpy conditions are associated with a significant excitation of internal molecular energy modes, which influence the vibrational state of the gas, as well as extensive chemical reactions that require a multi-species evaluation of the transport properties. While variations in gas composition affect both viscosity and thermal conductivity, the presence of vibrational modes does not inherently influence viscosity. Nevertheless, as already discussed in Section 2.4, instead of performing a full multi-component evaluation, several mixing-rule-based models have been proposed in the literature (Gupta et al., 1990; Blottner et al., 1971; Yos, 1967; Peng and Pindroh, 1962; Brokaw, 1958).

A comparative study by Palmer and Wright (2003b) evaluated four commonly used mixing rules for viscosity calculations: the Yos-Gupta mixing rule, the Armaly-Sutton mixing rule, Wilke's mixing rule, and the full multi-component formulation. These approaches were assessed in terms of both computational cost and predictive accuracy. The study concluded that the full multi-component formulation provides the highest accuracy, albeit at the greatest computational expense. The Yos-Gupta mixing rule was identified as the most computationally efficient option, yielding accurate results in temperature regimes below the onset of ionisation. The Armaly-Sutton mixing rule demonstrated improved accuracy at higher temperatures, including ionising regimes, but required approximately 15% greater computational effort than the Yos-Gupta approach. Wilke's mixing rule was found to be approximately 10% more expensive than the Yos-Gupta method while exhibiting the lowest overall accuracy. It is important to note that this comparison employed identical collision integrals across all mixing methods, thereby isolating the study to the influence of the mixing rule itself.

Thermal conductivity models were similarly assessed by Palmer and Wright (2003a), who compared first-order and second-order multi-component formulations with the Gupta-Yos and Hirschfelder-Eucken approximations. Both accuracy and computational efficiency were examined over a temperature range of 200-20,000 K. For non-ionised conditions, the Gupta-Yos method was shown to provide reliable predictions, with deviations of less than 3% relative to the second-order multi-component solution at temperatures below 8000 K. At higher temperatures, particularly around 15,000 K, the Hirschfelder-Eucken approximation was found to significantly underpredict the frozen thermal conductivity by approximately a factor of five. In terms of computational performance, the Eucken

approximation was the most efficient, offering a favourable balance between accuracy and cost at moderate temperatures, with deviations of only 5% observed at 6000 K.

5.2.2 Bulk Viscosity

The Chapman-Enskog theory provides a rigorous framework for the evaluation of viscosity and demonstrates that, for a monatomic gas, the bulk viscosity is identically zero. While Stokes proposed arguments suggesting that this result may extend to all gases, he also expressed reservations regarding the general validity of this conclusion (Vincenti and Kruger, 1965). In contrast, both kinetic theory based and experimental studies have shown that bulk viscosity is not necessarily zero for molecular gases.

Although investigations into wave propagation date back to the nineteenth century, experimental findings from the first half of the twentieth century demonstrated that classical sound dispersion theory—which incorporates Stokes' relation—does not correlate well with observations for molecular gases. This discrepancy motivated the introduction of the bulk viscosity coefficient, which characterises the finite-rate energy exchange between translational and internal degrees of freedom (rotational and vibrational) following volumetric expansion or compression of a gas, as well as the resulting dissipative effects (Kustova et al., 2023).

In the continuum derivation of the Navier-Stokes equations, the bulk viscosity appears multiplied by the divergence of the velocity field, indicating that its influence becomes significant when compressibility effects are important. Consequently, bulk viscosity can strongly affect wave propagation and shock-wave structure. Due to its physical origin, accounting for bulk viscosity may substantially alter the shock structure and the dynamics of compressible flows characterised by large velocity divergence.

Two principal definitions of bulk viscosity are reported in recent literature. The first assumes no coupling between the vibrational and rotational contributions to the bulk viscosity and is presented by Cramer (2012), where bulk-to-shear viscosity ratios of up to 10^3 have been reported for species such as CO_2. The second definition assumes coupling between these contributions and is adopted in more recent studies, including Billet et al. (2008); Kustova et al. (2023), where the corresponding ratios for CO_2 are reduced to $\mathcal{O}(10)$.

An extensive review of these modelling approaches has been conducted by Kustova et al. (2023). In addition, several recent studies have examined the effects of bulk viscosity in different flow configurations, including the work of Bruno and Giovangigli (2022), which investigated its influence on fluid mechanics and internal relaxation processes; Zheng et al. (2024), which analysed its impact on hypersonic compressible turbulent boundary layers; Pan and Johnsen (2017), which evaluated its role in the decay of compressible

homogeneous isotropic turbulence; and Boukharfane et al. (2019), which studied the influence of bulk viscosity in compressible reactive shear-layer development.

In relation to the simulations conducted in this thesis, bulk viscosity was evaluated for the mixing-layer configuration. However, considering the molecular species involved (nitrogen and oxygen) and the relatively low Mach number flow conditions, the influence of bulk viscosity was found to be negligible. Consequently, bulk viscosity effects were omitted from the simulations presented in this thesis.

5.2.3 Diffusion

When defining the effects of diffusion in Section 2.4.3, the driving force associated with mass diffusion was described as being relatively small compared to pressure and temperature gradients. As such, when evaluating diffusion, the influence of internal vibrational modes is non-impactful, similar to their effect on viscosity.

As a comparative study, Alkandry et al. (2014) evaluated four different diffusion models for flow-field simulations involving ablative heat shields. The four models considered were Fick's law, a modified Fick's law incorporating a correction factor, the self-consistent effective binary diffusion (SCEB) model, and the Stefan-Maxwell model. The first three models are defined in Section 2.4.3. The Stefan-Maxwell formulation was originally developed to solve for mole-fraction gradients; however, through a rearrangement of the governing equations, it can be adapted to compute mass diffusion fluxes. Detailed descriptions of the iterative solution procedures required for this approach are widely available in the literature (Alkandry et al., 2014; Sutton and Gnoffo, 1998).

A series of evaluations were conducted using these four models to predict the flow field around the Stardust sample return capsule (SRC). Parameters including total heat transfer, the convective and diffusive components of the heat transfer at the stagnation point, and the mass blowing rate consistently showed similar results for the modified Fick's model, the SCEB model, and the Stefan-Maxwell formulation. In contrast, the classical Fick's model exhibited discrepancies of up to 20%, primarily due to the lack of enforcement of a zero net diffusion mass flux. While the SCEB model consistently produced the most accurate results, with errors of less than 4% relative to the Stefan-Maxwell solution, the modified Fick's law yielded errors of less than 8%.

A more recent evaluation of mass diffusion models for high-temperature multi-component gases was presented by Tian et al. (2021). In this study, the same four diffusion models were assessed, and similar findings were reported. In particular, the absence of the self-consistency condition in the classical Fick's model resulted in errors of up to 18%. Good agreement was again observed among the remaining three models, further validating the applicability of the modified Fick's and SCEB formulations.

In summary, these studies demonstrate that existing diffusion models provide a robust and accurate representation of mass diffusion fluxes when appropriate self-consistency conditions are enforced.

5.3 New Transport Property Model

Based on the current state of evaluation methods for transport properties, it has been shown that diffusion modelling for high-enthalpy flows can be accurately captured using relatively computationally inexpensive approaches, such as the modified Fick's model and the self-consistent effective binary diffusion (SCEB) formulation. These models have been demonstrated to provide reliable results across a wide range of conditions. In contrast, bulk viscosity effects were shown to be significantly less influential for air species under the flow conditions of interest. However, this conclusion does not extend to viscosity and thermal conductivity, for which modelling choices play a much more critical role.

In high-enthalpy flows representative of hypersonic conditions, extensive calculations are often required to obtain accurate expressions for viscosity and thermal conductivity. Models such as that proposed by Yos (1963), presented in Section 2.4.2.4, involve detailed formulations that can significantly increase overall computational cost. Furthermore, such models do not accurately represent transport properties at lower temperatures. As a compromise between computational efficiency and accuracy, viscosity and thermal conductivity over their respective temperature ranges are here approximated using simpler polynomial expressions, with coefficients valid for temperatures between 100 K and 9000 K.

The polynomial formulation of the present model is expressed as

$$\Phi = \frac{\sum\limits_{i\in\text{atom}} 15X_i + \sum\limits_{i\in\text{mol}} 30X_i}{P(a,b,c,d)\sum\limits_{i\in\text{atom}} X_i + P(e,f,g,h)\sum\limits_{i\in\text{mol}} X_i}\,, \tag{5.1}$$

with

$$P(A,B,C,D) = |A + B\,T^2 + C\,\ln(T) + D/T|, \tag{5.2}$$

where X_i denotes the species mole fraction, and the coefficients a, b, c, d, e, f, g, and h are provided in Table 5.1. The separation into atomic and molecular contributions, together with the omission of an explicit mixing rule, simplifies the final formulation while retaining the required accuracy.

TABLE 5.1: Coefficients for viscosity and thermal conductivity for the present model.

	a	b	c	d	e	f	g	h
μ	-2.0989e+05	-5.2310e-06	1.9855e+04	-2.7244e+08	1.2667e+06	3.3933e-04	-1.3007e+05	3.5234e+08
K	3.2315e+02	2.1022e-07	-3.5288e+01	8.0676e+04	-4.5599e+02	-1.8431e-07	4.6392e+01	-3.0308e+05
K_{tr}	2.1762e+02	2.1403e-07	-2.4067e+01	1.0838e+05	-9.8842e+02	-5.1961e-07	1.0492e+02	-2.3396e+05

As mentioned in Chapter 2, a more complete definition of thermal conductivity allows the total thermal conductivity to be decomposed into different contributing modes as

$$K = K_t + K_r + K_v,$$

where K_t represents the contribution from the translational mode, K_r the contribution from the rotational mode, and K_v the contribution from the vibrational mode.

In the modelling of high-enthalpy effects, particularly for non-equilibrium air at temperatures below 9000 K, it is reasonable to assume that the rotational mode is strongly coupled with the translational mode and is therefore governed by the translational temperature. In contrast, the vibrational contribution is governed by the vibrational temperature. Consequently, for air mixtures within this temperature range, the present model expresses thermal conductivity in terms of K, K_{tr}, and K_v, corresponding to the total thermal conductivity, the ro-translational thermal conductivity, and the vibrational thermal conductivity, respectively.

Both the total thermal conductivity and the ro-translational thermal conductivity are defined using the expression provided in Equation 5.1, while the vibrational thermal conductivity for each species is defined using sixth-order polynomial expressions of the form

$$K_{v,i} = |X_i \left[A_i + B_i\, T_d + C_i\, T_d^2 + D_i\, T_d^3 + E_i\, T_d^4 + F_i\, T_d^5 + G_i\, T_d^6\right]| \,, \tag{5.3}$$

where T_d is defined as $\sqrt{TT_v}$, and the coefficients A_i, B_i, C_i, D_i, E_i, F_i, and G_i are provided in Table 5.2 for each molecular species. The total vibrational thermal conductivity is then obtained by summing the individual molecular contributions as

$$K_v = \sum_{i \in \text{mol}} K_{v,i}. \tag{5.4}$$

Following Eucken's expression for the total thermal conductivity, the ro-translational thermal conductivity can be evaluated by subtracting the vibrational contribution from the total value,

$$K_{tr} = K - \left(\sum_{i \in \text{mol}} K_{v,i} \right). \tag{5.5}$$

TABLE 5.2: Coefficients for the species vibrational thermal conductivity.

	A	B	C	D	E	F	G
K_{v,N_2}	1.9200e-04	-3.9290e-06	1.4026e-08	-4.8403e-12	7.5275e-16	-5.0128e-20	1.0884e-24
K_{v,O_2}	-1.1446e-03	7.2095e-06	6.2555e-09	-2.6587e-12	4.2901e-16	-2.5152e-20	3.0436e-25
$K_{v,NO}$	-4.2658e-04	9.8630e-07	1.1229e-08	-4.2799e-12	7.0384e-16	-4.8694e-20	1.1027e-24

The polynomial given as Equation 5.1 separates the contributions to the transport properties between molecular and atomic species. This separation enables a more accurate representation of transport properties in chemically non-equilibrium flows, where the local composition deviates from the equilibrium state for which many traditional models are optimised. In contrast, the polynomial given as Equation 5.3 is expressed in a standard form without a division between species types, as atomic species do not contribute to vibrational modes.

The selected polynomial forms and their associated coefficients were optimised to accurately represent the relevant transport properties across equilibrium and a range of non-equilibrium flow states over temperatures from 100 K to 9000 K. The reference data used for this optimisation included equilibrium compositions spanning temperatures from 100 K to 9000 K, as well as four additional frozen-composition datasets over the temperature range 1000 K to 9000 K, representing highly chemically non-equilibrium conditions. Data points across the full temperature range were weighted toward lower temperatures to improve accuracy in this regime. Restricting the optimisation to equilibrium compositions below 1000 K allows greater fidelity at low temperatures, where non-equilibrium effects are unlikely to occur in practical applications. Conversely, the inclusion of frozen-composition data above 1000 K improves the representation of chemically non-equilibrium states. As a result, Equation 5.1 is employed to define the total viscosity, total thermal conductivity, and ro-translational thermal conductivity, while Equation 5.3 is used to define the species vibrational thermal conductivity. The total vibrational thermal conductivity is then obtained using Equation 5.4.

In establishing reference values for the optimisation data, the Hirschfelder-Lennard-Jones (HLJ) model was selected for viscosity in the temperature range 100 K to 1400 K, while the Yos-Gupta model was used from 1400 K to 9000 K. Hirschfelder et al. (1954) demonstrate that the Lennard-Jones potential provides accurate predictions for gas viscosity up to approximately 1100 K, provided appropriate force constants are applied. The collision integrals used in the Yos-Gupta formulation are directly correlated with experimental data reported by Yun et al. (1962) and Vanderslice et al. (1962), which are considered reliable over the temperature range 1000 K to 15,000 K. The combination of these two models is therefore assumed to provide a suitable reference across the entire temperature range of interest.

TABLE 5.3: Results from the present model for code verification.

T	X_O	X_{O_2}	X_N	X_{N_2}	X_{NO}	μ	K	K_{tr}	K_v
100	0.00	0.21	0.00	0.79	0.00	7.1580e-06	9.1655e-03	1.0545e-02	1.2805e-04
298	0.00	0.21	0.00	0.79	0.00	1.7564e-05	2.4819e-02	2.5514e-02	4.2750e-04
2000	0.01	0.20	0.00	0.78	0.01	6.5898e-05	1.1750e-01	9.6982e-02	2.0617e-02
5000	0.33	0.00	0.03	0.62	0.02	1.3187e-04	2.5485e-01	2.1730e-01	3.6434e-02
9000	0.21	0.00	0.78	0.01	0.00	2.4960e-04	5.3366e-01	5.2967e-01	1.2956e-03

For thermal conductivity, the HLJ model was applied over the temperature range 100 K to 700 K using the semi-empirical approach described by Hirschfelder et al. (1954), with species-specific correction factors taken from the model of Lemmon and Jacobsen (2004). As the air composition within this temperature range consists solely of N_2 and O_2, the gas was treated as a binary mixture. The semi-empirical approach, combined with experimental correction factors, was adopted due to the limited availability of theoretical models for the thermal conductivity of polyatomic gas mixtures. Under this framework, thermal conductivity is computed assuming monatomic behaviour, with vibrational contributions incorporated through experimental data. It is noted that Eucken's correction factor for polyatomic species does not provide acceptable results for mixture thermal conductivity (Hirschfelder et al., 1954). The Lemmon-Jacobsen model, defined by Lemmon and Jacobsen (2004), used to represent experimental data, was reduced by 0.5% for N_2 to improve agreement at temperatures above 300 K. The default Lemmon-Jacobsen model and its accuracy relative to experimental measurements are documented by Lemmon and Jacobsen (2004). For temperatures between 700 K and 9000 K, thermal conductivity was evaluated using the Yos-Gupta model.

Overall, while the selection of reference models was guided primarily by accuracy within their respective temperature ranges, the transition temperatures were chosen at the intersections of the individual models. This approach ensures a smoother composite representation of the transport properties and improves consistency during the optimisation of the polynomial coefficients. A standard least-squares method was employed for the optimisation procedure.

Comments on implementation

Table 5.3 presents a selection of calculated transport properties at various temperatures, together with their corresponding compositions. The compositions were selected to be close to the equilibrium composition at each respective temperature.

To compute the mixture viscosity, Equation 5.1 should be used with the appropriate coefficients provided in Table 5.1. This formulation is applicable to both equilibrium and non-equilibrium states. For thermal conductivity, it should be noted that the fitting

procedure yields values of K that are not exactly equal to the sum of K_{tr} and K_v, particularly at the extremes of the temperature range. The most accurate results are obtained by accounting for whether the flow is in equilibrium, weakly non-equilibrium, or strongly non-equilibrium. The recommended approaches are summarised as follows:

1. **Equilibrium state:** For thermally equilibrium simulations, in which the heat flux is expressed using the gradient of a single temperature in the governing equations, a single expression for the total thermal conductivity is sufficient. In this case, K should be evaluated using Equation 5.1 with the K coefficients provided in Table 5.1.

2. **Weakly non-equilibrium state:** For thermal non-equilibrium simulations in which the translational, rotational, and vibrational contributions to thermal conductivity are treated separately through gradients of translational and vibrational temperatures, K should be expressed in terms of K_{tr} and K_v. Under near thermal and chemical equilibrium conditions, it is recommended to evaluate K_v using Equation 5.4 and K_{tr} using Equation 5.5.

3. **Strongly non-equilibrium state:** For flows exhibiting strong chemical and thermal non-equilibrium, Equation 5.1 should be used to evaluate K_{tr} and Equation 5.4 for K_v, with an additional correction applied to K_{tr} as

$$K_{tr} = \Phi - |\, 2.03\,(T - T_v)\,T \times 10^{-10}| \tag{5.6}$$

   where Φ denotes the prediction obtained from Equation 5.1. This correction improves the agreement of the ro-translational thermal conductivity under thermal non-equilibrium conditions by explicitly incorporating the vibrational temperature.

The practical cases presented in the following sections provide guidance on identifying conditions that can be considered close to equilibrium. If the extent of non-equilibrium cannot be estimated a priori, the third approach may be adopted. In equilibrium flows, this option results in a maximum error of approximately 14% at 100 K and less than 4% for temperatures above 200 K.

5.4 Model Evaluation

The model proposed in the previous section is evaluated for accuracy against existing transport property models through a series of assessments. Three primary evaluations are conducted. First, the ability of the model to reproduce transport properties under thermal and chemical equilibrium conditions is examined. Second, a zero-dimensional (0D) heat-bath case is employed to investigate strongly non-equilibrium states in the absence

of fluid motion. Third, numerical simulations of two- and three-dimensional mixing-layer flows under thermo-chemical non-equilibrium conditions are considered. Finally, the computational savings achieved within the OpenSBLI framework are quantified and discussed.

5.4.1 Equilibrium Conditions

To assess the performance of the present model under equilibrium conditions, a five-species air mixture at atmospheric pressure in thermal and chemical equilibrium is considered. Transport properties predicted by various models are evaluated over a temperature range from 100 K to 9000 K. Figure 5.1 shows the equilibrium air composition in terms of mole fraction over this temperature range.

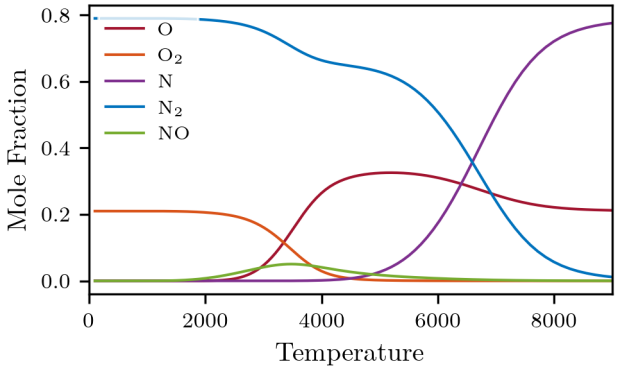

FIGURE 5.1: Equilibrium mole fraction of each five species of air at the respective temperature.

Figure 5.2a compares the viscosity predicted by the present model with those obtained from the reference models discussed in this thesis. The equilibrium formulation of the present model is represented by the solid black line. A subset of the same data, focusing on the lower temperature range from 100 K to 1000 K, is shown in Figure 5.2b. It is evident that no single existing model accurately captures viscosity across the entire temperature range. In particular, the HLJ and Sutherland models exhibit large errors at high temperatures, while the Yos-Gupta and Blottner models show significant discrepancies at low temperatures. It is also observed that the Blottner and Yos-Gupta models diverge at higher temperatures, notably between 4000 K and 8000 K.

In contrast, the present model closely follows the selected reference data across the full temperature range. Strong agreement is observed with the HLJ model for temperatures below 1000 K and with the Yos-Gupta model for temperatures above this threshold, demonstrating the ability of the proposed formulation to provide accurate viscosity predictions across both low- and high-temperature regimes.

Figure 5.2c, covering the full temperature range, and Figure 5.2d, focusing on the lower temperature regime, present the thermal conductivity predicted by the present

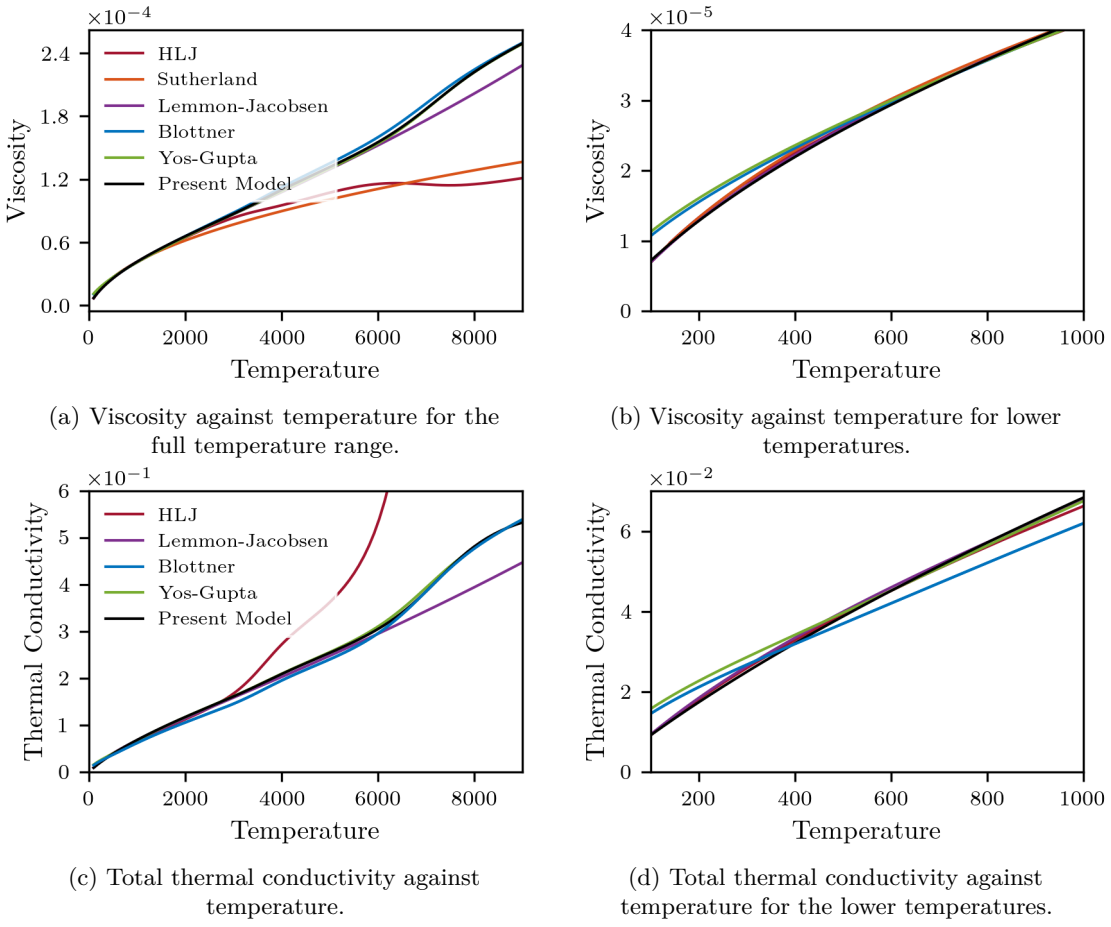

(a) Viscosity against temperature for the full temperature range.

(b) Viscosity against temperature for lower temperatures.

(c) Total thermal conductivity against temperature.

(d) Total thermal conductivity against temperature for the lower temperatures.

FIGURE 5.2: Comparison of total thermal conductivity of the present model against other models for thermo-chemical equilibrium air. Different colours refer to the different models.

model alongside other existing models. Significant discrepancies are observed among the Blottner, Yos-Gupta, and HLJ models. As in the viscosity comparison, a clear divergence is evident between the Blottner and Yos-Gupta models at higher temperatures, as well as between the HLJ model and the other two models at lower temperatures.

Figure 5.3 presents a comparison of the translational and vibrational contributions to the thermal conductivity. The ro-translational thermal conductivity is shown in Figure 5.3a, where similar trends are observed among the three models. The vibrational contribution to the thermal conductivity is shown in Figure 5.3b, with the solid line representing the total vibrational contribution. A clear discrepancy is evident between the Yos-Gupta and Blottner models, particularly at higher temperatures, where the Blottner formulation under-predicts the vibrational thermal conductivity. This behaviour arises from the use of Eucken's assumption for molecular species in the evaluation of the vibrational mode contribution within the Blottner model, which is known to be less accurate than semi-empirical or experimentally based approaches such as those employed in the Yos-Gupta and HLJ models. This under-prediction directly correlates with the

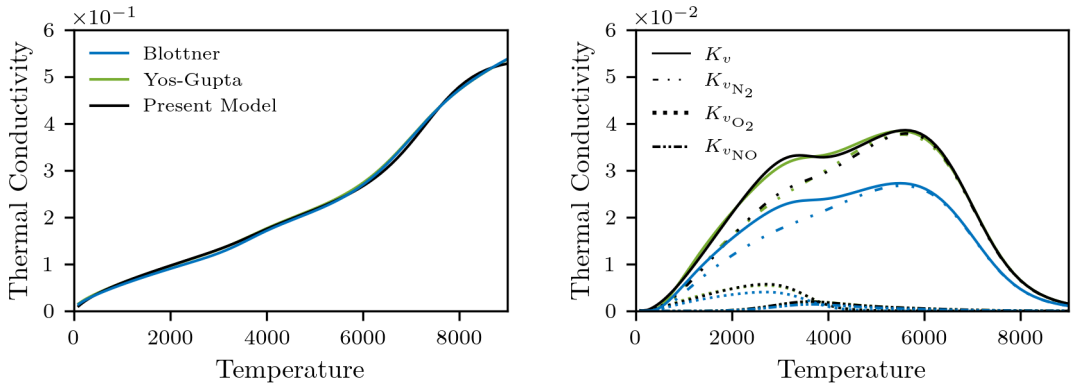

(a) Translational thermal conductivity against temperature for the full temperature range.

(b) Vibrational thermal conductivity against temperature for the full temperature range.

FIGURE 5.3: Comparison of translational and vibrational thermal conductivity of the present model against other models for thermo-chemical equilibrium air. The colour scheme is given in the legend in (a) and the line style is given in the legend in (b).

lower values of total thermal conductivity predicted by the Blottner model relative to Yos-Gupta, as observed in Figure 5.2c.

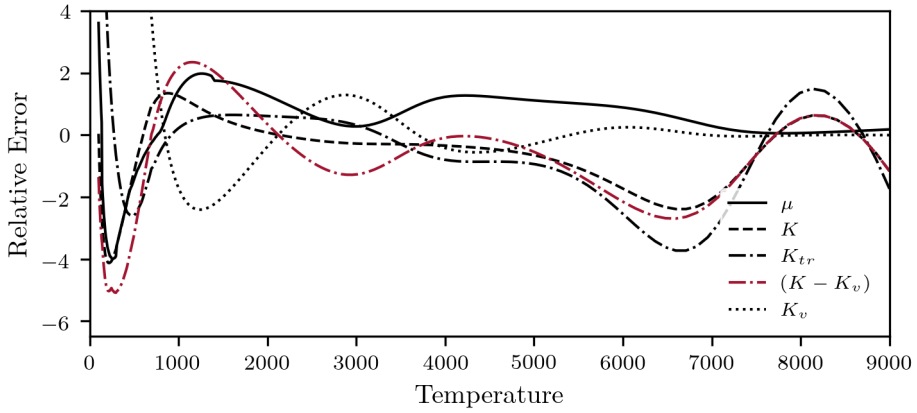

FIGURE 5.4: Relative error in percentage of each property against the respective reference model at each temperature.

Figure 5.4 presents the relative percentage error of the present model compared to the selected reference models over the full temperature range. For viscosity, the present model exhibits relatively higher errors at lower temperatures, with a maximum error of 4% at 300 K relative to the HLJ model, and errors below 2% for temperatures above 400 K when compared to the Yos-Gupta model. The total thermal conductivity K, calculated using Equation 5.1, shows small discrepancies, with a maximum error of approximately 4% at around 200 K. The ro-translational thermal conductivity K_{tr} exhibits a maximum error of 14% at 100 K, but remains below 4% for temperatures above 200 K. In addition, evaluating K_{tr} using Equation 5.5 results in a reduced maximum error of 5% at 300 K.

Errors in the vibrational thermal conductivity K_v at temperatures below 800 K can be neglected, as $K_v \ll K_{tr}$ in this regime.

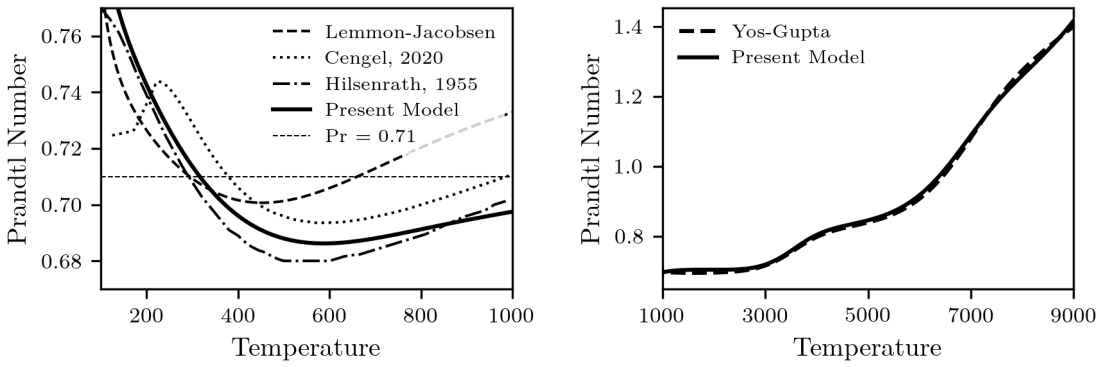

(a) Prandtl number against temperature for lower temperatures.

(b) Prandtl number against temperature for higher temperatures.

FIGURE 5.5: Comparison of Prandtl number from the present model against other data.

Figure 5.5 shows the Prandtl number, defined as $Pr = c_p\mu/K$, computed using the transport properties obtained from the present model and compared with values reported in the literature based on empirical and experimental data. For these comparisons, the specific heat of air was calculated using the NASA-9 polynomial fits (Mcbride et al., 2002). The selection of force constants in the Lennard-Jones model for viscosity has a notable influence on the agreement with different datasets. For instance, the force constants reported by Hirschfelder et al. (1954) show good agreement with the data of Hilsenrath et al. (1955), while those proposed by Lemmon and Jacobsen (2004) are inherently consistent with the Lemmon-Jacobsen model. The Prandtl number for air reported by Cengel et al. (2019) follows a trend similar to that predicted by the present model, albeit with a slight offset. Considering the significant scatter in experimental data above 400 K and the differences between the transport properties derived from the Yos-Gupta model and the Lemmon-Jacobsen data, the Prandtl number predicted by the present model is considered to lie within the range of available reference data.

Additional evaluations were conducted to assess the accuracy of the present model under varying pressure conditions and to examine its robustness when applied to arbitrary chemical compositions. These results are presented in Section 5.4.4.

5.4.2 Thermo-Chemical Non-Equilibrium (0D Heat Bath)

As an initial assessment of non-equilibrium behaviour, a zero-dimensional (0D) heat-bath configuration is considered. This simplified setup consists of a fluid at rest and is well suited for examining the evolution of viscosity and thermal conductivity under the influence of chemical reactions and vibrational relaxation. To evaluate the performance of the transport property formulation, including the correction given by Equation 5.6, a

heat-bath simulation was conducted in which the flow initially exists in a strongly thermal and chemical non-equilibrium state and subsequently relaxes towards equilibrium.

The simulation is initialised with a standard air composition at atmospheric pressure, a vibrational temperature of 300 K, a density of 0.05 $\mathrm{kg/m^3}$, and a pressure of 100,000 Pa. The corresponding translational temperature is approximately 7000 K, placing the system in a severe non-equilibrium regime. A time step of 2.0×10^{-8} s is used. Time integration was performed using both third- and fourth-order Runge–Kutta (RK) schemes, with the fourth-order scheme found to provide improved accuracy during the initial stages of highly non-equilibrium chemical relaxation. All results presented here were obtained using the fourth-order RK scheme with the time step specified above.

Figure 5.6 shows the temporal evolution of selected flow parameters as the system relaxes towards equilibrium using implementation (3) from Section 5.3. The evolution of the species mole fractions is shown in Figure 5.6a. As the simulation begins from a chemically non-equilibrium state, chemical reactions are initiated, leading to molecular dissociation and the formation of NO. The evolution of translational and vibrational temperatures is shown in Figure 5.6b, illustrating the transition from the initial vibrational non-equilibrium state to thermal equilibrium. The overshoot of the vibrational temperature above the translational temperature, followed by relaxation to equilibrium, is attributed to the ongoing chemical reactions. The markers in Figure 5.6a and Figure 5.6b correspond to simulations performed with half the original time step, demonstrating identical trends with errors on the order of 0.008%. This confirms the temporal convergence and validates the chosen time-integration scheme.

The temporal evolution of viscosity and thermal conductivity is shown in Figure 5.6c and Figure 5.6d, respectively. In both figures, different line styles correspond to different transport property models, while in Figure 5.6d different colours indicate the individual contributions to thermal conductivity. The transport properties predicted by the present model closely follow the trends obtained using the Yos-Gupta and Blottner formulations throughout the simulation. As the flow approaches the final equilibrium state, the present model exhibits very close agreement with the Yos-Gupta model. Throughout the non-equilibrium regime, the predictions of the present model remain consistently closer to those of Yos-Gupta than to Blottner, despite the simplified mixing-rule formulation employed.

5.4.3 Two-Dimensional and Three-Dimensional Mixing Layer

Mixing layers are canonical examples of inhomogeneous flows that have been widely used to study the properties of compressible turbulence (Ho and Huerre, 1984; Dimotakis, 1991). Starting from an initially laminar state, the transition to turbulence is triggered by a Kelvin-Helmholtz instability arising from the inflectional nature of the initial

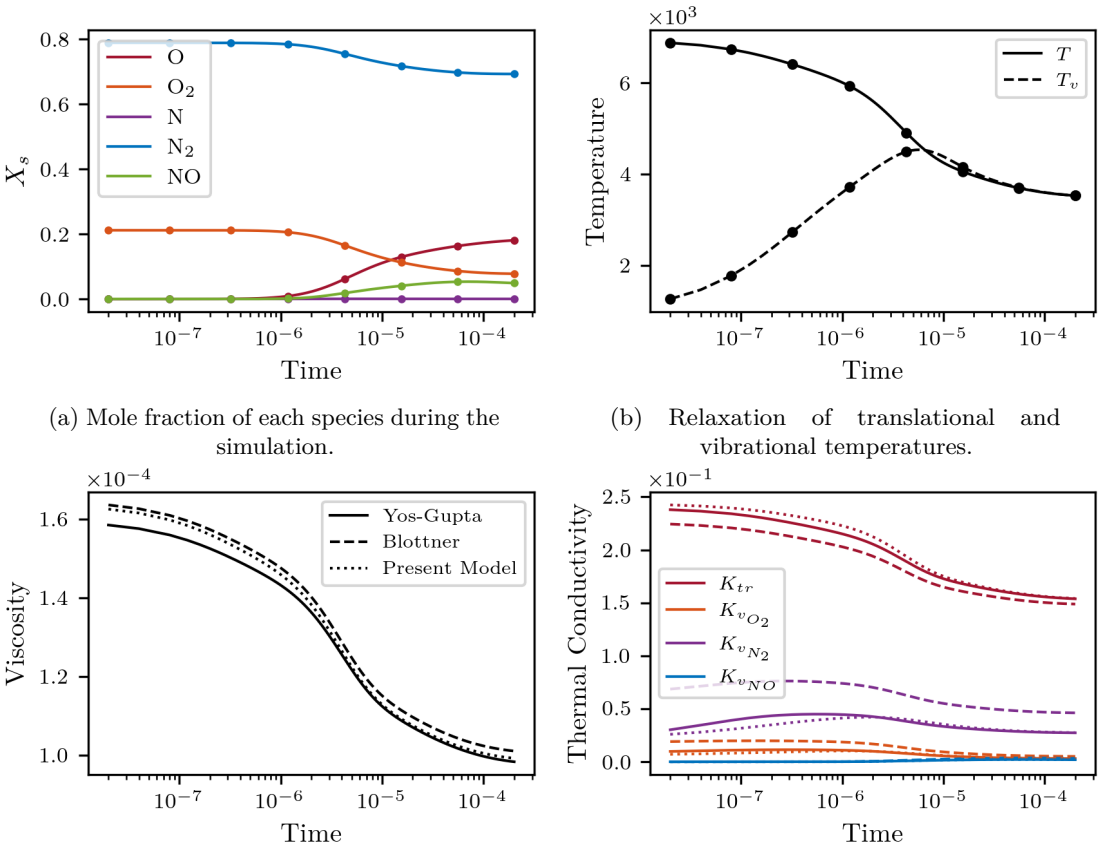

(a) Mole fraction of each species during the simulation.

(b) Relaxation of translational and vibrational temperatures.

(c) The viscosity calculated against time for the simulation.

(d) The thermal conductivity calculated against time for the simulation.

FIGURE 5.6: Heat bath simulation initiated from a highly non-equilibrium initial condition. The markers in (a) and (b) correspond to simulations performed with half the original time step, confirming the temporal numerical convergence.

velocity profile (Smits and Dussauge, 2006). This flow configuration has been extensively investigated in Chapter 4. In the present study, a temporally evolving mixing layer, periodic in the streamwise direction, is constructed in both two- and three-dimensional computational domains.

The initial velocity field consists of two uniform streams moving in opposite directions and is prescribed using a hyperbolic tangent profile. A perturbation is superimposed through the wall-normal velocity component to initiate the instability. The velocity components are defined as

$$u(x,y) = u_\infty \tanh\left(\frac{2y}{\delta_\omega}\right), \tag{4.27}$$

$$v(x,y) = A\, u_\infty \cos\left(\frac{2\pi x}{L_x}\right) \exp\left[-\frac{1}{10}\left(\frac{y}{\delta_\omega}\right)\right], \tag{4.28}$$

where u_∞ denotes the free-stream velocity, A denotes the magnitude of the disturbance set to 0.01, y the cross-stream direction, δ_ω the vorticity thickness, x the streamwise direction, and L_x the domain length in the streamwise direction. The temperature is initially uniform throughout the domain and equal to the free-stream temperature.

For the present simulations, the initial conditions and problem parameters are summarised in Table 5.4. The chemical composition of the flow is initialised close to equilibrium. Periodic boundary conditions are applied in the streamwise (x) direction, while extrapolation boundary conditions are imposed at the upper and lower boundaries of the domain. The domain length is set to $L_x = 0.044\,\mathrm{m}$ in the streamwise direction and $L_y = 0.197\,\mathrm{m}$ in the cross-stream direction, in order to minimise the influence of acoustic wave reflections on the mixing process. The computational grid consists of 180×325 points in the x and y directions, respectively, with a hyperbolic stretching applied in the y direction to increase resolution in regions of interest.

The grid resolution was selected following an initial sensitivity study, with further grid-sensitivity results presented later for the more demanding three-dimensional case. In addition, a binomial filter is applied near the upper and lower boundaries to attenuate acoustic waves, effectively approximating a quiet free-stream environment. For the modelling of the mixing-layer cases, the third approach described in Section 5.3 is employed.

TABLE 5.4: Initial conditions for the shear layer case.

$u_\infty(m/s)$	$\rho_\infty(kg/m^3)$	$p_\infty(Pa)$	$\Delta t(s)$	$\delta^\circ_\omega(m)$	Y°_{O}	$Y^\circ_{\mathrm{O_2}}$	Y°_{N}	$Y^\circ_{\mathrm{N_2}}$	Y°_{NO}
752.05	0.02	49271.1	5.0×10^{-8}	0.00417	0.208	0.000	0.227	0.562	0.003

Figure 5.7 illustrates the development of the two-dimensional mixing layer, with each panel representing the same spatial domain. Each column corresponds to a different non-dimensional time in the simulation, while each row illustrates a different flow parameter. Row (a) shows the passive scalar, providing a clear visualisation of the vortex roll-up process. As the vortex develops, the temperature at the vortex core decreases, while the temperature at the stagnation point increases. Chemical activity remains minimal, with less than a 3% change in composition, primarily due to the dissociation of N_2 into N in regions experiencing significant temperature variations. Given that chemical reaction timescales are much shorter than the characteristic flow timescales, the flow can be considered locally in chemical equilibrium.

Thermal non-equilibrium is primarily confined to the vortex core and to regions of flow expansion and compression, where the vibrational temperature lags behind the translational temperature. Row (b) and (c) of Figure 5.7 presents the absolute percentage relative difference in viscosity across the flow field, computed by comparing the Yos-Gupta model with the present and Blottner formulation, respectably. Row (d) and (e) shows the corresponding percentage difference in total thermal conductivity between the present

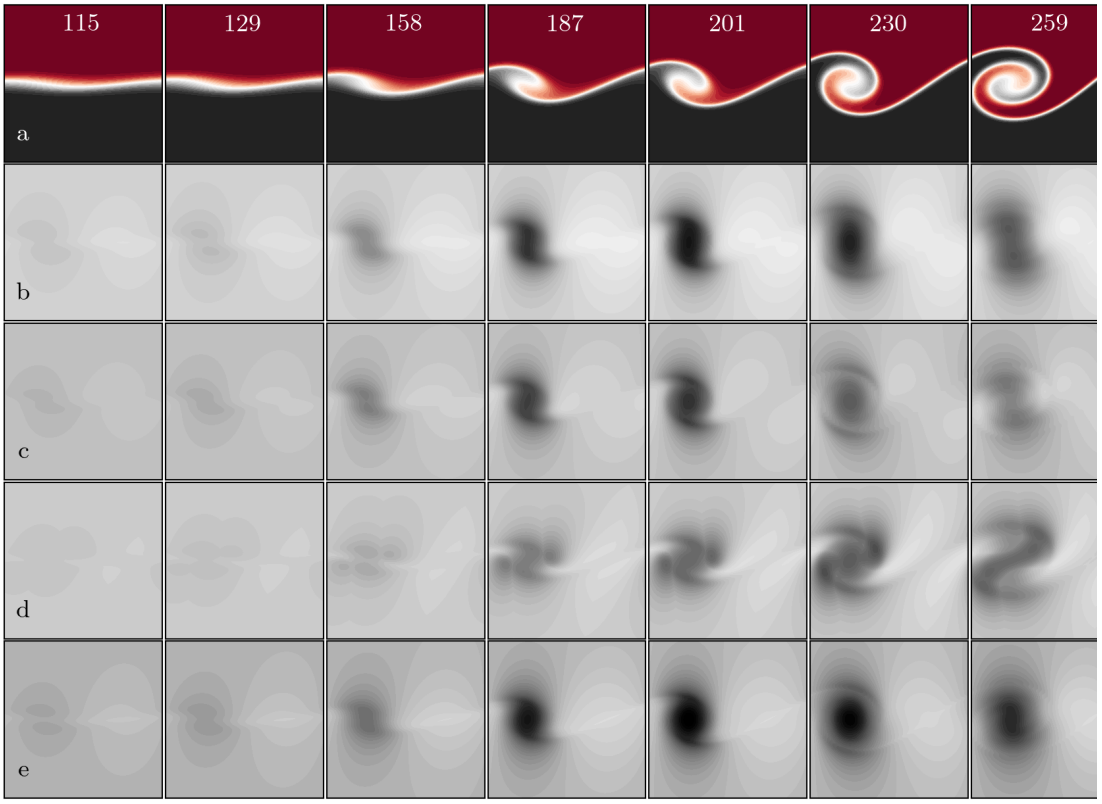

FIGURE 5.7: Error in viscosity and thermal conductivity of the present model and Blottner compared to the Yos-Gupta model, each column depicting a different non-dimensional time (τ_θ). (a) Passive scalar [min:-1, max:+1], (b) Error in viscosity for the present model in percentage [min:0.60, max:0.72], (c) Error in viscosity for the Blottner model in percentage [min:3.8, max:4.1], (d) Error in total thermal conductivity for the present model in percentage [min:2.0, max:2.3], (e) Error in total thermal conductivity for the Blottner model in percentage [min:6.8, max:7.2].

and Blottner model to Yos-Gupta. The present model exhibits a maximum error of 0.7% for viscosity and 2.2% for thermal conductivity.

In terms of spatial distribution of the present model, row (b) indicates that the largest viscosity deviations are localised within the vortex core. For thermal conductivity, row (d) reveals a similar error distribution, with additional discrepancies appearing in regions of thermal non-equilibrium where the vibrational temperature exceeds the translational temperature. For comparison, the Blottner model produces substantially larger maximum errors of 4.0% for viscosity and 7.1% for thermal conductivity under the same flow conditions.

Figure 5.8 illustrates a three-dimensional mixing layer under the same flow conditions as the corresponding two-dimensional case. Periodic boundary conditions are applied in the lateral directions, while extrapolation boundary conditions are imposed at the upper and lower boundaries, consistent with the two-dimensional configuration. The initial velocity profile and the imposed three-dimensional disturbance are defined as

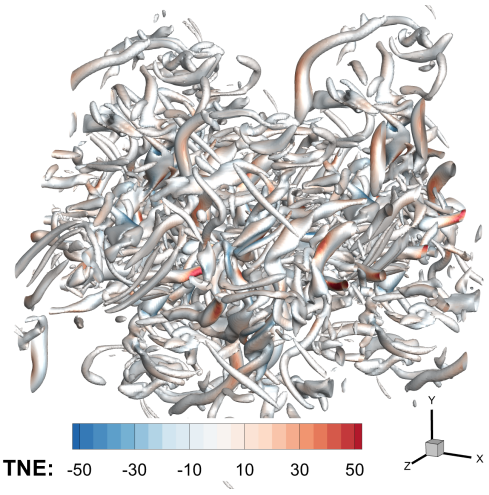

(a) Colour contours of thermal non-equilibrium $(T_v - T)$ superimposed on a Q-Criterion iso-surface at time $2.8 \times 10^{-4} s$.

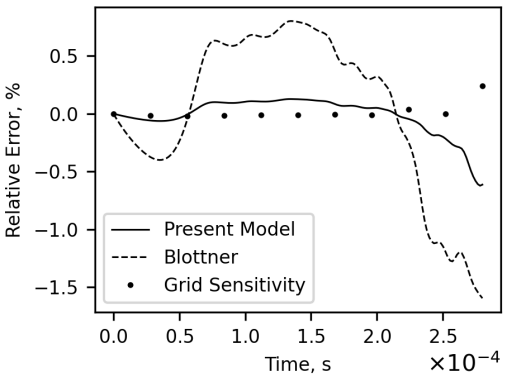

(b) Relative error of momentum thickness in percentage relative to Yos-Gupta, with dots showing the grid sensitivity of the Yos-Gupta results based on a fine grid simulation.

FIGURE 5.8: Three dimensional simulation of the mixing layer and comparison between the transport models.

$$u(x, y) = u_\infty \tanh\left(\frac{2y}{\delta_\omega}\right), \tag{4.27}$$

$$v(x, y, z) = A\, u_\infty \cos\left(\frac{2\pi x}{L_x}\right) \cos\left(\frac{2\pi z}{L_z}\right) \exp\left[-\frac{1}{10}\left(\frac{y}{\delta_\omega}\right)\right], \tag{4.29}$$

$$w(x, y) = 0 \quad , \tag{4.30}$$

where A denotes the magnitude of the disturbance set to 0.05, L_z denotes the domain length in the z direction, and w is the initial velocity component in the z direction. The temperature is initialised uniformly at the free-stream temperature. The grid resolution is set to $220 \times 385 \times 220$ points in the x, y, and z directions, respectively. The domain length in the z direction is chosen to be identical to that in the x direction, $L_z = 0.044\,\text{m}$.

Figure 5.8a shows iso-surfaces of the Q-criterion at a value of $6 \times 10^{10}\,\text{s}^{-2}$, coloured by contours of thermal non-equilibrium. The thermal non-equilibrium metric is defined as the difference between the vibrational and translational temperatures, $(T_v - T)$, and provides a measure of the degree of thermal non-equilibrium within the flow. Regions shown in red correspond to thermally hot states, where the vibrational temperature exceeds the translational temperature, while blue regions indicate thermally cold states, where the translational temperature is higher. By the end of the simulation at $t = 2.8 \times 10^{-4}\,\text{s}$, as shown in Figure 5.8a, the large-scale vortical structures have broken down into smaller-scale features.

Figure 5.8b compares the relative error in the non-dimensional momentum thickness predicted by the Blottner model and the present model with respect to the Yos-Gupta reference. The momentum thickness is a key indicator of the development of shear mixing layers. Consistent with the two-dimensional results, the Blottner model exhibits larger discrepancies relative to the Yos-Gupta formulation, whereas the present model shows close agreement. The markers in this figure correspond to simulations performed on a denser grid, refined by a factor of 1.6 in each spatial direction, and are included to demonstrate grid sensitivity and to validate grid convergence for the present case studies. As shown, the grid is effectively converged, with errors remaining close to zero throughout most of the mixing-layer development. Slight deviations observed in the dissipation region reflect differences in the turbulent structures resolved at different grid resolutions.

It should be noted that towards the end of the simulation the turbulent flow loses determinism, such that small perturbations in the initial conditions are sufficiently amplified to break spanwise symmetry. Consequently, the increased discrepancies observed at later times in Figure 5.8b are attributed to the transition from deterministic to stochastic turbulence dynamics, rather than to grid sensitivity or deficiencies in the transport property modelling.

Overall, this case provides a representative example of a three-dimensional flow exhibiting high-enthalpy effects and enables a comprehensive evaluation of the present model for predicting transport properties in complex thermo-chemical non-equilibrium turbulence.

5.4.4 Accuracy and Robustness

Two additional cases are considered in this section to further evaluate the accuracy and robustness of the present model. First, Figure 5.9 shows the transport properties calculated by the present model for equilibrium air at various constant pressures over a temperature range from 100 K to 9000 K. As the equilibrium composition depends on both pressure and temperature, variations in pressure lead to corresponding changes in the equilibrium composition at a given temperature. This case therefore serves as an effective assessment of the model's ability to capture the influence of chemically non-equilibrium conditions arising from pressure variations.

The present model produces reasonable agreement when compared with the more accurate Yos-Gupta formulation at high temperatures, with negligible differences observed for temperatures below 5000 K. In practical applications where turbulence is expected to develop, simulations at temperatures exceeding this range are typically associated with pressures above 10^4 Pa (Volpiani, 2021; Passiatore et al., 2023), for which the observed discrepancies are smaller. If required, the polynomial coefficients of the present model could be re-optimised for extreme pressure conditions using the same optimisation procedure described earlier.

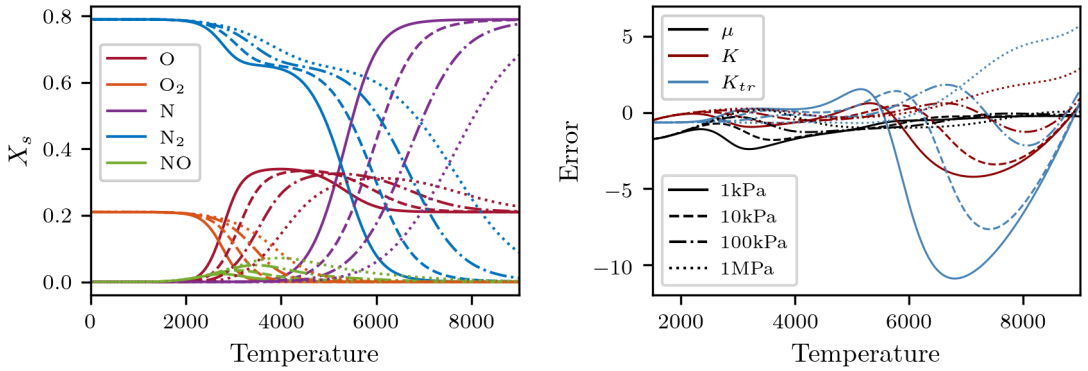

(a) Species mole fraction against temperature.

(b) Relative error for each property for different pressures.

FIGURE 5.9: Evaluation of the proposed viscosity and thermal conductivity model for varying pressures. Different line styles correspond to the pressures defined in the legend in (b).

Second, to assess the robustness of the present model under strongly chemically non-equilibrium conditions, a set of hundred randomly generated chemical compositions was considered and evaluated over a temperature range from 1000 K to 9000 K. For each composition, transport properties were computed using both the present model and the Yos-Gupta formulation, while holding the composition fixed across the temperature

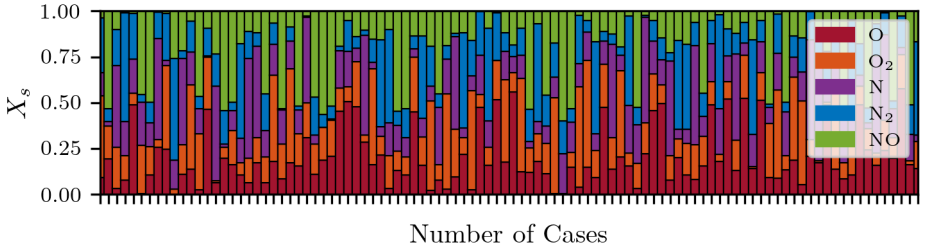

(a) The mixture composition of the 100 test cases evaluated.

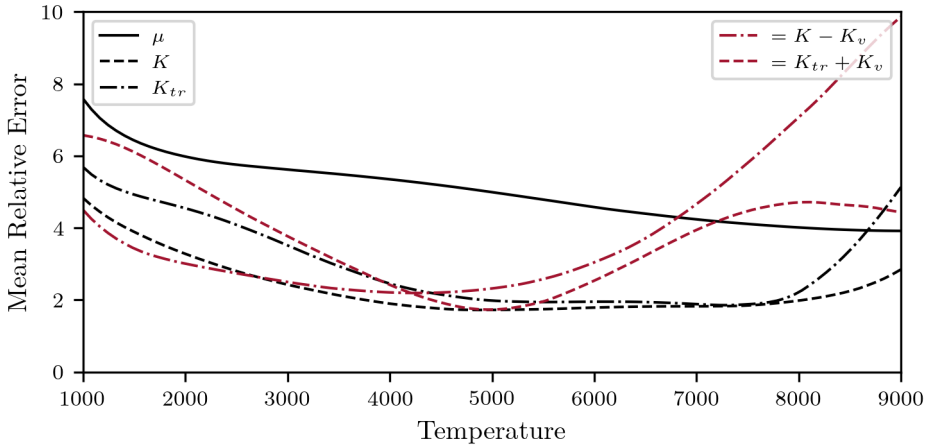

(b) The mean relative error of different terms across the temperature range evaluated.

FIGURE 5.10: Evaluation of the robustness of the present model in highly chemical non-equilibrium state.

range. The relative mean error was then calculated as a percentage through statistical analysis. This approach provides insight into the performance of the present model for highly chemically non-equilibrium mixtures. The resulting error distributions are shown in Figure 5.10.

5.4.5 Computational Performance

To assess the computational cost of the transport property models, simulations were performed on a single computational node using one NVIDIA A100 GPU. The computational cost was quantified in terms of the wall-clock run time, excluding input/output operations. Figure 5.11 presents the computing times for the different viscosity and thermal conductivity formulations employed in the two- and three-dimensional cases. Any observed differences in performance reflect the combined efficiency gains associated with both viscosity and thermal conductivity evaluations.

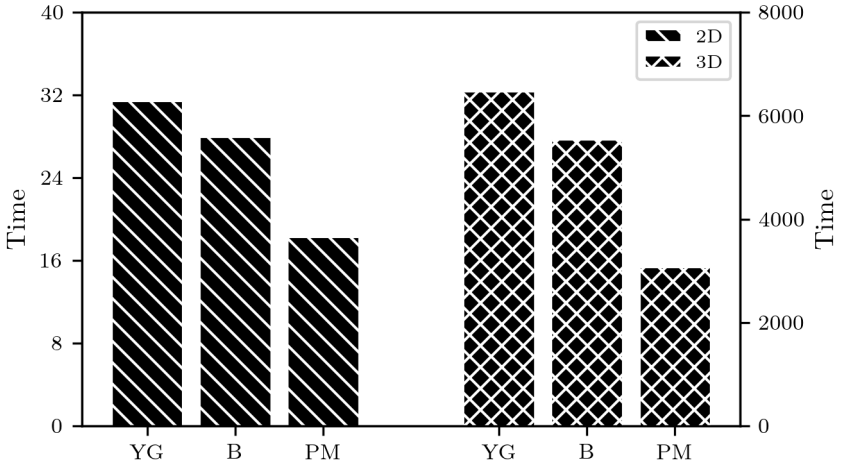

FIGURE 5.11: Computational cost of each model for a 2D and 3D mixing layer simulation, given in terms of time. YG: Yos-Gupta, B: Blottner, PM: Present Model.

For the two-dimensional simulations, the present model demonstrates a 45% improvement in computational efficiency relative to the Yos-Gupta formulation, while the Blottner model yields an 11% improvement. In the three-dimensional cases, the present model achieves a 58.5% increase in efficiency, compared to a 16.7% improvement obtained with the Blottner model relative to Yos–Gupta. Simulations employing constant viscosity and thermal conductivity were also conducted as a reference baseline.

These performance gains were obtained using a finite-difference solver that has been optimised across nearly all computational aspects, including reductions in work-array storage and the exploitation of automatic code generation techniques (Jammy et al., 2019). Under such conditions, the cost associated with evaluating transport properties becomes a comparatively significant contributor to the overall computational expense. Given the large number of operations required to compute viscosity and thermal

conductivity coefficients in the Yos-Gupta formulation, its impact on total run time is substantial. It is noted that smaller relative performance improvements would be expected in applications requiring shock-capturing schemes. Nevertheless, the combination of increased computational efficiency and consistent accuracy over a wide temperature range should make the present model attractive for use in scale-resolving simulations.

5.5 Conclusion

The objective of this chapter was to develop a streamlined and computationally efficient model for viscosity and thermal conductivity that maintains a balance between accuracy and performance. The proposed model is intended for five-species air (O, O_2, N, N_2, NO) under thermal and chemical non-equilibrium conditions. Viscosity and total thermal conductivity are represented using eight coefficients expressed as functions of species mole fraction and temperature, while the vibrational contribution to thermal conductivity is described using sixth-order polynomial expressions. In order to remain consistent with high-enthalpy non-equilibrium governing equations, the translational and rotational contributions to thermal conductivity are combined into a single ro-translational term, with the vibrational contribution specified separately for each molecular species. The explicit separation between molecular and atomic contributions improves accuracy in chemically non-equilibrium flows.

For equilibrium air at atmospheric pressure, the proposed viscosity model exhibits a worst-case error of approximately 4% at low temperatures and errors below 1.5% for temperatures above 3000 K relative to the reference model. The total and ro-translational thermal conductivity predictions remain within 4% error for temperatures exceeding 300 K. The Prandtl number computed using the proposed model shows an error of approximately 1.5% over the temperature range 150 K to 3000 K, with a maximum deviation of 3.5% relative to the reference Prandtl number. To assess the model under more practical flow conditions, additional validation cases were considered. These included a zero-dimensional heat-bath configuration exhibiting strong thermal and chemical non-equilibrium, as well as free shear layer simulations performed in both two and three dimensions, with the three-dimensional case including transition to turbulence. In the 0D heat-bath case, the proposed model demonstrated improved accuracy compared to the Blottner formulation when benchmarked against the Yos-Gupta model. In the two-dimensional mixing-layer simulation, the proposed viscosity model exhibited a maximum error of 0.7% throughout the flow evolution, compared to 4.0% for the Blottner model. For thermal conductivity, the maximum error of the proposed model was 2.2%, whereas the Blottner model exhibited errors of up to 7.1%. These case studies demonstrate that the proposed formulation accurately represents transport properties under thermo-chemical non-equilibrium conditions.

In terms of computational performance, the proposed model achieves a 45% reduction in run time for two-dimensional mixing-layer simulations relative to the Yos-Gupta model, while the Blottner model provides an 11% improvement. For three-dimensional simulations, the proposed model yields a 58.5% improvement in efficiency compared to Yos-Gupta, whereas the Blottner model achieves a 16.7% reduction in computational cost. Overall, the viscosity and thermal conductivity model developed in this chapter provides a favourable balance between accuracy and efficiency across a wide temperature range from 100 K to 9000 K. It closely matches the accuracy of the Yos-Gupta formulation while offering substantial computational savings and improved performance relative to the Blottner model under non-equilibrium conditions.

The modelling framework presented for viscosity and thermal conductivity provides a general approach as as middle ground for achieving both computational efficiency and improved accuracy relative to existing methods. In principle, the same framework could be extended to other chemical mixtures or to additional transport properties, such as diffusion coefficients.

5.6 Future Works

Based on the findings and developments presented in this chapter, several directions for future research can be identified to further extend the applicability and understanding of high-enthalpy transport property modelling. These are outlined below:

- **Inclusion of diffusion effects:** While the simulations presented in this chapter predominantly exhibited near-equilibrium chemical states, for which existing efficient polynomial formulations (e.g. those provided by Gupta) are sufficient for evaluating diffusion, future studies could focus on flows with a high degree of chemical non-equilibrium. In such cases, the diffusion models described in Section 2.4.3.2 could be simplified using the same polynomial-based framework developed in this chapter, thereby improving computational efficiency while retaining accuracy.
- **Extension to more multi-species air mixtures:** The present model has been optimised for a five-species air mixture. Future work could extend this framework to more complex air models involving seven to eleven species. In addition, ionisation effects could be incorporated by introducing additional expressions to account for contributions from electronic energy modes, thereby extending the applicability of the model to higher-temperature regimes.
- **Updated molecular collision data:** Much of the molecular collision data employed in classical models such as Yos–Gupta originates from studies conducted in the 1950s, where certain collision integrals were extrapolated to very high

temperatures (above 15,000 K). The availability of more recent molecular data for high-temperature collisions presents an opportunity to reassess and improve the representation of high-enthalpy effects on transport properties using updated datasets.

Chapter 6

Turbulent Channel Flow

6.1 Introduction

Following the study carried out on temporally developing mixing layers, one of the main observations was the distinct flow characteristics observed between turbulent deterministic and non-deterministic states. While the latter stages of the flow demonstrated a direct influence of the thermophysical state on turbulence characteristics, the mixing-layer configuration itself did not provide the most suitable framework for investigating high-enthalpy effects on fully developed, small-scale turbulent flows.

With the added benefit of a more efficient transport-property model derived in Chapter 5, the study of a fully developed channel flow under thermo-chemical non-equilibrium conditions emerged as a logical next step. The motivation for this investigation is further strengthened by the current gap in the literature regarding fully high-enthalpy, thermo-chemically reacting flows examined within a channel-flow framework.

The channel-flow configuration, extensively employed in the early development of direct numerical simulation (DNS), has proven to be a highly effective framework for the study of wall-bounded turbulence (Moin and Mahesh, 1998). Early experimental investigations of channel flows date back to 1929 and 1938, during which measurements of mean flow properties and velocity fluctuations in different flow directions were analysed. The first DNS of plane channel flow was conducted by Kim et al. (1987). This work was followed by numerous modified channel configurations incorporating effects such as rotation, heat transfer, mean three-dimensionality, transpiration, and riblets, as comprehensively reviewed by Moin and Mahesh (1998).

Kim et al. (1987) studied a channel flow with a centreline Reynolds number of $Re_c = 3300$ ($Re_\tau = 180$), where turbulence statistics were computed and compared with experimental data. Importantly, this work presented several statistical correlations that had not previously been evaluated experimentally. Subsequently, Coleman et al.

(1995) investigated compressible supersonic turbulent channel flow with isothermal wall conditions. The study was conducted at a bulk Mach number of $M_b = 1.5$, with a centreline Reynolds number of $Re_c = 3000$ and friction Reynolds numbers of $Re_\tau = 222$ and 451. Due to the isothermal wall condition, strong wall-normal gradients of mean density and temperature were present, which were found to enhance the streamwise coherence of near-wall streaks. The study also demonstrated that, with appropriate scaling, turbulence statistics were in good agreement with those from incompressible channel-flow simulations.

Subsequent work by Huang et al. (1995) extended this by conducting similar test cases with cold isothermal walls. Conventional Reynolds and Favre averaging techniques were compared for the evaluation of mean flow and turbulence statistics, and the differences between the two approaches were shown to be small, primarily confined to regions close to the wall. In addition, an extensive energy-budget analysis demonstrated that compressibility effects arising from turbulent density and pressure fluctuations were insignificant.

As a continuation of the work by Kim et al. (1987), Moser et al. (1999) performed channel-flow simulations at higher friction Reynolds numbers of $Re_\tau = 395$ and 590, and also repeated simulations at $Re_\tau = 180$. The study showed that increasing the Reynolds number significantly reduces low-Reynolds-number effects, such as shortened logarithmic layers and larger intercepts in the logarithmic velocity profile.

Moving towards higher friction Reynolds numbers, Hoyas and Jiménez (2006) carried out numerical simulations at $Re_\tau = 2003$ and briefly compared the results with those obtained at lower Reynolds numbers. The study concluded that fluctuation intensities, particularly those of the streamwise velocity component, do not scale well in wall units both near and away from the wall. The subsequent work of Hoyas and Jiménez (2008) expanded on these earlier simulations by examining the scaling behaviour of various flow quantities with increasing Reynolds number, while also presenting new energy budgets for the components of the Reynolds-stress tensor. More recent work includes that of Lee and Moser (2015), who conducted a direct numerical simulation of incompressible channel flow at a friction Reynolds number of $Re_\tau = 5186$. This study demonstrated several characteristic features of high-Reynolds-number wall-bounded turbulent flows, including the presence of a region where the mean velocity exhibits logarithmic behaviour, a logarithmic dependence of the variance of the spanwise velocity component, and a clear separation of scales between large outer-layer structures and small inner-layer structures.

When considering channel flows under thermo-chemical non-equilibrium conditions, relatively little work has been reported. Chen et al. (2024) investigated a temporally evolving high-enthalpy channel flow with finite-rate chemistry. In their study, a five-species air model was employed with isothermal wall conditions. For wall temperatures of 1733.2 K and 3500 K, the authors showed that turbulence intensity is weakened and mean

fluctuations are reduced when compared with cases without finite-rate reactions. The study was conducted using a finite-difference framework based on the OpenCFD-EC solver (Dang et al., 2022).

For studies involving other species, Cao et al. (2022) investigated supersonic turbulent channel flow of carbon dioxide using a three-temperature model. The numerical framework was based on a gas-kinetic scheme (GKS) employing the Bhatnagar–Gross–Krook (BGK) model, in which separate translational, rotational, and vibrational temperatures were considered. When comparing the one-temperature and three-temperature formulations, the study reported significant changes in the density and temperature fields, while only minor differences were observed in the Van Driest–transformed streamwise velocity.

It is evident that very limited research has been conducted on thermo-chemical non-equilibrium turbulent channel flows, particularly for thermally non-equilibrium air. While this may be partly attributed to the extensive body of work on high-enthalpy turbulent boundary layers (Williams et al., 2025; Duan and Martín, 2011; Passiatore, 2021; Huang et al., 2022; Passiatore et al., 2022; Knisely and Zhong, 2020; Zheng et al., 2024), a clear gap remains in the literature for thermo-chemical channel-flow configurations. Additionally, since thermo-chemical reactions can significantly alter the flow state and its characteristics, the use of turbulent channel flow as a canonical configuration to assess high-enthalpy effects across the channel can provide valuable insight into the influence of high-enthalpy phenomena on wall-bounded turbulent flows. Therefore, the objective of this chapter is to evaluate the influence of thermal and chemical non-equilibrium in a turbulent channel flow, serving as a canonical wall-bounded configuration to better understand the impact of high-enthalpy effects on wall turbulence.

6.2 Canonical Flow Setup

Channel flows are among the earliest configurations studied for turbulent flows. In this setup, the mean flow is in the x-direction, while the mean velocity varies significantly in the wall-normal (y) direction due to the presence of confining walls across the channel height h. The channel is periodic in the spanwise (z) direction such that the flow can be considered statistically homogeneous in z, with the mean cross-stream velocity in this direction equal to zero. For fully developed channel flows, the flow is statistically stationary and effectively one-dimensional, with velocity statistics depending only on the wall-normal coordinate y. Furthermore, channel-flow statistics are symmetric about the centreline, a feature that has also been confirmed experimentally (Pope, 2000).

6.2.1 Flow Characteristics

The bulk mean velocity is defined as

$$U_b = \frac{1}{2}\int_{-\delta}^{\delta} \bar{u}\, d\left(\frac{y}{\delta}\right) = \frac{1}{\delta}\int_{0}^{\delta} \overline{u}\, dy \quad , \tag{6.1}$$

where it is normalised by the wall-shear velocity. Using this value, the Reynolds numbers based on the half channel width (δ) can be evaluated as

$$Re_b = \frac{U_m\, 2\delta\, \rho}{\mu}, \qquad Re_c = \frac{u_c\, \delta\, \rho_c}{\mu_c}, \qquad Re_\tau = \frac{u_\tau\, \delta\, \rho_w}{\mu_w} \quad , \tag{6.2}$$

which correspond to the bulk Reynolds number, the centreline Reynolds number, and the friction Reynolds number, respectively. Consequently, the Mach numbers are defined as

$$M_b = \frac{U_b}{\sqrt{\gamma_w\, R\, T_w}}, \qquad M(y) = \frac{U}{\sqrt{\gamma\, R\, T}}, \qquad M_\tau = \frac{u_\tau}{a_w} \quad , \tag{6.3}$$

where the bulk Mach number M_b is based on the bulk velocity and the wall speed of sound, as defined by Coleman et al. (1995). The local Mach number $M(y)$ is based on the local velocity and local speed of sound, where all quantities vary with channel height, i.e. $U(y)$, $\gamma(y)$, $R(y)$, and $T(y)$. The specific heat ratio γ is evaluated using Equation 2.31. The friction Mach number M_τ is based on the wall speed of sound and the friction velocity u_τ, defined as

$$u_\tau = \sqrt{\tau_w/\rho_w} \quad , \tag{6.4}$$

where the wall shear stress is defined as

$$\tau_w = \rho_w\, \nu_w \left(\frac{d\overline{U}}{dy}\right)_{y=0} \quad . \tag{6.5}$$

The skin-friction coefficient for channel flow is defined as

$$C_f = \frac{\tau_w}{0.5\, \rho_w\, U_b^2}, \qquad C_{f_c} = \frac{\tau_w}{0.5\, \rho_w\, u_c^2} \quad , \tag{6.6}$$

where C_f is based on the bulk mean velocity, while C_{f_c} is based on the centreline velocity.

Similarly, a viscous length scale is defined as

$$\delta_\nu = \nu_w \sqrt{\frac{\rho_w}{\tau_w}} = \frac{\nu_w}{u_\tau} \quad . \tag{6.7}$$

The distance from the wall measured in viscous units (or wall units) is defined as

$$y^+ = \frac{y}{\delta_\nu} = \frac{u_\tau\, y}{\nu_w} \quad , \tag{6.8}$$

where y^+ is analogous to a Reynolds number in the sense that its magnitude indicates the relative importance of viscous and turbulent processes (Pope, 2000). Similarly, the velocity expressed in viscous units is defined as

$$u^+ = \frac{\overline{U}}{u_\tau} \quad . \tag{6.9}$$

The quantities y^+ and u^+ are widely used for flow characterisation and are employed throughout the following sections.

6.2.2 Statistical Terms

Reynolds and Favre averaged stresses assist in characterising turbulence and its nature when evaluating flow behaviour across the channel. In order to evaluate these quantities for the DNS simulations conducted in this study, two approaches may be adopted. In the first approach, the fluctuating fields are evaluated at each iteration step, followed by temporal averaging and subsequent spatial averaging. Alternatively, the mean flow components can be evaluated through temporal averaging, after which the fluctuating quantities are obtained relative to these mean components.

The latter approach is adopted in this chapter, where flow quantities are first averaged in time and the fluctuating terms are subsequently evaluated using the corresponding mean components. Consequently, the expressions for the fluctuating velocity components take the form

$$\overline{u_i' u_j'} = \overline{u_i u_j} - \overline{u_i}\ \overline{u_j} \quad , \tag{6.10}$$

$$\widetilde{u_i'' u_j''} = \frac{\overline{\rho u_i u_j}}{\overline{\rho}} - \left(\frac{\overline{\rho u_i}}{\overline{\rho}}\right)\left(\frac{\overline{\rho u_j}}{\overline{\rho}}\right) \quad , \tag{6.11}$$

where $\overline{u_i' u_j'}$ is the Reynolds averaged stresses and $\widetilde{u_i'' u_j''}$ is the Favre averaged stresses.

Similarly, the fluctuating Mach number terms are defined as

$$M_\mathrm{t} = \frac{\sqrt{\overline{u'u'} + \overline{v'v'} + \overline{w'w'}}}{\sqrt{\gamma R \overline{T}}} \quad , \tag{6.12}$$

$$M_\mathrm{rms} = \sqrt{\overline{M'M'}} = \sqrt{\frac{\overline{u'u'}}{\gamma R \overline{T}} + \frac{\overline{M}^2}{4\overline{T}^2}\overline{T'T'} - \frac{\overline{M}}{\overline{T}\sqrt{\gamma R \overline{T}}}\overline{u'T'}} \quad . \tag{6.13}$$

The turbulent Mach number (M_t) quantifies the intensity of velocity fluctuations relative to the mean speed of sound, whereas the Mach-number fluctuation (M_rms) measures the variability of the Mach number itself arising from coupled velocity and thermodynamic fluctuations.

The temperature fluctuation terms are similarly evaluated as

$$\overline{T'\,T'} = \overline{T\,T} - \overline{T}^{\,2} \quad , \tag{6.14}$$

$$\overline{T_v'\,T_v'} = \overline{T_v\,T_v} - \overline{T_v}^{\,2} \quad , \tag{6.15}$$

where the RMS of each term is calculated by $\phi_{\text{rms}} = \sqrt{\overline{\phi'\,\phi'}}$.

6.3 Numerical Setup

This section describes the numerical aspects of the simulation framework. Specifically, it outlines the initial disturbance imposed to trigger transition to turbulence, the forcing term used to sustain the channel flow, additional numerical modifications applied to the splitting forms to mitigate simulation breakdown, adjustments made to the boundary conditions to handle multi-species formulation, and the grid study conducted for the channel-flow domain.

6.3.1 Turbulence Transition

To promote transition from laminar to turbulent flow, an initial disturbance is imposed on the flow field across the channel domain. This disturbance is defined as

$$\begin{aligned}
u' &= A\,u_c\,\cos\!\left(\frac{4\,\pi\,x}{L_x}\right)\,\sin\!\left(\frac{\pi\,y}{\delta}\right)\,\sin\!\left(\frac{4\,\pi\,z}{L_z}\right) \quad , \\
v' &= -B\,u_c\,\left(1+\cos\!\left(\frac{\pi\,y}{\delta}\right)\right)\,\sin\!\left(\frac{4\,\pi\,x}{L_x}\right)\,\sin\!\left(\frac{4\,\pi\,z}{L_z}\right) \quad , \\
w' &= -C\,u_c\,\sin\!\left(\frac{\pi\,y}{\delta}\right)\,\sin\!\left(\frac{4\,\pi\,x}{L_x}\right)\,\cos\!\left(\frac{4\,\pi\,z}{L_z}\right) \quad ,
\end{aligned} \tag{6.16}$$

where u_c is the velocity at the centre of the channel, and A, B, and C are constants defining the initial magnitude of the imposed disturbance, set to 0.1 in this study. Additionally, x, y, and z denote the grid-point coordinates in the streamwise, wall-normal, and spanwise directions, respectively, while L_x, L_y, and L_z represent the corresponding domain lengths.

6.3.2 Forcing Term

For fully developed turbulent channel flows, the mean velocity in the spanwise direction is zero, and the mean streamwise velocity is independent of the streamwise coordinate x. In addition, the no-slip boundary condition enforces zero mean velocity at the wall in the wall-normal direction. Under these assumptions, the mean continuity equation

reduces to

$$\frac{d\overline{v}}{dy} = 0.$$

Considering the mean lateral momentum equation, it follows that the mean axial pressure gradient is uniform across the channel (Pope, 2000), such that

$$\frac{d\overline{p}}{dx} = \frac{dp_w}{dx} \quad . \tag{6.17}$$

Similarly, the mean axial momentum equation reduces to $d\tau/dy = dp_w/dx$, where the total shear stress across the channel height is defined as

$$\tau = \rho\nu\frac{d\overline{U}}{dy} - \rho\,\overline{uv} \quad . \tag{6.18}$$

This expression shows that the total shear stress is composed of the viscous stress, $\rho\nu\, d\overline{U}/dy$, and the Reynolds stress, $-\rho\overline{uv}$. It also illustrates the force balance in which the axial pressure gradient is balanced by the wall-normal gradient of shear stress. Consequently, the pressure gradient can be expressed explicitly in terms of the wall shear stress as (Pope, 2000)

$$\Phi = -\frac{d\overline{p_w}}{dx} = \frac{\tau_w}{\delta} \quad , \tag{6.19}$$

Equation 6.19 indicates that the flow is driven by the pressure drop between the channel inlet and outlet. For a fully developed turbulent channel flow, this pressure difference is balanced by the shear-stress on the channel walls. Consequently, for a prescribed pressure gradient, the resulting wall shear stress is determined, or conversely, for a given wall shear stress, the pressure gradient required to drive the flow can be specified. In the simulations performed using OpenSBLI, Equation 6.19 is employed to define the forcing term for all cases.

6.3.3 Wall Boundary Condition

For a viscous fluid interacting with a solid wall, the no-slip condition dictates that the velocity at the wall is zero. As a result, there is no need to solve the momentum equation at the wall, and the convective terms conveniently reduce to the pressure terms alone (Blazek, 2015). Hence,

$$u_j|_w = 0 \quad . \tag{6.20}$$

For a wall at a fixed temperature (isothermal wall), the total energy at the wall can be computed using the specified temperature. By assuming a constant species concentration along the wall (i.e., a non-catalytic wall) and constant pressure, the density of each

species at the wall can be expressed as

$$\rho_s|_w = Y_s^{+1} \frac{p^{+1}}{R^{+1} T_w} \quad , \tag{6.21}$$

where $\rho_s|_w$ is the species density at the wall. Here, the superscript $+1$ denotes the first grid point above the wall. With the momentum and density defined, the vibrational energy can be calculated, followed by the total energy.

The treatment of the halo points differs slightly where

$$T^{-l} = 2\, T_w - T^{+l} \qquad u_j^{-l} = -u_j^{+l} \tag{6.22}$$

$$\rho_s^{-l} = \rho_s^{+l} \qquad E^{-l} = E^{+l} \quad . \tag{6.23}$$

The superscript l ranges from 1 to the number of halo points. The index $-l$ refers to the halo points below the wall, while $+l$ refers to stencil points above the wall.

This wall boundary condition is based on two key assumptions. First, a zero normal gradient of the species concentration s is imposed at the wall. While this formulation is formally classified as non-catalytic, the zero-gradient condition allows the wall composition to adjust dynamically in response to the near-wall flow state rather than enforcing a prescribed surface composition. Second, thermal equilibrium is assumed at the wall, such that $T_w = T_{v,w}$. Unless stated otherwise, all simulations presented in this section employ this boundary condition. Recent studies have, however, investigated the impact of relaxing the thermal-equilibrium assumption by accounting for thermal non-equilibrium effects at the wall (Kustova et al., 2012).

6.3.4 Split Formulation of Convective Terms

Central finite-difference schemes are non-dissipative and therefore enable highly accurate evaluation of smooth regions of the flow. However, the low level of numerical dissipation can lead to difficulties when simulating shock waves or highly vortical structures. In practice, aliasing errors arising from the non-linearity of the convective terms in the equations of motion must be addressed. Energy-conserving or skew-symmetric schemes form a class of numerical approaches that mitigate these issues by controlling the transfer of energy across scales (Josyula, 2015).

The use of secondary conservation properties has deep roots in computational fluid dynamics. One prominent approach to achieving numerical stability is through the conservation of kinetic energy. Notable examples include the works of Kennedy and Gruber (2008) and Pirozzoli (2010), which employ innovative splittings of the non-linear conservative terms to derive stable formulations. Three such schemes have been discussed in Section 2.5.1, namely the Blaisdell, Feiereisen, and KGP formulations.

While the Blaisdell scheme was shown to provide stable results for the mixing layer simulations presented in the previous chapters, it was observed that, for channel flow configurations, the scheme does not offer sufficient robustness. In these cases, aliasing errors were found to grow over long simulation times, ultimately leading to numerical instability. For this reason, the non-linear convective terms in the momentum, vibrational energy, and total energy equations are split using the cubic KGP formulation, whereas the species mass conservation terms and the pressure work contribution in the energy equation are expanded using the quadratic Blaisdell scheme.

Accordingly, the convective terms and their corresponding expanded forms are given as follows.

$$\frac{\partial(\rho_s u_j)}{\partial x_j} = \frac{1}{2}\left(\frac{\partial(\rho_s u_j)}{\partial x_j} + u_j\frac{\partial \rho_s}{\partial x_j} + \rho_s\frac{\partial u_j}{\partial x_j}\right) \quad . \tag{6.24}$$

$$\begin{aligned}\frac{\partial(\rho u_j u_i)}{\partial x_j} = &\frac{1}{4}\frac{\partial(\rho u_j u_i)}{\partial x_j} + \frac{1}{4}\left(u_i\frac{\partial(\rho u_j)}{\partial x_j} + \rho u_j\frac{\partial u_i}{\partial x_j} + u_j\frac{\partial(\rho u_i)}{\partial x_j} + \rho u_i\frac{\partial u_j}{\partial x_j}\right)\\ &+ \frac{1}{4}\left(\rho\frac{\partial(u_j u_i)}{\partial x_j} + u_i u_j\frac{\partial \rho}{\partial x_j}\right)\end{aligned} \tag{6.25}$$

$$\begin{aligned}\frac{\partial(\rho e_{v,s} u_j)}{\partial x_j} = &\frac{1}{4}\frac{\partial(\rho e_{v,s} u_j)}{\partial x_j} + \frac{1}{4}\left(\frac{\rho e_{v,s}}{\rho_s}\frac{\partial}{\partial x_j}\left(\rho u_j\frac{\rho_s}{\rho}\right) + \rho u_j\frac{\rho_s}{\rho}\frac{\partial}{\partial x_j}\left(\frac{\rho e_{v,s}}{\rho_s}\right)\right)\\ &+ \frac{1}{4}\left(u_j\frac{\partial(\rho e_{v,s})}{\partial x_j} + \rho e_{v,s}\frac{\partial u_j}{\partial x_j} + \rho_s\frac{\partial}{\partial x_j}\left(u_j\frac{\rho e_{v,s}}{\rho_s}\right) + u_j\frac{\rho e_{v,s}}{\rho_s}\frac{\partial \rho_s}{\partial x_j}\right)\end{aligned} \tag{6.26}$$

$$\begin{aligned}\frac{\partial(\rho E u_j)}{\partial x_j} = &\frac{1}{4}\frac{\partial(\rho E u_j)}{\partial x_j} + \frac{1}{4}\left(\frac{\rho E}{\rho}\frac{\partial(\rho u_j)}{\partial x_j} + \rho u_j\frac{\partial}{\partial x_j}\left(\frac{\rho E}{\rho}\right) + u_j\frac{\partial(\rho E)}{\partial x_j} + \rho E\frac{\partial u_j}{\partial x_j}\right)\\ &+ \frac{1}{4}\left(\rho\frac{\partial}{\partial x_j}\left(u_j\frac{\rho E}{\rho}\right) + u_j\frac{\rho E}{\rho}\frac{\partial \rho}{\partial x_j}\right)\end{aligned} \tag{6.27}$$

$$\frac{\partial(p u_j)}{\partial x_j} = \frac{1}{2}\left(\frac{\partial(p u_j)}{\partial x_j} + p\frac{\partial u_j}{\partial x_j} + u_j\frac{\partial p}{\partial x_j}\right) \tag{6.28}$$

6.3.5 Grid Convergence

Conducting grid studies, including convergence assessments or sensitivity analyses, is a fundamental requirement for any computational fluid dynamics simulation. A commonly accepted approach is to systematically increase the grid resolution in all spatial directions until the results exhibit negligible variation (Cummings et al., 2015). This method seems to be technically sufficient for canonical channel flow simulations.

As one of the most prominent studies on turbulent channel flows, the work of Coleman et al. (1995) was used as a reference for the present channel flow configuration. Accordingly, the centreline Mach number (M_c) was set to 1.5, the Reynolds number based on the bulk mean velocity (Re_b) was set to 3000, and the friction Reynolds number (Re_τ) was set to 222. The thermo-chemical equilibrium flow model was employed, assuming a constant

TABLE 6.1: Initial parameters for the channel flow grid study.

$u_\circ$	$p_\circ$	$\rho_\circ$	T_{wall}	Φ	δ	β
1862.645	18124.52	0.02	3000	-4181.369	0.00790885	1.2

TABLE 6.2: Grid specification for each refinement step.

Refinement Factor	Δt	N_{iter}	N_x	N_y	N_z
1.0	2.250×10^{-7}	2700	180	181	180
1.5	1.500×10^{-7}	4050	270	271	270
2.25	1.000×10^{-7}	6075	404	405	404
3.375	0.625×10^{-7}	9720	648	647	648

Schmidt number and using the transport property model described in Chapter 5. The computational domain dimensions were $4\pi\delta$, $4\pi\delta/3$, and $4\pi\delta$ in the x, y, and z directions, respectively, where h denotes the half-channel height. Periodic boundary conditions were applied in the streamwise and spanwise directions, while no-slip isothermal wall boundary conditions were imposed at the top and bottom walls. Grid stretching (β) was applied towards the wall boundaries to increase grid density in regions with high velocity and temperature gradients, a characteristic of channel flow configurations. The formulation used for the grid stretching is detailed in Section 2.5.3. The initial flow parameters and simulation settings used for this study are summarised in Table 6.1.

To conduct the grid study, the number of grid points in all spatial directions was increased simultaneously by a constant factor of 1.5. Table 6.2 lists the four simulations performed, along with their corresponding grid resolutions and time-step sizes, which were adjusted to satisfy numerical stability requirements.

As previously discussed, channel flows are statistically one-dimensional. Therefore, when selecting quantities for evaluation, two categories were considered. First, a series of local quantities (varying in the y direction while averaged over the x and z directions) was examined. Second, more global statistical quantities were evaluated.

Figure 6.1 presents the results of the grid study, where the local quantities are shown in Figure 6.1a and the statistical quantities are illustrated in Figure 6.1b. In both cases, the quantities have been normalised by the most refined case (refinement factor of 3.375), allowing for a unified comparison across all grid resolutions. For both categories of quantities, clear convergence is observed as the grid is progressively refined, although the rate of convergence differs between them. As shown in Figure 6.1a, the centreline quantities exhibit satisfactory convergence from a refinement factor of 1.5 onwards for temperature (T), pressure (p), and density (ρ), with errors below 1%. In contrast, the velocity shows larger discrepancies, with errors of approximately 3% for the refinement factor of 1.5, reducing to below 1% for the refinement factor of 2.25. Similar convergence

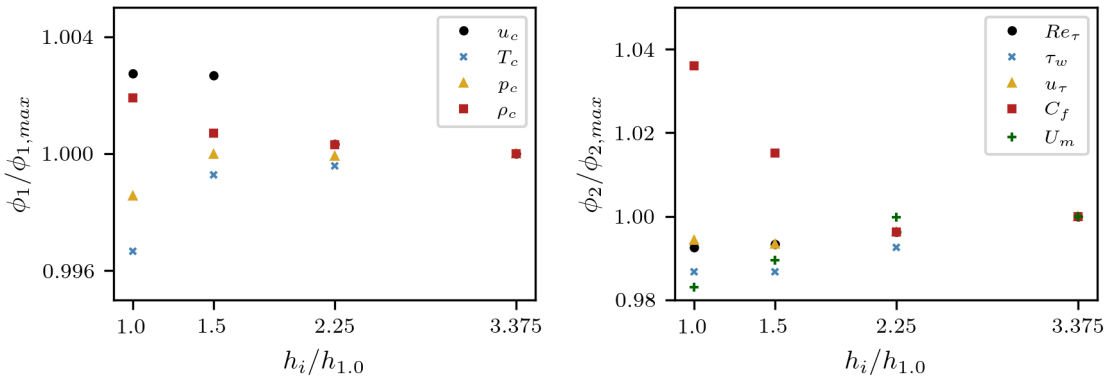

(a) Normalised local (y-dependent) quantities for each refinement factor.

(b) Normalised statistical (y-dependent) quantities for each refinement factor.

FIGURE 6.1: Quantities evaluated in the grid study, demonstrating convergence as the grid is refined.

trends are observed for the statistical quantities, albeit with generally lower errors; for a refinement factor of 1.5, the flow statistics converge with errors below 2%.

Table 6.3 presents additional quantities evaluated at each refinement factor for the grid study. More global measures, such as the bulk Reynolds number (Re_b), bulk velocity (u_b), and bulk density (ρ_b), are also included.

Overall, based on the convergence behaviour observed, it can be concluded that a stretching factor of 1.5 or higher is acceptable for the evaluation of statistical quantities. However, local quantities—particularly the velocity—may require a refinement factor of 2.25 or greater to achieve comparable levels of accuracy. As a general conclusion for the subsequent simulations, a refinement factor of 1.5 provides a reasonable balance between accuracy and computational cost, yielding errors on the order of 2% while avoiding excessive demands on computational resources.

TABLE 6.3: Grid refinement study results for key flow parameters.

Variable	1.0	1.5	2.25	3.375
τ_w	215.63	215.63	216.92	218.52
u_τ	91.600	91.526	91.796	92.133
Re_τ	212.87	213.04	213.69	214.48
Re_c	2909.1	2899.8	2891.2	2888.5
Re_b	2500.1	2511.6	2533.6	2533.6
C_f	0.0081273	0.0079641	0.0078156	0.0078452
$C_{f,c}$	0.005633	0.0056405	0.0057031	0.0057509
M	1.4992	1.5090	1.5247	1.5250
ITKE	0.91111	0.94480	0.96506	0.95738
u_b	1646.0	1656.8	1674.0	1674.3
ρ_b	0.019585	0.019727	0.019809	0.019873
μ_b	0.00010198	0.00010292	0.00010351	0.00010387

6.4 Validation

To validate the channel flow configuration, the results reported by Coleman et al. (1995) are compared with a corresponding flow simulation conducted using OpenSBLI. The numerical model employed in the present study is a multi-species thermo-chemical equilibrium formulation, where the flow properties and the evaluation of transport parameters, such as viscosity and thermal conductivity, were adjusted to match those specified in Coleman et al. (1995).

The differences between the two simulations are substantial. The work of Coleman et al. (1995) employs a Fourier-Legendre spectral discretisation with a hybrid implicit-explicit third-order, four-substep time-advancement method, whereas the present study uses a fourth-order central finite-difference scheme coupled with a fourth-order Runge-Kutta method for time discretisation. Furthermore, the reference case is formulated as a non-dimensional single-mixture/species flow with constant specific heat and Prandtl number, and viscosity modelled using a simple power-law relationship. The flow is driven by maintaining a constant mass flux across the channel, rather than a constant pressure gradient, which is used in the simulations carried out in this study. Additionally, the multi-species formulation adopted here accounts for vibrational energy contributions, which are neglected in the reference case.

To facilitate validation, the viscosity power-law model was implemented, and both the specific heat and Prandtl number were set to constant values when evaluating the transport properties. Although the original multi-species formulation considers contributions from vibrational energy, the simulations were performed for air at 300 K; therefore, the evaluation and contribution of vibrational energy were omitted. The reference temperature was kept low to remain consistent with the intent of the validation case, where high-enthalpy effects are not considered. As an additional measure, to assess the influence of non-dimensionalisation, two different flow states were examined for the dimensional multi-species formulation, such that their corresponding non-dimensional states would match but their dimensional densities differ.

Table 6.4 presents the physical parameters and time-averaged results for the cases considered in this section. The Mach number is defined based on the bulk velocity and the wall speed of sound. The bulk Reynolds number, Re_b, is based on the bulk density, bulk velocity, channel half-width, and wall viscosity. The centreline and friction Reynolds numbers (Re_c and Re_τ) are expressed as defined in Equation 6.2. All remaining parameters are non-dimensionalised using the wall temperature, channel half-width, bulk velocity, and bulk-averaged density. In all cases, the specific heat ratio γ is set to 1.4, the Prandtl number is fixed at 0.7, and the viscosity is modelled using a power-law relationship, with the dimensional form given by $\mu = \mu_w \left(T/T_w\right)^{0.7}$.

TABLE 6.4: DNS physical parameters and time-averaged results reported by Coleman et al. (1995).

M	M_c	Re_m	Re_c	Re_τ	$\frac{\overline{\rho_w}}{\rho_{bulk}}$	$\frac{\overline{\rho_c}}{\rho_{bulk}}$	$\frac{\overline{T_c}}{\overline{T_w}}$	$\frac{\overline{\mu_c}}{\mu_w}$
1.5	1.502	3000	2760	222	1.355	0.980	1.378	1.252

Table 6.5 presents the physical and simulation parameters for the OpenSBLI cases considered in this study. As reiterated, the non-dimensional states for both cases match those reported in Table 6.4. To reproduce the same flow conditions as those given by Coleman et al. (1995), the bulk velocity, u_b, is determined using the bulk Mach number, M_b, and the speed of sound evaluated at the wall temperature, T_w. The bulk density is subsequently calculated using the bulk Reynolds number, Re_b.

Using the shear Mach number at the wall, M_τ, the shear velocity, u_τ, is obtained based on the speed of sound under wall conditions. Since the simulations are carried out in dimensional form, the channel half-height, δ, is then calculated using Re_τ together with wall properties and u_τ. The wall shear stress is computed as $\tau_w = u_\tau^2 \rho_w^4$, where ρ_w is expressed as a ratio with respect to the reference density, ρ_{ref}. The pressure gradient driving the flow, i.e. the forcing term, is then calculated as $\Phi = u_\tau^2 \rho_w / \delta$.

The dimensional wall pressure is evaluated using the ideal gas law, while the initial centreline velocity, u_c, is defined using the centreline Reynolds number. It is noted, however, that the centreline velocity may also be imposed as an initial estimate, since the applied forcing adjusts this quantity during the simulation. The grid dimensions in each spatial direction are defined in terms of the channel half-height, with $4.0\delta\pi$, 2δ, and $4.0\delta\pi/3$ corresponding to the x, y, and z directions, respectively. The number of grid points is set to 250, 289, and 250 along the x, y, and z directions, respectively, with a stretching factor of $\beta = 1.3$ applied in the wall-normal (y) direction.

TABLE 6.5: Initial conditions for the simulations carried out on OpenSBLI.

Case	u_c°	$p_\circ$	$\rho_\circ$	T_{wall}	dt	Φ	δ
A	521.7	105847.6	1.225	300	1×10^{-9}	-15596142	0.00008657
B	601.3	1728.12	0.02	300	6×10^{-8}	-4157.24	0.00530231

The simulation is initialised with a constant temperature, pressure, and density across the channel. The composition is assumed to be air at standard atmospheric conditions, with frozen mass fractions of $Y_{O_2} = 0.21$ and $Y_{N_2} = 0.79$. The initial velocity profile is defined as

$$u^\circ(y) = u_c^\circ \left(1.0 - \left(\frac{y}{\delta}\right)^{6.0}\right), \tag{6.29}$$

where y denotes the wall-normal location across the channel height in the y-direction, and δ is the half channel height. Additionally, the initial disturbance used to trigger transition to turbulence is defined in Equation 6.16. The initial species densities are calculated using the ideal gas law, with the pressure specified during the definition of the simulation parameters and the wall temperature. For cases in which vibrational energy is considered, the vibrational energy is evaluated using the translational temperature, and its contribution is added to the total energy. This contribution is omitted for cases where vibrational energy effects are not included.

Since the simulation is initialised with a constant temperature and density across the channel height, the flow must be evolved for a sufficient duration to allow transition to turbulence and subsequent statistical stabilisation, such that local flow quantities converge to their steady statistical values. Figure 6.2 illustrates the duration in seconds for which the simulation was run prior to reaching this statistically converged state, based on local parameters evaluated at every other iteration. The shaded region indicates the time interval over which data were averaged to obtain the mean flow quantities, corresponding to approximately 150 000 iterations required for convergence, followed by an additional 150 000 iterations used for statistical averaging.

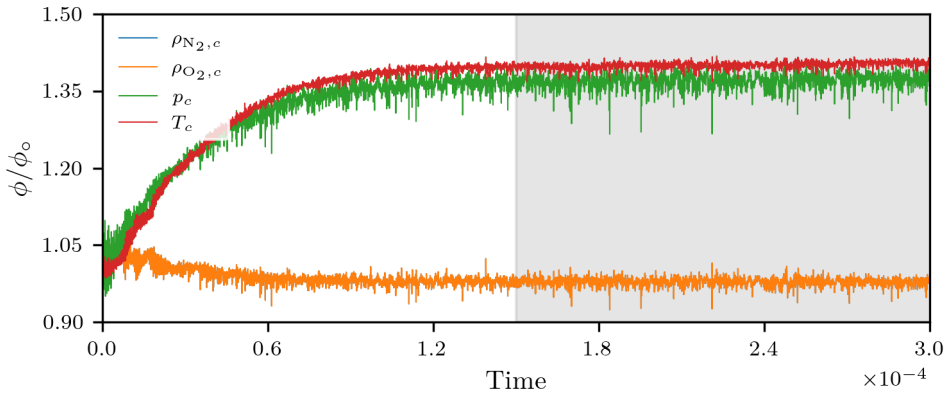

FIGURE 6.2: Flow convergence for the channel flow validation case. The shaded region indicates the time interval over which statistical averaging was performed.

Results

To compare the results, the parameters selected for comparison were first extracted from the reference work of (Coleman et al., 1995). As the data were manually extracted from the published figures, polynomial fits were constructed for each quantity to facilitate quantitative comparison.

Figure 6.3 presents the results for Case A, in which the flow properties correspond to air density at atmospheric conditions. A selection of mean local quantities, expressed as functions of the channel height, is shown, including temperature, density, and velocity (Figure 6.3a). In addition, the local Mach number and Reynolds number distributions are

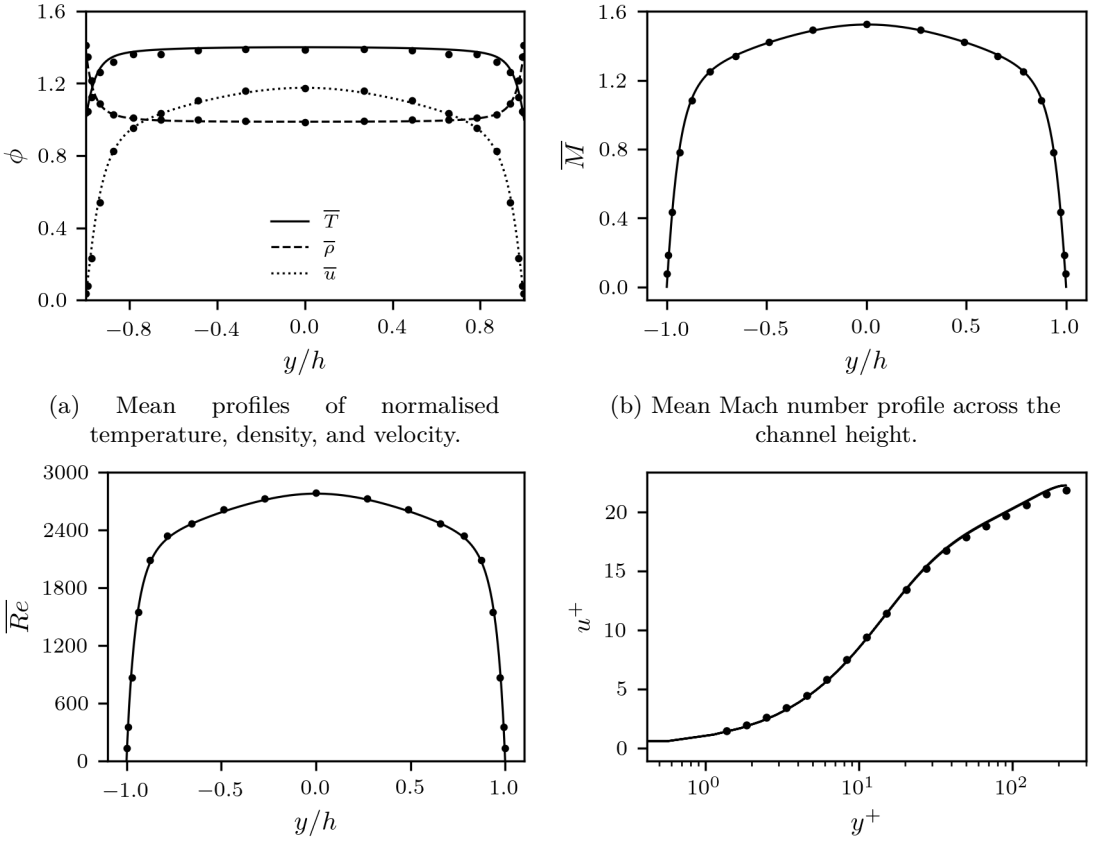

(a) Mean profiles of normalised temperature, density, and velocity.

(b) Mean Mach number profile across the channel height.

(c) Mean Reynolds number profile across the channel height.

(d) Mean velocity profile in wall-normal coordinates, expressed in viscous units.

FIGURE 6.3: Mean flow quantities for a fully developed turbulent channel flow for the validation of Case A. Markers on each figure represent the same quantity evaluated by Coleman et al. (1995).

presented in Figure 6.3b and Figure 6.3c, respectively. Finally, the mean velocity profile against wall-normal coordinates in viscous units for the channel flow cases is compared in Figure 6.3d. In all figures, the markers represent the data reported by Coleman et al. (1995).

The mean density (dashed line) and velocity (dotted line) profiles shown in Figure 6.3a exhibit excellent agreement with those reported by Coleman et al. (1995), while the temperature (solid line) profile is observed to be slightly higher in the near-wall region. Similarly, the mean local Mach number, mean local Reynolds number, and the mean velocity profile expressed in wall coordinates (viscous units) show strong agreement with the reference data, as demonstrated in Figure 6.3b-6.3d.

Table 6.6 summarises the numerical results for the three cases considered, namely the reference case from Coleman et al. (1995) and the two OpenSBLI cases with differing flow states. While good agreement is observed between the OpenSBLI simulations and the reference data, there is negligible difference between the two cases simulated at

different densities. This further reinforces that the multi-species channel flow formulation employed in this study is consistent with the behaviour reported in the literature.

TABLE 6.6: Flow properties for the different simulation cases.

Case	M_c	Re_c	Re_τ	$\overline{\rho}_w$	$\overline{\rho}_c$	$\overline{T}_c$	c_f
Coleman	1.502	2760	222	1.355	0.980	1.378	–
Case A	1.5214	2770.9	222.24	1.389	0.988	1.4007	0.0078023
Case B	1.525	2776.6	223.16	1.391	0.988	1.4028	0.0078163

6.5 High Enthalpy Turbulent Channel Flow

High-enthalpy channel flows are characterised by extreme thermal conditions, chemical reactions, or a combination of both. In practice, such flows arise in applications including scramjet combustors and rocket engine cooling channels. These configurations pose significant modelling challenges due to the strong gradients present across the channel and in the near-wall regions, where compressibility effects interact with variations in chemical composition and thermal energy transfer.

Channel flows, however, are not limited to these specific applications. As discussed previously, turbulent channel flow has long served as a canonical configuration for the study of wall-bounded turbulence, with numerical simulations dating back to as early as 1987. Consequently, turbulent channel flows provide a well-established framework for gaining physical insight into wall-bounded turbulent behaviour. Building on this foundation, the present section investigates high-enthalpy turbulent channel flow in which thermo-chemical processes are present, considering air as the working fluid under different flow conditions.

Two distinct flow states are considered in this study: a lower-temperature (LT) case and a higher-temperature (HT) case, corresponding to wall temperatures of 3000 K and 6000 K, respectively. While wall temperatures on the order of 3000 K may realistically occur during planetary re-entry, the higher wall temperature of 6000 K is deliberately artificiality high to isolate and examine the effects associated with substantially different thermo-chemical time scales. For each flow state, four modelling configurations are examined: thermally equilibrated and chemically frozen (TE-CF), thermally equilibrated and chemically non-equilibrium (TE-CNE), thermally non-equilibrium and chemically frozen (TNE-CF), and fully thermo-chemically non-equilibrium (TCNE).

In all cases, the flow is initialised with uniform temperature and density across the channel, and transition to turbulence is achieved using the formulation defined in Equation 6.16. Periodic boundary conditions are applied in the streamwise and spanwise directions, while isothermal wall conditions are imposed at both walls. The wall state is maintained

TABLE 6.7: Initial parameters for the turbulent channel flow simulations carried out on OpenSBLI.

Case	u_c°	$p_\circ$	$\rho_\circ$	T_{wall}	dt	Φ	δ
LT	1862.64	18124.52	0.02	3000	3×10^{-8}	-27627.74	0.007909
HT	3496.18	49271.14	0.02	6000	1.5×10^{-8}	-77317.15	0.008330

TABLE 6.8: Domain properties for the turbulent channel flow simulations carried out.

L_x	L_y	L_z	N_x	N_y	N_z	β
$4\delta\pi$	2δ	$4\delta\pi/3$	250	289	250	1.3

in thermally equilibrium throughout the simulation. For chemically reacting cases, the diffusion model described in Section 2.4.3.2 is employed. Transport properties for all simulations are evaluated using the efficient transport model presented in Chapter 5. The overall domain configuration follows that of Coleman et al. (1995), consistent with the setup adopted earlier in the validation study. This configuration is primarily used to define the turbulent characteristics of the flow, which are specified in terms of the wall shear Mach number M_τ and friction Reynolds number Re_τ.

The procedure for determining the flow conditions differs slightly from that employed in the validation case. While the non-dimensional parameters defined by Coleman et al. (1995) are retained—namely $M_\tau = 0.082$, $Re_\tau = 222$, and a density ratio of $\rho_w/\rho_c = 1.355$—the flow composition is evaluated based on the equilibrium composition corresponding to the wall temperature. Flow properties required for defining the channel height and the applied forcing, such as the wall viscosity, are computed using high-enthalpy air viscosity formulations instead of a power law. Aside from these high-enthalpy considerations, the detailed procedure for defining the flow conditions is described in Section 6.4.

The flow properties for the two temperature cases (LT and HT) are summarised in Table 6.7, while the corresponding domain parameters are provided in Table 6.8.

The grid dimensions in each spatial direction are defined in terms of the channel half-height, with $4\delta\pi$, 2δ, and $4\delta\pi/3$ corresponding to the x, y, and z directions, respectively. The number of grid points is set to 250, 289, and 250 along the x, y, and z directions, respectively, with a stretching factor of $\beta = 1.3$ applied in the wall-normal (y) direction.

The two flow conditions considered provide distinct focal points for evaluation. The low-temperature case, as demonstrated through analyses presented in previous chapters, exhibits a higher degree of thermal non-equilibrium, where thermal relaxation time scales are significantly slower than the characteristic flow time scales. This thermal state involves multiple molecular species, with more than one species contributing to

the overall relaxation behaviour. As such, the LT case provides an ideal framework for evaluating the influence of thermal non-equilibrium effects.

In contrast, the high-temperature case is predominantly characterised by a single molecular species (N_2) since oxygen molecule (O_2) is fully dissociated in these temperatures, reducing the influence of multi-species interactions in the formulation. Instead, at elevated temperatures, variations in chemical composition with temperature become more pronounced, with equilibrium chemistry exhibiting increased sensitivity to temperature, particularly through large ratios between N and N_2. Consequently, the HT case is well suited for evaluating the impact of chemical effects within a turbulent channel flow configuration.

6.5.1 Low-Temperature Case

As mentioned earlier, four different simulations were conducted for this temperature range. Since the flow is initialised with uniform temperature and density across the channel, a finite amount of time is required for the flow to reach a statistically converged state after the initial disturbance is imposed.

Figure 6.4 illustrates the convergence behaviour for all four simulations carried out for the low-temperature flow, normalised by the initial conditions. The key distinction to note is between the chemically frozen cases (Figure 6.4a and Figure 6.4b) and the chemically reacting cases (Figure 6.4c and Figure 6.4d). In the chemically reacting configurations, the time required for the flow to reach a statistically steady state is significantly longer, owing to the continuous influence of finite-rate chemical reactions on the flow evolution. The shaded region in each figure indicates the time interval over which the statistics were collected, corresponding to 150,000 iterations.

Additionally, Figure 6.5 presents an instantaneous flow field for the TCNE case. Figure 6.5a shows an iso-surface of the Q-criterion at 8×10^9 s^{-2}, overlaid with the extent of thermal non-equilibrium, quantified as the temperature difference $(T_v - T)$ in K. The distribution of turbulent structures across the channel is clearly visible. Near the walls, horseshoe vortices develop as a result of the no-slip boundary condition, accompanied by elongated streaks aligned with the streamwise direction. Further towards the centre of the channel, larger turbulent structures dominate the flow. The figure also indicates that, in the near-wall region, there exists a pronounced degree of thermally cold non-equilibrium, where the vibrational temperature is lower than the translational temperature. This behaviour reflects a region in which the flow is effectively thermally frozen. Further discussion of these observations is provided in the following sections.

Figure 6.5b presents a contour of the Q-criterion, where in addition to regions of high-intensity vorticity, areas of strong shear are also observed. The slice corresponds to the centre of the domain in the z-direction. Regions of high vorticity are associated

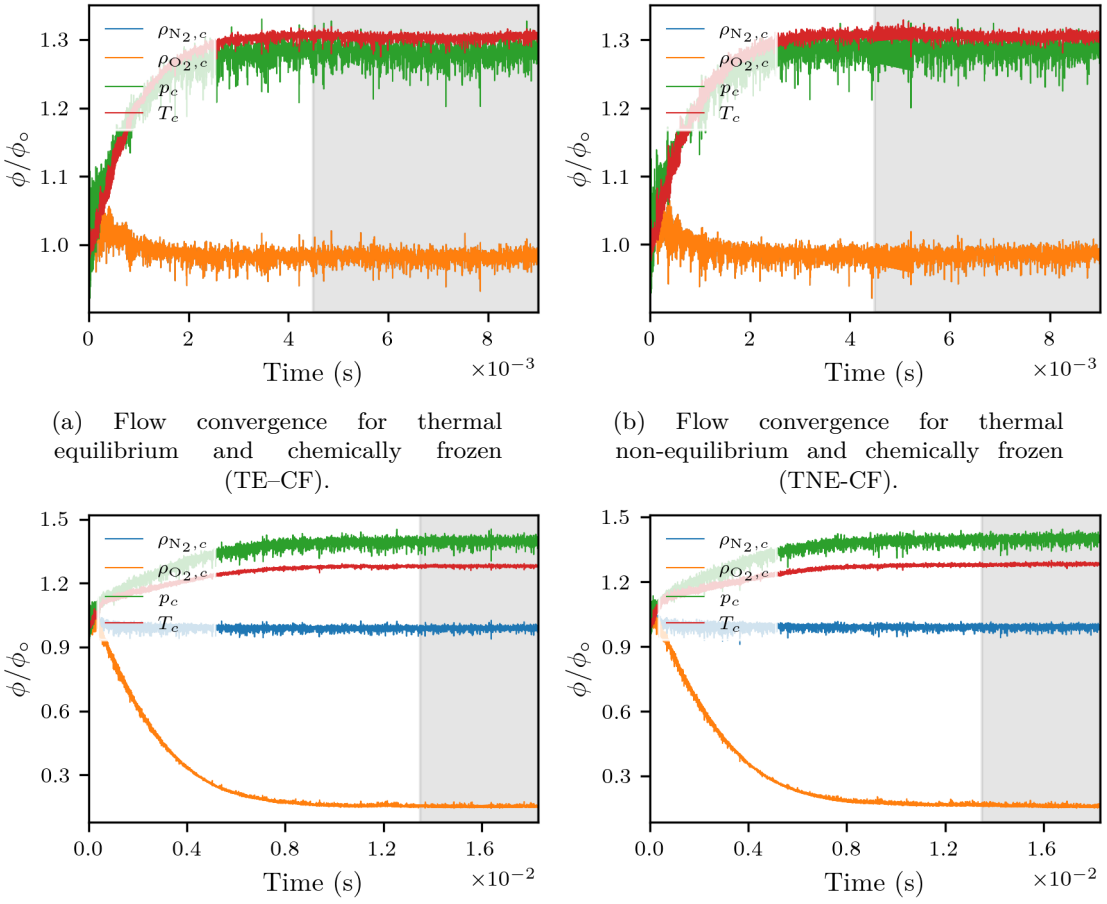

(a) Flow convergence for thermal equilibrium and chemically frozen (TE–CF).

(b) Flow convergence for thermal non-equilibrium and chemically frozen (TNE-CF).

(c) Flow convergence for thermal equilibrium and chemically reacting (TE-CNE).

(d) Flow convergence for thermal non-equilibrium and chemically reacting (TCNE).

FIGURE 6.4: Flow convergence of turbulent channel flow from the initial condition for the low-temperature case, showing the normalised centreline N_2 and O_2 density, pressure, and temperature against time in seconds.

with the horseshoe vortex structures, with significantly higher intensities observed closer to the walls. Figure 6.5c shows the vorticity magnitude at the same slice, with values ranging between 0.0 and 1.1×10^6 s^{-1}. The vorticity magnitude closely aligns with the contours of the Q-criterion, exhibiting strong gradients near the walls and elongated streaks extending towards the centre of the channel. In both cases, there is a clear indication that the flow is driven from the walls towards the channel centre, accompanied by a reduction in vorticity intensity in the core region.

Figure 6.5d illustrates the extent to which the flow departs from thermal equilibrium. The near-wall regions exhibit a pronounced thermally cold non-equilibrium state, as also observed in Figure 6.5a. Towards the centre of the channel, the flow approaches thermal equilibrium, where the vibrational temperature converges towards the translational temperature. This behaviour highlights how thermally non-equilibrium fluid originating near the walls is transported towards the channel centre by highly vortical structures, where it subsequently relaxes towards equilibrium. Even though the wall condition

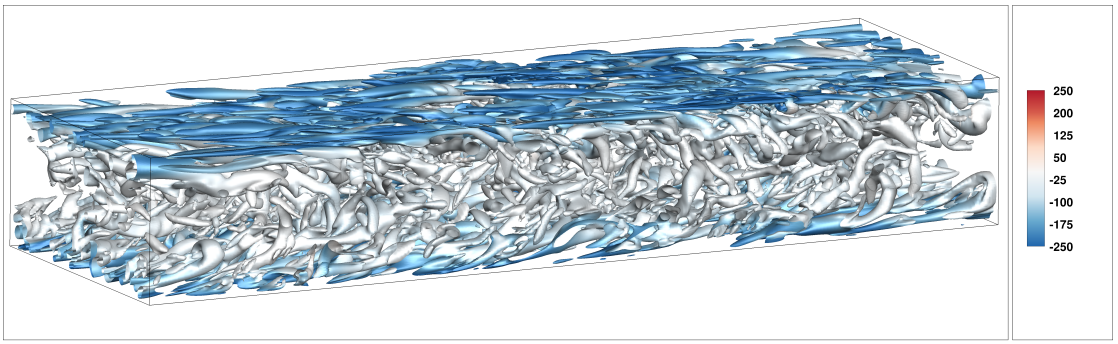

(a) Iso-surfaces of the Q-criterion at $8 \times 10^9 \mathrm{s}^{-2}$, overlaid with $T_v - T$. Colour bar ranges from $-250\,\mathrm{K}$ to $250\,\mathrm{K}$.

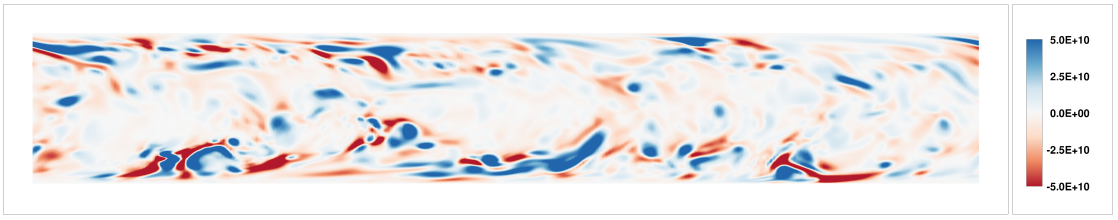

(b) Contour slice of the Q-criterion at $z = 50\%$. Colour bar ranges from -5×10^{10} s^{-2} to 5×10^{10} s^{-2}.

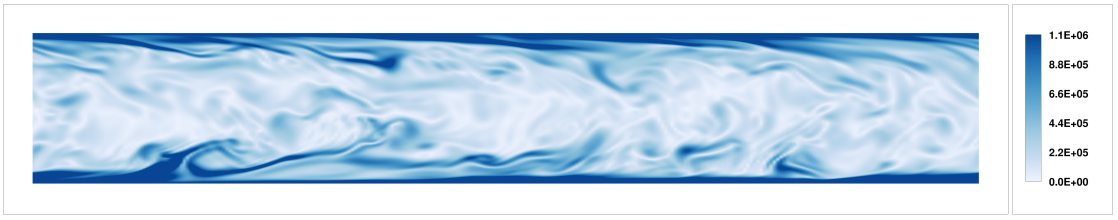

(c) Contour slice of vorticity magnitude at $z = 50\%$. Colour bar ranges from 0.0 to 1.1×10^6 s^{-1}.

(d) Contour slice of $T_v - T$ at $z = 50\%$. Colour bar ranges from $-250\,\mathrm{K}$ to $250\,\mathrm{K}$.

(e) Contour slice of N_2 mass fraction at $z = 50\%$. Colour bar ranges from 77% to 77.5%.

FIGURE 6.5: Instantaneous flow visualisation of turbulent channel flow with thermo-chemical reactions (TCNE) for the LT case.

imposes equilibrium temperature ($T = T_v$) at the surface, the regions exhibiting the strongest non-equilibrium effects remain, closely associated with the near-wall structures and the wall-driven transport mechanisms.

Finally, Figure 6.5e shows the mass fraction of nitrogen molecules (N_2), illustrating

how the air composition varies across the channel in response to local temperature changes. The variation is limited to a narrow range of only 0.5%, between 77% and 77.5%, indicating that the overall air composition remains nearly uniform across the channel. This behaviour is attributed to the equilibrium composition of air within this temperature range. Consequently, the flow may be reasonably assumed to be in chemical equilibrium, with an associated error on the order of 0.5%.

Statistical Evaluation

As mentioned previously, channel flows are statistically one-dimensional. In OpenSBLI, this is accounted for by performing averaging operations during the simulation when evaluating the flow quantities. As a result, time-averaged values of selected quantities are exported for every grid point. Post-processing of this data is then performed to compute additional quantities or to apply further spatial averaging, allowing the results to be presented as profiles across the channel height. The results discussed in this section correspond to the four simulations conducted for the low-temperature case: TE-CF, TE-CNE, TNE-CF, and TCNE.

Figure 6.6 presents temperature-related profiles, where Figure 6.6a shows the mean translational and vibrational temperatures, and Figure 6.6b shows the extent to which the flow departs from thermal equilibrium for the thermally relaxing cases. Examination of the mean temperature profiles (Figure 6.6a) reveals two key observations. First, the differences between the thermally equilibrium and thermally non-equilibrium cases (TE-CF versus TNE-CF, and TE-CNE versus TCNE) are primarily concentrated near the wall regions. In the presence of thermally cold non-equilibrium, where a larger fraction of energy resides in the translational mode, the translational temperature is elevated, while the vibrational temperature exhibits a smoother spatial variation. Second, the inclusion of chemical non-equilibrium leads to a reduction in temperature within the channel core and steeper temperature gradients near the walls. This behaviour correlates with changes in the equilibrium composition driven by the local temperature variations, although the effect remains relatively weak for the low-temperature case.

The difference between thermal non-equilibrium profiles shown in Figure 6.6b highlights the influence of chemical reactions on thermal relaxation. In particular, steeper near-wall gradients are observed for the chemically reacting TCNE case. A notable feature in both thermally relaxing cases is that full thermal equilibrium is not attained in the channel core. In addition, the near-wall regions exhibit a consistently higher degree of thermal non-equilibrium. When these observations are considered alongside the turbulent structures across the channel height (Figure 6.5a), a clear correlation emerges between the turbulent length scales and the persistence of thermal non-equilibrium. Smaller turbulent structures dominate near the walls, while larger structures are present in the channel core. As a result, the characteristic time scales of the near-wall structures are shorter

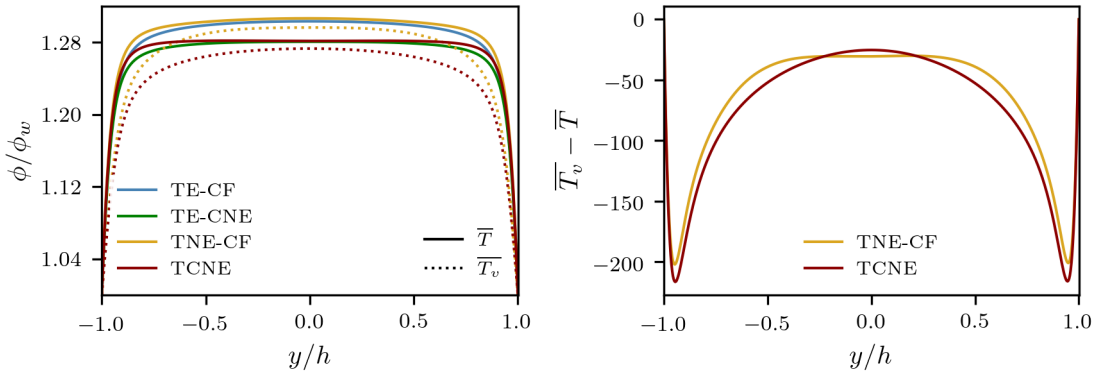

(a) Mean temperature profiles across the channel height.

(b) Extent of thermal non-equilibrium ($\overline{T_v} - \overline{T}$) shown in K.

FIGURE 6.6: Averaged profiles of temperature-related quantities across the channel height for the LT case.

relative to the thermal relaxation time scales. Combined with the initially thermally uniform flow state (requiring the temperatures to converge), this suggests the existence of a thermal state in which the flow becomes effectively thermally frozen, such that the degree of thermal non-equilibrium remains approximately constant and is governed by the relative time scales of turbulence and thermal relaxation.

Figure 6.7 presents quantities related to the Mach number for the simulations performed. Figure 6.7a shows the local Mach number across the channel height. When considering the influence of thermal non-equilibrium, which is more prominent in the LT case, almost no discernible difference is observed. In contrast, a clear difference is evident for the chemically reacting cases, where the flow composition evolves, resulting in a lower Mach number in the channel core. This behaviour is expected, as thermal non-equilibrium does not directly affect the velocity and has only a limited influence on the speed of sound through variations in the specific heat ratio and translational temperature, which were shown to differ by only 1-2% near the wall. Conversely, the mixture gas constant is strongly influenced by the local mixture composition, explaining the differences observed in the chemically reacting cases.

Figure 6.7b exhibits similar trends for the fluctuating and turbulent Mach numbers. Thermal non-equilibrium again has a negligible effect, whereas chemical reactions lead to a reduction in these quantities, particularly in the near-wall region where the peak values occur.

Figure 6.8 presents profiles related to temperature fluctuations and Favre averaged stresses. Figure 6.8a shows that translational temperature fluctuations (solid lines) are reduced in the presence of thermal non-equilibrium, while vibrational temperature fluctuations are increased, reflecting enhanced activity in the vibrational energy mode when thermal non-equilibrium is present.

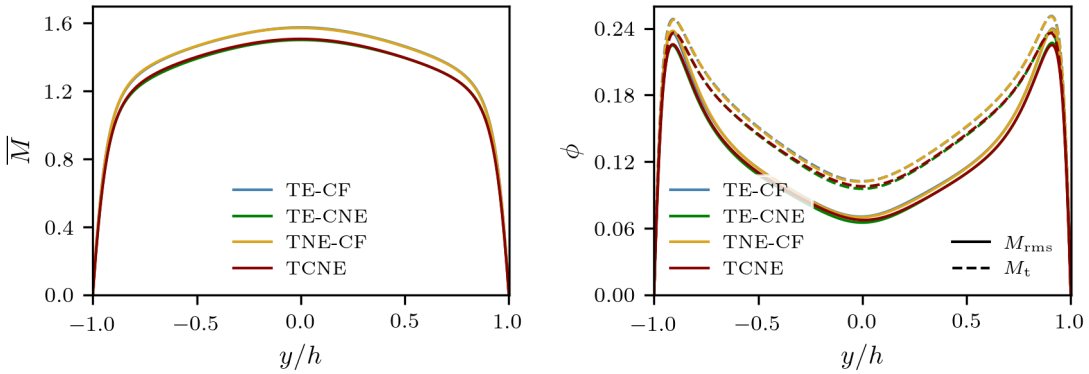

(a) Profile of local Mach number across the channel height.

(b) Profile of fluctuating and turbulent Mach number across the channel height.

FIGURE 6.7: Averaged profiles of Mach-number-related quantities across the channel height for the LT case.

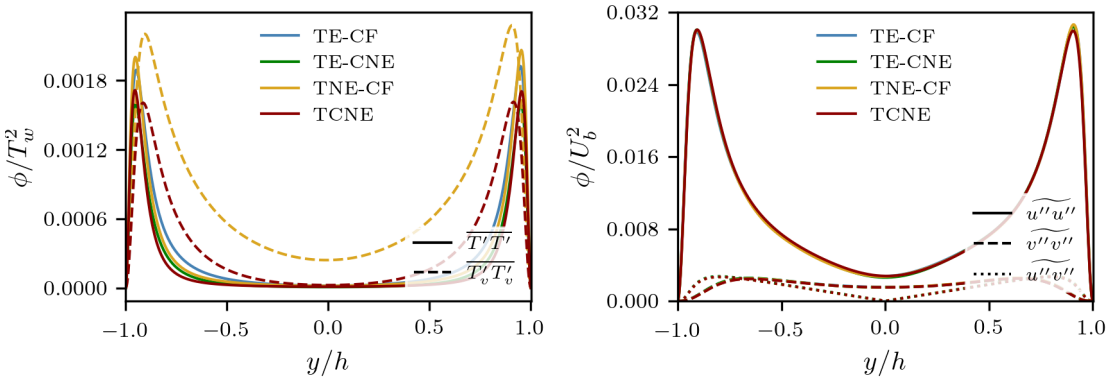

(a) Profile of fluctuating temperatures across the channel height.

(b) Profile of Favre-averaged stresses across the channel height.

FIGURE 6.8: Averaged profiles of fluctuating quantities across the channel height for the LT case.

The similarity between the translational temperature fluctuation profiles and the thermal non-equilibrium profiles shown in Figure 6.6b for the TNE cases reinforces findings from the literature and earlier chapters (Chapter 4), where elevated thermal non-equilibrium has been attributed to translational temperature fluctuations.

For the thermally non-equilibrium cases, higher translational temperature fluctuations are observed near the wall regions, while reduced fluctuation levels are present towards the channel centre. In shear-layer configurations (Section 4.4), it has been shown that reductions in translational temperature due to thermally hot non-equilibrium—where a portion of the energy is retained in the vibrational mode—lead to steeper temperature gradients and, consequently, enhanced fluctuating terms. A similar mechanism is observed here. Comparison of the mean temperature profiles (Figure 6.6b) with the corresponding fluctuation magnitudes (Figure 6.8a) indicates that regions with steeper translational temperature gradients, particularly near the walls for the TNE cases, exhibit larger fluctuations. Conversely, in regions where the mean temperature gradients are

weaker, such as towards the channel centre, the magnitude of translational temperature fluctuations is reduced.

In contrast, vibrational temperature fluctuations are significantly increased due to incomplete coupling between the translational and vibrational modes. Compared to earlier shear-layer studies, where thermally hot non-equilibrium led to reduced vibrational temperature fluctuations owing to weak mean T_v gradients, the present case corresponds to a thermally cold non-equilibrium regime. Here, the translational temperature is higher, and the vibrational temperature exhibits stronger local gradients in the region $0.5 < y/h < 0.75$ when compared to the translational temperature, resulting in increased vibrational temperature fluctuations.

Figure 6.8b shows the Favre-averaged stress profiles across the channel height. Near the walls, the streamwise velocity fluctuations ($\widetilde{u''u''}$) are amplified, while they decrease significantly towards the channel centre. Meanwhile, the spanwise velocity fluctuations ($\widetilde{v''v''}$) remain relatively uniform across the channel. The shear stress component ($\widetilde{u''v''}$) approaches zero in the core region. Overall, the Favre-averaged stress profiles exhibit minimal sensitivity to thermo-chemical non-equilibrium effects. It should be noted, that the differences between Reynolds-averaged and Favre-averaged stresses, as discussed in Section 6.2.2, are small and are primarily confined to the near-wall region.

Figure 6.9 presents the mass fraction profiles of air species together with the mean streamwise velocity across the channel height. The results show negligible variation in flow composition across the channel, which is expected given the small change in the equilibrium composition of air between 3000 K and 4000 K. In addition, the mean streamwise velocity profile expressed in viscous units shows excellent agreement with the results reported by Coleman et al. (1995). This confirms that, despite the presence of pronounced thermal non-equilibrium, the mean velocity profile in wall units of the channel flow remain largely unaffected for the low-temperature case.

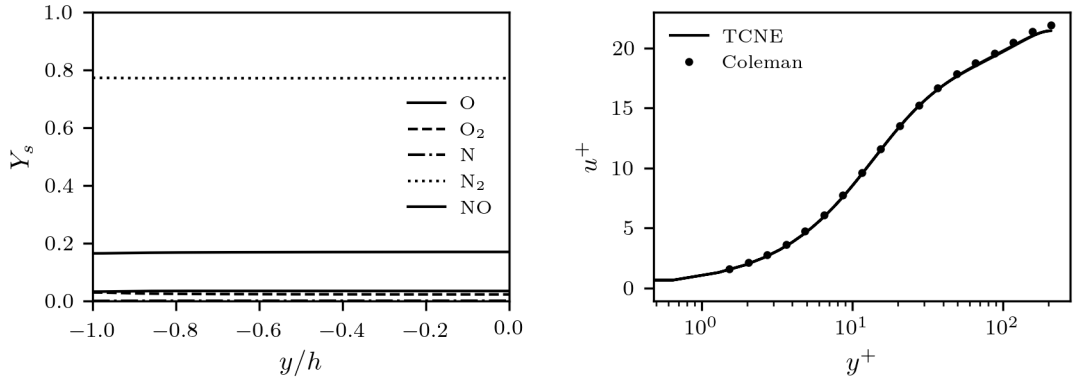

(a) Profile of mass fraction of air species across the channel height.

(b) Mean velocity profile in wall units across the channel height.

FIGURE 6.9: Profiles of mass fraction and mean velocity for the LT case.

Finally, Table 6.9 summarises selected global flow quantities for the four low-temperature cases. Overall, the results indicate very little influence of thermal non-equilibrium on the global flow quantities, despite thermal non-equilibrium being more prominent for the LT condition. Similarly, only minor changes are observed due to chemical reactions, which is expected given the limited extent of chemical activity observed for this temperature range.

TABLE 6.9: Global flow quantities for the low-temperature (LT) turbulent channel flow cases.

Quantity	TE-CF	TE-CNE	TNE-CF	TCNE
u_τ	91.613	92.270	91.336	91.975
Re_τ	213.14	208.67	213.39	208.78
Re_b	2523.9	2498.4	2522.7	2508.6
C_f	0.0078500	0.0078921	0.0077936	0.0077689
M_c	1.5177	1.5163	1.5219	1.5261
ITKE	0.96117	0.97463	0.96979	1.0004

6.5.2 High-Temperature Case

The earlier simulations focused on a wall temperature of 3000 K, for which thermal non-equilibrium effects were dominant and chemical non-equilibrium remained weak. In this section, simulations are conducted at a higher temperature of 6000 K, where vibrational modes relax more rapidly and the chemical composition becomes increasingly sensitive to relatively small temperature variations. As with the low-temperature case, four simulations are performed for this temperature range.

Since the flow is initialised with uniform temperature and density across the channel, a finite amount of time is required for the flow to reach a statistically converged state following the introduction of the initial disturbance. Figure 6.10 shows the convergence behaviour for all four simulations conducted for the high-temperature case. The chemically frozen cases (Figure 6.10a and Figure 6.10b) reach statistical convergence in fewer iterations compared to the chemically reacting cases (Figure 6.10c and Figure 6.10d), where ongoing chemical reactions continue to influence the flow evolution. The shaded region in each figure denotes the interval over which statistical averaging is performed, corresponding to 150,000 iterations.

Figure 6.11 shows an instantaneous state of the turbulent channel flow for the high-temperature case. Figure 6.11a presents an iso-surface of the Q-criterion at 6×10^{10} s^{-2}, overlaid with the extent of thermal non-equilibrium expressed as the temperature difference $(T_v - T)$ in K. Similar to the low-temperature case, regions of thermally cold non-equilibrium are observed near the wall. In contrast to the LT case, however, the channel core contains a mixture of thermally hot and thermally cold

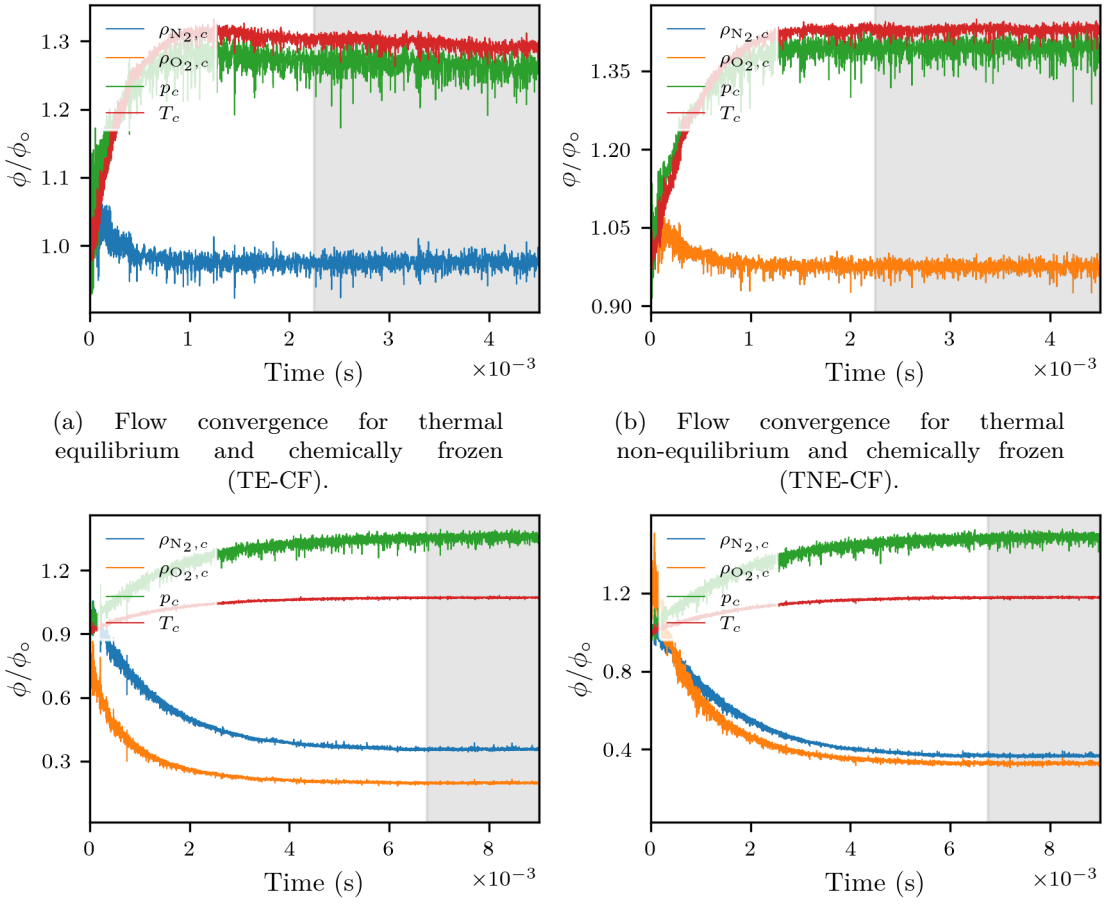

(a) Flow convergence for thermal equilibrium and chemically frozen (TE-CF).

(b) Flow convergence for thermal non-equilibrium and chemically frozen (TNE-CF).

(c) Flow convergence for thermal equilibrium and chemically reacting (TE-CNE).

(d) Flow convergence for thermal non-equilibrium and chemically reacting (TCNE).

FIGURE 6.10: Flow convergence of turbulent channel flow from the initial condition for the HT case.

non-equilibrium regions. The thermally hot regions correlate strongly with the heads of the horseshoe-like vortical structures. The reduced dominance of near-wall thermally cold non-equilibrium, together with the coexistence of thermally hot and cold regions, reflects the faster vibrational relaxation processes at this higher temperature condition.

Figure 6.11b shows a contour slice of the Q-criterion, while Figure 6.11c presents the corresponding vorticity magnitude, with values ranging from 0.0 to 1.1×10^6 s^{-1}. Compared to the low-temperature case, the vorticity is more strongly concentrated near the wall, exhibiting steeper gradients relative to the channel centre. Nevertheless, the same qualitative behaviour observed in the LT case persists, whereby flow structures originating near the wall are transported towards the channel centre due to the development of hairpin-like vortices.

Figure 6.11d illustrates the extent of thermal non-equilibrium across the channel. Very close to the wall, the flow remains in a thermally cold non-equilibrium state, characterised by strong gradients in $T_v - T$. The thermally cold non-equilibrium region

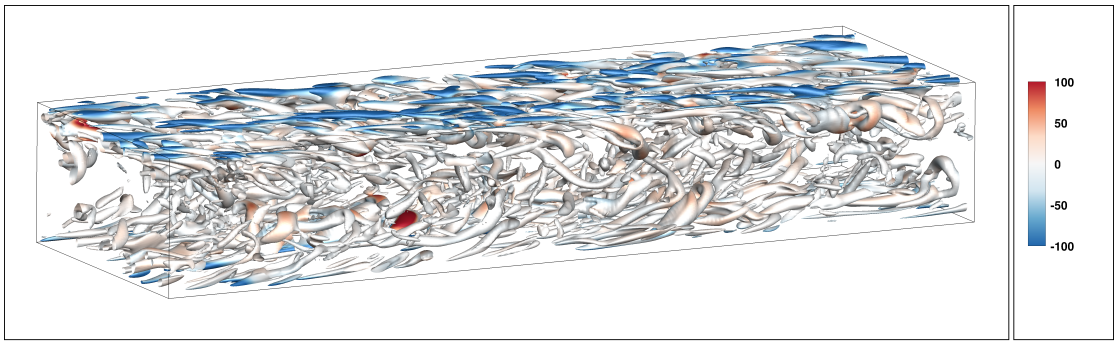

(a) Iso-surfaces of the Q-criterion at 6×10^{10} s^{-2}, overlaid with $T_v - T$. Colour bar ranges from -100 K to 100 K.

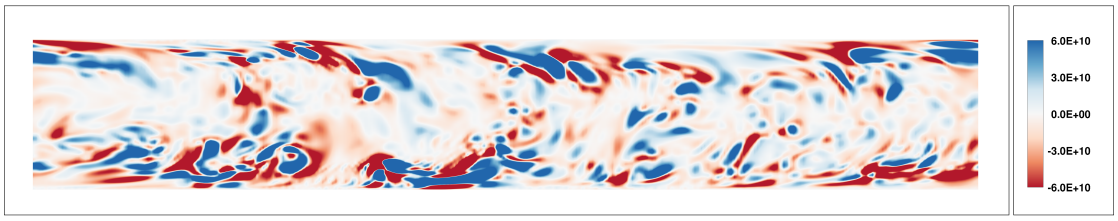

(b) Contour slice of the Q-criterion at $z = 50\%$. Colour bar ranges from -6×10^{10} s^{-2} to 6×10^{10} s^{-2}.

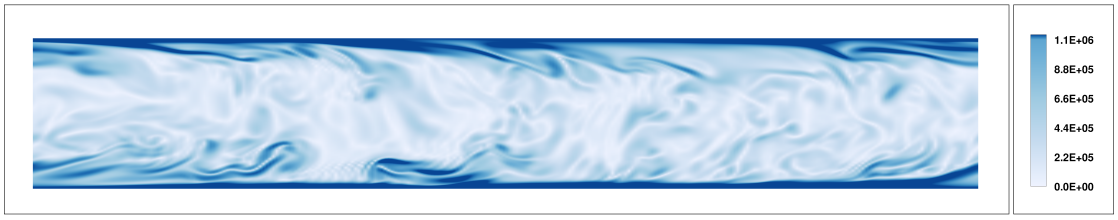

(c) Contour slice of vorticity magnitude at $z = 50\%$. Colour bar ranges from 0.0 to 1.1×10^6 s^{-1}.

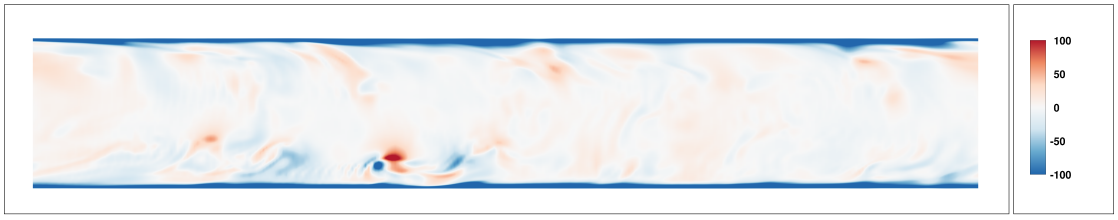

(d) Contour slice of $T_v - T$ at $z = 50\%$. Colour bar ranges from -100 K to 100 K.

(e) Contour slice of N_2 mass fraction at $z = 50\%$. Colour bar ranges from 20% to 30%.

FIGURE 6.11: Instantaneous flow visualisation of turbulent channel flow with thermo-chemical reactions (TCNE) for the HT case.

is confined to a thin layer near the wall, while further towards the channel centre, alternating regions of thermally hot and cold non-equilibrium are observed. Unlike the LT case, which was dominated by thermally cold non-equilibrium throughout the domain, the present case demonstrates the coexistence of both thermal states around

intense vortical structures. This behaviour is consistent with observations reported for the three-dimensional mixing-layer configurations (Section 4.4.2).

Finally, Figure 6.11e shows the mass fraction of nitrogen molecules (N_2), illustrating the variation in air composition across the channel in response to local temperature changes. A clear transition is observed from the wall towards the channel centre, where molecular nitrogen dissociates into atomic nitrogen (N). While the LT case exhibited variations of less than 1%, the present figure shows a colour bar range of approximately 10%, making it well suited for evaluating the influence of chemical non-equilibrium on near-wall flow characteristics.

Statistical Evaluation

The data curation and post-processing procedures are identical to those employed for the low-temperature case. The results presented here correspond to the four simulations conducted for the high-temperature case: TE-CF, TE-CNE, TNE-CF, and TCNE.

Figure 6.12 presents temperature-related profiles, where Figure 6.12a shows the mean translational and vibrational temperatures, and Figure 6.12b shows the extent to which the flow departs from thermal equilibrium for the thermally non-equilibrium cases. Examination of the mean temperature profiles (Figure 6.12a) reveals a clear distinction between the chemically frozen (CF) and chemically reacting (CNE) configurations. Owing to changes in the chemical composition, namely the endothermic dissociation of N_2, the channel core in the chemically reacting cases is significantly cooler, resulting in reduced temperature ratios. In contrast, the influence of thermal non-equilibrium on the mean temperature profiles is comparatively weak, particularly when compared to the low-temperature case, as expected given the different relative time scales governing thermal relaxation.

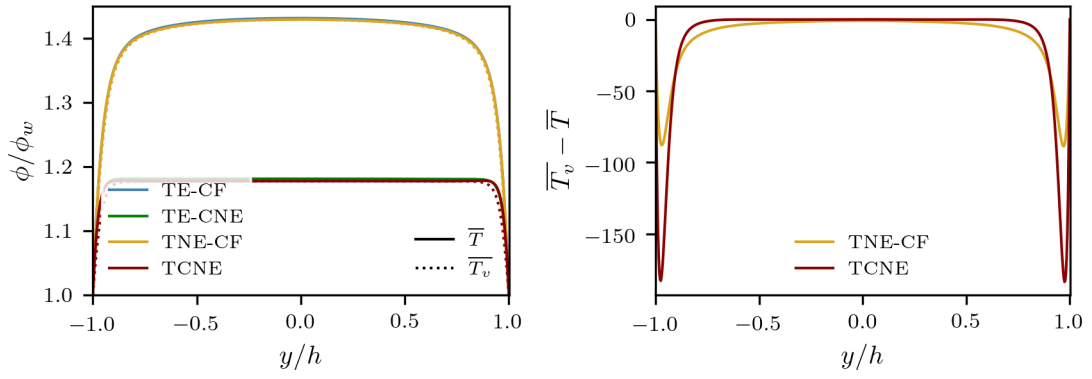

(a) Mean temperature profiles across the channel height.

(b) Extent of thermal non-equilibrium ($\overline{T_v} - \overline{T}$) shown in K.

FIGURE 6.12: Averaged profiles of temperature-related quantities across the channel height for the HT case.

Figure 6.12b shows the thermal non-equilibrium profiles for the high-temperature case. Pronounced gradients with sharp near-wall peaks are observed, indicating strong departures from equilibrium in the immediate vicinity of the wall. These highly non-equilibrium regions can be attributed to the small-scale turbulent structures generated by the no-slip boundary condition. In contrast to the low-temperature case, the channel core approaches a thermally equilibrated state. Similar arguments regarding the relative time scales of flow dynamics and thermal relaxation apply here. However, for the present high-temperature condition, the faster relaxation processes and the coexistence of thermally hot and cold non-equilibrium states result in the flow evolving beyond a thermally frozen regime, such that thermal equilibrium is effectively attained for the mean profiles in the channel core.

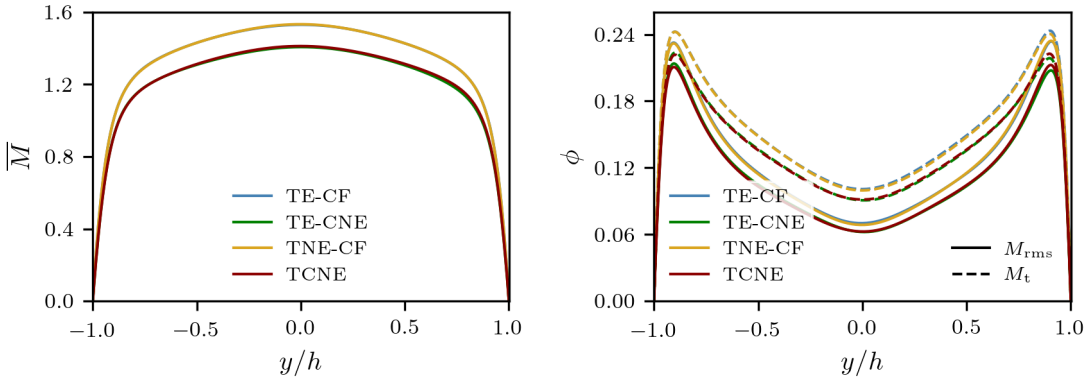

(a) Profile of local Mach number across the channel height.

(b) Profile of fluctuating and turbulent Mach number across the channel height.

FIGURE 6.13: Averaged profiles of Mach-number-related quantities across the channel height for the HT case.

Figure 6.13 presents Mach-number-related quantities for the simulations performed. Figure 6.13a shows the local Mach number across the channel height, while Figure 6.13b presents the corresponding fluctuating and turbulent Mach numbers. Owing to the strong composition gradients present in the high-temperature case (due to chemical reactions), a reduction in the local Mach number is observed, accompanied by a decrease in the turbulent and fluctuating Mach numbers. In contrast, Mach number fluctuations exhibit minimal variation across all cases. On the other hand, consistent with the conclusions drawn for the LT case, thermal non-equilibrium has a negligible influence on both the mean and fluctuating Mach number profiles. This behaviour is expected, as thermal non-equilibrium primarily affects energy redistribution between modes (translational and vibrational), while the Mach number is more strongly governed by changes in composition through the mixture gas constant.

Figure 6.14 presents profiles related to temperature fluctuations and Favre averaged stresses. Figure 6.14a shows that there is very little influence of thermal non-equilibrium on the temperature fluctuation terms when comparing the thermally equilibrium (TE) and thermally non-equilibrium (TNE) cases. In contrast to the low-temperature case,

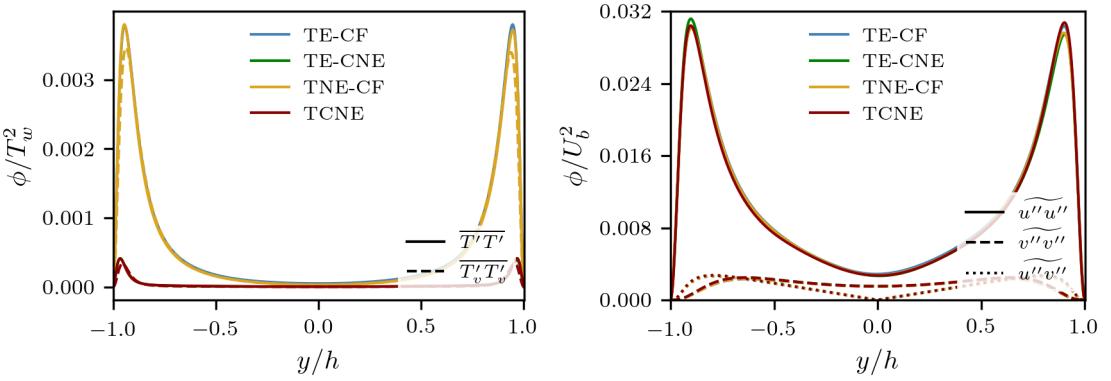

(a) Profile of fluctuating temperatures across the channel height.

(b) Profile of Favre-averaged stresses across the channel height.

FIGURE 6.14: Averaged profiles of fluctuating quantities across the channel height for the HT case.

where vibrational temperature fluctuations exhibited significantly different behaviour, the high-temperature case shows only minor differences between translational and vibrational temperature fluctuations. As discussed for the LT case, regions characterised by steeper mean temperature gradients correspond to larger fluctuation magnitudes, and this trend is again observed here.

Figure 6.14b shows the Favre-averaged stress profiles across the channel height. In general, near the wall, the streamwise velocity fluctuations ($\widetilde{u''u''}$) are amplified and decrease significantly towards the channel centre, as seen here. Most notably, the presence of strong concentration gradients and differing local thermo-chemical states, there is almost no influence on the stress terms. The relatively small differences observed between the peaks are likely attributable to insufficient averaging time for these higher-order statistics.

The consistent trend observed for Figure 6.12 to 6.14 for the chemically reacting cases, where the centre of the channel exhibits reduced magnitudes, can be attributed primarily to the effects of chemical reactions. In particular, during endothermic dissociation reactions, such as the conversion of molecular nitrogen to atomic nitrogen, energy is absorbed from the internal energy modes. As a result, the translational and vibrational energies decrease while the chemical energy of the flow, represented by the enthalpy of formation, increases. This process occurs while conserving the total energy of the system. However, when analysing the total energy in simulations of this type, the increase in chemical energy can dominate due to the strong binding energy of the N_2 molecule, giving the appearance of an increase in total energy. As discussed in Chapter 2, this behaviour arises from the use of reference enthalpies defined relative to a standard state. Consequently, although total energy is conserved, the partitioning between sensible and chemical energy changes, leading to an apparent increase in total energy associated with the flow.

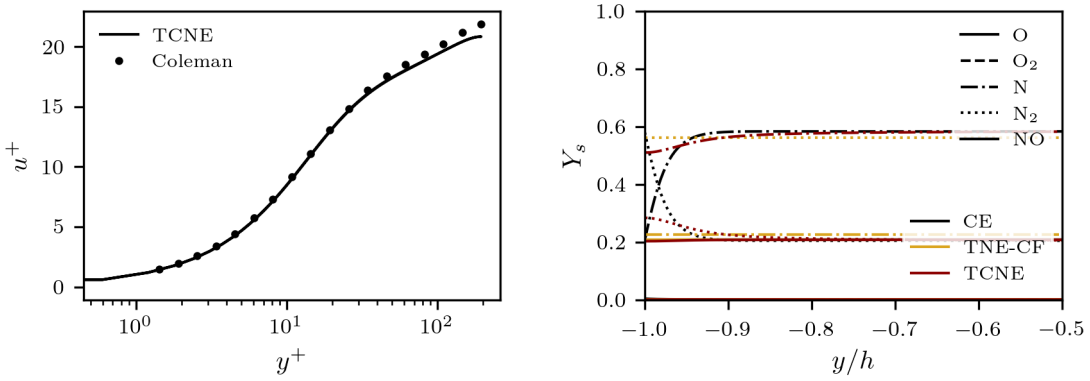

(a) Mean velocity profile in wall units across the channel height.

(b) Profile of mass fraction of air species across the channel height.

FIGURE 6.15: Profiles of mass fraction and mean velocity for the HT case.

Figure 6.15a shows the mean velocity profile, including results reported by Coleman et al. (1995). While the near-wall region exhibits almost no difference between the profiles, slight deviations are observed in the outer layer. These differences can be attributed to the significant chemical effects present in the high-temperature simulations, which are not accounted for in the chemically frozen formulation used in the study by Coleman et al. (1995).

Figure 6.15b shows the mass fraction profiles of all species across the channel height for the two thermally non-equilibrium cases, TNE-CF and TCNE. The compositions of these two cases differ significantly. In the chemically frozen (CF) case, where the composition is initialised based on the near-equilibrium state corresponding to the wall temperature of 6000 K, the flow remains predominantly composed of molecular nitrogen. In contrast, the chemically reacting (CNE) case exhibits a profile in which atomic nitrogen constitutes the majority of the composition across the channel. In addition, the local equilibrium composition for the TCNE case is shown for reference (black line), indicating the extent to which the flow departs from chemical equilibrium.

The equilibrium profiles directly reflect the equilibrium composition of air at the corresponding temperature and pressure conditions discussed in Chapter 3, where substantial differences are observed between air compositions at 6000 K and 8000 K. This comparison highlights the importance of accounting for chemical reactions in the flow, given the significant differences between the CF and CNE cases and their impact on the resulting flow characteristics. This effect is particularly pronounced at the core due to the temperature ratios of about 1.18 ($T_c \sim 7000$K).

An additional observation is that the wall composition for the TCNE case does not remain consistent with the equilibrium conditions prescribed at the start of the simulation. Although the wall is maintained isothermally at 6000 K and the local density varies only modestly (approximately 20%, from 0.02 to ~ 0.024), the near-wall chemical composition deviates from equilibrium. This indicates that, while the channel core evolves towards a

local equilibrium state, the near-wall region departs from equilibrium. This behaviour is directly linked to the applied boundary-condition treatment; although the wall is formally modelled as non-catalytic, the species composition at the wall is governed by a zero-gradient condition rather than a fixed or prescribed equilibrium composition, thereby allowing it to adjust dynamically in response to the near-wall flow state.

Two important implications follow from this observation. First, the chemical composition near the wall appears to be effectively frozen relative to the characteristic flow time scales. Second, the near-wall characteristics of the chemical species are strongly dependent on the imposed wall chemistry model. Depending on whether the wall is treated as catalytic, non-catalytic, or fully specified in composition, the resulting near-wall behaviour of the species considered here may differ significantly. Given the strong influence of chemistry observed in this case, the choice of wall chemistry treatment represents an important modelling consideration for high-enthalpy turbulent channel flows.

Finally, Table 6.10 summarises selected global flow quantities for the four high-temperature cases. As established earlier, comparisons between the thermally equilibrium (TE) and thermally non-equilibrium (TNE) cases show very little impact on the overall flow behaviour, whereas comparisons between the chemically frozen (CF) and chemically reacting (CNE) cases reveal much more significant differences. One of the most notable effects is observed in the friction Reynolds number, where the initially prescribed value of $Re_\tau = 222$ decreases to approximately 195 for the chemically reacting cases. In addition, the bulk Reynolds number Re_b, the wall friction coefficient C_f, and the integral of turbulent kinetic energy are all influenced by the presence of chemical reactions.

Table 6.10: Global flow quantities for the high-temperature (HT) turbulent channel flow cases.

Quantity	TE-CF	TE-CNE	TNE-CF	TCNE
u_τ	150.41	160.48	150.36	159.81
Re_τ	221.52	195.91	221.18	195.13
Re_b	2304.0	2431.1	2305.3	2433.9
C_f	0.0077686	0.0079785	0.0077615	0.0079365
M_c	1.8496	1.8232	1.8487	1.8190
ITKE	3.2216	3.4645	3.1821	3.4508

6.6 Conclusion

The objective of this chapter was to evaluate the influence of thermal and chemical non-equilibrium in a turbulent channel flow, serving as a canonical wall-bounded configuration to improve understanding of high-enthalpy effects on wall turbulence.

First, the thermo-chemical non-equilibrium turbulent channel-flow setup was validated against the reference study of Coleman et al. (1995). Two validation cases were considered, differing in dimensional density while maintaining identical non-dimensional flow characteristics. Mean profiles across the channel height, including temperature, density, velocity, local Mach number, and Reynolds number, showed excellent agreement with the published data, confirming the accuracy of the numerical framework and modelling approach adopted in this study.

Following validation, two distinct flow states were investigated: a lower-temperature case and a higher-temperature case, corresponding to nominal wall temperatures of 3000 K and 6000 K, respectively. For each flow state, four modelling configurations were examined: thermally equilibrated and chemically frozen (TE-CF), thermally equilibrated and chemically non-equilibrium (TE-CNE), thermally non-equilibrium and chemically frozen (TNE-CF), and fully thermo-chemically non-equilibrium (TCNE).

Both flow conditions exhibited classical turbulent channel-flow characteristics. Near the walls, horseshoe vortices formed as a result of the no-slip boundary condition, accompanied by elongated low- and high-speed streaks aligned with the streamwise direction. Away from the walls, larger turbulent structures dominated the flow within the channel core. Regions exhibiting the strongest thermal non-equilibrium effects were found to be closely associated with the near-wall region, effectively behaving as thermally frozen. A clear correlation emerged between turbulent length scales and the persistence of thermal non-equilibrium: smaller turbulent structures dominate near the walls while larger structures prevail towards the channel centre, such that the shorter near-wall turbulent time scales relative to the thermal relaxation time scales lead to a regime where the degree of thermal non-equilibrium remained approximately constant and governed by the relative time scales of turbulence and thermal relaxation.

For the thermally non-equilibrium cases, elevated translational temperature fluctuations were observed near the walls, while reduced fluctuation levels occurred towards the channel centre, whereas vibrational temperature fluctuations were comparatively increased. This behaviour is consistent with observations made in earlier chapters, where regions with steeper mean temperature gradients were found to exhibit larger temperature fluctuations.

The low-temperature case exhibited more pronounced thermal non-equilibrium and therefore provided a suitable flow state for evaluating thermal non-equilibrium effects. The flow remained in a persistent state of cold thermal non-equilibrium across the channel.

However, comparison of mean statistical profiles revealed only minor differences between the thermally equilibrated (TE) and thermally non-equilibrium (TNE) cases. Overall, the results indicate that thermal non-equilibrium has a negligible influence on global flow quantities, despite being more prominent under LT conditions.

In contrast, the high-temperature case exhibited comparable thermal and flow time scales, resulting in a flow field characterised by regions of both thermally cold and thermally hot non-equilibrium. Most notably, significant compositional variations developed across the channel in the chemically reacting cases. Substantial differences were observed between chemically frozen and chemically reacting simulations, driven by the dissociation of N_2 in the channel-centre changing the composition towards its local equilibrium state based on the local temperature and density. Consequently, pronounced species concentration gradients formed near the walls. As a result of chemical reactions, a consistent trend emerged in which the channel centre exhibited reduced magnitudes of mean flow quantities, primarily attributable to chemical effects. These changes were driven by endothermic dissociation reactions, such as the conversion of molecular nitrogen to atomic nitrogen, during which energy is absorbed from the internal energy modes and transferred into chemical energy. Consequently, the translational and vibrational energies were shown to decrease, while the chemical energy of the flow—represented by the enthalpy of formation—increased. For the same reasons, chemical reactions were shown to exert a significant influence across the channel, leading to reductions in local temperature, Mach number, turbulent Mach number, turbulent fluctuation intensities, and friction Reynolds number, while in contrast having no influence on Favre averaged stresses.

Additionally, for the HT case, it was demonstrated that the near-wall region resides in a state of chemical non-equilibrium, primarily as a result of the non-catalytic wall boundary condition prescribed in the simulations. Given the strong influence of chemical reactions observed under these conditions, the treatment of wall chemistry emerges as an important modelling consideration for high-enthalpy turbulent channel flows.

Overall, this study demonstrates that high-enthalpy effects can play a significant role in the modelling of wall-bounded turbulent flows. The findings presented here provide a framework for future investigations of wall-bounded high-enthalpy configurations, while highlighting sensitive modelling aspects—particularly the treatment of chemical reactions at the wall—that are critical for accurately capturing thermo-chemical non-equilibrium effects.

6.7 Future Works

Following the simulations conducted in this chapter, several directions for future work are proposed to further advance the understanding of high-enthalpy turbulent channel

flows:

- **Energy budget analysis:** Similar to the analyses carried out for the shear-layer configurations in earlier chapters, there is scope to perform detailed energy budget evaluations for turbulent channel flows. Such analyses would help elucidate the interactions between different energy components and provide further insight into the role of thermal and chemical non-equilibrium in wall-bounded turbulence.
- **Investigation of wall boundary conditions:** As demonstrated in this study, chemical reactions exert a significant influence on local flow characteristics. Given the critical importance of near-wall regions, the modelling of the chemical state at the wall boundary is expected to strongly affect both wall-region profiles and overall flow behaviour. Future studies should therefore consider comparative investigations of different wall chemistry treatments, such as fully catalytic, partially catalytic, and chemically frozen wall conditions.
- **More complex turbulent channel-flow configurations:** At higher Mach numbers, channel flows may develop shocklets accompanied by strong density gradients. Investigating turbulent channel flows with embedded shocklets would provide a more realistic representation of high-enthalpy flow conditions. Additionally, more complex configurations, such as counter-flow channel arrangements under high-enthalpy conditions, could be explored to assess their impact on turbulence–thermo-chemical interactions.
- **Sensitivity to transport-property modelling:** Earlier chapters demonstrated significant differences between accurate high-enthalpy transport-property models and simplified formulations that neglect high-enthalpy effects. A systematic comparative study examining different transport-property models would be valuable for quantifying their influence on near-wall flow characteristics and assessing the sensitivity of turbulent channel flows to transport-property modelling assumptions.

Chapter 7

Summary and Future Work

7.1 Summary

With the increasing interest in hypersonic flows across space exploration and defence-related applications, the importance of accurately accounting for high-enthalpy effects has become increasingly evident in supporting the advancement of these fields. As discussed in Chapter 1, although hypersonic flight research is well established, several fundamental aspects of these complex flows remain insufficiently understood. In particular, limited understanding persists regarding the coupling between turbulence and thermo-chemical non-equilibrium effects under high-enthalpy conditions.

Motivated by this gap, the primary objective of this research was to assess the influence of thermo-chemical non-equilibrium on turbulence using high-fidelity, scale-resolving computational frameworks. To address this objective, four principal research questions were formulated. While each individual study presented in this thesis includes its own dedicated conclusions, this section synthesises the relationship between the individual chapters and the overarching research framework.

In Chapter 2, a detailed description of the governing equations relevant to modelling high-enthalpy effects within a compressible Navier-Stokes framework was presented. This chapter outlined the fundamental characteristics of high-enthalpy flows, including finite-rate chemical reactions and thermal relaxation processes, while also addressing the modelling of key flow properties such as transport coefficients. Subsequently, Chapter 3 presented a series of simplified numerical simulations designed to evaluate and validate the modelling approaches introduced previously. Through comparative studies and validation exercises, this chapter demonstrated the implications of different modelling choices and concluded with a final thermo-chemical model for five-species reacting air, shown to be valid for temperatures below 9000 K. Together, these two chapters addressed the first research question by establishing an appropriate thermo-chemical non-equilibrium kinetic

framework suitable for implementation within a scale-resolving solver, which in this work was OpenSBLI.

Building on this foundation, Chapter 4 employed the validated high-enthalpy framework to perform scale-resolved simulations of a free shear mixing layer. The primary objective of this study was to investigate the influence of high-enthalpy effects on turbulent structures within a time-dependent flow configuration. The findings can be categorised into two main aspects. First, a qualitative analysis demonstrated that, in the presence of thermal non-equilibrium, distinct non-equilibrium states emerge around vortex structures depending on the local flow conditions. Second, a quantitative assessment showed that while thermal non-equilibrium directly affects turbulent characteristics such as turbulent kinetic energy in two-dimensional simulations, its influence on the dynamics of three-dimensional turbulent structures is minimal. This chapter addressed the second and third research questions by providing both qualitative insight and quantitative evaluation of the coupling between turbulence and thermo-chemical non-equilibrium in unsteady flows.

Following the shear-layer investigation, a clear gap in the literature was identified regarding accurate yet computationally efficient representations of transport properties under high-enthalpy conditions for large-scale simulations. To address this need, Chapter 5 proposed an efficient formulation for viscosity and thermal conductivity specifically designed for scale-resolved, computationally intensive frameworks. The proposed model demonstrated strong agreement with the most accurate available reference models while achieving computational cost reductions of up to 50%. This chapter further contributed to addressing the first research question by advancing the modelling of flow properties under high-enthalpy conditions, with particular emphasis on the balance between accuracy and computational efficiency.

Using the transport property model introduced in Chapter 5, Chapter 6 extended the investigation to a more computationally demanding configuration: a scale-resolved turbulent channel flow. This wall-bounded, statistically one-dimensional configuration enabled a detailed assessment of thermo-chemical non-equilibrium effects in a canonical turbulent flow. Two key findings emerged from this study. First, qualitative analysis revealed that regions near the wall experience pronounced thermal and potentially chemical non-equilibrium. Second, while thermal non-equilibrium was shown to have a minimal impact on global flow statistics, chemical non-equilibrium near the wall exerted a significant influence, not only locally but across the entire channel. These results highlight the importance of chemical non-equilibrium effects in wall-bounded turbulent flows and directly address the third research question concerning the interaction between turbulence and non-equilibrium phenomena.

Finally, with respect to the fourth research question, which focuses on understanding the underlying mechanisms governing thermo-chemical non-equilibrium, both Chapter 4 and

Chapter 6 provided insight into the characteristic behaviour of such flows in relation to turbulence. In both configurations, a clear link between thermal non-equilibrium and temperature fluctuations was observed, consistent with findings reported in the literature. Furthermore, the relationship between thermal and chemical relaxation timescales and the characteristic flow timescales was clearly demonstrated, providing insight into the nature and classification of the resulting thermo-chemical non-equilibrium states.

In summary, while this thesis highlights the inherent complexity associated with modelling high-enthalpy flows and their interaction with turbulence—and recognises that substantial scope for future research remains—it establishes a robust foundation for the systematic evaluation of thermo-chemical non-equilibrium effects in canonical turbulent flow configurations.

7.2 Future Work

Finally, while each chapter of this thesis includes a dedicated discussion of future work specific to the research questions addressed therein, there also exists a broader set of research directions that are expected to play a significant role in advancing the understanding and modelling of high-enthalpy effects in the coming years. Three such overarching research areas are highlighted below.

- When considering hypersonic flight, particularly under atmospheric re-entry conditions, the simulation of transitional flows—where portions of the flow are well described by continuum assumptions while others are rarefied—remains a significant challenge. Such flow regimes commonly arise at high altitudes, within strong expansion regions, or in applications such as rocket plumes operating in near-vacuum environments. To address this limitation, hybrid numerical frameworks coupling Direct Simulation Monte Carlo (DSMC) methods with computational fluid dynamics (CFD)—applied to the rarefied and continuum regions, respectively—have been developed in recent years (Nompelis et al., 2025; Tatsios et al., 2025; Nompelis et al., 2023; Burt and Boyd, 2009; Espinoza et al., 2016). Preliminary results reported in the literature demonstrate that these hybrid approaches can significantly improve the accuracy of flow predictions across mixed-regime conditions while maintaining computational efficiency. The implementation of such hybrid DSMC–CFD capabilities within a scalable, high-order, open-source solver such as OpenSBLI therefore represents an exciting and highly relevant direction for future work.

- In the context of scale-resolved hypersonic simulations and the coupling of high-enthalpy effects with advanced CFD frameworks, thermo-chemical non-equilibrium is typically modelled using relatively simple representations based

on polynomial fits or tabulated thermodynamic data. While such approaches are computationally efficient, they may limit the fidelity with which chemical kinetics and internal energy modes are represented, particularly when all turbulent scales are explicitly resolved. Although the flow-field dynamics are treated with high accuracy, the underlying chemical and thermodynamic models are often comparatively simplified. Developing more accurate and expressive representations of thermo-chemical properties that are compatible with scale-resolved simulations therefore constitutes an important avenue for future research. In this regard, data-driven thermodynamic databases and neural-network-based surrogate models have emerged as a promising research area over the past several decades. Recent studies, such as those by Qu et al. (2024) and Wang et al. (2025), demonstrate the use of constrained artificial neural networks for modelling chemical source terms while enforcing physical consistency. Additionally, reduced-order surrogate approaches, such as those proposed by Scherding et al. (2025), have already been successfully applied to hypersonic flows and are expected to become increasingly prevalent in future high-fidelity simulations.

- The potential of the discontinuous Galerkin spectral element method (DG-SEM) as a numerical framework for solving compressible flows has been recognised for several decades. More recently, its suitability as a future modelling approach for hypersonic applications has gained increased attention, particularly due to its ability to achieve high-order accuracy on arbitrarily shaped grid elements while maintaining strict local conservation properties (Josyula, 2015). These characteristics make discontinuous Galerkin formulations a compelling alternative to the high-order finite-difference framework adopted in this thesis, especially for applications involving complex geometries, strong gradients, and multi-physics coupling. DG-SEM formulations are well suited for modern parallel computing architectures due to their element-local data structures and favourable communication patterns, making them attractive for large-scale simulations incorporating detailed chemistry and multi-temperature models. A number of recent advancements have demonstrated the applicability of discontinuous Galerkin methods to hypersonic and reacting flow simulations, including the works of Lueth et al. (2026); Keeton et al. (2025); Hoskin et al. (2024); Peyvan et al. (2022); Terrana et al. (2020). Collectively, these studies highlight the growing maturity of discontinuous Galerkin approaches and underline their strong potential as a complementary and, in some cases, advantageous alternative for future investigations of scale-resolved hypersonic flows with thermo-chemical non-equilibrium effects.

Appendix A

Thermo-Chemical Model

This appendix documents the thermo-chemical models employed in the present study. It includes the chemical reactions considered, the associated reaction-rate coefficients, and equilibrium constant formulation. In addition, a complete formulation of the final chemical model selected in Chapter 3 is provided.

A.1 Chemical Model

A.1.1 Park 2001

The 'P2001' chemical model refers to that presented by Park et al. (2001). Within this publication, four chemical reactions are considered for a five-species air composition. The chemical reactions associated with the five-species air mixture, when expanded for computational modelling using the provided coefficients, are defined in the form

$$
\begin{aligned}
R_1: &\quad \mathrm{O_2 + M \leftrightarrow 2O + M}, && (\mathrm{M = N,\ O}) \\
R_2: &\quad \mathrm{O_2 + M \leftrightarrow 2O + M}, && (\mathrm{M = N_2,\ O_2,\ NO}) \\
R_3: &\quad \mathrm{N_2 + M \leftrightarrow 2N + M}, && (\mathrm{M = N,\ O}) \\
R_4: &\quad \mathrm{N_2 + M \leftrightarrow 2N + M}, && (\mathrm{M = N_2,\ O_2,\ NO}) \\
R_5: &\quad \mathrm{NO + O \leftrightarrow N + O_2} \\
R_6: &\quad \mathrm{N_2 + O \leftrightarrow N + NO}
\end{aligned}
$$

The coefficients for the equilibrium constant and the reaction rates are given in Table A.1. The equilibrium constant for this model is evaluated at temperatures of 3000 K, 6000 K, 9000 K, 12000 K, and 15000 K, and is expressed in terms of a polynomial in the form of

$$K_c = \exp\left[A_1/Z + A_2 + A_3 \ln(Z) + A_4 Z + A_5 Z^2\right] \quad , \tag{A.1}$$

TABLE A.1: 'P2001' chemical model coefficients for the five-species air system.

	R_1	R_2	R_3	R_4	R_5	R_6
C	1.0×10^{22}	2.0×10^{21}	3.0×10^{22}	7.0×10^{21}	8.4×10^{12}	5.7×10^{12}
n	-1.5	-1.5	-1.6	-1.6	0.00	0.42
T_r	5.936×10^4	5.936×10^4	1.132×10^5	1.132×10^5	1.940×10^4	4.2938×10^4
A_1	$+1.578640$	$+1.578640$	-3.293682	-3.293682	-1.840133	-3.032189
A_2	$+2.688744$	$+2.688744$	$+0.998998$	$+0.998998$	-1.768215	$+0.078464$
A_3	$+4.215573$	$+4.215573$	-8.237028	-8.237028	-4.759554	-7.693047
A_4	-8.091354	-8.091354	-5.526183	-5.526183	$+1.153872$	$+1.411299$
A_5	$+0.174260$	$+0.174260$	-0.582174	-0.582174	-0.238985	-0.517448
T_a	$\sqrt{TT_v}$	$\sqrt{TT_v}$	$\sqrt{TT_v}$	$\sqrt{TT_v}$	T	T

where

$$Z = 10,000/T \quad .$$

The forward reaction-rate coefficients are expressed in the form of

$$k_{r_f} = CT_a^n \exp(-T_r/T_a) \quad , \tag{2.60}$$

where T_a is evaluated according to the definition given in Table A.1, and the forward reaction-rate coefficient k_{r_f} used to calculate the backward reaction-rate coefficient is evaluated using $T_a = T$.

A.1.2 Park 1989 - GGS

The 'P1989-GGS' chemical model refers to that presented by Gnoffo et al. (1989). In this model, five chemical reactions are considered for a five-species air mixture. When expanded for computational modelling using the provided coefficients, the chemical reaction set is defined in the form

$$\begin{aligned}
R_1 &= \quad \mathrm{O_2 + M \leftrightarrow 2O + M} && (\mathrm{M = N, O}) \\
R_2 &= \quad \mathrm{O_2 + M \leftrightarrow 2O + M} && (\mathrm{M = N_2, O_2, NO}) \\
R_3 &= \quad \mathrm{N_2 + M \leftrightarrow 2N + M} && (\mathrm{M = N}) \\
R_4 &= \quad \mathrm{N_2 + M \leftrightarrow 2N + M} && (\mathrm{M = O}) \\
R_5 &= \quad \mathrm{N_2 + M \leftrightarrow 2N + M} && (\mathrm{M = N_2, O_2}) \\
R_6 &= \quad \mathrm{N_2 + M \leftrightarrow 2N + M} && (\mathrm{M = NO}) \\
R_7 &= \quad \mathrm{NO + M \leftrightarrow N + O + M} && (\mathrm{M = N, O, N_2, O_2, NO}) \\
R_8 &= \quad \mathrm{NO + O \leftrightarrow N + O_2} \\
R_9 &= \quad \mathrm{N_2 + O \leftrightarrow N + NO}
\end{aligned}$$

TABLE A.2: 'P1989-GGS' chemical model coefficients from Gnoffo et al. (1989).

Reaction	C	n	T_f	A_1	A_2	A_3	A_4	A_5
R_1	2.900×10^{23}	-2.0	5.975×10^4	$+2.855$	$+0.988$	-6.181	-0.023	-0.001
R_2	9.680×10^{22}	-2.0	5.975×10^4	$+2.855$	$+0.988$	-6.181	-0.023	-0.001
R_3	1.600×10^{22}	-1.6	1.132×10^5	$+1.858$	-1.325	-9.856	-0.174	$+0.008$
R_4	4.980×10^{22}	-1.6	1.132×10^5	$+1.858$	-1.325	-9.856	-0.174	$+0.008$
R_5	3.700×10^{21}	-1.6	1.132×10^5	$+1.858$	-1.325	-9.856	-0.174	$+0.008$
R_6	4.980×10^{21}	-1.6	1.132×10^5	$+1.858$	-1.325	-9.856	-0.174	$+0.008$
R_7	7.950×10^{23}	-2.0	7.550×10^4	$+0.792$	-0.492	-6.761	-0.091	$+0.004$
R_8	8.370×10^{12}	0.0	1.945×10^4	-2.063	-1.480	-0.580	-0.114	$+0.005$
R_9	6.440×10^{17}	-1.0	3.837×10^4	$+1.066$	-0.833	-3.095	-0.084	$+0.004$

The coefficients used for evaluating the equilibrium constants and reaction-rate expressions are given in Table A.2. The reacting temperature T_a in this model is defined as $\sqrt{TT_v}$ for all forward reaction-rate evaluations and as T for all backward reaction-rate evaluations.

The equilibrium constant for this model is evaluated at temperatures of 1000 K, 2000 K, 4000 K, 8000 K, and 16000 K, taken from the work of Park (1985) and is expressed in terms of a polynomial in the form of

$$K_c = \exp\left[A_1 + A_2 \ln(Z) + A_3 Z + A_4 Z^2 + A_5 Z^3\right] \quad , \tag{A.2}$$

where

$$Z = 10,000/T \quad .$$

A.1.3 Selected Model

The following chemical model incorporates the latest coefficients given by Park et al. (2001), with the addition of coefficients for the missing reaction from Park (1993). The chemical reactions for a five-species air mixture are

$$\begin{aligned}
R_1 &= \mathrm{N_2 + M \leftrightarrow 2N + M} && (\mathrm{M = N, O}) \\
R_2 &= \mathrm{N_2 + M \leftrightarrow 2N + M} && (\mathrm{M = N_2, O_2, NO}) \\
R_3 &= \mathrm{O_2 + M \leftrightarrow 2O + M} && (\mathrm{M = N, O}) \\
R_4 &= \mathrm{O_2 + M \leftrightarrow 2O + M} && (\mathrm{M = N_2, O_2, NO}) \\
R_5 &= \mathrm{NO + M \leftrightarrow N + O + M} && (\mathrm{M = O, N, NO}) \\
R_6 &= \mathrm{NO + M \leftrightarrow N + O + M} && (\mathrm{M = O_2, N_2}) \\
R_7 &= \mathrm{N_2 + O \leftrightarrow N + NO} \\
R_8 &= \mathrm{NO + O \leftrightarrow N + O_2}
\end{aligned}$$

The coefficients used for the equilibrium constant and reaction-rate expressions are given in Table A.3. The equilibrium constant is obtained from the in-house polynomial representation of the NASA-9 database, as discussed and presented in Section 3.1.2 . The reaction-rate coefficient is written as

$$k = C T_a^n \exp(-T_r/T_a) \quad , \tag{2.60}$$

where the backward reaction-rate coefficient is evaluated using $T_a = T$.

The formulation for the forward reaction rates is

$$\begin{aligned}
R_{f1} &= 1000\, k_{f1} \left(0.001\frac{\rho_{\mathrm{N_2}}}{M_{\mathrm{N_2}}}\right)\left(0.001\frac{\rho_{\mathrm{O}}}{M_{\mathrm{O}}} + 0.001\frac{\rho_{\mathrm{N}}}{M_{\mathrm{N}}}\right) \quad , \\
R_{f2} &= 1000\, k_{f2} \left(0.001\frac{\rho_{\mathrm{N_2}}}{M_{\mathrm{N_2}}}\right)\left(0.001\frac{\rho_{\mathrm{O_2}}}{M_{\mathrm{O_2}}} + 0.001\frac{\rho_{\mathrm{N_2}}}{M_{\mathrm{N_2}}} + 0.001\frac{\rho_{\mathrm{NO}}}{M_{\mathrm{NO}}}\right) \quad , \\
R_{f3} &= 1000\, k_{f3} \left(0.001\frac{\rho_{\mathrm{O_2}}}{M_{\mathrm{O_2}}}\right)\left(0.001\frac{\rho_{\mathrm{O}}}{M_{\mathrm{O}}} + 0.001\frac{\rho_{\mathrm{N}}}{M_{\mathrm{N}}}\right) \quad , \\
R_{f4} &= 1000\, k_{f4} \left(0.001\frac{\rho_{\mathrm{O_2}}}{M_{\mathrm{O_2}}}\right)\left(0.001\frac{\rho_{\mathrm{O_2}}}{M_{\mathrm{O_2}}} + 0.001\frac{\rho_{\mathrm{N_2}}}{M_{\mathrm{N_2}}} + 0.001\frac{\rho_{\mathrm{NO}}}{M_{\mathrm{NO}}}\right) \quad , \\
R_{f5} &= 1000\, k_{f5} \left(0.001\frac{\rho_{\mathrm{NO}}}{M_{\mathrm{NO}}}\right)\left(0.001\frac{\rho_{\mathrm{O}}}{M_{\mathrm{O}}} + 0.001\frac{\rho_{\mathrm{N}}}{M_{\mathrm{N}}} + 0.001\frac{\rho_{\mathrm{NO}}}{M_{\mathrm{NO}}}\right) \quad , \\
R_{f6} &= 1000\, k_{f6} \left(0.001\frac{\rho_{\mathrm{NO}}}{M_{\mathrm{NO}}}\right)\left(0.001\frac{\rho_{\mathrm{O_2}}}{M_{\mathrm{O_2}}} + 0.001\frac{\rho_{\mathrm{N_2}}}{M_{\mathrm{N_2}}}\right) \quad , \\
R_{f7} &= 1000\, k_{f7} \left(0.001\frac{\rho_{\mathrm{N_2}}}{M_{\mathrm{N_2}}}\right)\left(0.001\frac{\rho_{\mathrm{O}}}{M_{\mathrm{O}}}\right) \quad , \\
R_{f8} &= 1000\, k_{f8} \left(0.001\frac{\rho_{\mathrm{NO}}}{M_{\mathrm{NO}}}\right)\left(0.001\frac{\rho_{\mathrm{O}}}{M_{\mathrm{O}}}\right) \quad ,
\end{aligned}$$

and the formulation for the backward reaction rates is

$$\begin{aligned}
R_{b1} &= 1000\, k_{b1} \left(0.001\frac{\rho_{\mathrm{N}}}{M_{\mathrm{N}}}\right)^2\left(0.001\frac{\rho_{\mathrm{O}}}{M_{\mathrm{O}}} + 0.001\frac{\rho_{\mathrm{N}}}{M_{\mathrm{N}}}\right) \quad , \\
R_{b2} &= 1000\, k_{b2} \left(0.001\frac{\rho_{\mathrm{N}}}{M_{\mathrm{N}}}\right)^2\left(0.001\frac{\rho_{\mathrm{O_2}}}{M_{\mathrm{O_2}}} + 0.001\frac{\rho_{\mathrm{N_2}}}{M_{\mathrm{N_2}}} + 0.001\frac{\rho_{\mathrm{NO}}}{M_{\mathrm{NO}}}\right) \quad , \\
R_{b3} &= 1000\, k_{b3} \left(0.001\frac{\rho_{\mathrm{O}}}{M_{\mathrm{O}}}\right)^2\left(0.001\frac{\rho_{\mathrm{O}}}{M_{\mathrm{O}}} + 0.001\frac{\rho_{\mathrm{N}}}{M_{\mathrm{N}}}\right) \quad , \\
R_{b4} &= 1000\, k_{b4} \left(0.001\frac{\rho_{\mathrm{O}}}{M_{\mathrm{O}}}\right)^2\left(0.001\frac{\rho_{\mathrm{O_2}}}{M_{\mathrm{O_2}}} + 0.001\frac{\rho_{\mathrm{N_2}}}{M_{\mathrm{N_2}}} + 0.001\frac{\rho_{\mathrm{NO}}}{M_{\mathrm{NO}}}\right) \quad , \\
R_{b5} &= 1000\, k_{b5} \left(0.001\frac{\rho_{\mathrm{N}}}{M_{\mathrm{N}}}\right)\left(0.001\frac{\rho_{\mathrm{O}}}{M_{\mathrm{O}}}\right)\left(0.001\frac{\rho_{\mathrm{O}}}{M_{\mathrm{O}}} + 0.001\frac{\rho_{\mathrm{N}}}{M_{\mathrm{N}}} + 0.001\frac{\rho_{\mathrm{NO}}}{M_{\mathrm{NO}}}\right) \quad , \\
R_{b6} &= 1000\, k_{b6} \left(0.001\frac{\rho_{\mathrm{N}}}{M_{\mathrm{N}}}\right)\left(0.001\frac{\rho_{\mathrm{O}}}{M_{\mathrm{O}}}\right)\left(0.001\frac{\rho_{\mathrm{O_2}}}{M_{\mathrm{O_2}}} + 0.001\frac{\rho_{\mathrm{N_2}}}{M_{\mathrm{N_2}}}\right) \quad , \\
R_{b7} &= 1000\, k_{b7} \left(0.001\frac{\rho_{\mathrm{NO}}}{M_{\mathrm{NO}}}\right)\left(0.001\frac{\rho_{\mathrm{N}}}{M_{\mathrm{N}}}\right) \quad , \\
R_{b8} &= 1000\, k_{b8} \left(0.001\frac{\rho_{\mathrm{O_2}}}{M_{\mathrm{O_2}}}\right)\left(0.001\frac{\rho_{\mathrm{N}}}{M_{\mathrm{N}}}\right) \quad .
\end{aligned}$$

TABLE A.3: The chemical model coefficients for the selected model.

Reaction	C	n	T_r	T_a	A_1	A_2	A_3	A_4	A_5	A_6
R_1	$3.0e22$	-1.6	$1.132e5$	$\sqrt{TT_v}$	$2.091870e+03$	$-1.134452e+05$	$-6.427685e-01$	$5.610081e-01$	$-3.300745e-04$	$1.836761e-08$
R_2	$7.0e21$	-1.6	$1.132e5$	$\sqrt{TT_v}$	$2.091870e+03$	$-1.134452e+05$	$-6.427685e-01$	$5.610081e-01$	$-3.300745e-04$	$1.836761e-08$
R_3	$1.0e22$	-1.5	$5.936e4$	$\sqrt{TT_v}$	$6.275151e+03$	$-6.017939e+04$	$3.082217e+00$	$9.324624e-02$	$-2.147384e-04$	$7.298221e-09$
R_4	$2.0e21$	-1.5	$5.936e4$	$\sqrt{TT_v}$	$6.275151e+03$	$-6.017939e+04$	$3.082217e+00$	$9.324624e-02$	$-2.147384e-04$	$7.298221e-09$
R_5	$1.1e17$	0.00	$7.550e4$	$\sqrt{TT_v}$	$5.029763e+03$	$-7.594795e+04$	$7.563820e-01$	$1.817658e-01$	$-6.685894e-06$	$4.489270e-09$
R_6	$5.0e15$	0.00	$7.550e4$	$\sqrt{TT_v}$	$5.029763e+03$	$-7.594795e+04$	$7.563820e-01$	$1.817658e-01$	$-6.685894e-06$	$4.489270e-09$
R_7	$5.7e12$	0.42	$4.2938e4$	T	$-2.937898e+03$	$-3.749727e+04$	$-1.399152e+00$	$3.792425e-01$	$-1.086524e-04$	$-6.685894e-06$
R_8	$8.4e12$	0.00	$1.940e4$	T	$-1.245460e+03$	$-1.576855e+04$	$-2.325883e+00$	$8.852601e-02$	$-6.685894e-06$	$4.489270e-09$

The species reaction rate is then expressed as

$$\begin{aligned}
\dot{\omega}_{\mathrm{O}} &= M_{\mathrm{O}} \left[\, 2(R_{f3} - R_{b3}) + 2(R_{f4} - R_{b4}) + (R_{f5} - R_{b5}) + (R_{f6} - R_{b6}) \right. \\
&\qquad \left. - (R_{f7} - R_{b7}) - (R_{f8} - R_{b8}) \, \right] \\
\dot{\omega}_{\mathrm{O_2}} &= M_{\mathrm{O_2}} \left[-(R_{f3} - R_{b3}) - (R_{f4} - R_{b4}) + (R_{f8} - R_{b8}) \right] \\
\dot{\omega}_{\mathrm{N}} &= M_{\mathrm{N}} \left[\, 2(R_{f1} - R_{b1}) + 2(R_{f2} - R_{b2}) + (R_{f5} - R_{b5}) \right. \\
&\qquad \left. + (R_{f6} - R_{b6}) + (R_{f7} - R_{b7}) + (R_{f8} - R_{b8}) \, \right] \\
\dot{\omega}_{\mathrm{N_2}} &= M_{\mathrm{N_2}} \left[-(R_{f1} - R_{b1}) - (R_{f2} - R_{b2}) - (R_{f7} - R_{b7}) \right] \\
\dot{\omega}_{\mathrm{NO}} &= M_{\mathrm{NO}} \left[-(R_{f5} - R_{b5}) - (R_{f6} - R_{b6}) + (R_{f7} - R_{b7}) - (R_{f8} - R_{b8}) \right]
\end{aligned}$$

A.2 Thermal Model

A.2.1 Park 1993 Relaxation Time

The coefficients for the vibrational relaxation time proposed by Park (1993) are summarised in Table A.4.

TABLE A.4: Coefficients for the vibrational relaxation time as defined by Park (1993).

A					
	O	O_2	N	N_2	NO
N_2	72.4	229	180	221	225
O_2	47.7	138	72.4	134	136
NO	49.5	49.5	49.5	49.5	49.5
B					
	O	O_2	N	N_2	NO
N_2	0.0150	0.0295	0.0262	0.0290	0.0293
O_2	0.0590	0.0300	0.0150	0.0295	0.0298
NO	0.042	0.042	0.042	0.042	0.042

A.3 Transport Properties

A.3.1 Collision Integrals

The evaluation of the collision integrals are carried out by the polynomial fits given by Gupta et al. (1990), revisited here

$$\pi\bar{\Omega}_{ij}^{(1,1)} = \exp\left(D_{11}\right) T^{\left[A_{11}\ln(T)^2+B_{11}\ln(T)+C_{11}\right]} \quad , \tag{2.82}$$

$$\pi\bar{\Omega}_{ij}^{(2,2)} = \exp\left(D_{22}\right) T^{\left[A_{22}\ln(T)^2+B_{22}\ln(T)+C_{22}\right]} \quad , \tag{2.83}$$

where T is the translational temperature, and the coefficients A_{11}, B_{11}, C_{11}, D_{11}, A_{22}, B_{22}, C_{22}, and D_{22} are provided in Table A.5 and A.6.

Aditionally, the ratio B_{ij}^{*} is represented using a curve-fit expression of the form

$$B_{ij}^{*} = \exp\left(C\right) T^{[A\ln(T)+B]} \quad , \tag{2.111}$$

with coefficients A, B, and C provided in Table A.7.

Table A.5: Curve-fit constants for the collision cross-section $\bar{\Omega}_{ij}^{(1,1)}$.

Interaction pair $(i-j)$	$A_{\bar{\Omega}_{ij}^{(1,1)}}$	$B_{\bar{\Omega}_{ij}^{(1,1)}}$	$C_{\bar{\Omega}_{ij}^{(1,1)}}$	$D_{\bar{\Omega}_{ij}^{(1,1)}}$
$N_2 - N_2$	0	−0.0112	−0.1182	4.8464
$O_2 - N_2$	0	−0.0465	0.5729	1.6185
$O_2 - O_2$	0	−0.0410	0.4977	1.8302
$N - N_2$	0	−0.0194	0.0119	4.1055
$N - O_2$	0	−0.0179	0.0152	3.9996
$N - N$	0	−0.0033	−0.0572	5.0452
$O - N_2$	0	−0.0139	−0.0825	4.5785
$O - O_2$	0	−0.0226	0.1300	3.3363
$O - N$	0	0.0048	−0.4195	5.7774
$O - O$	0	−0.0034	−0.0572	4.9901
$NO - N_2$	0	−0.0291	0.2324	3.2082
$NO - O_2$	0	−0.0438	0.5352	1.7252
$NO - N$	0	−0.0185	0.0118	4.0590
$NO - O$	0	−0.0179	0.0152	3.9996
$NO - NO$	0	−0.0364	0.3825	2.4718

TABLE A.6: Curve-fit constants for the collision cross-section $\bar{\Omega}_{ij}^{(2,2)}$.

Interaction pair $(i-j)$	$A_{\bar{\Omega}_{ij}^{(2,2)}}$	$B_{\bar{\Omega}_{ij}^{(2,2)}}$	$C_{\bar{\Omega}_{ij}^{(2,2)}}$	$D_{\bar{\Omega}_{ij}^{(2,2)}}$
$N_2 - N_2$	0	−0.0203	0.0683	4.0900
$O_2 - N_2$	0	−0.0558	0.7590	0.8955
$O_2 - O_2$	0	−0.0485	0.6475	1.2607
$N - N_2$	0	−0.0190	0.0239	4.1782
$N - O_2$	0	−0.0203	0.0730	3.8818
$N - N$	0	−0.0118	−0.0960	4.3252
$O - N_2$	0	−0.0169	−0.0143	4.4195
$O - O_2$	0	−0.0247	0.1783	3.2517
$O - N$	0	0.0065	−0.4467	6.0426
$O - O$	0	−0.0207	0.0780	3.5658
$NO - N_2$	0	−0.0385	0.4226	2.4507
$NO - O_2$	0	−0.0522	0.7045	1.0738
$NO - N$	0	−0.0196	0.0478	4.0321
$NO - O$	0	−0.0203	0.0730	3.8818
$NO - NO$	0	−0.0453	0.5624	1.7669

TABLE A.7: Curve-fit constants for the collision cross-section ratio B_{ij}^* ($1000\,\mathrm{K} \leq T \leq 30{,}000\,\mathrm{K}$).

Interaction pair $(i-j)$	$A_{B_{ij}^*}$	$B_{B_{ij}^*}$	$C_{B_{ij}^*}$
$N_2 - N_2$	−0.0073	0.1444	−0.5625
$O_2 - N_2$	−0.0019	0.0602	−0.2175
$O_2 - O_2$	0.0001	0.0181	−0.0306
$N - N_2$	0.0043	−0.0494	0.2850
$N - O_2$	0.0033	−0.0366	0.2332
$N - N$	0.0002	0.0002	0.0537
$O - N_2$	0.0042	−0.0471	0.2747
$O - O_2$	0.0024	−0.0245	0.1808
$O - N$	0.0147	−0.2628	1.2943
$O - O$	0.0002	0	0.0549
$NO - N_2$	−0.0045	0.1010	−0.3872
$NO - O_2$	−0.0010	0.0410	−0.1312
$NO - N$	0.0038	−0.0425	0.2574
$NO - O$	0.0033	−0.0366	0.2332
$NO - NO$	−0.0027	0.0700	−0.2553

A.3.2 Binary Diffusion Coefficients

The binary diffusion coefficient is expressed in terms of polynomials given by Gupta et al. (1990) in the form

$$\mathscr{D}_{ij} = \frac{kT}{p\Delta_{ij}^{(1)}} = \frac{\mathscr{D}_{ij}^{G}}{p} \quad , \tag{2.129}$$

TABLE A.8: Constants for diffusion coefficient curve fits.

Interaction pair $(i-j)$	$A_{\bar{D}_{ij}}$	$B_{\bar{D}_{ij}}$	$C_{\bar{D}_{ij}}$	$D_{\bar{D}_{ij}}$
$N_2 - N_2$	0	0.0112	1.6182	−11.3091
$O_2 - N_2$	0	0.0465	0.9271	−8.1137
$O_2 - O_2$	0	0.0410	1.0023	−8.3597
$N - N_2$	0	0.0195	1.4880	−10.3654
$N - O_2$	0	0.0179	1.4848	−10.2810
$N - N$	0	0.0033	1.5572	−11.1616
$O - N_2$	0	0.0140	1.5824	−10.8819
$O - O_2$	0	0.0226	1.3700	−9.6631
$O - N$	0	−0.0048	1.9195	−11.9261
$O - O$	0	0.0034	1.5572	−11.1729
$NO - N_2$	0	0.0291	1.2676	−9.6878
$NO - O_2$	0	0.0438	0.9647	−8.2380
$NO - N$	0	0.0185	1.4882	−10.3301
$NO - O$	0	0.0179	1.4848	−10.3155
$NO - NO$	0	0.0364	1.1176	−8.9695

where $\mathscr{D}_{ij}^{G}$ is given in the form

$$\mathscr{D}_{ij}^{G} = \frac{kT}{\Delta_{ij}^{(1)}} = \exp(D)\, T^{(A\ln(T)^2 + B\ \ln(T) + C)} \quad , \tag{2.130}$$

where the coefficients A, B, C, D are given in Table A.8.

A.3.3 Lemmon-Jacobsen Coefficients

This section includes the coefficients required to evaluate the transport properties using the form given by Lemmon and Jacobsen (2004). The coefficients defined in Table A.9 are those for viscosity and thermal conductivity, Table A.10 are those for residual viscosity and Table A.11 include those for residual thermal conductivity.

TABLE A.9: Parameters of the viscosity and thermal conductivity equations.

Parameter	Nitrogen	Oxygen	Air
T_c (K)	126.192	154.581	132.6312
ρ_c (mol·dm^{-3})	11.1839	13.63	10.4477
ρ_c (MPa)	3.3958	5.043	3.78502
M (g·mol^{-1})	28.01348	31.9988	28.9586
ε/k (K)	98.94	118.5	103.3
σ (nm)	0.3656	0.3428	0.360
ξ_0 (nm)	0.17	0.24	0.11
T_{ref} (K)	252.384	309.162	265.262

TABLE A.10: Coefficients and exponents of the residual fluid viscosity equations.

	Nitrogen				Oxygen				Air			
i	N_i	t_i	d_i	l_i	N_i	t_i	d_i	l_i	N_i	t_i	d_i	l_i
1	10.72	0.1	2	0	17.67	0.05	1	0	10.72	0.2	1	0
2	0.03989	0.25	10	1	0.4042	0.0	5	0	1.122	0.05	4	0
3	0.001208	3.2	12	1	0.0001077	2.10	12	0	0.002019	2.4	9	0
4	−7.402	0.9	2	2	0.3510	0.0	8	1	−8.876	0.6	1	1
5	4.620	0.3	1	3	−13.67	0.5	1	2	−0.02916	3.6	8	1

TABLE A.11: Coefficients and exponents of the residual fluid thermal conductivity equations.

	Nitrogen				Oxygen				Air			
i	N_i	t_i	d_i	l_i	N_i	t_i	d_i	l_i	N_i	t_i	d_i	l_i
1	1.511	0.0	0	0	1.036	0.0	0	0	1.308	0.0	0	0
2	2.117	−1.0	0	0	6.283	−0.9	0	0	1.405	−1.1	0	0
3	−3.332	−0.7	0	0	−4.262	−0.6	0	0	−1.036	−0.3	0	0
4	8.862	0.0	1	0	15.31	0.0	1	0	8.743	0.1	1	0
5	31.11	0.03	2	0	8.898	0.0	3	0	14.76	0.0	2	0
6	−73.13	0.2	3	1	−0.7336	0.3	4	0	−16.62	0.5	3	2
7	20.03	0.8	4	2	6.728	4.3	5	2	3.793	2.7	7	2
8	−0.7096	0.6	8	2	−4.374	0.5	7	2	−6.142	0.3	7	2
9	0.2672	1.9	10	2	−0.4747	1.8	10	2	−0.3778	1.3	11	2

Appendix B

Supplementary Simulation Data

This appendix presents supplementary data and simulation results complementary to those discussed in the main body of the thesis. The results included here follow the same methodology and flow conditions as the corresponding chapters, and are intended to provide additional context and support for the findings presented therein.

B.1 Mixing Layer Pairing Case

Figure B.1 illustrates the flow development within the three-dimensional large-domain configuration, where each sub-figure corresponds to a different stage of the vortex roll-up at $\tau_\theta = 100,\ 500$, and 2400 respectively. Iso-surfaces of the Q-criterion at 4.0×10^9 are shown, overlaid with colour contours of $T_v - T$ indicating the magnitude of thermal non-equilibrium (in K). Following the initial disturbance, and similarly to the single-vortex simulations, large-scale vortex tubes develop in the form of horseshoe vortices (Figure B.1a), around which regions of thermal non-equilibrium emerge. At later times (Figure B.1b), the vortices begin to shed and break down, while the initially strong non-equilibrium regions relax progressively towards equilibrium. By the end of the simulation ($\tau_\theta > 1500$), the small-scale vortices have largely dissipated and only weak non-equilibrium pockets remain (Figure B.1c).

This case is in contrast to those presented earlier, due to the presence of larger turbulent structures in the initial phase and a more clearer and stronger development of non-equilibrium regions.

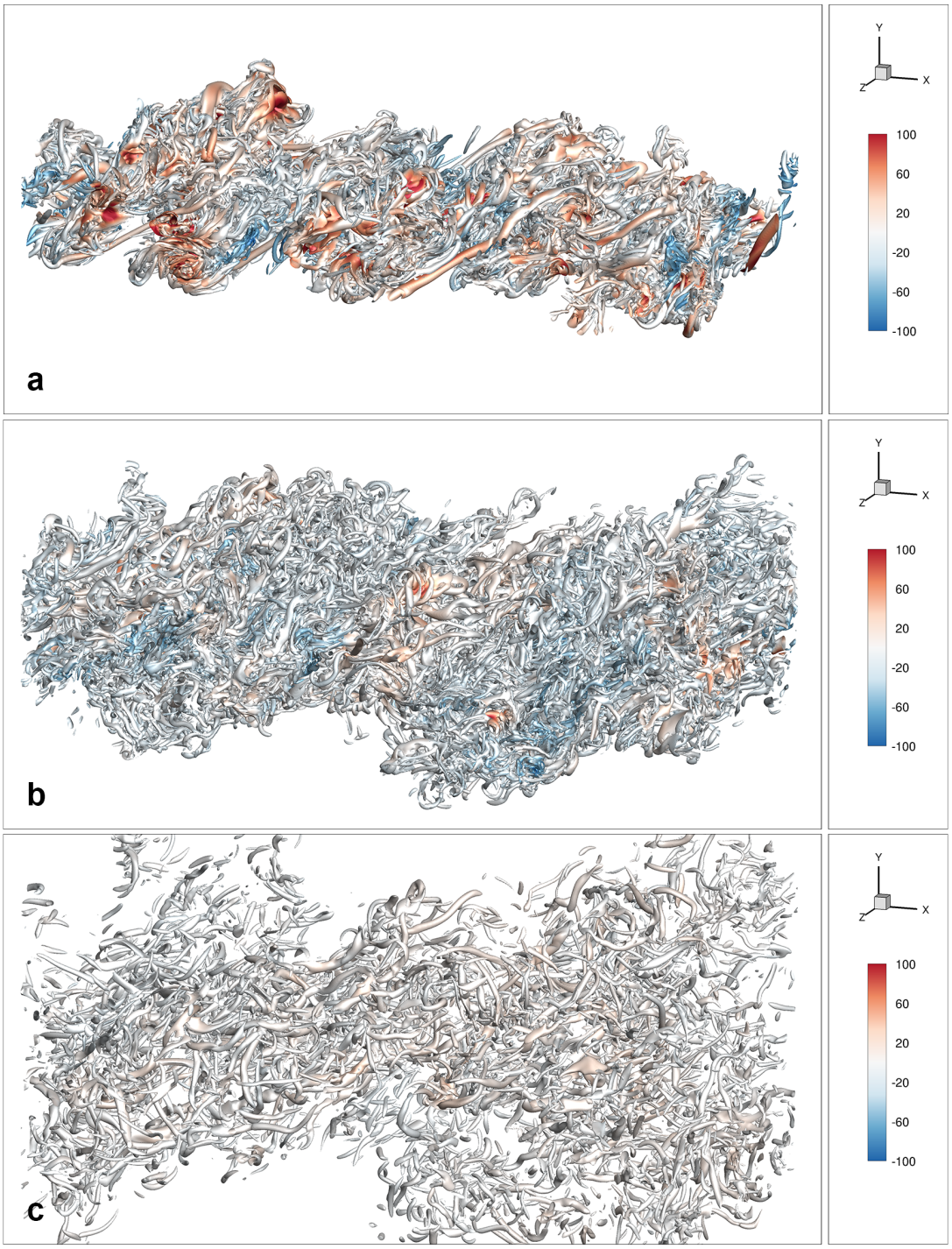

FIGURE B.1: Iso-surfaces of the Q-criterion for a three-dimensional, temporally developing mixing layer, coloured by $T_v - T$. (a)–(c) correspond to $\tau_\theta = 100,\ 500$, and 2400, respectively.

B.2 Validation Polynomials

The data for different validation cases were converted to polynomials to be plotted aside the simulations. This section includes the polynomial format and coefficients for those validation data. Equation B.1 gives the form in which the polynomials are in. For

validation Case A, Table B.1 includes the lines related to the LeMANs simulation while Table B.2 includes the lines corresponding to the HTR simulations.

$$q = \log_{10}(x) \qquad f(x) = \frac{\sum_{k=0}^{4} q_k \, \xi^k}{1 + \sum_{k=5}^{9} q_k \, \xi^k} \tag{B.1}$$

TABLE B.1: Case A LeMANS log-rational coefficients q_k. N refers to non-preferential and P refers to the preferential simulations.

k	NP - T	NP - T_v	P - T	P - T_v
0	2.20871772×10^{5}	9.34257977×10^{5}	2.44126191×10^{5}	$-3.41207327 \times 10^{6}$
1	6.26178098×10^{4}	2.84528399×10^{5}	7.16922665×10^{4}	1.07450312×10^{6}
2	5.35843147×10^{3}	2.76755989×10^{4}	6.53394861×10^{3}	2.05712018×10^{6}
3	1.20366816×10^{2}	7.84789441×10^{2}	1.70109699×10^{2}	7.93285892×10^{5}
4	$-1.58106325 \times 10^{1}$	$-2.09051173 \times 10^{2}$	$-1.62554547 \times 10^{1}$	1.46234802×10^{5}
5	-6.64441374	$-1.13017694 \times 10^{2}$	-6.83350105	1.45238596×10^{4}
6	-1.03529253	$-2.32999796 \times 10^{1}$	-1.06510817	7.50708812×10^{2}
7	$-7.16991182 \times 10^{-2}$	-2.16041246	$-7.37268517 \times 10^{-2}$	1.58938845×10^{1}
8	$-1.87717709 \times 10^{-3}$	$-7.57635193 \times 10^{-2}$	$-1.92661425 \times 10^{-3}$	-

TABLE B.2: Case A HTR log-rational coefficients q_k. N refers to non-preferential and P refers to the preferential simulations.

k	NP - T	NP - T_v	P - T	P - T_v
0	8.52870925×10^{4}	2.41527707×10^{6}	1.19171138×10^{5}	8.37421473×10^{5}
1	2.38712937×10^{4}	7.67499552×10^{5}	3.52873040×10^{4}	2.61761546×10^{5}
2	1.95866995×10^{3}	7.88945031×10^{4}	3.23071777×10^{3}	2.69520253×10^{4}
3	3.75087030×10^{1}	2.50506212×10^{3}	8.39276305×10^{1}	8.83183452×10^{2}
4	-6.27045150	$-3.92285547 \times 10^{2}$	-8.15511621	$-1.06064802 \times 10^{2}$
5	-2.74675589	$-2.07480993 \times 10^{2}$	-3.54841050	$-5.44144303 \times 10^{1}$
6	$-4.38678364 \times 10^{-1}$	$-4.19844056 \times 10^{1}$	$-5.66149069 \times 10^{-1}$	$-1.07697145 \times 10^{1}$
7	$-3.10267673 \times 10^{-2}$	-3.83548591	$-4.00018690 \times 10^{-2}$	$-9.69431507 \times 10^{-1}$
8	$-8.28924031 \times 10^{-4}$	$-1.33017721 \times 10^{-1}$	$-1.06525946 \times 10^{-3}$	$-3.33211935 \times 10^{-2}$

For the validation Case B, the coefficients are give in Table B.3. Similarly, for Case C, the coefficients are given in Table B.4.

TABLE B.3: Log-rational coefficients q_k for Validation Case B. The first two columns correspond to LeMANS, while the latter two correspond to HTR. NP refers to non-preferential.

	LeMANS		HTR	
k	NP - T	NP - T_v	NP - T	NP - T_v
0	1.56079555×10^{3}	1.26987332×10^{7}	$-1.20863931 \times 10^{9}$	1.28381956×10^{6}
1	4.04112902×10^{2}	3.85594450×10^{6}	$-6.41470834 \times 10^{8}$	3.83347269×10^{5}
2	2.69249680×10^{1}	3.87887412×10^{5}	$-1.07300882 \times 10^{8}$	3.81034564×10^{4}
3	$-1.51055024 \times 10^{-3}$	1.28951554×10^{4}	$-5.85962117 \times 10^{6}$	1.25917455×10^{3}
4	$5.15956569 \times 10^{-1}$	$-1.39174706 \times 10^{3}$	$-7.95771197 \times 10^{3}$	$-1.26011915 \times 10^{2}$
5	$1.09070404 \times 10^{-1}$	$-6.36763947 \times 10^{2}$	$-1.51976292 \times 10^{3}$	$-5.56582926 \times 10^{1}$
6	$1.17785234 \times 10^{-2}$	$-1.09951557 \times 10^{2}$	$-1.88775747 \times 10^{1}$	-9.25550163
7	$6.46329976 \times 10^{-4}$	-8.48781225	6.09033611	$-6.87098895 \times 10^{-1}$
8	$1.42143247 \times 10^{-5}$	$-2.47038602 \times 10^{-1}$	$-9.61477381 \times 10^{-2}$	$-1.92108664 \times 10^{-2}$

TABLE B.4: Log-rational coefficients q_k for Validation Case C (HyFoam).

k	T	T_v
0	5.30014937×10^{3}	4.87874105×10^{6}
1	2.31211275×10^{3}	$-1.35395643 \times 10^{6}$
2	3.35542330×10^{2}	$-5.40627465 \times 10^{5}$
3	1.59467841×10^{1}	$-4.08410361 \times 10^{4}$
4	$5.42772803 \times 10^{-1}$	9.54434600×10^{2}
5	$1.17014983 \times 10^{-1}$	9.05885748×10^{2}
6	$1.28158379 \times 10^{-2}$	2.55341068×10^{2}
7	$7.53876804 \times 10^{-4}$	2.83883296×10^{1}
8	$2.01903469 \times 10^{-5}$	1.04918358

Appendix C

Carbon Dioxide Modelling

For high-enthalpy flows, thermal and chemical non-equilibrium effects have a significant impact on the characteristic behaviour of the flow and, consequently, on its physical description. As a result, specific considerations are required when modelling such flows. Furthermore, when polyatomic species such as carbon dioxide are involved, additional complications arise compared to diatomic species, primarily due to the increased number of internal energy modes. This document therefore includes a brief discussion on the modelling of carbon dioxide as a polyatomic species within OpenSBLI for continuum-flow conditions.

C.1 Introduction

Further complications arise when modelling polyatomic species, primarily due to their thermal modes, which are strongly influenced by molecular structure. In macroscopic terms, CO_2 is a linear polyatomic molecule, as sketched in C.1.

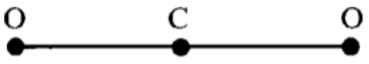

FIGURE C.1: CO_2 macroscopic description (Anderson, 2019).

As a result of its linear configuration, the molecule possesses three geometric degrees of freedom associated with translational motion and two geometric degrees of freedom associated with rotational motion, since the rotational kinetic energy about the molecular axis is negligible. In addition, CO_2 exhibits multiple degrees of freedom associated with vibrational motion (Anderson, 2019).

C.2 Literature review

A significant increase in the modelling of CO_2 has been observed over the past decade, driven largely by renewed interest in the Martian atmosphere and atmospheric entry problems. As will become evident, the substantial portion of the available literature originates from a specific research group. This concentration of work may be attributed both to the accessibility of their published sources and to the advanced modelling frameworks they have developed, which incorporate macroscopic flow descriptions informed by quantum-mechanical considerations. Consequently, these frameworks enable a more detailed representation of non-equilibrium processes. It should also be noted that this research group has a long-standing history of work on non-equilibrium flows and their physical modelling.

Kosareva et al. (2021) compares the three-temperature (3T) model, which is discussed in the present work, with a state-to-state formulation and a proposed four-temperature (4T) model, concluding that the latter exhibits improved agreement with the StS results. The primary distinction between the 3T and 4T models lies in the treatment of energy exchange, specifically the replacement of the Landau–Teller expression (Landau and Teller, 1936) with an alternative formulation. This study therefore provides a valuable reference for assessing the validity of the 3T thermal model for CO_2 used here in comparison with more detailed StS approaches. It is noted that the 3T model generally predicts slower relaxation processes. Moreover, the 3T formulation referenced by Kosareva is based on the model of Losev et al. (1999), which in turn adopts the framework proposed by Candler (1990) and employs relaxation parameters from Camac (1966). The latter assumes a single relaxation time for all vibrational modes, rather than distinguishing between individual modes, as is commonly done for air species. This raises the question of whether a more detailed treatment of vibrational relaxation would yield closer agreement with StS predictions. In this context, it is worth noting that Kustova and Mekhonoshina (2020) investigates vibrational relaxation in CO_2 using both the Schwartz–Slawsky–Herzfeld (SSH) and Forced Harmonic Oscillator (FHO) models within a three-temperature framework.

Kustova et al. (2020) further evaluates the accuracy of vibrational energy production terms in the three-temperature model, concluding that while vibrational–translational relaxation may be adequately described using the Landau–Teller expression, inter-mode energy exchange requires the introduction of relaxation times that depend explicitly on the vibrational temperature.

In a related study, Kustova et al. (2023) investigates bulk viscosity in non-equilibrium flows, comparing various models proposed in the literature. The results demonstrate significant discrepancies in predicted bulk viscosity values for CO_2, depending on the chosen formulation. This reference provides methodologies for computing bulk viscosity across different flow descriptions and shows consistency with models developed

by researchers working within the framework established by Giovangigli (Bruno and Giovangigli, 2011; Boukharfane et al., 2019; Giovangigli et al., 2010).

Kustova and Mekhonoshina (2021a) studies the calculation of vibrational relaxation times using the forced harmonic oscillator approach, while Kustova and Mekhonoshina (2021b) evaluates vibrational relaxation of CO_2 by comparing FHO-based predictions with experimental data. The primary focus of these studies is the comparison between cross-sections obtained from the SSH model and those derived from the FHO formulation.

Cao et al. (2022) investigates a supersonic channel flow of CO_2 using a three-temperature model. In this work, the internal energy modes are represented using the harmonic oscillator model, while viscosity and relaxation times are prescribed through power-law relations.

When modelling CO_2 under non-equilibrium conditions, the governing equations and numerical framework must be formulated to account for high-enthalpy effects. For thermo-chemical non-equilibrium flow models expressed in terms of multi-species gas mixtures, the reader is referred to Lee (1985); Gnoffo et al. (1989); Gupta et al. (1990); Park (1985); Anderson (2019); Vincenti and Kruger (1965).

C.3 Chemical Kinetic Model

For simulations involving only CO_2, the following set of chemical reactions must be considered:

$$\begin{aligned} CO_2 + M &\longleftrightarrow CO + O + M \\ CO + M &\longleftrightarrow C + O + M \\ O_2 + M &\longleftrightarrow O + O + M \\ CO_2 + O &\longleftrightarrow CO + O_2 \\ CO + O &\longleftrightarrow C + O_2 \\ CO + C &\longleftrightarrow C_2 + O \\ C_2 + M &\longleftrightarrow C + C + M \end{aligned} \tag{C.1}$$

The reactions listed above represent a combination of those proposed in Park et al. (1994) and Candler (1990). Further assessment is required to establish a definitive reaction set, as certain reactions are present in one reference but not in the other. Moreover, for comprehensive multi-species Mars entry simulations, including ionisation processes and a more detailed treatment of each reaction listed above, Park et al. (1994) may be referred to.

For a finite-rate chemical kinetic model, the forward reaction rate, backward reaction rate, and equilibrium constant are required to describe the equilibrium composition at a given temperature and pressure. The temperature dependence of chemical reaction rates was originally introduced by Arrhenius (1889). Accordingly, the forward reaction rate is expressed in Arrhenius form, with the addition of Park's two-temperature model (Park, 1985) to account for multi-temperature effects, as

$$k_f = C T_x^n \exp(-T_d/T_x) \quad , \tag{C.2}$$

given in $cm^3 mole^{-1} s^{-1}$ where T_x corresponds to T_a for dissociation reactions (k_f) and to T for recombination reactions (k_b). The constants T_d, C, and n are provided in Park et al. (1994). For dissociation reactions, the rate coefficients are evaluated using a geometric mean temperature between the translational and vibrational modes in order to account for the influence of vibrational excitation on chemical reactions. This effective temperature is defined as

$$T_a = \sqrt{T T_v} \quad , \tag{C.3}$$

where T denotes the translational temperature and T_v represents the vibrational temperature, which is evaluated separately through the governing equations. The backward reaction rate is then defined as

$$k_b = \frac{k_f(T)}{K_c} \quad . \tag{C.4}$$

where K_c is the equilibrium constant. The equilibrium constant characterises the equilibrium composition of the mixture at a specified temperature and pressure. While polynomial fits for air mixtures are available in the literature (Park et al., 2001; Park, 1984; Gnoffo et al., 1989), no equivalent formulation was identified for Martian atmospheres or mixtures arising from CO_2 dissociation. In such cases, the equilibrium composition may be determined using Gibbs free energy minimisation, whereby the equilibrium state corresponds to the minimum of the Gibbs function. Using this approach, thermochemical databases such as NASA-9 (Mcbride et al., 2002) can be employed to derive the equilibrium constant of the mixture. A similar methodology has previously been applied by Musawi and Sandham (2025) for air mixtures and may be followed here.

C.4 Thermal Kinetic Model

For polyatomic molecules, vibrational motion is inherently more complex, and multiple vibrational modes may be excited (Anderson, 2019). In the present work, the translational and rotational modes are assumed to remain in equilibrium.

The harmonic oscillator model is employed to describe the vibrational potential associated with each vibrational mode of the molecules. Carbon dioxide possesses three vibrational modes, one of which is doubly degenerate (Candler, 1990). Consequently, the vibrational energy per unit mass of CO_2 is expressed as

$$e_{v_{CO_2}} = e_{v_{CO_2},1} + e_{v_{CO_2},2} + e_{v_{CO_2},3} \quad , \tag{C.5}$$

where

$$e_{v_{CO_2},r} = g_r \frac{\mathscr{R}}{M_{CO_2}} \frac{\Theta_{vCO_2,r}}{e^{\Theta_{vCO_2,r}/T_v} - 1} \quad , \tag{C.6}$$

with $\mathscr{R}$ denoting the universal gas constant, M_{CO_2} the molecular weight of CO_2, $\Theta_{vCO_2,r}$ the characteristic vibrational temperature of mode r, and g_r the corresponding degeneracy. The vibrational energy of the remaining diatomic species is defined as

$$e_{v_s,r} = \frac{\mathscr{R}}{M_s} \frac{\Theta_{v_s}}{e^{\Theta_{v_s}/T_v} - 1} \quad . \tag{C.7}$$

The constants associated with each molecular species are listed in Table C.1. The energy exchange between the translational and vibrational modes is described using the Landau–Teller formulation (Landau and Teller, 1936), given by

$$Q_{vs} = \rho_s \frac{e_{v_s}(T) - e_{v_s}}{\tau_s} \quad , \tag{C.8}$$

where $e_{v_s}(T)$ represents the equilibrium vibrational energy evaluated at the translational temperature, and τ_s is the species-specific vibrational relaxation time.

Several expressions have been proposed for vibrational relaxation between the translational and vibrational modes. Relations based on the Millikan–White formulation were adapted for CO_2 by Camac (1966). Although this reference is not available in digital form, it is accessible through the university library. The relaxation behaviour of CO_2 reported by Camac was investigated up to temperatures of approximately 6000 K. Furthermore, Camac demonstrated that all vibrational modes of CO_2 relax at the same rate (Candler, 1990).

It should be noted that, for Mars entry conditions, the translational temperature immediately behind the shock wave for entry velocities of 6–9 km/s ranges between approximately 25,000 K and 59,000 K prior to significant vibrational excitation, with equilibrium temperatures in the range of 4,800–7,300 K (Park et al., 1994). As a result, the applicability of relaxation rates derived from lower-temperature experiments may be questionable under such extreme conditions. For a comprehensive review of experimental and theoretical relaxation times available up to 1994, the introduction section of Park et al. (1994) is recommended.

An alternative approach is to apply the Millikan–White expression, which results in distinct relaxation times for each vibrational mode of CO_2 (Millikan and White, 1963). However, given that Camac demonstrated identical relaxation rates for all vibrational modes (Candler, 1990), Candler compared Camac's formulation with the Millikan–White model and ultimately adopted Camac's expression. No explicit justification for this choice was provided. Consequently, a direct comparison between the full Millikan–White relaxation formulation and experimental data could be of interest, even though Candler performs a comparison using relaxation rates derived from Camac's formulation.

In summary, three alternative relaxation expressions may be employed. The first is the original Millikan–White formulation,

$$\ln \tau_{sr} p = 0.00116 \, \mu_{sr}^{1/2} \, \Theta_{v_s}^{4/3} \, (T^{-1/3} - \mu sr^{1/4}) - 18.42 \quad , \tag{C.9}$$

where μ_{sr} is the reduced molecular weight of the colliding pair, defined as $M_s M_r/(M_s + M_r)$, and Θ_{v_s} is the characteristic vibrational temperature.

The second approach is a modified Millikan–White formulation with empirically fitted coefficients,

$$\tau_{sr} p = \exp\Big(a \, (T^{-1/3} - b) - 18.42\Big) \quad . \tag{C.10}$$

where the coefficients a and b are provided in Park et al. (1994).

Finally, Camac's expression for CO_2 relaxation is given by

$$\ln \, \tau_{\mathrm{CO_2}} p = 36.5 \, T^{-1/3} - 17.71 \quad . \tag{C.11}$$

This formulation is applicable only to CO_2; therefore, the Millikan–White expression must be employed for the remaining molecular species.

Table C.1: Thermal kinetic model constants.

Molecular species	CO_2			CO	O_2
	Mode 1	Mode 2	Mode 3		
$\Theta_{v,s}$ (K)	1903	945	3329	3074	2239
g	1	2	1	1	1

C.5 Transport Properties

The description of transport properties (TP) for a multi-species mixture is significantly more complex than for a single-species flow. The former requires the use of the full Chapman–Enskog formulation or suitable approximations, such as mixing rules. Consequently, both approaches are addressed separately in this section.

C.5.1 Viscosity

From molecular dynamics and kinetic theory, the viscosity of an individual species can be expressed in terms of the intermolecular potential and force constants as (Hirschfelder et al., 1954)

$$\mu_s = 266.93 \left(\frac{\sqrt{M_s T}}{\sigma_s^2 \Omega^{(2,2)\star}(T^*)} \right) \times 10^{-8} \quad , \tag{C.12}$$

where μ_s denotes the viscosity of species s in kg/(m,s), M_s is the molecular weight of species s, and T^* is the reduced temperature, defined as $T^* = kT/\epsilon_s$. Here, k is the Boltzmann constant, while ϵ_s and σ_s are the species-specific Lennard–Jones force constants, as given in Hirschfelder et al. (1954); Chapman and Cowling (1970); Poling et al. (2000). The term $\Omega^{(2,2)\star}(T^*)$ represents the collision integral, which may be obtained from tabulated Lennard–Jones potential data (Hirschfelder et al., 1954).

Alternatively, the viscosity may be approximated using Sutherland's law, expressed as

$$\mu_s = \mu_{s_\circ} \left(\frac{T}{T_{s_\circ}} \right)^{3/2} \frac{T_{s_\circ} + S}{T + S} \quad , \tag{C.13}$$

where $\mu_{s_\circ}$ is the experimentally measured viscosity at the reference temperature $T_{s_\circ}$, and S is the Sutherland constant, which characterises the strength of intermolecular attractive forces. Values for these constants are available in White and Majdalani (2022).

Candler (1990) refers to the full species viscosity formulation based on the Lennard–Jones potential, but ultimately adopts a simplified curve fit for the viscosity of CO_2, which is acknowledged to be relatively crude and inaccurate. For the remaining species, Blottner's model is employed (Blottner et al., 1971). The mixture viscosity is then evaluated using Wilke's semi-empirical mixing rule (Wilke, 1950).

For gas mixtures, Wilke's mixing rule may be written as (Wilke, 1950; Blottner et al., 1971)

$$\mu = \sum_{i=1}^{s} \frac{X_i \mu_i}{\sum_{j=1}^{s} X_j \phi_{ij}} \quad , \tag{C.14}$$

where X_i denotes the mole fraction of species i, and the interaction parameter ϕ_{ij} is defined as

$$\phi_{ij} = \left[1 + \sqrt{\frac{\mu_i}{\mu_j}} \left(\frac{M_j}{M_i} \right)^{1/4} \right]^2 \left[\sqrt{8} \sqrt{1 + \frac{M_i}{M_j}} \right]^{-1} \quad . \tag{C.15}$$

A more accurate representation of mixture viscosity may be obtained from the full Chapman–Enskog formulation, with the approximation that non-diagonal terms are

neglected. Under this assumption, the mixture viscosity can be expressed as

$$\mu_{mix} = 10^{-8} \sum_{i=1}^{s} \frac{X_i^2}{X_i^2/\mu_i + 2.308 \sum_{k \neq i} \frac{X_i X_k}{A_{ik}^{\star} \mu_{ik}} \frac{M_k}{(M_i + M_k)}} \quad , \tag{C.16}$$

where

$$\mu_{ik} = 266.93 \left(\frac{2 M_i M_k T/(M_i + M_k)}{\sigma_{ik}^2 \Omega_{ik}^{(2,2)\star}(T_{ik}^*)} \right) \times 10^{-8} \quad .$$

C.5.2 Thermal Conductivity

The theoretical evaluation of thermal conductivity for polyatomic species is considerably more challenging than for monatomic gases. Without resorting to extensive experimental datasets or semi-empirical methods that combine theory with experimental calibration, a practical approach is to employ the theoretical expression for the thermal conductivity of a monatomic species augmented by the Eucken correction factor. This yields

$$K_{i,mon} = \frac{15}{4} \frac{\mathscr{R}}{M_i} \mu_i \quad , \tag{C.17}$$

$$K_{i,pol} = \frac{15}{4} \frac{\mathscr{R}}{M_i} \mu_i \left(\frac{4}{15} \frac{\tilde{C}_v}{\mathscr{R}} + \frac{3}{5} \right) \quad , \tag{C.18}$$

where Ki, mon and $K_{i,\mathrm{pol}}$ denote the thermal conductivity of monatomic and polyatomic species, respectively, and $\tilde{C}_v$ is the molar heat capacity at constant volume. For CO_2, this approximation has been shown to yield errors in the range of 1–3.5% for temperatures between 230 and 390 K when compared with experimental measurements (Hirschfelder et al., 1954).

For the thermal conductivity of a gas mixture, the same Wilke mixing rule employed for viscosity may be applied, giving

$$K = \sum_{i=1}^{s} \frac{X_i k_i}{\sum_{j=1}^{s} X_j \phi_{ij}} \quad , \tag{C.19}$$

where the interaction parameter ϕ_{ij} is defined as in (C.15). Alternatively, more sophisticated semi-empirical approaches may be adopted, which incorporate experimental data or rely on the detailed calculations described by Hirschfelder et al. (1954).

C.5.3 Bulk Viscosity

In recent years, increased attention has been directed toward bulk viscosity, particularly for CO_2, motivated by studies such as Cramer (2012), which report models yielding relatively large bulk-to-shear viscosity ratios (μ_b/μ). A comprehensive comparison

performed by Kustova et al. (2023) evaluates several bulk-viscosity models and identifies a formulation that couples the effects of rotational and vibrational relaxation in the computation of bulk viscosity. This approach is consistent with models developed by research groups working within the framework established by Giovangigli (Billet et al., 2008; Bruno and Giovangigli, 2011; Boukharfane et al., 2019; Giovangigli et al., 2010).

Expressions for bulk viscosity are provided by Kustova et al. (2023) for two distinct flow regimes: weakly non-equilibrium flows, in which no separate transport equation for vibrational energy is solved, and strongly non-equilibrium flows. In the former case, the bulk viscosity depends on both rotational and vibrational relaxation times, whereas in the latter it depends solely on the rotational relaxation time. For strongly non-equilibrium conditions, the bulk viscosity is defined as

$$\mu_b = \frac{4}{25} p \tau_{rot} \quad , \tag{C.20}$$

where p is the pressure and τ_{rot} is the rotational relaxation time, as given by Parker et al. (1953). For weakly non-equilibrium flows, the bulk viscosity is expressed as

$$\mu_b = pR \left(\frac{c_{int}}{C_v} \right) \left(\frac{c_{rot}}{\tau_{rot}} \frac{c_{vib}}{\tau_{vib}} \right)^{-1} \quad , \tag{C.21}$$

where C_v is the heat capacity at constant volume, c_{int} is the internal heat-capacity contribution, c_{rot} and c_{vib} are the rotational and vibrational contributions to the heat capacity, respectively, τ_{rot} is the rotational relaxation time, and τ_{vib} is the vibrational relaxation time, which may be evaluated using one of Equation C.9, Equation C.10, or Equation C.11.

For gas mixtures, the bulk viscosity corresponding to the weakly non-equilibrium formulation is given by (Billet et al., 2008)

$$\mu_{b_{mix}} = \frac{pR}{C_v^2} \sum_{i=m} X_i \frac{C_{int}^2}{\left[\frac{c_{rot}}{\tau_{rot}} \frac{c_{vib}}{\tau_{vib}} \right]} \quad . \tag{C.22}$$

For simulations of strongly non-equilibrium flows, it is necessary to subtract the relaxation (dynamic) pressure from the thermodynamic pressure when accounting for bulk-viscous effects, since bulk viscosity represents the deviation between the dynamic pressure and the kinetic pressure (Vincenti and Kruger, 1965).

C.5.4 Diffusion

For diffusion, species diffusion coefficients may be derived using expressions based on collisional cross sections, either obtained theoretically or from experimental data. An approximate expression for species diffusion is given by (Curtiss and Hirschfelder, 1949;

Lee, 1985)

$$D_s = \frac{\gamma_t^2 M_s (1 - M_s \gamma_s)}{\sum_{r \neq s} \gamma_r / D_{sr}} \quad , \tag{C.23}$$

where D_{sr} denotes the binary diffusion coefficient between species s and r. The accuracy of this formulation is dependent on the availability of reliable binary diffusion data, which can be limited, particularly for mixtures involving CO_2.

As a simplified alternative, a constant Schmidt number may be employed as a rough approximation, defined as

$$Sc = \frac{\mu_{mix}}{\rho D} \quad , \tag{C.24}$$

where μ_{mix} is the mixture viscosity and D is the diffusion coefficient. While this approach significantly simplifies the modelling, it results in a uniform diffusion coefficient for all species and therefore neglects species-specific diffusion effects.

C.6 Conclusion

In conclusion, this document has presented a brief discussion on the modelling of carbon dioxide as a polyatomic species within the framework of continuum thermo-chemical non-equilibrium flows. The chemical kinetic model section introduced the set of chemical reactions that may occur during CO_2 dissociation, leading to a multi-species gas mixture. Consequently, the subsequent sections addressing thermal non-equilibrium and transport properties considered not only pure-gas formulations but also the extensions required for multi-species mixtures.

References

P. H. Adam and H. G. Hornung. Enthalpy Effects on Hypervelocity Boundary Layer Transition: Experiments and Free Flight Data. *35th Aerospace Sciences Meeting and Exhibit*, 1997. doi: 10.2514/6.1997-764. URL .

H. Alkandry, I. D. Boyd, and A. Martin. Comparison of Transport Properties Models for Flowfield Simulations of Ablative Heat Shields. *Journal of Thermophysics and Heat Transfer*, 28(4):569–582, 10 2014. ISSN 15336808. doi: 10.2514/1.T4233.

J. D. Anderson. *Hypersonic and High-Temperature Gas Dynamics*. American Institute of Aeronautics and Astronautics Inc., Reston, third edition, 2019. ISBN 9781624105142.

J. D. Anderson. *Modern compressible flow : with historical perspective*. McGraw-Hill Education, 2021. ISBN 9781260471441.

D. A. Andrienko and I. D. Boyd. Vibrational energy transfer and dissociation in O2-N2 collisions at hyperthermal temperatures. *Journal of Chemical Physics*, 148(8), 2 2018. ISSN 00219606. doi: 10.1063/1.5007069.

A. F. Antoniadis, D. Drikakis, P. S. Farmakis, L. Fu, I. Kokkinakis, X. Nogueira, P. A. Silva, M. Skote, V. Titarev, and P. Tsoutsanis. UCNS3D: An open-source high-order finite-volume unstructured CFD solver. *Computer Physics Communications*, 279: 108453, 10 2022. ISSN 0010-4655. doi: 10.1016/J.CPC.2022.108453.

S. Arrhenius. Über die Dissociationswärme und den Einfluss der Temperatur auf den Dissociationsgrad der Elektrolyte. *Zeitschrift für Physikalische Chemie*, 4U(1):96–116, 7 1889. ISSN 0942-9352. doi: 10.1515/zpch-1889-0408.

M. Bauer, S. Treichler, E. Slaughter, and A. Aiken. Legion: Expressing locality and independence with logical regions. In *International Conference for High Performance Computing, Networking, Storage and Analysis, SC*, 2012. ISBN 9781467308069. doi: 10.1109/SC.2012.71.

G. Bellas-Chatzigeorgis, A. Viladegut, P. F. Barbante, O. Chazot, and T. E. Magin. Development of catalytic and ablative gas-surface interaction models for the simulation of reacting gas mixtures. In *23rd AIAA Computational Fluid Dynamics Conference,*

2017. American Institute of Aeronautics and Astronautics Inc, AIAA, 2017. ISBN 9781624105067. doi: 10.2514/6.2017-4499. URL .

M. Bernardini, D. Modesti, F. Salvadore, and S. Pirozzoli. STREAmS: A high-fidelity accelerated solver for direct numerical simulation of compressible turbulent flows. *Computer Physics Communications*, 263:107906, 6 2021. ISSN 0010-4655. doi: 10.1016/J.CPC.2021.107906.

G. Billet, V. Giovangigli, and G. de Gassowski. Impact of volume viscosity on a shock–hydrogen-bubble interaction. *Combustion Theory and Modelling*, 12(2):221–248, 4 2008. ISSN 13647830. doi: 10.1080/13647830701545875. URL .

R. B. Bird, W. E. Stewart, and E. N. Lightfoot. *Transport Phenomena*. Number 2. Wiley, 2nd edition, 2007. ISBN 978-0-470-11539-8.

G. Blaisdell. *Numerical simulation of compressible homogeneous turbulence*. PhD thesis, 1 1991.

G. A. Blaisdell, N. N. Mansour, and W. C. Reynolds. Compressibility effects on the growth and structure of homogeneous turbulent shear flow. *Journal of Fluid Mechanics*, 256(6):443–485, 1993. ISSN 1469-7645. doi: 10.1017/S0022112093002848. URL .

G. A. Blaisdell, E. T. Spyropoulos, and J. H. Qin. The effect of the formulation of nonlinear terms on aliasing errors in spectral methods. *Applied Numerical Mathematics*, 21(3):207–219, 7 1996. ISSN 0168-9274. doi: 10.1016/0168-9274(96)00005-0.

J. Blazek. *Chapter 7 – Turbulence Modeling*. 2015. ISBN 9780080999951. URL .

F. Blottner, M. Johnson, and M. Ellis. Chemically Reacting Viscous Flow Program for Multi-Component Gas Mixtures. Technical report, Sandia National Laboratories (SNL), Albuquerque, NM, and Livermore, CA (United States), 12 1971.

R. Boukharfane, P. J. M. Ferrer, A. Mura, and V. Giovangigli. On the role of bulk viscosity in compressible reactive shear layer developments. *European Journal of Mechanics - B/Fluids*, 77:32–47, 9 2019. ISSN 0997-7546. doi: 10.1016/J.EUROMECHFLU.2019.02.005.

I. D. Boyd and T. E. Schwartzentruber. *Nonequilibrium Gas Dynamics and Molecular Simulation*. Cambridge University Press, 3 2017. ISBN 9781107073449. doi: 10.1017/9781139683494. URL .

R. S. Brokaw. Approximate Formulas for the Viscosity and Thermal Conductivity of Gas Mixtures. *The Journal of Chemical Physics*, 29(2):391–397, 8 1958. ISSN 0021-9606. doi: 10.1063/1.1744491. URL .

D. Bruno and V. Giovangigli. Relaxation of internal temperature and volume viscosity. *Physics of Fluids*, 23(9):93104, 9 2011. ISSN 10706631. doi: 10.1063/1.3640083.

D. Bruno and V. Giovangigli. Internal Energy Relaxation Processes and Bulk Viscosities in Fluids. *Fluids 2022, Vol. 7, Page 356*, 7(11):356, 11 2022. ISSN 2311-5521. doi: 10.3390/FLUIDS7110356. URL .

J. M. Burt and I. D. Boyd. A hybrid particle approach for continuum and rarefied flow simulation. *Journal of Computational Physics*, 228(2):460–475, 2 2009. ISSN 0021-9991. doi: 10.1016/J.JCP.2008.09.022.

M. Camac. CO2 Relaxation Processes in Shock Waves. In J. G. Hall, editor, *Fundamental phenomena in hypersonic flow*. Cornell University Press, Ithaca, New York,, 1966.

G. V. Candler. Computation of thermo-chemical nonequilibrium Martian atmospheric entry flows. In *AIAA/ASME 5th Joint Thermophysics and Heat Transfer Conference, 1990*. American Institute of Aeronautics and Astronautics Inc, AIAA, 1990. doi: 10.2514/6.1990-1695. URL .

G. V. Candler. Rate Effects In Hypersonic Flows. *Annual Review of Fluid Mechanics*, 51 (1):379–402, 1 2019. ISSN 0066-4189. doi: 10.1146/annurev-fluid-010518-040258. URL .

G. V. Candler and I. Nompelis. Computational Fluid Dynamics for Atmospheric Entry. Technical report, University of Minnesota, Minnesota, 2009. URL .

G. V. Candler, H. B. Johnson, I. Nompelis, P. K. Subbareddy, T. W. Drayna, V. Gidzak, and M. D. Barnhardt. Development of the US3D code for advanced compressible and reacting flow simulations. In *53rd AIAA Aerospace Sciences Meeting*. American Institute of Aeronautics and Astronautics Inc, AIAA, 2015. ISBN 9781624103438. doi: 10.2514/6.2015-1893. URL .

C. D. Cantwell, D. Moxey, A. Comerford, A. Bolis, G. Rocco, G. Mengaldo, D. De Grazia, S. Yakovlev, J. E. Lombard, D. Ekelschot, B. Jordi, H. Xu, Y. Mohamied, C. Eskilsson, B. Nelson, P. Vos, C. Biotto, R. M. Kirby, and S. J. Sherwin. Nektar++: An open-source spectral/hp element framework. *Computer Physics Communications*, 192: 205–219, 7 2015. ISSN 0010-4655. doi: 10.1016/J.CPC.2015.02.008.

G. Cao, Y. Shi, K. Xu, and S. Chen. Modeling and Simulation in Supersonic Three-Temperature Carbon Dioxide Turbulent Channel Flow. *Physics of Fluids*, 34(12), 10 2022. doi: 10.1063/5.0129353. URL .

V. Casseau. *An Open-Source CFD Solver For Planetary Entry*. PhD thesis, University of Strathclyde, 2017.

V. Casseau, D. Espinoza, T. Scanlon, and R. Brown. A Two-Temperature Open-Source CFD Model for Hypersonic Reacting Flows, Part Two: Multi-Dimensional Analysis. *Aerospace*, 3(4):45, 12 2016a. ISSN 2226-4310. doi: 10.3390/aerospace3040045. URL .

V. Casseau, R. C. Palharini, T. J. Scanlon, and R. E. Brown. A Two-Temperature Open-Source CFD Model For Hypersonic Reacting Flows, Part One: Zero-Dimensional Analysis. *Aerospace*, 3(4):34, 10 2016b. ISSN 22264310. doi: 10.3390/aerospace3040034. URL .

I. Celik and O. Karatekin. Numerical experiments on application of richardson extrapolation with nonuniform grids. *Journal of Fluids Engineering, Transactions of the ASME*, 119(3):584–590, 9 1997. ISSN 1528901X. doi: 10.1115/1.2819284.

I. B. Celik, U. Ghia, P. J. Roache, C. J. Freitas, H. Coleman, and P. E. Raad. Procedure for estimation and reporting of uncertainty due to discretization in CFD applications. *Journal of Fluids Engineering, Transactions of the ASME*, 130(7):0780011–0780014, 7 2008. ISSN 00982202. doi: 10.1115/1.2960953.

Y. A. Cengel, M. A. Boles, and M. Kanoglu. *Thermodynamics: An Engineering Approach*. McGraw-Hill Education, Singapore, 2019. ISBN 9789813157873.

S. Chapman and T. G. Cowling. *The Mathematical Theory of Non-Uniform Gases: An Account of the Kinetic Theory of Viscosity*. Cambridge University Press, 1970. ISBN 9780521408448.

X. P. Chen, Y. T. Yang, and S. Zhao. Direct Numerical Simulations of High-Enthalpy Supersonic Turbulent Channel Flows Including Finite-Rate Reactions. *Physics of Fluids*, 36(4):45153, 4 2024. ISSN 10897666. doi: 10.1063/5.0203414.

G. E. Childs and H. J. M. Hanley. The Viscosity and Thermal Conductivity Coefficients of Dilute Nitrogen and Oxygen. Technical report, U.S. Government Printing Office, 1966.

A. K. Chinnappan and M. Kim. Species-Specific Vibrational Energy Model for Hypersonic Flow Simulations. 2025. URL .

G. N. Coleman, J. Kim, and R. D. Moser. A numerical study of turbulent supersonic isothermal-wall channel flow. *Journal of Fluid Mechanics*, 305:159–183, 1995. ISSN 1469-7645. doi: 10.1017/S0022112095004587. URL .

T. Colonius, S. K. Lele, and P. Moin. Sound generation in a mixing layer. *Journal of Fluid Mechanics*, 330:375–409, 1 1997. ISSN 1469-7645. doi: 10.1017/S0022112096003928. URL .

A. B. Cortesi, B. L. Smith, G. Yadigaroglu, and S. Banerjee. Numerical Investigation of the Entrainment and Mixing Processes in Neutral and Stably-stratified Mixing Layers. *Physics of Fluids*, 11(1):162–185, 1 1999. ISSN 1070-6631. doi: 10.1063/1.869910. URL .

M. S. Cramer. Numerical estimates for the bulk viscosity of ideal gases. *Physics of Fluids*, 24(6):66102, 6 2012. ISSN 10706631. doi: 10.1063/1.4729611/257584. URL .

P. G. Cross and I. D. Boyd. Two-Dimensional Modeling of Ablation and Pyrolysis with Application to Rocket Nozzles. *Journal of Spacecraft and Rockets*, 54(1):212–224, 10 2016. ISSN 15336794. doi: 10.2514/1.A33656. URL .

R. M. Cummings, S. A. Morton, W. H. Mason, and D. R. McDaniel. *Applied computational aerodynamics : a modern engineering approach*. Cambridge University Press, New York, NY, 2015. ISBN 9781107053748.

C. F. Curtiss and J. O. Hirschfelder. Transport Properties of Multicomponent Gas Mixtures. *The Journal of Chemical Physics*, 17(6):550–555, 6 1949. ISSN 0021-9606. doi: 10.1063/1.1747319.

G. Dang, S. Liu, T. Guo, J. Duan, and X. Li. Direct numerical simulation of compressible turbulence accelerated by graphics processing unit: An open-source high accuracy accelerated computational fluid dynamic software. *Physics of Fluids*, 34(12):126106, 12 2022. ISSN 10897666. doi: 10.1063/5.0127684/2845086. URL .

F. De Vanna, F. Avanzi, M. Cogo, S. Sandrin, M. Bettencourt, F. Picano, and E. Benini. URANOS: A GPU accelerated Navier-Stokes solver for compressible wall-bounded flows. *Computer Physics Communications*, 287:108717, 6 2023. ISSN 0010-4655. doi: 10.1016/J.CPC.2023.108717.

M. Di Renzo. HTR-1.3 solver: Predicting electrified combustion using the hypersonic task-based research solver. *Computer Physics Communications*, 272:108247, 3 2022. ISSN 0010-4655. doi: 10.1016/J.CPC.2021.108247.

M. Di Renzo and S. Pirozzoli. HTR-1.2 solver: Hypersonic Task-based Research solver version 1.2. *Computer Physics Communications*, 261:107733, 4 2021. ISSN 0010-4655. doi: 10.1016/J.CPC.2020.107733.

M. Di Renzo and J. Urzay. Direct Numerical Simulation of A Hypersonic Transitional Boundary Layer At Suborbital Enthalpies. *Journal of Fluid Mechanics*, 912:A29, 2021. ISSN 14697645. doi: 10.1017/jfm.2020.1144.

M. Di Renzo, L. Fu, and J. Urzay. HTR solver: An open-source exascale-oriented task-based multi-GPU high-order code for hypersonic aerothermodynamics. *Computer Physics Communications*, 255:107262, 10 2020. ISSN 0010-4655. doi: 10.1016/J.CPC.2020.107262.

P. E. Dimotakis. Turbulent Free Shear Layer Mixing and Combustion. Technical report, California Inst of Tech Pasadena Graduate Aeronautical Labs, 1991. URL .

L. Duan and M. P. Martín. Direct numerical simulation of hypersonic turbulent boundary layers. Part 4. Effect of high enthalpy. *Journal of Fluid Mechanics*, 684:25–59, 10 2011. ISSN 1469-7645. doi: 10.1017/JFM.2011.252.

D. E. Espinoza, V. Casseau, T. J. Scanlon, and R. E. Brown. An open-source hybrid CFD-DSMC solver for high speed flows. *AIP Conference Proceedings*, 1786(1), 11 2016. ISSN 15517616. doi: 10.1063/1.4967557/885241. URL .

W. J. Feiereisen, W. C. Reynolds, and J. H. Ferziger. *Numerical simulation of a compressible homogeneous, turbulent shear flow*. PhD thesis, 1981.

R. Fiévet, S. Voelkel, V. Raman, and P. L. Varghese. Numerical Investigation of The Coupling of Vibrational Nonequilibrium and Turbulent Mixing Using State-Specific Description. *Physical Review Fluids*, 4(1):013401, 1 2019. ISSN 2469990X. doi: 10.1103/PhysRevFluids.4.013401.

J. B. Freund, S. K. Lele, and P. Moin. Compressibility effects in a turbulent annular mixing layer. Part 1. Turbulence and growth rate. *Journal of Fluid Mechanics*, 421: 229–267, 2000a. ISSN 1469-7645. doi: 10.1017/S0022112000001622. URL .

J. B. Freund, P. Moin, and S. K. Lele. Compressibility effects in a turbulent annular mixing layer. Part 2. Mixing of a passive scalar. *Journal of Fluid Mechanics*, 421: 269–292, 2000b. ISSN 1469-7645. doi: 10.1017/S0022112000001634. URL .

T. J. Fuller, A. G. Hsu, R. Sanchez-Gonzalez, J. C. Dean, S. W. North, and R. D. Bowersox. Radiofrequency plasma stabilization of a low-Reynolds-number channel flow. *Journal of Fluid Mechanics*, 748(2):663–691, 4 2014. ISSN 0022-1120. doi: 10.1017/JFM.2014.189. URL .

P. D. Germain and H. G. Hornung. Transition on a Slender Cone in Hypervelocity Flow. *Experiments in Fluids*, 22(3):183–190, 1997. ISSN 07234864. doi: 10.1007/S003480050036. URL .

S. F. Gimelshein, I. J. Wysong, A. J. Fangman, D. A. Andrienko, O. V. Kunova, E. V. Kustova, F. Morgado, C. Garbacz, M. Fossati, and K. M. Hanquist. Kinetic and Continuum Modeling of High-Temperature Air Relaxation. *Journal of Thermophysics and Heat Transfer*, pages 1–23, 2 2022. doi: 10.2514/1.t6462.

V. Giovangigli. Transport Coefficients. In *Multicomponent Flow Modeling*, pages 97–117. Birkhäuser, Boston, MA, 1999. doi: 10.1007/978-1-4612-1580-6_5. URL .

V. Giovangigli, B. Graille, T. Magin, and M. Massot. Multicomponent transport in weakly ionized mixtures. *Plasma Sources Science and Technology*, 19(3):034002, 5 2010. ISSN 0963-0252. doi: 10.1088/0963-0252/19/3/034002. URL .

P. A. Gnoffo. Upwind-biased, point-implicit relaxation strategies for viscous, hypersonic flows. In *9th Computational Fluid Dynamics Conference, 1989*. American Institute of Aeronautics and Astronautics Inc, AIAA, 1989. doi: 10.2514/6.1989-1972. URL .

P. A. Gnoffo, R. N. Gupta, and J. L. Shinn. Conservation Equations and Physical Models For Hypersonic Air Flows In Thermal and Chemical Nonequilibrium. Technical Report 2867, National Aeronautics and Space Administration (NASA), 1989.

S. Gordon and B. J. McBride. Computer Program for Calculation of Complex Chemical Equilibrium Compositions and Applications I. Analysis. Technical report, 1994.

S. I. Green, editor. *Fluid Vortices*. Fluid Mechanics and Its Applications. Springer Netherlands, Dordrecht, 1995. ISBN 978-94-010-4111-9. doi: 10.1007/978-94-011-0249-0. URL .

R. N. Gupta, J. M. Yos, R. A. Thompson, and K.-P. Lee. A Review of Reaction Rates and Thermodynamic and Transport Properties for an 11-Species Air Model for Chemical and Thermal Nonequilibrium Calculations to 30000 K. Technical report, National Aeronautics and Space Administration (NASA), 1990.

R. N. Gupta, K.-P. Lee, R. A. Thompson, and J. M. Yos. Calculations and Curve Fits of Thermodynamic and Transport Properties for Equilibrium Air to 30000 K. Technical report, National Aeronautics and Space Administration (NASA), 10 1991.

C. F. Hansen and S. P. Heims. A Review of the Thermodynamic, Transport, and Chemical Reaction Rate Properties of High-temperature Air. Technical report, Ames Aeronautical Labratory, Moffet Field, California, 1958. URL .

J. Hao, J. Wang, Z. Gao, C. Jiang, and C. Lee. Comparison of transport properties models for numerical simulations of Mars entry vehicles. *Acta Astronautica*, 130:24–33, 1 2017. ISSN 0094-5765. doi: 10.1016/J.ACTAASTRO.2016.10.009.

J. Hilsenrath and Y. S. Touloukian. The Viscosity, Thermal Conductivity, and Prandtl Number for Air, O2, N2, NO, H2, CO, CO2, H2O, He, and Argon. *Journal of Fluids Engineering*, 76(6):967–983, 8 1954. ISSN 0098-2202. doi: 10.1115/1.4015029.

J. Hilsenrath, W. S. Benedict, L. Fano, H. J. Hoge, J. F. masa, R. L. Nuttall, Y. S. Touloukian, and H. W. Woolley. *Tables of Thermal Properties of Gases*. Gaithersburg, MD, 1955. doi: 10.6028/NBS.CIRC.564.

E. H. Hirschel. *Basics of Aerothermodynamics*. Springer International Publishing, second, revised edition, 1 2015. ISBN 9783319143736. doi: 10.1007/978-3-319-14373-6.

J. O. Hirschfelder. Heat conductivity in polyatomic, electronically excited, or chemically reacting mixtures. III. *Symposium (International) on Combustion*, 6(1):351–366, 1 1957. ISSN 0082-0784. doi: 10.1016/S0082-0784(57)80049-6.

J. O. Hirschfelder, C. F. Curtiss, and R. B. Bird. *Molecular Theory of Gases and Liquids*. John Wiley & Sons Inc, 1954. ISBN 9780471400653.

C. M. Ho and P. Huerre. Perturbed Free Shear Layers. *Annual Review of Fluid Mechanics*, 16(1):365–422, 1 1984. ISSN 0066-4189. doi: 10.1146/annurev.fl.16.010184.002053.

A. E. Honein and P. Moin. Higher entropy conservation and numerical stability of compressible turbulence simulations. *Journal of Computational Physics*, 201(2):531–545, 12 2004. ISSN 0021-9991. doi: 10.1016/J.JCP.2004.06.006.

D. S. Hoskin, R. L. Van Heyningen, N. C. Nguyen, J. Vila-Pérez, W. L. Harris, and J. Peraire. Discontinuous Galerkin methods for hypersonic flows. *Progress in Aerospace Sciences*, 146:100999, 4 2024. ISSN 0376-0421. doi: 10.1016/J.PAEROSCI.2024.100999.

S. Hoyas and J. Jiménez. Scaling of the velocity fluctuations in turbulent channels up to Reτ=2003. *Physics of Fluids*, 18(1):11702, 1 2006. ISSN 10706631. doi: 10.1063/1.2162185/255572. URL .

S. Hoyas and J. Jiménez. Reynolds number effects on the Reynolds-stress budgets in turbulent channels. *Physics of Fluids*, 20(10):101511, 10 2008. ISSN 10706631. doi: 10.1063/1.3005862/103275. URL .

J. Huang, L. Duan, and M. M. Choudhari. Direct numerical simulation of hypersonic turbulent boundary layers: effect of spatial evolution and Reynolds number. *Journal of Fluid Mechanics*, 937:A3, 4 2022. ISSN 0022-1120. doi: 10.1017/JFM.2022.80. URL .

P. G. Huang, G. N. Coleman, and P. Bradshaw. Compressible turbulent channel flows: DNS results and modelling. *Journal of Fluid Mechanics*, 305:185–218, 1995. ISSN 1469-7645. doi: 10.1017/S0022112095004599. URL .

C. T. Jacobs, S. P. Jammy, and N. D. Sandham. OpenSBLI: A Framework for the Automated Derivation and Parallel Execution of Finite Difference Solvers on a Range of Computer Architectures. *Journal of Computational Science*, 18:12–23, 1 2017. ISSN 18777503. doi: 10.1016/j.jocs.2016.11.001.

R. L. Jaffe. Rate Constants For Chemical Reactions In High-Temperature Nonequilibrium Air. In *AIAA 20th Thermophysics Conference*. American Institute of Aeronautics and Astronautics Inc. (AIAA), 1 1986.

R. L. Jaffe, D. W. Schwenke, G. M. Chaban, D. K. Prabhu, C. O. Johnston, and M. Panesi. On The Development of A New Nonequilibrium Chemistry Model For Mars Entry. In *AIAA SciTech Forum - 55th AIAA Aerospace Sciences Meeting*. American Institute of Aeronautics and Astronautics Inc. (AIAA), 2017. ISBN 9781624104473. doi: 10.2514/6.2017-1372.

A. Jameson. Formulation of kinetic energy preserving conservative schemes for gas dynamics and direct numerical simulation of one-dimensional viscous compressible flow in a shock tube using entropy and kinetic energy preserving schemes. *Journal of Scientific Computing*, 34(2):188–208, 2 2008. ISSN 08857474. doi: 10.1007/S10915-007-9172-6. URL .

S. P. Jammy, C. T. Jacobs, and N. D. Sandham. Performance Evaluation of Explicit Finite Difference Algorithms with Varying Amounts of Computational and Memory Intensity. *Journal of Computational Science*, 36:100565, 9 2019. ISSN 1877-7503. doi: 10.1016/J.JOCS.2016.10.015.

N. Jansson, M. Karp, A. Podobas, S. Markidis, and P. Schlatter. Neko: A modern, portable, and scalable framework for high-fidelity computational fluid dynamics. *Computers & Fluids*, 275:106243, 5 2024. ISSN 0045-7930. doi: 10.1016/J.COMPFLUID.2024.106243.

S. M. Jo, S. Venturi, M. P. Sharma, A. Munafò, and M. Panesi. Rovibrational-Specific QCT and Master Equation Study on N2 X^1 \Sigma_g + O^3 P and NO X^2\Pi + N^4 S Systems in High-Energy Collisions. *The Journal of Physical Chemistry*, 11 2021. doi: 10.1021/acs.jpca.1c10346. URL .

S. M. Jo, A. Munafò, M. P. Sharma, S. Venturi, and M. Panesi. Rovibrational-Specific Master Equation Analysis of High-Temperature Air Mixture. In *AIAA SciTech 2022 Forum*. American Institute of Aeronautics and Astronautics Inc. (AIAA), 2022. ISBN 9781624106316. doi: 10.2514/6.2022-0342.

C. O. Johnston and A. M. Brandis. Modeling of Nonequilibrium CO Fourth-Positive and CN Violet Emission In CO2-N2 Gases. *Journal of Quantitative Spectroscopy and Radiative Transfer*, 149:303–317, 12 2014. ISSN 00224073. doi: 10.1016/j.jqsrt.2014.08.025.

H. L. Johnston and E. R. Grilly. The Thermal Conductivites of Eight Common Gases between 80° and 380°K. *The Journal of Chemical Physics*, 14(4):233–238, 4 1946. ISSN 0021-9606. doi: 10.1063/1.1724125. URL .

E. Josyula. *Hypersonic Nonequilibrium Flows: Fundamentals and Recent Advances*, volume 247. American Institute of Aeronautics and Astronautics, Inc., 2 2015. doi: 10.2514/4.103292.

B. W. Keeton, M. Ameen, and P. Pal. A discontinuous Galerkin spectral element method for compressible reacting flows. *Computer Methods in Applied Mechanics and Engineering*, 446:118277, 11 2025. ISSN 0045-7825. doi: 10.1016/J.CMA.2025.118277.

C. A. Kennedy and A. Gruber. Reduced aliasing formulations of the convective terms within the Navier–Stokes equations for a compressible fluid. *Journal of Computational Physics*, 227(3):1676–1700, 1 2008. ISSN 0021-9991. doi: 10.1016/J.JCP.2007.09.020.

P. P. Kerkar and S. Ghosh. DNS of High-Enthalpy Effects On Turbulent Flows. In *AIAA Scitech 2019 Forum*. American Institute of Aeronautics and Astronautics Inc. (AIAA), 2019. ISBN 9781624105784. doi: 10.2514/6.2019-1903.

A. Kessler. Russian Hypersonic Glide Vehicles: What to Know and What to Fear. *Orbis*, 66(2):213–223, 1 2022. ISSN 0030-4387. doi: 10.1016/J.ORBIS.2022.02.009.

H. Khatri and L. Zhang. Shock Standoff Distance in Viscous Hypersonic Flows around a Blunt Body. San Diego, CA and Online, 6 2023. AIAA AVIATION 2023 Forum. doi: 10.2514/6.2023-4417.

S. Khurshid and D. A. Donzis. Decaying Compressible Turbulence With Thermal Non-Equilibrium. *Physics of Fluids*, 31(1):015103, 1 2019. ISSN 10897666. doi: 10.1063/1.5080369. URL .

J. Kim, P. Moin, and R. Moser. Turbulence statistics in fully developed channel flow at low Reynolds number. *Journal of Fluid Mechanics*, 177:133–166, 1987. ISSN 1469-7645. doi: 10.1017/S0022112087000892. URL .

J. G. Kim and I. D. Boyd. Master Equation Analysis of Thermochemical Nonequilibrium of Nitrogen. In *43rd AIAA Thermophysics Conference 2012*. American Institute of Aeronautics and Astronautics Inc. (AIAA), 2012. ISBN 9781624101861. doi: 10.2514/6.2012-3305.

I. Klotz. SpaceOps: Global Orbital Launch Rate Jumped 25% In 2025, 1 2026. URL .

C. P. Knisely and X. Zhong. Impact of Vibrational Nonequilibrium On The Supersonic Mode In Hypersonic Boundary Layers. *AIAA Journal*, 58(4):1704–1714, 4 2020. ISSN 0001-1452. doi: 10.2514/1.J058758. URL .

A. Kosareva, O. Kunova, E. Kustova, and E. Nagnibeda. Four-temperature kinetic model for CO2vibrational relaxation. *Physics of Fluids*, 33(1):16103, 1 2021. ISSN 10897666. doi: 10.1063/5.0035171/1061169.

E. Kustova and M. Mekhonoshina. Multi-temperature vibrational energy relaxation rates in CO2. *Physics of Fluids*, 32(9), 9 2020. ISSN 10897666. doi: 10.1063/5.0021654.

E. Kustova and M. Mekhonoshina. Calculation of Vibrational Relaxation Times in Carbon Dioxide Using Forced Harmonic Oscillator Model. In *AIP Conference Proceedings*, volume 2351, page 040031. American Institute of Physics Inc., 5 2021a. ISBN 9780735440999. doi: 10.1063/5.0052238. URL .

E. Kustova and M. Mekhonoshina. Novel approach for evaluation of CO2 vibrational relaxation times. *Chemical Physics Letters*, 764:138288, 2 2021b. ISSN 0009-2614. doi: 10.1016/J.CPLETT.2020.138288.

E. Kustova, E. Nagnibeda, I. Armenise, and M. Capitelli. Nonequilibrium Kinetics and Heat Transfer in O/O Mixtures near Catalytic Surfaces. *https://doi.org/10.2514/2.6673*, 16(2):238–244, 5 2012. ISSN 08878722. doi: 10.2514/2.6673. URL .

E. Kustova, A. Lukasheva, and M. Mekhonoshina. Improvement of the Landau-Teller model for CO2 on the basis of the Chapman–Enskog method. *IOP Conference Series: Materials Science and Engineering*, 927(1):012047, 9 2020. ISSN 1757-899X. doi: 10.1088/1757-899X/927/1/012047. URL .

E. Kustova, M. Mekhonoshina, A. Bechina, S. Lagutin, and Y. Voroshilova. Continuum Models for Bulk Viscosity and Relaxation in Polyatomic Gases. *Fluids*, 8(2):48, 1 2023. ISSN 2311-5521. doi: 10.3390/FLUIDS8020048. URL .

Y. Kuya, K. Totani, and S. Kawai. Kinetic energy and entropy preserving schemes for compressible flows by split convective forms. *Journal of Computational Physics*, 375: 823–853, 12 2018. ISSN 0021-9991. doi: 10.1016/J.JCP.2018.08.058.

S. Laizet, S. Lardeau, and E. Lamballais. Direct Numerical Simulation of a Mixing Layer Downstream a Thick Splitter Plate. *Physics of Fluids*, 22(1), 1 2010. ISSN 1070-6631. doi: 10.1063/1.3275845. URL .

L. Landau and E. Teller. On the Theory of Sound Dispersion. *Physik Zeitschrift der Sowjetunion*, 10:34–38, 1936.

C. B. Laney. *Computational Gasdynamics*. Cambridge University Press, 6 1998. ISBN 9780521570695. doi: 10.1017/CBO9780511605604. URL .

B. E. Launder and N. D. Sandham. *Closure Strategies for Turbulent and Transitional Flows*. Cambridge University Press, 2 2002. ISBN 9780511755385. doi: 10.1017/CBO9780511755385. URL .

J. H. Lee. Basic Governing Equations for the Flight Regimes of Aeroassisted Orbital Transfer Vehicles. In *19th Thermophysics Conference*, Reston, Virigina, 6 1984. American Institute of Aeronautics and Astronautics Inc. (AIAA). doi: 10.2514/6.1984-1729.

J.-H. Lee. Basic Governing Equations for the Flight Regimes of Aeroassisted Orbital Transfer Vehicles. In H. F. Nelson, editor, *Thermal Design of Aeroassisted Orbital Transfer Vehicles*, volume 96, pages 3–53. American Institute of Aeronautics and Astronautics, 1 1985. doi: 10.2514/4.865718.

M. Lee and R. D. Moser. Direct numerical simulation of turbulent channel flow up to Reτ 5200. *Journal of Fluid Mechanics*, 774:395–415, 6 2015. ISSN 0022-1120. doi: 10.1017/JFM.2015.268. URL .

S. Lele. Direct Numerical Simulation of Compressible Free Shear Flows. In *27th Aerospace Sciences Meeting*. American Institute of Aeronautics and Astronautics (AIAA), 1 1989. doi: 10.2514/6.1989-374. URL .

S. K. Lele. Compressibility effects on turbulence. *Annual Review of Fluid Mechanics*, 26 (1):211–254, 1 1994. ISSN 00664189. doi: 10.1146/ANNUREV.FL.26.010194.001235.

E. W. Lemmon and R. T. Jacobsen. Viscosity and Thermal Conductivity Equations for Nitrogen, Oxygen, Argon, and Air. *International Journal of Thermophysics*, 25(1): 21–69, 1 2004. ISSN 0195928X. doi: 10.1023/B:IJOT.0000022327.04529.F3.

E. W. Lemmon, R. T. Jacobsen, S. G. Penoncello, and D. G. Friend. Thermodynamic Properties of Air and Mixtures of Nitrogen, Argon, and Oxygen From 60 to 2000 K at Pressures to 2000 MPa. *Journal of Physical and Chemical Reference Data*, 29(3): 331–385, 5 2000. ISSN 0047-2689. doi: 10.1063/1.1285884.

Y. Lin, J. J. Wallington, C. M. James, T. Bui, T. J. van den Herik, E. W. K. Chang, and T. A. Hermann. Expansion tube capabilities for studying boost-glide re-entry conditions. *CEAS Space Journal*, pages 1–22, 4 2025. ISSN 18682510. doi: 10.1007/S12567-025-00606-X. URL .

S. A. Losev, P. V. Kozlov, L. A. Kuznetsova, V. N. Makarov, Y. V. Romanenko, S. T. Surzhikov, and G. N. Zalogin. Radiation of a Mixture CO2-N2-Ar in Shock Waves: Experiment & Modelling. *ESASP*, 426:437, 1999. ISSN 1609-042X. URL .

S. K. Loyalka, E. L. Tipton, and R. V. Tompson. Chapman-Enskog solutions to arbitrary order in Sonine polynomials I: Simple, rigid-sphere gas. *Physica A: Statistical Mechanics and its Applications*, 379(2):417–435, 6 2007. ISSN 03784371. doi: 10.1016/J.PHYSA.2006.12.001.

J. Lueth, P. K. Subbareddy, and V. G. Candler. A Discontinuous Galerkin Spectral Element Method for Chemically Reacting Flows. In *AIAA SCITECH 2026 Forum*. American Institute of Aeronautics and Astronautics Inc, AIAA, 1 2026. doi: 10.2514/6.2026-2332.

D. J. Lusher, S. P. Jammy, and N. D. Sandham. OpenSBLI: Automated Code-Generation for Heterogeneous Computing Architectures Applied to Compressible Fluid Dynamics on Structured Grids. *Computer Physics Communications*, 267:108063, 10 2021. ISSN 0010-4655. doi: 10.1016/J.CPC.2021.108063.

D. J. Lusher, A. Sansica, N. D. Sandham, J. Meng, B. Siklósi, and A. Hashimoto. OpenSBLI v3.0: High-Fidelity Multi-Block Transonic Aerofoil CFD Simulations Using Domain Specific Languages on GPUs. *Computer Physics Communications*, 307:109406, 2 2025. ISSN 0010-4655. doi: 10.1016/J.CPC.2024.109406.

R. L. MacDonald, R. L. Jaffe, and M. Panesi. Hybrid Reduced Order Model For N2-N Interactions For Application To Dissociation and Energy Transfer Processes. In *AIP Conference Proceedings*, volume 2132. American Institute of Physics Inc., 8 2019. ISBN 9780735418745. doi: 10.1063/1.5119638.

W. T. Maier, J. T. Needels, C. Garbacz, F. Morgado, J. J. Alonso, and M. Fossati. SU2-NEMO: An Open-Source Framework for High-Mach Nonequilibrium Multi-Species Flows. *Aerospace 2021, Vol. 8, Page 193*, 8(7):193, 7 2021. ISSN 2226-4310. doi: 10.3390/AEROSPACE8070193. URL .

A. T. Margaritis, C. Scherding, O. Marxen, P. J. Schmid, and T. Sayadi. Development of a High-Fidelity Computational Tool For Chemically Reacting Hypersonic Flow Simulations, 10 2022.

D. V. Matyushov and R. Schmid. Calculation of Lennard-Jones Energies of Molecular Fluids. *The Journal of Chemical Physics*, 104(21):8627–8638, 6 1996. ISSN 0021-9606. doi: 10.1063/1.471551.

B. J. Mcbride, M. J. Zehe, and S. Gordon. NASA Glenn Coefficients for Calculating Thermodynamic Properties of Individual Species. Technical report, National Aeronautics and Space Administration (NASA), 2002. URL .

J. McFarland. The Development of Hypersonic Weapons in the US, China and Russia. *The RUSI Journal*, 168(1-2):10–18, 2023. ISSN 17440378. doi: 10.1080/03071847.2023.2199785. URL .

R. C. Millikan and D. R. White. Systematics of Vibrational Relaxation. *The Journal of Chemical Physics*, 39(12):3209–3213, 12 1963. ISSN 00219606. doi: 10.1063/1.1734182.

F. Miró Miró. *Numerical Investigation of Hypersonic Boundary-Layer Stability and Transition In The Presence of Ablation Phenomena*. PhD thesis, 2020. URL .

P. Moin and K. Mahesh. Direct numerical simulation: A Tool in Turbulence Research. *Annual Review of Fluid Mechanics*, 30:539–578, 1998. ISSN 00664189. doi: 10.1146/annurev.fluid.30.1.539.

P. Moin, A. Leonard, and J. Kim. Evolution of a curved vortex filament into a vortex ring. *The Physics of Fluids*, 29(4):955–963, 4 1986. ISSN 0031-9171. doi: 10.1063/1.865690. URL .

Y. Morinishi. Skew-symmetric form of convective terms and fully conservative finite difference schemes for variable density low-Mach number flows. *Journal of Computational Physics*, 229(2):276–300, 1 2010. ISSN 0021-9991. doi: 10.1016/J.JCP.2009.09.021.

R. D. Moser. *Numerical Methods in Turbulence Simulation*. Elsevier, 1 2022. ISBN 9780323911443. doi: 10.1016/C2020-0-04511-1.

R. D. Moser and M. M. Rogers. Mixing transition and the cascade to small scales in a plane mixing layer. *Physics of Fluids A: Fluid Dynamics*, 3(5):1128–1134, 5 1991. ISSN 0899-8213. doi: 10.1063/1.858094. URL .

R. D. Moser, J. Kim, and N. N. Mansour. Direct numerical simulation of turbulent channel flow up to Reτ=590. *Physics of Fluids*, 11(4):943–945, 4 1999. ISSN 1070-6631. doi: 10.1063/1.869966. URL .

A. Musawi and N. D. Sandham. Efficient Viscosity and Thermal Conductivity Formulation for Scale-Resolved Hypersonic Flow Simulations. *American Institute of Aeronautics and Astronautics*, 63(12), 2025. doi: https://doi.org/10.2514/1.J065564. URL .

A. Musawi and N. D. Sandham. Effects of thermal non-equilibrium during transition to turbulence of a high enthalpy free shear layer. *Physics of Fluids*, 38(1):15157, 1 2026. ISSN 1070-6631. doi: 10.1063/5.0311454. URL .

E. Nagnibeda and E. Kustova. *Non-Equilibrium Reacting Gas Flows*. Heat and Mass Transfer. Springer Berlin Heidelberg, Berlin, Heidelberg, 2009. ISBN 978-3-642-01389-8. doi: 10.1007/978-3-642-01390-4.

A. G. Neville, I. Nompelis, P. K. Subbareddy, and G. V. Candler. Thermal Non-Equilibrium Effects In Turbulent Compressible Shear Flows. In *45th AIAA Fluid Dynamics Conference*. American Institute of Aeronautics and Astronautics Inc. (AIAA), 2015. ISBN 9781624103629. doi: 10.2514/6.2015-3218.

I. Nompelis, T. W. Drayna, and G. V. Candler. Development of a hybrid unstructured implicit solver for the simulation of reacting flows over complex geometries. *34th AIAA Fluid Dynamics Conference and Exhibit*, 2004. doi: 10.2514/6.2004-2227. URL .

I. Nompelis, T. W. Drayna, and G. V. Candler. A parallel unstructured implicit solver for hypersonic reacting flow simulation. In *17th AIAA Computational Fluid Dynamics Conference*. American Institute of Aeronautics and Astronautics Inc., 2005. ISBN 9781624100536. doi: 10.2514/6.2005-4867. URL .

I. Nompelis, M. Kroells, T. E. Schwartzentruber, and G. V. Candler. Towards a Fully Consistent DSMC-CFD Hybrid Method for Hypersonic Nonequilibrium Reacting Flows. In *AIAA SciTech Forum and Exposition*. American Institute of Aeronautics and Astronautics Inc, AIAA, 2023. ISBN 9781624106996. doi: 10.2514/6.2023-2136. URL .

I. Nompelis, M. Kroells, T. E. Schwartzentruber, and G. V. Candler. Verification of a Modular Hybrid DSMC-CFD Simulation Method Implementation for Expanding Rarefied Flows. In *AIAA Science and Technology Forum and Exposition, AIAA SciTech Forum 2025*. American Institute of Aeronautics and Astronautics Inc, AIAA, 2025. ISBN 9781624107238. doi: 10.2514/6.2025-0951. URL .

W. L. Oberkampf and C. J. Roy. *Verification and validation in scientific computing*. Cambridge University Press, New York :, 2010. ISBN 9780511903977.

G. A. Olchowy and J. V. Sengers. A Simplified Representation for the Thermal Conductivity of Fluids in the Critical Region. *International Journal of Thermophysics*, 10(2):417–426, 3 1989. ISSN 0195928X. doi: 10.1007/BF01133538.

K. G. Owen, D. F. Davidson, and R. K. Hanson. Oxygen Vibrational Relaxation Times: Shock Tube/Laser Absorption Measurements. *Journal of Thermophysics and Heat Transfer*, 30(4):791–798, 12 2016. ISSN 15336808. doi: 10.2514/1.T4505.

G. Palmer and M. J. Wright. A Comparison of Methods to Compute High Temperature Gas Thermal Conductivity. In *36th AIAA Thermophysics Conference*. American Institute of Aeronautics and Astronautics Inc., 2003a. ISBN 9781624100970. doi: 10.2514/6.2003-3913.

G. E. Palmer and M. J. Wright. Comparison of Methods to Compute High-Temperature Gas Viscosity. *Journal of Thermophysics and Heat Transfer*, 17(2):232–239, 5 2003b. ISSN 15336808. doi: 10.2514/2.6756.

S. Pan and E. Johnsen. The role of bulk viscosity onthe decay of compressible,homogeneous, isotropic turbulence. *Journal of Fluid Mechanics*, 833: 717–744, 12 2017. ISSN 0022-1120. doi: 10.1017/JFM.2017.598. URL .

C. Pantano and S. Sarkar. A study of compressibility effects in the high-speed turbulent shear layer using direct simulation. *Journal of Fluid Mechanics*, 451:329–371, 1 2002. ISSN 1469-7645. doi: 10.1017/S0022112001006978. URL .

D. Papamoschou and A. Roshko. The Compressible Turbulent Shear Layer: An Experimental Study. *Journal of Fluid Mechanics*, 197:453–477, 1988. ISSN 1469-7645. doi: 10.1017/S0022112088003325. URL .

C. Park. Problems of Rate Chemistry In The Flight Regimes Of Aeroassisted Orbital Transfer Vehicles. In *AIAA Paper*. American Institute of Aeronautics and Astronautics Inc. (AIAA), 1984. doi: 10.2514/6.1984-1730.

C. Park. On Convergence of Computation of Chemically Reacting Flows. In *AlAA 23rd Aerospace Sciences Meeting, 1985*. American Institute of Aeronautics and Astronautics Inc. (AIAA), 1985. doi: 10.2514/6.1985-247.

C. Park. Assessment of Two-Temperature Kinetic Model For Dissociating and Weakly-Ionizing Nitrogen. In *AIAA/ASME 4th Joint Thermophysics and Heat Transfer Conference*. American Institute of Aeronautics and Astronautics Inc. (AIAA), 1986. doi: 10.2514/6.1986-1347.

C. Park. Assessment of Two-Temperature Kinetic Model For Ionizing Air. *Journal of Thermophysics and Heat Transfer*, 3(3):233–244, 5 1987. ISSN 15336808. doi: 10.2514/3.28771.

C. Park. Assessment of A Two-Temperature Kinetic Model For Dissociating and Weakly Ionizing Nitrogen. *Journal of Thermophysics and Heat Transfer*, 2(1):8–16, 5 1988. ISSN 15336808. doi: 10.2514/3.55.

C. Park. A Review of Reaction Rates In High Temperature Air. In *AIAA 24th Thermophysics Conference*. American Institute of Aeronautics and Astronautics Inc. (AIAA), 1989. doi: 10.2514/6.1989-1740.

C. Park. *Nonequilibrium Hypersonic Aerothermodynamics*. Wiley, 3 1990. ISBN 0471510939.

C. Park. Review of Chemical-Kinetic Problems of Future NASA Missions, I: Earth Entries. *Journal of Thermophysics and Heat Transfer*, 7(3):385–398, 5 1993. ISSN 15336808. doi: 10.2514/3.431.

C. Park. Hypersonic Aerothermodynamics: Past, Present and Future. *International Journal of Aeronautical and Space Sciences*, 14(1):1–10, 3 2013. ISSN 2093-274X. doi: 10.5139/IJASS.2013.14.1.1. URL .

C. Park, J. T. Howe, R. L. Jaffe, and G. V. Candler. Review of Chemical-Kinetic Problems of Future NASA Missions, II: Mars Entries. *Journal of Thermophysics and Heat Transfer*, 8(1):9–23, 5 1994. ISSN 15336808. doi: 10.2514/3.496.

C. Park, R. L. Jaffe, and H. Partridge. Chemical-Kinetic Parameters of Hyperbolic Earth Entry. *Journal of Thermophysics and Heat Transfer*, 15(1):76–90, 5 2001. ISSN 15336808. doi: 10.2514/2.6582.

J. G. Parker, C. E. Adams, and R. M. Stavseth. Absorption of Sound in Argon, Nitrogen, and Oxygen at Low Pressures. *The Journal of the Acoustical Society of America*, 25 (2):263–269, 3 1953. ISSN 0001-4966. doi: 10.1121/1.1907030. URL .

D. Passiatore. *Direct Numerical Simulations of Hypersonic Turbulent Boundary Layers With Thermochemical Non-Equilibrium Effects*. PhD thesis, Politecnico di Bari, 12 2021. URL .

D. Passiatore, L. Sciacovelli, P. Cinnella, and G. Pascazio. Thermochemical Non-Equilibrium Effects In Turbulent Hypersonic Boundary Layers. *Journal of Fluid Mechanics*, 941:A21, 6 2022. ISSN 14697645. doi: 10.1017/jfm.2022.283.

D. Passiatore, L. Sciacovelli, P. Cinnella, and G. Pascazio. Shock Impingement on a Transitional Hypersonic High-Enthalpy Boundary Layer. *Physical Review Fluids*, 8(4): 044601, 4 2023. ISSN 2469990X. doi: 10.1103/PhysRevFluids.8.044601.

D. Passiatore, X. Gloerfelt, L. Sciacovelli, G. Pascazio, and P. Cinnella. Direct numerical simulation of subharmonic second-mode breakdown in hypersonic boundary layers with finite-rate chemistry. *International Journal of Heat and Fluid Flow*, 109:109505, 10 2024. ISSN 0142-727X. doi: 10.1016/J.IJHEATFLUIDFLOW.2024.109505.

D. Pelletier and P. J. Roache. Verification and Validation of Computational Heat Transfer. In *Handbook of Numerical Heat Transfer: Second Edition*, pages 417–442. John Wiley & Sons, Inc., 1 2002. ISBN 0471348783. doi: 10.1002/9780470172599.ch13.

T. L. Peng and A. L. Pindroh. An Improved Calculation of Gas Properties at High Temperatures: Air, D2-11722. *The Boeing Company*, 1962.

A. Peyvan, K. Shukla, J. Chan, and G. Karniadakis. High-Order Methods for Hypersonic Flows with Strong Shocks and Real Chemistry. *Journal of Computational Physics*, 490, 11 2022. doi: 10.1016/j.jcp.2023.112310. URL .

S. Pirozzoli. Generalized conservative approximations of split convective derivative operators. *Journal of Computational Physics*, 229(19):7180–7190, 9 2010. ISSN 0021-9991. doi: 10.1016/J.JCP.2010.06.006.

B. E. Poling, J. M. Prausnitz, and J. P. O'Connell. *Properties of Gases and Liquids*. McGraw-Hill Education, 2000. ISBN 9780070116825.

S. B. Pope. *Turbulent Flows*. Cambridge University Press, 8 2000. ISBN 9780511840531. doi: 10.1017/CBO9780511840531. URL .

J. Qu, S. Yousef, T. Faney, J. C. de Hemptinne, and P. Gallinari. NNEoS : Neural network-based thermodynamically consistent equation of state for fast and accurate flash calculations. *Applied Energy*, 374:124025, 11 2024. ISSN 0306-2619. doi: 10.1016/J.APENERGY.2024.124025.

B. R. Ramaprian, N. D. Sandham, M. G. Mungal, and W. C. Reynolds. Passive scalar tagging for the study of coherent structures in the plane mixing layer. *Physics of Fluids A: Fluid Dynamics*, 1(12):2034–2041, 12 1989. ISSN 0899-8213. doi: 10.1063/1.857477.

J. D. Ramshaw and C. H. Chang. Friction-Weighted Self-Consistent Effective Binary Diffusion Approximation. *Journal of Non-Equilibrium Thermodynamics*, 21(3):223–232, 1996. ISSN 03400204. doi: 10.1515/JNET.1996.21.3.223.

S. A. Richards. Completed Richardson extrapolation in space and time. *Communications in Numerical Methods in Engineering*, 13(7):573–582, 1997. ISSN 10698299. doi: 10.1002/(SICI)1099-0887(199707)13:7<573::AID-CNM84>3.0.CO;2-6.

L. Richardson and J. Gaunt. The Deferred Approach to the Limit. *Philosophical Transactions of the Royal Society of London. Series A, Containing Papers of a Mathematical or Physical Character*, 226(636-646):299–361, 1 1927. ISSN 0264-3952. doi: 10.1098/RSTA.1927.0008.

J. Riley and R. Metcalfe. Direct Numerical Simulation of a Perturbed, Turbulent Mixing Layer. In *18th Aerospace Sciences Meeting*. American Institute of Aeronautics and Astronautics (AIAA), 1 1980. doi: 10.2514/6.1980-274. URL .

R. S. Rogallo. Numerical experiments in homogeneous turbulence. Technical report, NASA Ames Research Center Moffett Field, 9 1981.

R. S. Rogallo and P. Moin. Numerical simulation of turbulent flows. *Annual Review of Fluid Mechanics*, 16:99–137, 1 1984.

M. M. Rogers and R. D. Moser. The three-dimensional evolution of a plane mixing layer: the Kelvin–Helmholtz rollup. *Journal of Fluid Mechanics*, 243:183–226, 1992. ISSN 1469-7645. doi: 10.1017/S0022112092002696. URL .

M. M. Rogers and R. D. Moser. Direct Simulation of a Self-similar Turbulent Mixing Layer. *Physics of Fluids*, 6(2):903–923, 2 1994. ISSN 1070-6631. doi: 10.1063/1.868325. URL .

J. Romero, J. Crabill, J. E. Watkins, F. D. Witherden, and A. Jameson. ZEFR: A GPU-accelerated high-order solver for compressible viscous flows using the flux reconstruction method. *Computer Physics Communications*, 250:107169, 5 2020. ISSN 0010-4655. doi: 10.1016/J.CPC.2020.107169.

B. Ruscic, R. E. Pinzon, M. L. Morton, G. Von Laszevski, S. J. Bittner, S. G. Nijsure, K. A. Amin, M. Minkoff, and A. F. Wagner. Introduction To Active Thermochemical Tables: Several "Key" Enthalpies Of Formation Revisited. *Journal of Physical Chemistry A*, 108(45):9979–9997, 11 2004. ISSN 10895639. doi: 10.1021/jp047912y.

N. D. Sandham and W. C. Reynolds. A Numerical Investigation of the Compressible Mixing Layer. Technical report, 1989. URL .

N. D. Sandham and W. C. Reynolds. Compressible mixing layer - Linear theory and direct simulation. *AIAA Journal*, 28(4):618–624, 5 1990. ISSN 00011452. doi: 10.2514/3.10437. URL .

N. D. Sandham and W. C. Reynolds. Three-dimensional simulations of large eddies in the compressible mixing layer. *Journal of Fluid Mechanics*, 224:133–158, 1991. ISSN 1469-7645. doi: 10.1017/S0022112091001684. URL .

N. D. Sandham and R. D. Sandberg. Direct Numerical Simulation of the Early Development of a Turbulent Mixing Layer Downstream of a Splitter Plate. *http://dx.doi.org/10.1080/14685240802698774*, 10(1):1–17, 2009. ISSN 14685248. doi: 10.1080/14685240802698774. URL .

G. Sanford and B. J. Mcbride. Computer Program for Calculation of Complex Chemical Equilibrium Compositions, Rocket Performance, Incident and Reflected Shocks, and Chapman-Jouguet Detonations. Technical report, 1976.

L. C. Scalabrin. *Numerical simulation of weakly ionized hypersonic flow over reentry capsules*. PhD thesis, 2007. URL .

L. C. Scalabrin and I. D. Boyd. Development of an Unstructured Navier-Stokes Solver For Hypersonic Nonequilibrium Aerothermodynamics. page 6. AIAA, 2005.

C. Scherding, G. Rigas, D. Sipp, P. J. Schmid, and T. Sayadi. An adaptive learning strategy for surrogate modeling of high-dimensional functions - Application to unsteady hypersonic flows in chemical nonequilibrium. *Computer Physics Communications*, 307: 109404, 2 2025. ISSN 0010-4655. doi: 10.1016/J.CPC.2024.109404. URL .

R. N. Schwartz, Z. I. Slawsky, and K. F. Herzfeld. Calculation of Vibrational Relaxation Times In Gases. *The Journal of Chemical Physics*, 20(10):1591–1599, 10 1952. ISSN 00219606. doi: 10.1063/1.1700221. URL .

J. Scoggins, J. Rabinovitch, B. Barros-Fernandez, A. Martin, J. Lachaud, R. Jaffe, N. Mansour, G. Blanquart, and T. Magin. Thermodynamic Properties of

Carbon–Phenolic Gas Mixtures. *Aerospace Science and Technology*, 66:177–192, 7 2017. ISSN 12709638. doi: 10.1016/j.ast.2017.02.025.

J. B. Scoggins and T. E. Magin. Development of Mutation++: Multicomponent Thermodynamic and Transport Properties for Ionized Plasmas written in C++. In *11th AIAA/ASME Joint Thermophysics and Heat Transfer Conference*, Reston, Virginia, 6 2014. American Institute of Aeronautics and Astronautics Inc. (AIAA). ISBN 978-1-62410-281-3. doi: 10.2514/6.2014-2966. URL .

J. B. Scoggins, V. Leroy, G. Bellas-Chatzigeorgis, B. Dias, and T. E. Magin. Mutation++: MUlticomponent Thermodynamic And Transport properties for IONized gases in C++. *SoftwareX*, 12:100575, 7 2020. ISSN 2352-7110. doi: 10.1016/J.SOFTX.2020.100575.

D. Sevastopulo and K. Hille. China tests new space capability with hypersonic missile, 10 2021. URL .

A. J. Smits and J. P. Dussauge. *Turbulent Shear Layers in Supersonic Flow*. Springer New York, second edition, 2006. ISBN 0387261400. doi: 10.1007/B137383.

B. Strand. Summation by Parts for Finite Difference Approximations for d/dx. *Journal of Computational Physics*, 110(1):47–67, 1 1994. ISSN 0021-9991. doi: 10.1006/JCPH.1994.1005.

J. W. Streicher, A. Krish, and R. K. Hanson. Shock-Tube Measurements of Vibrational Relaxation Times In Oxygen and Nitrogen Mixtures Using Ultraviolet Laser Absorption Spectroscopy. In *AIAA Scitech 2020 Forum*, volume 1 PartF, Reston, Virginia, 1 2020a. American Institute of Aeronautics and Astronautics Inc. (AIAA). ISBN 978-1-62410-595-1. doi: 10.2514/6.2020-1940. URL .

J. W. Streicher, A. Krish, and R. K. Hanson. Vibrational relaxation time measurements in shock-heated oxygen and air from 2000 K to 9000 K using ultraviolet laser absorption. *Physics of Fluids*, 32(8):86101, 8 2020b. ISSN 10897666. doi: 10.1063/5.0015890.

J. W. Streicher, A. Krish, R. K. Hanson, K. M. Hanquist, R. S. Chaudhry, and I. D. Boyd. Shock-tube measurements of coupled vibration-dissociation time-histories and rate parameters in oxygen and argon mixtures from 5000 K to 10 000 K. *Physics of Fluids*, 32(7), 7 2020c. ISSN 10897666. doi: 10.1063/5.0012426. URL .

J. W. Streicher, A. Krish, and R. K. Hanson. Coupled vibration-dissociation time-histories and rate measurements in shock-heated, nondilute O2and O2-Ar mixtures from 6000 to 14 000 K. *Physics of Fluids*, 33(5), 5 2021. ISSN 10897666. doi: 10.1063/5.0048059.

W. Sutherland. The Viscosity of Gases and Molecular Force. *The London, Edinburgh, and Dublin Philosophical Magazine and Journal of Science*, 36(223):507–531, 12 1893. ISSN 1941-5982. doi: 10.1080/14786449308620508.

K. Sutton and P. A. Gnoffo. Multi-component diffusion with application to computational aerothermodynamics. In *7th AIAA/ASME Joint Thermophysics and Heat Transfer Conference*. American Institute of Aeronautics and Astronautics Inc, AIAA, 1998. doi: 10.2514/6.1998-2575. URL .

G. Tatsios, A. K. Chinnappan, A. Kamal, N. Vasileiadis, S. Y. Docherty, C. White, L. Gibelli, M. K. Borg, J. R. Kermode, and D. A. Lockerby. A DSMC-CFD coupling method using surrogate modelling for low-speed rarefied gas flows. *Journal of Computational Physics*, 520:113500, 1 2025. ISSN 0021-9991. doi: 10.1016/J.JCP.2024.113500.

S. Terrana, C. Nguyen, and J. Peraire. GPU-accelerated Large Eddy Simulation of Hypersonic Flows. In *AIAA Scitech 2020 Forum*. American Institute of Aeronautics and Astronautics (AIAA), 1 2020. doi: 10.2514/6.2020-1062. URL .

Y. Tian, G. Lin, and J. Guo. Analysis of Mass Diffusion Theory and Models for High-Temperature Multi-Component Gases. *International Journal of Heat and Mass Transfer*, 181:121994, 12 2021. ISSN 00179310. doi: 10.1016/j.ijheatmasstransfer.2021.121994.

E. L. Tipton, R. V. Tompson, and S. K. Loyalka. Chapman-Enskog solutions to arbitrary order in Sonine polynomials II: Viscosity in a binary, rigid-sphere, gas mixture. *European Journal of Mechanics, B/Fluids*, 28(3):335–352, 5 2009a. ISSN 09977546. doi: 10.1016/J.EUROMECHFLU.2008.09.002.

E. L. Tipton, R. V. Tompson, and S. K. Loyalka. Chapman-Enskog solutions to arbitrary order in Sonine polynomials III: Diffusion, thermal diffusion, and thermal conductivity in a binary, rigid-sphere, gas mixture. *European Journal of Mechanics, B/Fluids*, 28 (3):353–386, 5 2009b. ISSN 09977546. doi: 10.1016/J.EUROMECHFLU.2008.12.002.

R. V. Tompson, E. L. Tipton, and S. K. Loyalka. Chapman-Enskog solutions to arbitrary order in Sonine polynomials IV: Summational expressions for the diffusion- and thermal conductivity-related bracket integrals. *European Journal of Mechanics, B/Fluids*, 28 (6):695–721, 11 2009. ISSN 09977546. doi: 10.1016/J.EUROMECHFLU.2009.05.002.

R. V. Tompson, E. L. Tipton, and S. K. Loyalka. Chapman-Enskog solutions to arbitrary order in Sonine polynomials V: Summational expressions for the viscosity-related bracket integrals. *European Journal of Mechanics, B/Fluids*, 29(2):153–179, 3 2010. ISSN 09977546. doi: 10.1016/J.EUROMECHFLU.2009.10.002.

E. Torres and T. E. Schwartzentruber. Direct Molecular Simulation of Nitrogen Dissociation Under Adiabatic Postshock Conditions. *Journal of Thermophysics and Heat Transfer*, 34(4):801–815, 5 2020. ISSN 15336808. doi: 10.2514/1.T5970.

E. Torres and T. E. Schwartzentruber. Direct Molecular Simulation of Dissociating Oxygen Under Adiabatic and Normal Shock Wave Conditions. In *AIAA Scitech 2021*

Forum, pages 1–13. American Institute of Aeronautics and Astronautics Inc. (AIAA), 2021. ISBN 9781624106095. doi: 10.2514/6.2021-0318.

E. Torres, R. L. Jaffe, D. Schwenke, and T. E. Magin. State-Resolved Coarse-Grain Cross Sections For Rovibrational Excitation and Dissociation of Nitrogen Based On ab initio Data For The N2-N System. *Chemical Physics*, 533, 10 2018. doi: 10.1016/j.chemphys.2020.110701. URL .

E. Torres, E. C. Geistfeld, and T. E. Schwartzentruber. Direct Molecular Simulation and Quasi-classical Trajectory Calculation Studies of 5-species Air Mixtures. In *AIAA SCITECH 2023 Forum*. American Institute of Aeronautics and Astronautics (AIAA), 1 2023. doi: 10.2514/6.2023-2429. URL .

P. Valentini, T. E. Schwartzentruber, J. D. Bender, I. Nompelis, and G. V. Candler. Direct Molecular Simulation of Nitrogen Dissociation Based On An ab initio Potential Energy Surface. *Physics of Fluids*, 27(8):086102, 8 2015. ISSN 10897666. doi: 10.1063/1.4929394. URL .

J. T. Vanderslice, S. Weissman, E. A. Mason, and R. J. Fallon. High-Temperature Transport Properties of Dissociating Hydrogen. *The Physics of Fluids*, 5(2):155–164, 2 1962. ISSN 0031-9171. doi: 10.1063/1.1706590.

W. G. Vincenti and C. H. Kruger. *Introduction to Physical Gas Dynamics*. Wiley, New York„ 1965.

P. S. Volpiani. Numerical Strategy To Perform Direct Numerical Simulations of Hypersonic Shock/Boundary-Layer Interaction In Chemical Nonequilibrium. *Shock Waves*, 31(4):361–378, 6 2021. ISSN 14322153. doi: 10.1007/s00193-021-01018-6.

A. W. Vreman, N. D. Sandham, and K. H. Luo. Compressible Mixing Layer Growth Rate and Turbulence Characteristics. *Journal of Fluid Mechanics*, 320:235–258, 8 1996. ISSN 1469-7645. doi: 10.1017/S0022112096007525. URL .

T. Wang, Y. Yi, J. Yao, Z. Q. J. Xu, T. Zhang, and Z. Chen. Enforcing physical conservation in neural network surrogate models for complex chemical kinetics. *Combustion and Flame*, 275:114105, 5 2025. ISSN 0010-2180. doi: 10.1016/J.COMBUSTFLAME.2025.114105.

X. Wang, J. Guo, J. Wang, and S. Chen. Interfaces of High- and Low-Speed Large-Scale Structures in Compressible Turbulent Mixing Layers: Compressibility Effects and Structures. *Journal of Fluid Mechanics*, 981, 2 2024. ISSN 14697645. doi: 10.1017/JFM.2024.55.

F. M. White and J. Majdalani. *Viscous fluid flow*. McGraw-Hill, New York, NY, 2022. ISBN 9781260597806.

C. R. Wilke. A Viscosity Equation for Gas Mixtures. *The Journal of Chemical Physics*, 18(4):517–519, 4 1950. ISSN 0021-9606. doi: 10.1063/1.1747673.

C. T. Williams, M. D. Renzo, and P. Moin. Turbulence–chemistry interaction in a non-equilibrium hypersonic boundary layer. *Journal of Fluid Mechanics*, 1017:A30, 8 2025. ISSN 0022-1120. doi: 10.1017/JFM.2025.10479. URL .

J. Williamson and J. J. Wirtz. Hypersonic or just hype? Assessing the Russian hypersonic weapons program. *Comparative Strategy*, 40(5):468–481, 2021. ISSN 15210448. doi: 10.1080/01495933.2021.1962198. URL .

F. D. Witherden, A. M. Farrington, and P. E. Vincent. PyFR: An open source framework for solving advection–diffusion type problems on streaming architectures using the flux reconstruction approach. *Computer Physics Communications*, 185(11):3028–3040, 11 2014. ISSN 0010-4655. doi: 10.1016/J.CPC.2014.07.011.

K. L. Wray. Shock-Tube Study of The Vibrational Relaxation of Nitric Oxide. *The Journal of Chemical Physics*, 36(10):2597–2603, 5 1962. ISSN 00219606. doi: 10.1063/1.1732339. URL .

M. J. Wright, D. Bose, G. E. Palmer, and E. Levin. Recommended Collision Integrals for Transport Property Computations Part 1: Air Species. *AIAA Journal*, 43(12): 2558–2564, 5 2005. ISSN 00011452. doi: 10.2514/1.16713.

M. J. Wright, H. H. Hwang, and D. W. Schwenke. Recommended Collision Integrals for Transport Property Computations Part II: Mars and Venus Entries. *AIAA Journal*, 45(1):281–288, 5 2007. ISSN 00011452. doi: 10.2514/1.24523.

J. M. Yos. Transport Properties of Nitrogen, Hydrogen, Oxygen, and Air to 30,000 K. Technical report, Massachusetts, 8 1963. URL .

J. M. Yos. Approximate Equations for the Viscosity and Translational Thermal Conductivity of Gas Mixtures. Technical report, Contract Report No. AVSSD-0112-67-RM, Avco Corporation, Wilmington, Massachusetts, 1967.

K. S. Yun and E. A. Mason. Collision Integrals for the Transport Properties of Dissociating Air at High Temperatures. *The Physics of Fluids*, 5(4):380–386, 4 1962. doi: 10.1063/1.1706629.

K. S. Yun, S. Weissman, and E. A. Mason. High-Temperature Transport Properties of Dissociating Nitrogen and Dissociating Oxygen. *The Physics of Fluids*, 5(6):672–678, 6 1962. ISSN 0031-9171. doi: 10.1063/1.1706683.

D. Zhang, J. Tan, and X. Yao. Direct Numerical Simulation of Spatially Developing Highly Compressible Mixing Layer: Structural Evolution and Turbulent Statistics. *Physics of Fluids*, 31(3):36102, 3 2019. ISSN 10897666. doi: 10.1063/1.5087540/260142. URL .

C. Zheng, Y. Feng, and X. Zheng. Effect of Bulk Viscosity on the Hypersonic Compressible Turbulent Boundary Layer. *Journal of Fluid Mechanics*, 982:A24, 3 2024. ISSN 0022-1120. doi: 10.1017/JFM.2024.117. URL .

Q. Zheng, J. Wang, M. Mahbub Alam, B. R. Noack, H. Li, and S. Chen. Transfer of Internal Energy Fluctuation in Compressible Isotropic Turbulence With Vibrational Non-Equilibrium. *Journal of Fluid Mechanics*, 919:A26, 2021. ISSN 14697645. doi: 10.1017/jfm.2021.381.

Q. Zheng, Y. Yang, J. Wang, and S. Chen. Enstrophy Production and Flow Topology in Compressible Isotropic Turbulence With Vibrational Non-equilibrium. *Journal of Fluid Mechanics*, 950:A21, 11 2022. ISSN 14697645. doi: 10.1017/jfm.2022.742.